

Università degli Studi di Napoli Federico II

Doctoral Degree in Industrial Engineering

XXXV Cycle

PhD Thesis

ELECTRICAL HEAT PUMPS: PERFORMANCE DEGRADATION UNDER FAULTY CONDITIONS, FAULT EVALUATION AND INTEGRATION WITH RENEWABLE ENERGY SOURCES

Doctorate Program Coordinator

Prof. Michele Grassi

Tutors:

Prof. Alfonso William Mauro

Prof.ssa Rita Mastrullo

Candidate

Francesco Pelella

Academic year 2021/2022

Summary

Nomenclature 5
1. Introduction 8
2. Context: Heating and Cooling sectors, heat pumps and future perspectives 10
2.1 Heating and cooling sectors 10
2.1.1 Energy demand and CO_2 emissions 10
2.1.2 Decarbonization scenarios 12
2.2 Heat pumps: technologies, regulations, market and common faults 15
2.2.1 Technology 15
2.2.2 Architectures and typical sizes 16
2.2.2.1 Split systems 16
2.2.2.2 Water heat pumps 17
2.2.2.3 VRV systems 18
2.2.2.4 Chillers 19
2.2.3 Regulations 20
2.2.3.1 F-gas Regulation 20
2.2.3.2 Energy Labelling and Eco-design: 24
2.2.4 Market data and future development 26
2.2.5 Common Faults 28
2.2.5.1 Heat exchanger fouling 29
2.2.5.2 Improper refrigerant charge 30
2.2.5.3 Non-condensable in the refrigerant 31
2.2.5.4 Compressor valve leakage 32
2.2.5.5 Liquid line restriction 32
2.2.5.6 Other faults 32
2.3 Future opportunities for heat pumps 32
2.3.1 Artificial intelligence and machine learning tools 33
2.3.1.1 Fault detection, diagnosis and evaluation strategies 33
2.3.1.2 Energy performance prediction, optimization and control 35
2.3.1.3 New Business Model 35
2.3.2 Options of multi-source integrations for traditional heat pumps 36
2.3.2.1 Ground source heat pumps 36
2.3.2.2 Solar assisted heat pumps 38
2.3.2.3 Water source waste heat recovery and sewage heat pumps 40

3. Faults, effects on energetic performance and possibility of fault detection, diagnosis and evaluation 43
3.1 Effect of soft fault on system performance: state of the art 43
3.2 Case study: Residential air-to-air heat pump for domestic heating and cooling 47
3.2.1 Component models in normal operations 48
3.2.1.1 Scroll compressor 48
3.2.1.2 Thermostatic Expansion Valve 48
3.2.1.3 Fin-and-tube heat exchangers 49
3.2.1.4 Refrigerant Charge 50
3.2.2 Fault modelling 50
3.2.2.1 Refrigerant Leakage 50
3.2.2.2 Heat exchangers Fouling 51
3.2.3 Resolution Algorithm 52
3.2.4 Case study data and model calibration 55
3.2.4.1 Case study 55
3.2.4.2 Compressor model calibration 57
3.2.4.3 Valve model calibration 58
3.2.5 Result in cooling mode 58
3.2.5.1 Performance maps of the case study 59
3.2.5.2 Effect of standalone faults on the thermodynamic cycle 62
3.2.5.3 Effect of multiple simultaneous faults on the thermodynamic cycle of the machine 64
3.2.5.4 Assumption and boundary conditions for dynamic simulations 68
3.2.5.5 SCOP and TEWI results for the simulated scenarios 72
3.2.6 Results in heating mode 82
3.2.6.1 Performance maps of the case study 83
3.2.6.2 Effect of standalone and combined faults on the thermodynamic cycle 84
3.2.6.3 Dynamic simulations 87
3.3 Possibility of Fault Detection, diagnosis and evaluation for residential heat pumps 96
3.3.1 State of the art of FDDE 97
3.3.2 Faults analyzed and methodology 102
3.3.3 Results: Fault detection 104
3.3.4 Results: Fault Diagnosis and Evaluation 104
3.3.5 Proof of concept of a ML FDDE tool implementation 110
3.4 Conclusions of Part 1 112
4. Integration of traditional heat pump with renewable energy sources 117

4.1 Multi-source heat pumps: state of the art 117
4.1.1 Energy source exploited 122
4.1.2 Application and thermal storage typology 123
4.1.3 Dynamic performance and comparison between different schemes 123
4.1.4 Optimization of system components and effect of design parameters 124
4.1.5 System control strategies 125
4.1.6 Economic Analysis 126
4.2 Case study 1: 5 kW direct expansion solar assisted heat pump for residential heating 127
4.2.1 Model 129
4.2.1.1 User Load 129
4.2.1.2 Scroll compressor, expansion valve and heat exchangers 129
4.2.1.3 Thermal solar collectors 129
4.2.2 Resolution Algorithm 130
4.2.3 Control strategy development 131
4.2.4 Boundary conditions 133
4.2.5 Results of dynamic simulations 133
4.2.6 Economic Analysis 137
4.3 Case study 2: 10 kW indirect expansion multi-source heat pump for residential heating 139
4.3.1 Component Model 139
4.3.1.1 User Load 141
4.3.1.2 Compressor and heat exchangers 142
4.3.1.3 Ground heat exchanger 144
4.3.1.4 Thermal and photovoltaic solar collectors 145
4.3.1.5 Storage Tank 146
4.3.2 System control strategy 148
4.3.3 Resolution algorithm 150
4.3.4 Case study, boundary conditions and optimization data 151
4.3.4.1 Case study data and boundary conditions 151
4.3.4.2 Optimization variables: decisional parameters and objective functions. 153
4.3.4.3 Optimization tools 155
4.3.4.4 Cost functions 156
4.3.5 Models Calibration and validation 158
4.3.5.1 Calibration of the compressor model 158
4.3.5.2 Validation of the storage tank 1D model 159

4.3.5.3 Efficiencies and specific costs of solar thermal and photovoltaic collectors 161
4.3.5.4 PCM storage tank cost 162
4.3.6 Results 163
4.3.6.1 Steady state and dynamic results 163
4.3.6.2 Sensitivity analysis and Pareto fronts 166
4.3.6.3 Total costs analysis in different price scenarios 171
4.4 Conclusions of Part 2 173
5. Conclusions of the thesis 176
5.1 Principal outcomes of Part 1 176
5.2 Principal outcomes of Part 2 177
References 178
Summary of Figures 194
Summary of Tables 199

Nomenclature

Roman		**Subscripts**	
A	Heat Transfer Surface [m^2]	a, air	Related to air
a	Discount rate [%]	amb	Related to the Ambient
a_1	Effective heat transfer coefficient of thermal solar panels [W/m^2K]	batt	Storage battery
a_2	Second-order coefficient of thermal solar panels [W/m^2K^2]	c	Convective
b_{scale}	Scale coefficient of the solar thermal collectors cost function [-]	clean	Clean surface
C	Costs [€]	co	Related to the condenser
c	Specific heat [J/kgK]	col	Related to Solar Thermal Collectors
$\dot{C}$	Heat capacity [W/K]	comp	Related to the compressor
C_{batt}	Battery Capacity [kWh]	desh	Desuperheating
COP	Coefficient of performance [-]	el	Electric
DF	Discount Factor [years]	equiv	Equivalent
ΔT_{ml}	Logarithmic mean temperature difference [K]	ev	Related to the evaporator
E_{el}	Electric Energy [kWh]	ext	External
F	Correction factor for the F-LMTD Approach [-]	fan	Related to the heat exchanger fan
f_{ee}	Conversion factor for electricity production [$kg_{co_2}/\ kWh$]	foul	Fouled surface
FI	Fault Intensity [%]	g	Global
G	Solar Irradiance [W/m^2]	hex	Related to the Heat Exchanger
GWP	Global Warming Potential [$kg_{CO_2}/\ kg_{ref}$]	hp	Heat pump
H	Height [m]	in	Inlet
HTC	Heat Transfer Coefficient	int	Internal
h	Enthalpy [kJ/kg]	inv	Investment
h_w	Water convective heat transfer coefficient [W/m^2K]	is	Iso-entropic
k	Thermal conductivity [W/mK]	k	Conductive
K_3	Compressor Displacement [-]	L	Liquid
K_4, K_5	Valve mass flow rate calibration coefficients [-]	leak	Refrigerant Leakage
L	Length [m]	max	Maximum
m	Refrigerant charge [kg]	melt	Melting
$\dot{m}$	Mass flow rate [kg/s]	out	Outlet
n	Compressor rotation speed [-]	penaliz	Penalization
N_c	Number of Solar Collectors [-]	pv	Related to Solar Photovoltaic Collectors
$Nh_{90\%}$	Number of hours to reach the 90% of the maximum fouling [h]	ref	Reference
P	Pressure [bar]	refr	Refrigerant
Q	Thermal Energy [kJ]	s	Surface
$\dot{Q}$	Thermal Power [kW]	sh	Superheating
q_1, q_2, q_3, q_4	Calibration coefficients for the compressor global efficiency [-]	sp	Single Phase
R	Thermal Resistance [K/W]	sun	solar
R_1, R_2, P_1, P_2	Parameters for the evaluation of factor F for the F-LMTD approach [-]	tot	Total
S	Transverse Cross-Section [m^2]	tp	Two Phases
s	Specific Entropy [kJ/kgK]	v	Volumetric

SCOP	Seasonal coefficient of performance [-]
T	Temperature [°C]
TEWI	Total Equivalent Warming Impact [kg_{CO_2}]
U	Overall heat transfer coefficient [W/m^{2}K]
UA	Thermal Conductance [W/K]
u_1, u_2, u_3	Fitting coefficients for the solar photovoltaic panel efficiency [-]
unc_T	Uncertainty of temperature sensors [°C]
unc_p	Uncertainty of pressure sensors [bar]
v	Specific Volume [m^3/kg]
V	Volume [m^3]
$\dot{V}$	Volumetric flow rate [m^3/s]
W	Electric Energy [kJ]
$\dot{W}$	Electrical Power [kW]
w	Width [m]
x	Vapor quality [-]
z	Position along the tube, depth in the ground [m]

Greek

α	Void fraction [-]
β	Compression Ratio [-]
γ, υ	Calibration coefficient for the thermal solar collector cost function [-]
Δ	Difference [-]
δ	Coefficient for the evaluation of ground temperature depending on soil properties [m]
η	Efficiency [-]
η_0	Zero-loss thermal solar collector efficiency [-]
η_{el}	Average electricity production efficiency [-]
$\eta_{s,h/c}$	Seasonal space heating/cooling efficiency [-]
ξ	Valve percentage opening [-]
ρ	Density [kg/m^3]
ρ_p	Pearson Coefficient [-]
ϕ_s	Phase of the ground temperature oscillation with external temperature [rad]
ψ	Percentage of the diagnosed fault index [-]
ω	Oscillation period of the ground temperature [years]

V	Vapor
w	Related to water

Prevision accuracy coefficients

$\delta_{\pm perc\%}$	Percentage of points falling into the error band ±perc% [%]
Err_{max}	Maximum Error

Mean Absolute Error:

$$MAE = \frac{1}{N}\sum_{i=1}^{N} |y_i - y_{pred,i}|$$

Mean Relative Error:

$$MRE = \frac{1}{N}\sum_{i=1}^{N} (y_i - y_{pred,i})$$

Mean Absolute Percentage Error [%]:

$$MAPE = \frac{\frac{1}{N}\sum_{i=1}^{N}|y_i - y_{pred,i}|}{y_i}$$

Mean Relative Percentage Error [%]:

$$MRPE = \frac{\frac{1}{N}\sum_{i=1}^{N}(y_i - y_{pred,i})}{y_i}$$

R^2	Coefficient of determination

Abbreviations

AC	Air Conditioning	HIT	Heterostructure with intrinsic thin layer photovoltaic panels
AI	Artificial intelligence	HTF	Heat Transfer Fluid
ANN	Artificial Neural Network	HVAC	Heating, ventilation and air conditioning
APS	Announced Pledges Scenario	IDX	Indirect Expansion systems
ASHP	Air source heat pump	IEA	International Energy Agency
CdTe	Cadmium telluride photovoltaic panels	IIR	International Institute of Refrigeration
CF	Condenser fouling	Inc	Incentives
CFCs	Chlorofluorocarbons	IoT	Internet of Things
CIGS	Copper indium gallium (di) selenide photovoltaic panels	LHS	Latin Hypercube Sampling
DHW	Domestic Hot Water	LMTD	Logarithmic Mean Temperature Difference
DPB	Discounted Payback Period	MEPS	Minimum energy performance standards
DX	Direct Expansion systems	ML	Machine Learning
ECrise	Energy Cost Rise Scenario	MPC	Model predictive control
EF	Evaporator fouling	NZE	Net Zero Emission Scenario
EHPA	European Heat Pump Association	PCM	Phase change material
FD	Fault Detection	PID	Proportional, Integrative and - Derivative controllers
FDD	Fault Detection and Diagnosis	RL	Refrigerant leakage
FDDE	Fault Detection, Diagnosis and Evaluation	SAHP	Solar Assisted heat pump
FXO	Fixed Orifice	SOC	State of Charge
GA	Genetic Algorithm	SPB	Simple Payback Period
GHE	Geothermal heat exchanger	STEPS	Stated Policies Scenario
GSHP	Ground Source Heat Pump	SVM	Support vector machine
HFCs	Hydrofluorocarbons	TXV	Thermostatic expansion valve
HFOs	Hydrofluoroolefines	VRV/VRF	Variant Refrigerant volume / variant refrigerant flow system
HGSHP	Hybrid ground source heat pumps	WSHP	Water source heat pump

1. Introduction

Heating, cooling and domestic hot water energy demand contributes for approximately 20% of the total building load and, due to regulations for future decarbonization, energy consumption of these sectors must be reduced. This will lead to the replacement of traditional technologies based on fossil fuels, towards an electrification generated by the increase of renewable sources. In a scenario where the availability of electric energy will increase, heat pumps will play a fundamental role in the energy transition of heating and hot water production to replace traditional boilers, whereas for cooling heat pumps are already the most commercially developed alternative. This is the reason why the number of heat pump units will increase in the future, and several future opportunities for such systems are already studied by researchers, in order to further reduce energy impact of the building sector. Among them, the development of technologies related to IoT (Internet of Things) and smart devices will allow to collect huge amounts of data from different heat pumps, which can be used in turn to train several artificial intelligence and machine learning models with the aim to predict the future behaviour of machines. As a matter of fact, these models can be used to predict the occurrence of anomalies and faulty conditions, to forecast the energy consumption of heat pumps and to optimize the control logic of complex systems. Regarding faults, indeed, there are several anomalies commonly named as “soft faults” which cannot be easily detected because they do not compromise the continuous machine operations. However, a prolonged functioning of the heat pump in faulty conditions leads to extra-consumptions for the machine itself, and for that reason these typologies of faults should be detected in order to guarantee a certain level of system performance. Therefore, intelligent strategies for the self-detection of soft faults will give a fundamental contribution to increase the average seasonal performances of systems, towards new business models in which user will pay not anymore for the only machine purchase, but for a package of services including heating and cooling delivery, the loan of use of the machine and the maintenance operations.

Another future opportunity for heat pumps regards the possibility to exploit multiple energy sources alternative to air such as the sun or the ground. In that sense, the main goal of the ongoing research is to understand if it is possible to achieve considerable energy savings, and if such systems are thermodynamically and economically convenient compared with the traditional ones, studying the effect of the control strategy adopted to maximise system performance and analysing the effect of sizing factors on seasonal performances and investment costs for such systems.

Therefore, according to these two macro-topics, the objective of this thesis is to carry out different numerical analyses on residential heat pumps, deepening several aspects related to fault occurrence and multi-source exploitation. Regarding faults, the first objective is to analyse the three common soft faults: refrigerant leakages, and evaporator and condenser fouling on domestic and residential heat pumps, analysing their effect on measured parameters and on the thermodynamic cycle of the machine. The dynamic behaviour of an air-to-air heat pump has been analysed along its entire lifetime, considering several scenarios in terms of fault intensities evolution, both standalone and simultaneous, and of maintenance strategies in different climate conditions. Therefore, a comparative investigation has been carried out, in order to understand the condition ranges in which a complete fault detection, diagnosis and evaluation strategy (FDDE) can be applied, or if only a simple anomaly detection can be done due to an overlapping effect of different faults on the measured variables.

Regarding the multi-source exploitation, instead, the main target of this work is to understand the energetic and the economic conveniences of domestic and residential heat pump by using alternative systems such as solar assisted (both thermal and photovoltaic) ground source heat pumps, both in direct expansion configuration, without the employment of a thermal storage, and in an indirect expansion configuration, with a thermal storage which can be sensible with water and latent with phase change materials (PCMs).

Therefore, this thesis has been divided into two different parts. Part 1 deals with to all the analysis conducted regarding soft faults, analysing firstly the effect and then the possibility of a fault detection, diagnosis and evaluation process. Part 2 instead is related to the possibility of integration of multiple sources in traditional air-source heat pumps. Several aspects analysed in this work are sometimes already employed for large capacity systems for which higher investment costs better justify more technologic alternatives. Therefore, the novelty of this thesis is to extend these aspects also for small capacity machines, numerically analysing several case studies of domestic, residential and small commercial heat pumps for heating and cooling.

2. Context: heating and cooling sectors, heat pumps and future perspectives

2.1 Heating and cooling sectors

2.1.1 Energy demand and CO_2 emissions

As a result of the economic growth of several energy intensive sectors, the final consumption of energy all over the world has largely increased in the last years, passing from approximately $25 \cdot 10^4$ PJ of 1990 to over $40 \cdot 10^4$ PJ of 2019 [1], as shown in Figure 2.1(a). Most energy intensive sectors are industry, transport and building, the latter further split in residential and commercial. Figure 2.1(b) shows the total final world consumption in 2019 for each of the sectors mentioned before. It can be noticed that only buildings contribute for almost the 20% of the global energy consumption nowadays.

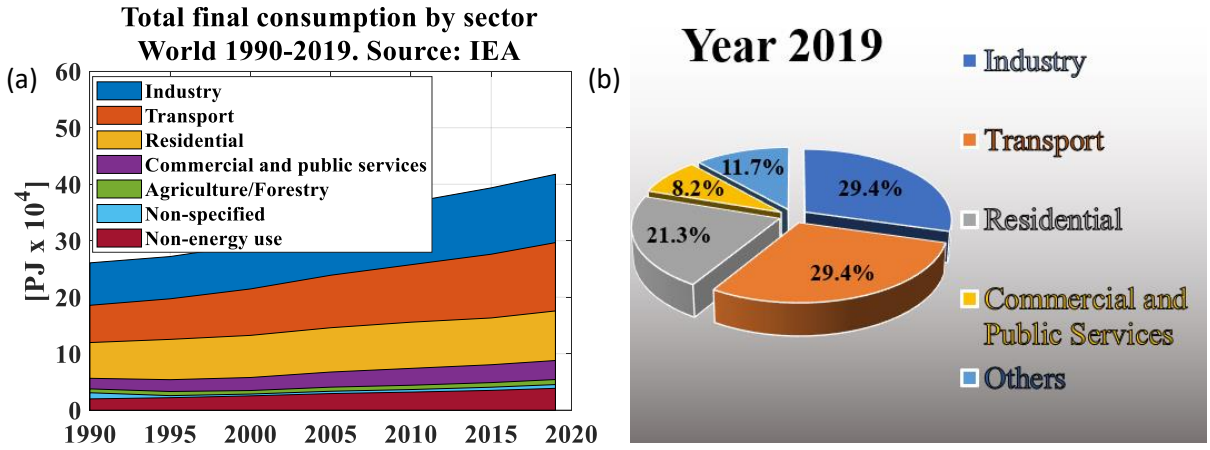


Figure 2.1. Total global final energy consumption by sector for the period from 1990 to 2019 (a) and percentages for year 2019 (b), according to the International Energy Agency (IEA) database [1]

According to the Quadriennial Technology Review of Department of Energy of USA [2], residential and commercial building primary energy use is basically destinated to space heating, space cooling, domestic hot water production, lightning, ventilation, refrigeration and energy consumption of other electric appliances. Particularly, it can be noticed that heating, cooling and water heating sectors represent about the 20% of the total energy use of buildings, as shown in Figure 2.2(a), with the percentage that increases up to almost 75% if only residential buildings are considered, as shown in Figure 2.2(b), according to Maasoumy and Sangiovanni-Vincentelli [3], for which contributions of ventilation, transport and others are almost negligible.

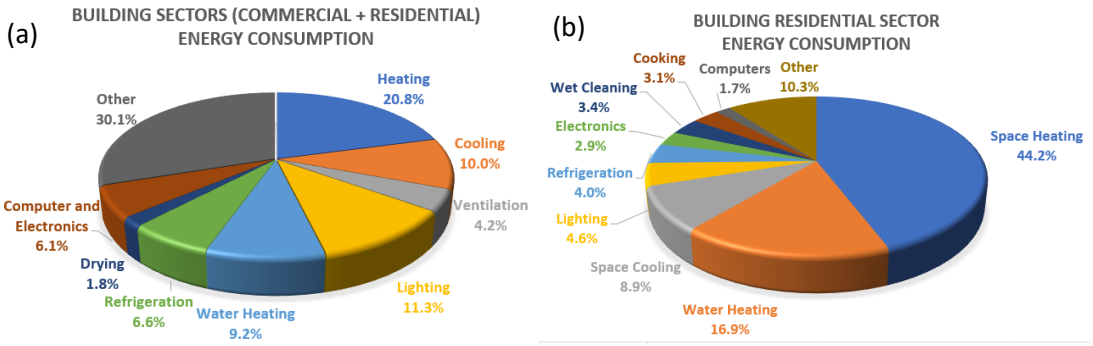


Figure 2.2. Percentages of final use energy consumption, for commercial (a) and residential (b) buildings

Therefore, more than half of the energy demand for residential buildings was used in 2021 to satisfy space and water heating purposes [4], with a total of approximately 2450 Mt of CO_2 emissions. Regarding space cooling, instead, it can be considered as the fastest-growing energy intensive sub-sector in buildings, especially in developed economies where thermal comfort expectations are increasing. As a matter of fact, according to the International Energy Agency (IEA) [5] the final energy use for space cooling in residential and commercial heating is more than tripled in the period between 1990 and 2016, with a share of cooling of the total which passes from 2.5% to 6%, as shown in Figure 2.3. Moreover, all the energy demand is almost covered by electricity, due to technologies available for space cooling.

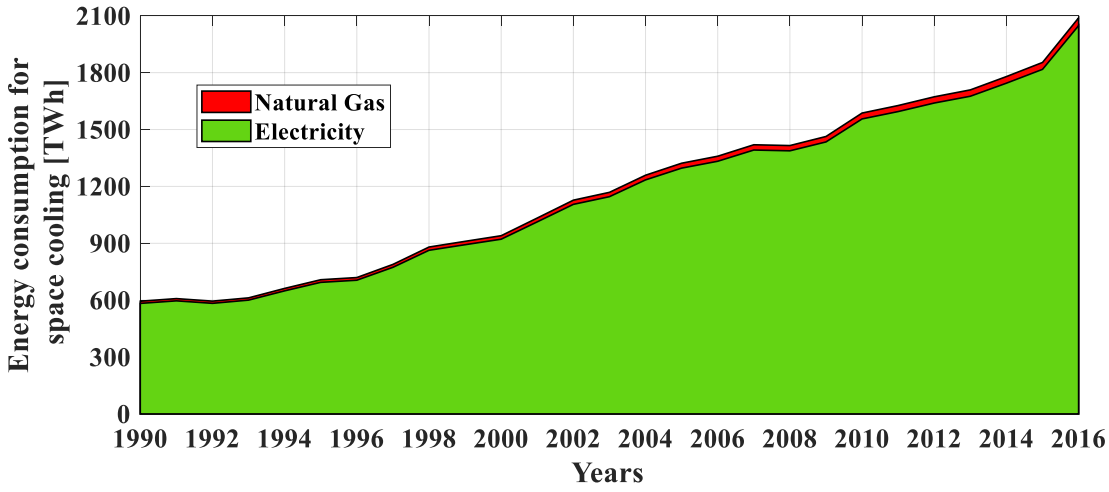


Figure 2.3. Growing of space cooling energy demand between 1990 and 2016, divided by source, according to IEA [5]

Although the considerable increase of renewable energies of the last 10 years, most of the energy production mainly occurs through the burning of fossil fuels, representing in 2021 almost the 77% of the total primary energy consumption, as shown in Figure 2.4(a) according to Ritchie et al. [6]. This reflects on the percentage of fossil fuels quota for the building sectors, which in 2021 amounts approximately to the 40% [7], without considering the actual fossil fuels for electricity production, as shown in Figure 2.4(b).

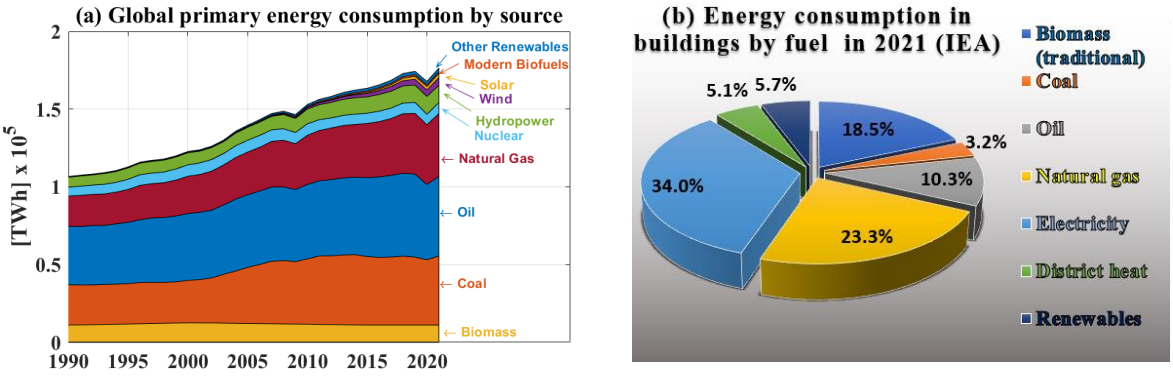


Figure 2.4. (a) Global primary energy consumption by fossil fuels and renewable sources, between 1990 and 2020, according to [6]. (b) Percentage of energy sources in buildings in 2021, according to IEA [7]

2.1.2 Decarbonization scenarios

Several goals and future scenarios for decarbonizing the most energy intensive sectors such as heating and cooling should be adopted. In this regard, the 26th UN Climate Change Conference of the Parties (COP26) [8] hosted in Glasgow in 2021 has fixed several goals in order to reach carbon neutrality by 2050 and to limit the temperature rise within 1.5 °C, fixed by the Intergovernmental Panel on Climate Change [9]. This target can be achieved by encouraging the investments in renewables and by improving the energy efficiency of buildings.

For that reason, the European Community has fixed the improvement target of the energy efficiency for energy production to 32.5%, and to increase the renewable quota on the energy final consumption of UE up to 32% by 2030 [10]. Moreover, by the same year, a reduction target for GHGs emissions of at least the 55% is presented, compared with 1990 levels [11].
Different scenarios to examinate future energy trends have been introduced by the IEA [12]. Among them, the Stated Policies Scenario (STEPS) reflects the current policy setting based on an assessment for each sector of the current policy, as well as those that have been announced in the world. In the run-up to COP26 conference, instead, more than 50 countries have defined their contribution to the global effort to reach the conference goals. The scenario in which all these are implemented by each country is referred as Announced Pledges Scenario (APS), that is, however unable to achieve zero emissions. A Net Zero Emission (NZE) Scenario by 2050 is therefore proposed, setting out a narrow but achievable pathway to the carbon neutrality by 2050.

In Figure 2.5 are presented CO_2 emissions trends in the roadmap to 2050 (Figure 2.5(a)), and the temperature rise in 2100 (Figure 2.5(b)), for each of the scenarios previously defined. Regarding CO_2 emissions, in the STEPS scenario these rises to 36 Gt in 2030, and then remain on a slight descendent plateau up to 2050. In the APS scenario, the emission peak occurs in the middle of 2020 and drops below 30 Gt around 2035. Finally, in the NZE scenario emissions

drop below 21Gt in 2030, and below 10 Gt around 2037. Regarding the temperature rise, instead, the STEPS scenario would lead to a rise in global average temperatures of approximately 2.6 °C in 2100, whereas the APS scenario would lead to a lower average temperature rise of 2.1 °C. However, only the NZE scenario is able to guarantee a global temperature increment below 1.5 °C.

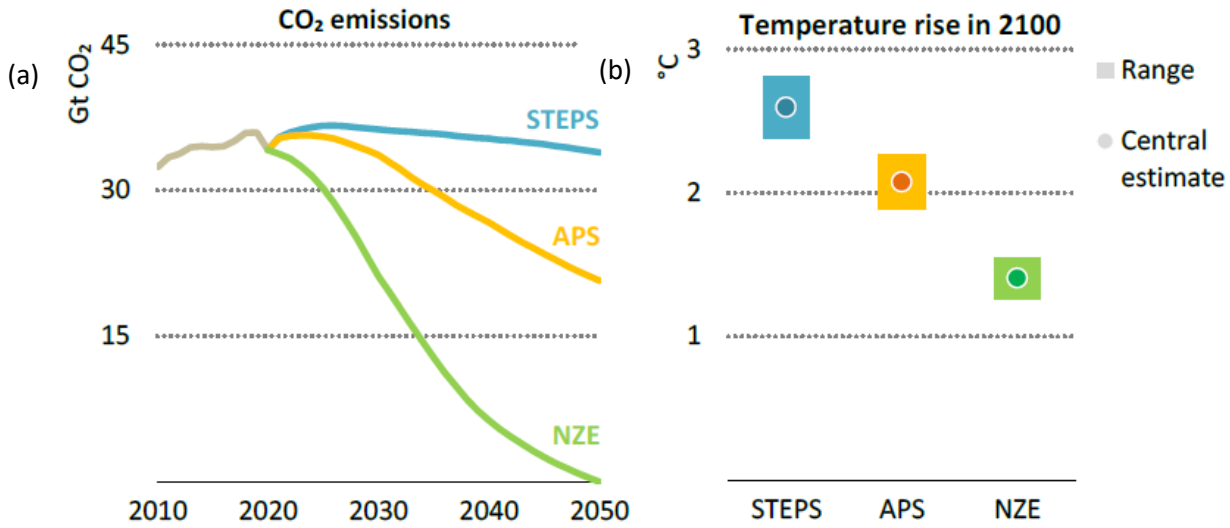


Figure 2.5. CO_2 total emission trends by 2050 (a) and temperature rise prediction in 2100, in the three future scenarios STEPS, APS and NZE defined by IEA [12]

Specifically for the building sectors, the World Energy Outlook 2021 [13] has defined the CO_2 emissions pathways for the APS and NZE scenarios by end-use by 2030, and the final consumption distinguished by source for space heating, hot water production and others, as shown in Figure 2.6. For space heating, direct emissions (Figure 2.6(a)) would be reduced of 15% by 2030 in the APS scenario, and of almost of 40% in the NZE scenario by the same year. Similarly, for water heating a slight reduction of CO_2 emission is expected, to and below 0.5 Gt respectively for APS and NZE scenarios. Regarding instead the energy mix employed to satisfy building needs (Figure 2.6(b)), in the APS scenario it is expected an increase of above 8% of usage of renewable energy sources and a 40% rise of electricity, balanced by a reduction of oil and natural gas. Finally, in the NZE scenario the energy mix changes are even stronger, with a 46% increase of electric energy, a 16% increase of renewable sources, and eliminating the traditional use of biomass.

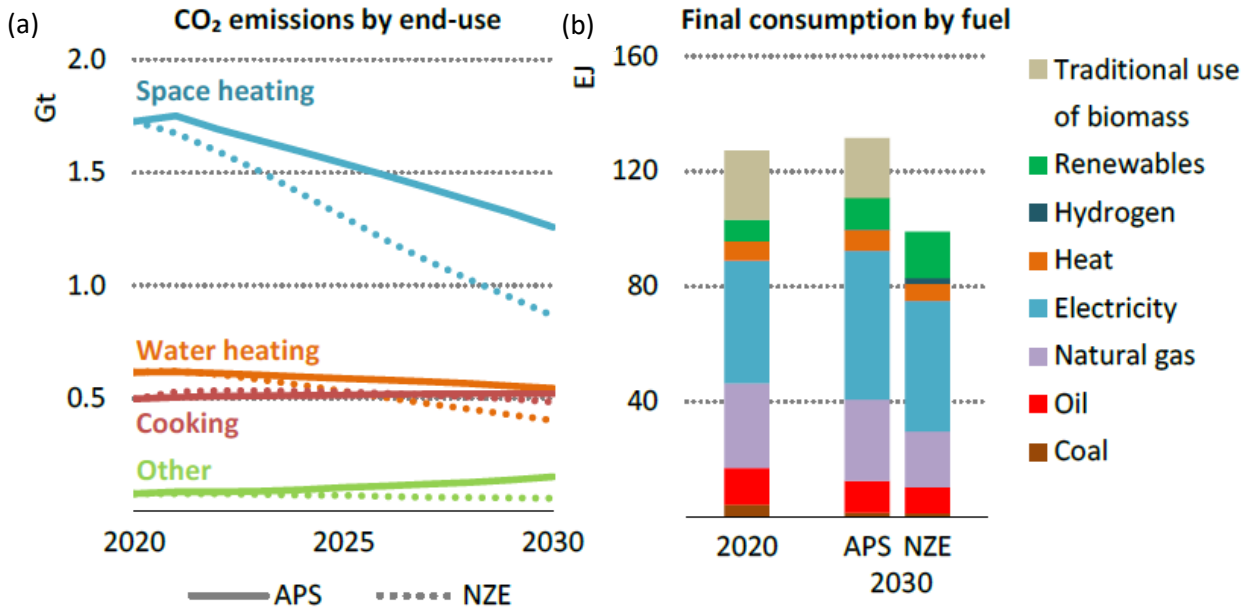


Figure 2.6. (a) CO2 emission trends in buildings up to 2030 for space heating, water heating, cooking and other in the APS and NZE scenarios. (b) Final energy consumption divided by fuel in buildings with future prevision in APS and NZE scenarios

For space cooling, IEA [5] has defined two different possible scenarios to describe future energy trends, which are Baseline and Efficient Cooling. The Baseline scenario considers the effect of current policies and targets, with an energy need for space cooling which will triple by 2050. The Efficient Cooling scenario instead considers an energy pathway based on stronger policy actions to limit energy needs for space cooling, and it is compatible with the goals fixed in the Paris Agreement in 2015. Both future scenarios consider an increase of the energy consumption for space cooling, related to the rise of energy request by 2050, as shown in Figure 2.7. However, while a Baseline scenario predicts an increment of the energy consumption for space cooling of about 200%, an Efficient Cooling scenario would reduce this rise to approximately 43%, with India and China accounting for more than one third of the achievable energy savings.

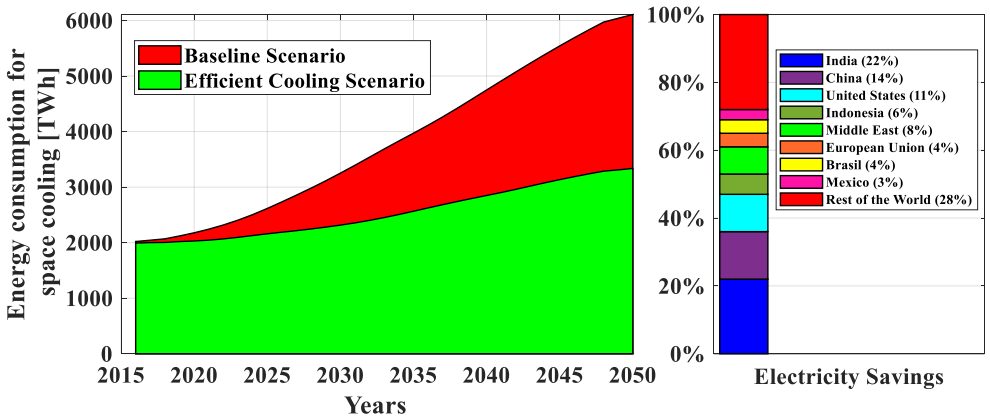


Figure 2.7. Energy consumption trend for space cooling up to 2050, in a baseline and efficient cooling scenarios, and divided per country, according to [5]

2.2 Heat pumps: technologies, regulations, market and common faults

The ongoing increase of renewable energy towards a clean electricity production, such as solar photovoltaic, hydroelectric and wind developments in future scenarios, would lead to an electrification in almost all every energy intensive sectors. In buildings, the increase of electricity would lead to a replacement of traditional fossil fuel boilers with electric heat pumps, both for space heating and hot water production. Therefore, in future scenarios in which electric energy availability due to renewables will further increase, heat pumps will play a fundamental role in the energy transition of heating sector. Furthermore, following the increase of cooling energy request occurring in the last years, heat pumps are already the most commercial technology to provide space cooling, therefore the number of units has largely increased especially in regions both requiring space heating and cooling, especially in their reversible version [13].

2.2.1 Technology

A heat pump is a device that provides heating, cooling and hot water, and it is able to operate a vapor compression thermodynamic cycle, delivering heat from a low-temperature source to a high-temperature sink. As well as in residential applications, a heat pump can be employed also for commercial and industrial applications, in different capacities and efficiencies. However, the heat pump terminology usually refers to an array of different technologies that can be used to deliver heat. Among them, the most common is the vapor compression cycle, which is employed in most of the heat pumps available on the market. This technology employs a refrigerant fluid which is compressed by a compressor and condensate in a first heat exchangers commonly named as condenser. Then, it expands in an expansion valve and finally it evaporated in a second heat exchanger commonly names as evaporator. The most common schematic and the corresponding temperature – specific entropy diagram is reported in Figure 2.8.

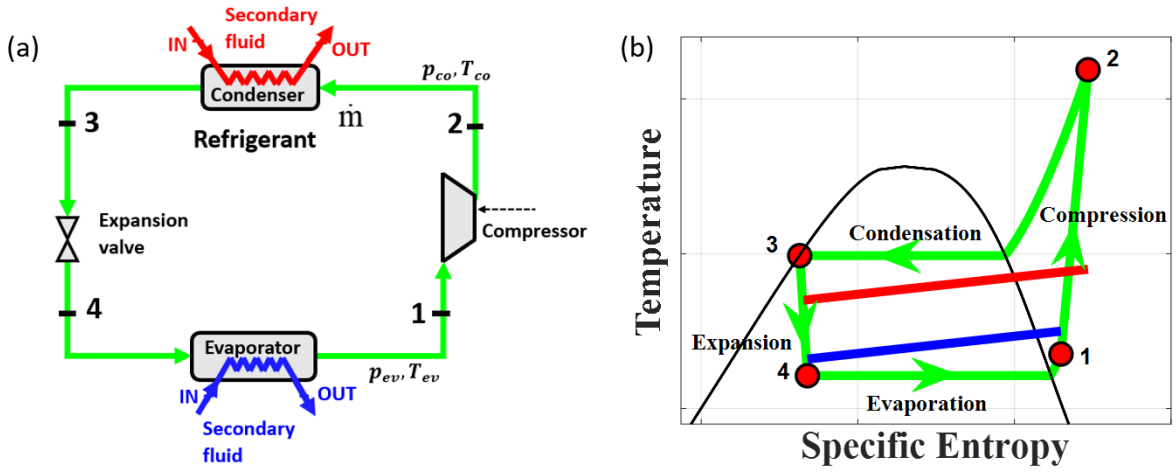


Figure 2.8. General scheme of a vapor compression technology system (a), and thermodynamic cycle on the temperature – specific entropy diagram (b)

Apart from electric vapor compression systems, there are several other less common technologies available. A heat pump compressor indeed can be driven by an electric motor or a fossil fuel engine, with the so-called "Gas-engine driven" heat pumps. Moreover, another alternative to electric energy can be the exploitation of other sources such as solar or waste heat, in absorption or adsorption chillers. Finally, other less common and still prototypal technologies are available to deliver heat from a low-temperature source to a high-temperature sink, based on cold gas compression, thermo-electric, thermo-magnetic and thermo-elastic processes [14].

2.2.2 Architectures and typical sizes

Depending on the kind of application and of the number of users, heat pumps can be characterized by different schematics and system capacities.

2.2.2.1 Split systems

Regarding domestic mono-family applications for air conditioning, the most commonly used machines are split systems. They employ an external unit in which a scroll compressor and a fin-and-tube heat exchanger are placed, and an internal unit equipped with an expansion device and another fin-and-tube heat exchanger. A representation of the external and internal units for a split air conditioning system is provided in Figure 2.9(a), whereas an example of typical schematic, according to Bolaji (2012) [15], is presented in Figure 2.9(b) for cooling mode. These systems are of air-to-air direct expansion (DX) typology.

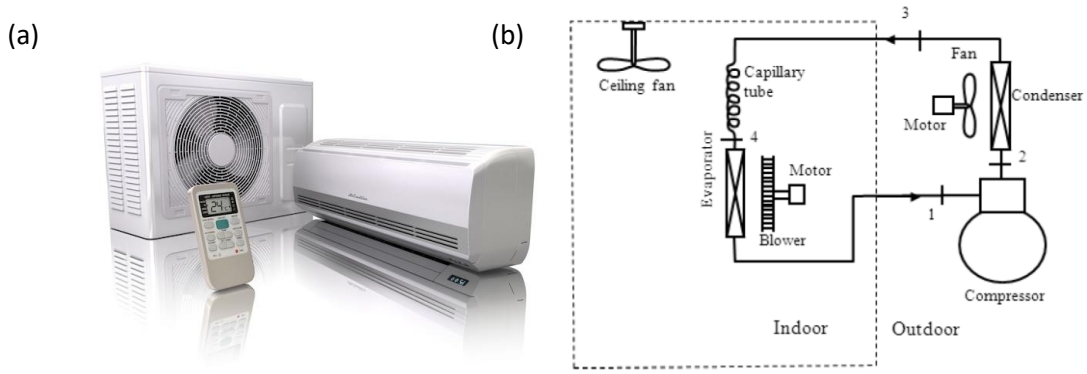


Figure 2.9. Example of a split system (a) and schematic according to Bolaji (2012) [15] (b)

In case of multiple users (up to 2-3), there can be more internal units operating with the same external unit with multi-split systems. In this case, the outdoor unit is equipped with multiple compressors, and the different machines usually operate in parallel. Capacities for this kind of systems can oscillate between 2.5 and 7 kW for mono-split units and between 4 and 12.5 kW for multi-split systems [16]. Apart from stationary split systems, there can be also movable room air-conditioning equipment, used especially when the installation of the external unit is neither easy nor possible due to architectural constraints. These systems are characterized by all the components situated in a unique internal unit. However, they are characterized by a higher level of noise during their operation, therefore several manufacturers (Olympia Splendid Unico) [17] are studying different hybrid options, with stationary units characterized by invisible external units. Refrigerant fluid most commonly used for these systems is R32, and refrigerant charge is usually less than 3 kg.

2.2.2.2 Water heat pumps

For residential heating, cooling and domestic hot water production, when the secondary fluid employed is water, air-to-water heat pumps can be used. For heating and cooling purposes, heat pumps are usually equipped with an air external unit and a water internal unit, and they have to satisfy the user request load through low-temperature heat transfer terminals such as fan coils or floor heating systems. For domestic hot water production, instead, the condenser is placed around a storage tank for water storage, whereas the evaporator can be also placed within a room, without the employment of an external unit. An example of heat pump water heater, from the US Department of Energy [18], is provided in Figure 2.10.

(a) (b)

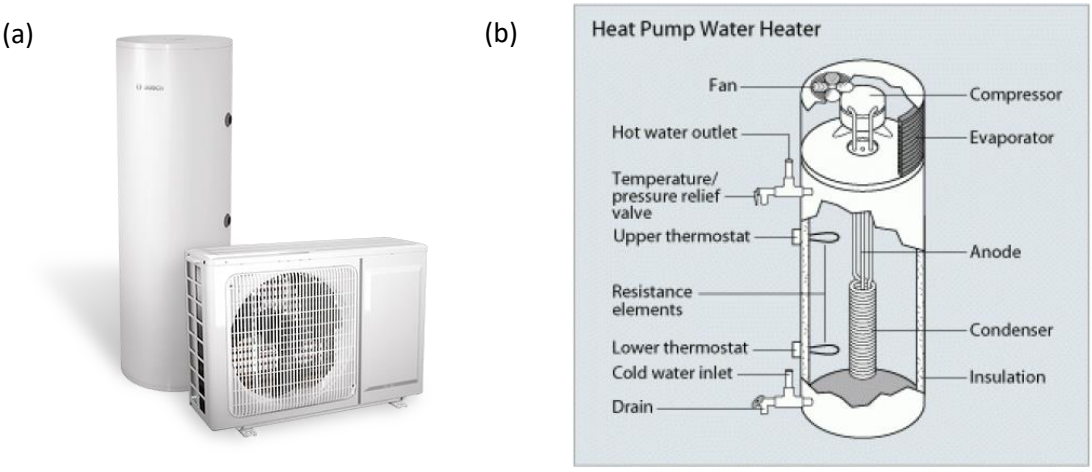


Figure 2.10. Example of a water heat pump (a) and schematic according to [18]

Typical capacities may vary from 3 to 10 kW, and typical refrigerants employed are R134a, R513A [19], R32 [20] and CO_2 [21]. Similar to split systems and due to their limited capacity, these systems almost never overcome 3 kg of refrigerant charge.

2.2.2.3 VRV systems

For a larger number of users requiring thermal load, up to 50-60 [22] and up to a maximum altitude difference between external and internal units of 90-100 m [23], variable refrigerant volume (VRV) or variant refrigerant flow (VRF) systems can be used. In the most diffused version, systems are equipped with only one external unit and several internal units, and three different tubes connecting the external and internal units, as shown in Figure 2.11. As well as split systems, VRF systems are air-to-air DX machines.

(a) (b)

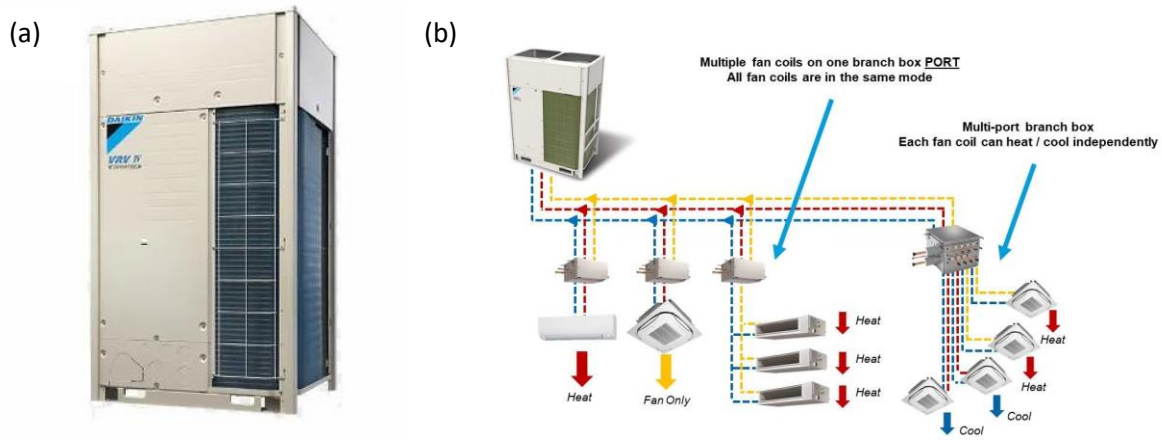


Figure 2.11. Example of a VRF system (a) and schematic (b)

Therefore, the great advantage of such systems is their ability of satisfying contemporary heating and cooling energy demand. As a matter of fact, the external heat exchanger is used only to reject/extract the exceeded heat exchanged between users requiring heating and cooling loads. This is the reason why these systems are very convenient in intermediate climate

conditions when contemporary heating and cooling loads are required (e.g. due to different orientated zones of a building), in which they can reach very high performances. Typical system capacities could vary from 10 to 150 kW, and mostly employed refrigerant fluids are R410A and R32, with refrigerant charges which may vary between 10 and 100 kg. The main problem with these systems is related to the length of the compressor suction lines, and this may cause both high pressure drops and high refrigerant charge amounts. Therefore, several safety measurements must be applied to avoid high refrigerant concentrations within a confined space in case of refrigerant leakages. This is also one of the reasons why the maximum number of users must be limited to 50-60 for such kind of architecture.

2.2.2.4 Chillers

In case of a number of users over 50, no DX system can be used for safety issues. Therefore, the only solutions employable are the indirect expansion (IDX) chillers. These are usually used for air conditioning of large office buildings and can be of two typologies: water-cooled and air-cooled types. Most common water-cooled chillers are equipped with a centrifugal compressor, a flooded evaporator and an outside-tube condenser, and can be entirely situated in a dedicated machine room. An example of centrifugal chiller and of a system schematic, according to Li et al. [24], is provided in Figure 2.12.

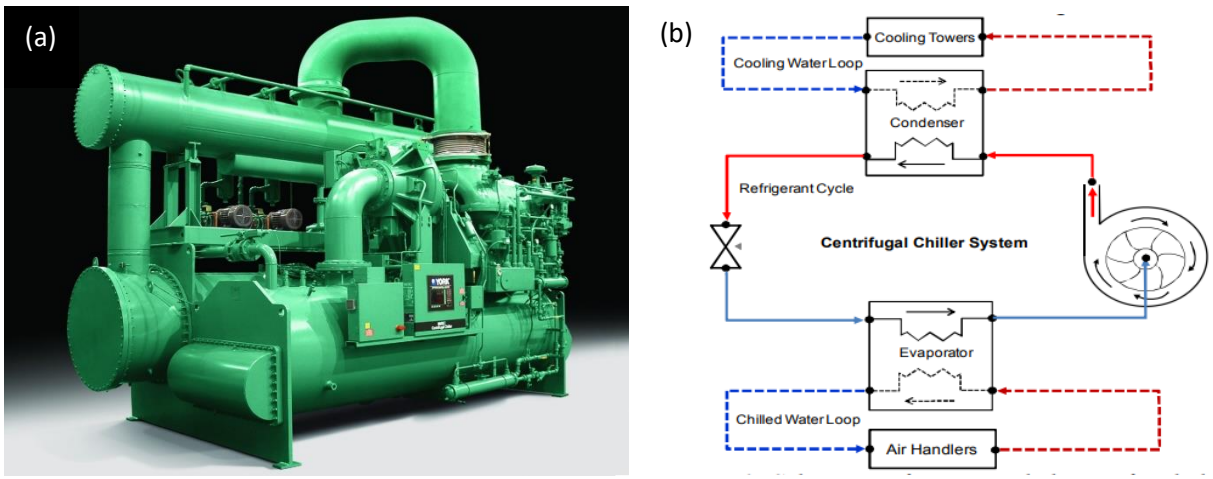


Figure 2.12. Example of a water chiller (a) and schematic according to Li et al. [24](b)

Air-cooled chiller instead can be equipped with scroll or screw compressors, with evaporative condensers, and usually are placed on the top of building roofs. Air-cooled chillers are usually characterized by smaller system capacities between 50 kW and 2 MW [25], whereas higher capacities are reached for water-cooled chillers, from 50 kW to 25 MW [26]. Refrigerants commonly employed are R410A for small capacities, R134a, R1233zd and R513A for higher capacities. Finally, a huge refrigerant charge are required in this case, especially for systems with evaporation and condensing outside tubes, with values up to 2000 kg. However, the

refrigerant charge remains confinated in a service room, without representing a big issue for safety.

2.2.3 Regulations

2.2.3.1 F-gas regulation

In order to protect the environment by the direct emission of refrigerants, the Montreal Protocol in 1987 has phased out numerous substances, such as chlorofluorocarbons (CFCs) held responsible for the ozone depletion potential. In October 2016, instead, the Kigali Amendment to the Montreal Protocol was signed, in order to gradually reduce the consumption and the production of hydrofluorocarbons (HFCs), which are considered as powerful greenhouse gases that contribute to global warming. Particularly, Kigali Amendment [27] fixed different limits in terms of HFCs depending on the typology and on the individual economic condition at the time of the agreement of the country considered. Indeed, countries have been divided into three groups: the first including the "old" industrialized countries for which an HFC reduction of 45% by 2024 and of 85% by 2036 compared with the emissions between 2011 and 2013 has been fixed. The second group includes countries such as China and Brazil, and a HFC reduction of 80% by 2045 has been fixed for them. The same limitations have been imposed for the third group, including several countries such as India and from Middle East, with the deadline extended to 2047.

Regarding air conditioning and refrigeration systems and the direct impact of the refrigerant employed, a report of the European Commission produced in collaboration with Öko-Institut [28] has collected several data of the mass of different kinds of refrigerant banked and leaked in 11000 refrigeration systems in Hungary, in order to evaluate the leakage rate of different high GWP refrigerant on the market. The results of the investigation are reported in Table 2.1. Most of the leakages are related to R404A employed in supermarkets and refrigerated trucks, and to R407C and R410A for air conditioning systems.

Table 2.1. Mass of refrigerant banked, leaked and leakage rate data from 11000 air conditioning systems in Hungary [28], distinguished for type of refrigerant

Refrigerant	**Banked [kg]**	**Leaked [kg]**	**Leakage rate [%]**
R134a	45807.5	2108.0	4.60
R404A	194998.1	21023.1	10.78
R407C	68221.5	8016.1	11.75
R410A	10303.8	468.0	4.54
R413A	116.1	8.0	6.89
R507	216.0	20.0	9.26
Others	169.9	255.4	150.3
Total	319832.9	31898.6	9.97

Regarding the system typology instead, the 24th IIR Informatory Note on Refrigeration Technologies [29] reports a range of values for refrigerant charge and emission factors, for refrigeration and air-conditioning equipment. Particularly, for building air conditioning systems, Chiller are characterized by a leakage rate between 2 and 15%/year of the initial refrigerant charge, whereas this value becomes between 1 and 10%/year for residential and commercial stationary heat pumps and air conditioning systems, and between 10 and 20%/year for mobile air conditioning systems. Results are reported in Table 2.2.

Table 2.2. Values for refrigerant charge amount, installation emission factor, operating emissions, refrigerant remaining at the disposal and recovered for several typology of refrigeration and air-conditioning equipment, according to [29]

Type of Equipment	Refrigerant charge amount [kg]	Installation emission factor [% of the initial charge]	Operating emissions [% of initial charge/year]	Refrigerant remaining at disposal [% of initial charge]	Refrigerant recovered [% of remaining charge]
Domestic Refrigeration	0.05 - 0.5	0.2 – 1.0	0.1 – 0.5	0 – 80	0 – 70
Standalone Commercial Applications	0.2 – 6.0	0.5 – 3.0	1.0 – 15	0 – 80	0 – 70
Medium & Large Commercial Applications	50 - 2000	0.5 – 3.0	10 – 35	50 – 100	0 – 70
Transport Refrigeration	3.0 – 8.0	0.2 – 1	15 – 50	0 – 50	0 – 70
Industrial Refrigeration	10 – 10000	0.5 – 3.0	7 – 25	50 – 100	0 – 90
Chillers	10 – 2000	0.2 – 1.0	2 – 15	80 – 100	0 – 95
Residential and commercial A/C and heat pumps	0.5 – 100	0.1 – 1.0	1 – 10	0 – 80	0 – 80
Mobile air conditioning	0.5 - 1.5	0.2 – 0.5	10 – 20	0 – 50	0 – 80

Therefore, all these studies laid the foundation for the actual "F-gas" regulation 517/2014 [30]. This regulation, which is applied from 1st January 2015, imposes a drastic reduction of the employment of greenhouse gases, with a reduction target of 79% by 2030 (compared with the average emissions between 2009 and 2012). Particularly, this regulation acts by setting two intervention methods:

1) Limiting the market spreading, with a reduction of HFCs depending on their global warming potential (GWP) value, increasing and fixing refrigerant market prices.
2) Constraints and bans for new refrigeration and air conditioning plants, depending on the system typology. In detail:
    - Domestic refrigerators and freezers that contains HFCs with GWP greater than 150, banned from 1st January 2015.
    - Refrigerators and freezers for commercial use (hermetically sealed equipment) that contain HFCs with GWP higher than 2500 banned from 1st January 2020, and higher than 150 banned from 1st January 2022.

- Stationary refrigeration equipment, that contains HFCs with GWP greater than 2500 banned from 1st January 2020, except equipment to cool products below -50 °C.
- Multipack centralised refrigeration systems for commercial use with a rated capacity more than 40 kW, that contain refrigerants with GWP higher than 150 banned from 1st January 2022. The GWP limits becomes 1500 in case of primary refrigerant circuits of cascade systems.
- Movable room air-conditioning equipment (hermetically sealed equipment movable between rooms by the end user) that contain HFCs with GWP higher than 150 banned from 1st January 2020.
- Single split air-conditioning systems containing less than 3 kg of refrigerant with GWP higher than 750, banned by 1st January 2025.

Finally, considering these limitations, all the market sectors have been adapted with new low-GWP alternatives and drop-in fluids, in order to replace high GWP HFCs. Usually, most long-term alternatives are hydrofluoroolefines (HFOs) such as R1234ze and R1234yf, or natural hydrocarbons such as propane, isobutane, or CO_2. The most commonly used high GWP refrigerants with their lower GWP alternatives are reported in Table 2.3, for each of the most developed market sectors and according to the IEA Cooling Emissions Report [31].

Table 2.3. High GWP refrigerants in common use and lower GWP alternatives depending on the refrigeration and air-conditioning sector, according to [31]

Market Sector	**High GWP refrigerant in common use (GWP)**	**Lower GWP alternatives (GWP)**
Small split room for air-conditioning	▪ R407C (1732) ▪ R410A (2088)	▪ R32 (675) ▪ Propane (3)
Mobile air-conditioning	▪ R134a (1430)	▪ R1234yf (4) ▪ R152a (124) ▪ CO_2 (1)
Water chillers for air-conditioning	▪ R134a (1430)	▪ R1234ze (7) ▪ R1233zd (5) ▪ R513A (573)
Domestic refrigeration	▪ R134a (1430)	▪ Isobutane (3)
Food retail systems	▪ R404A (3922)	▪ CO_2 (1) ▪ R448A (1187) ▪ R449A (1397)

2.2.3.2 Energy labelling and eco-design:

The energy efficiency of air conditioning systems can be defined in different ways, considering the following parameters [5]:

- Coefficient of performance (COP), defined as the ratio between the heating energy output to deliver at the user and the electric energy input to the compressor. Similarly, for cooling mode the Energy efficiency ratio (EER) is defined as the ratio between the cooling energy to the user and the electric energy. Whereas COP is a non-dimensional parameter, often EER considers the cooling energy expressed in Btu and the electric energy in kWh.
- Seasonal coefficient of performance (SCOP) or seasonal energy efficiency ratio (SEER), defined as the ratio between the total heating/cooling energy delivered to the user along a certain period, and the total electricity consumption requested by the system to deliver the user load during the same period. It is evaluated considering the same indoor temperature, but over a range of outside temperatures.

Values for energy efficiencies of available commercial air conditioning systems are reported in Figure 2.13 for different system typologies, according to IEA [5]. It can be seen that the global best available technology is characterized by efficiencies which are twice as the market average, and three times the worst efficiency machines for each sector.

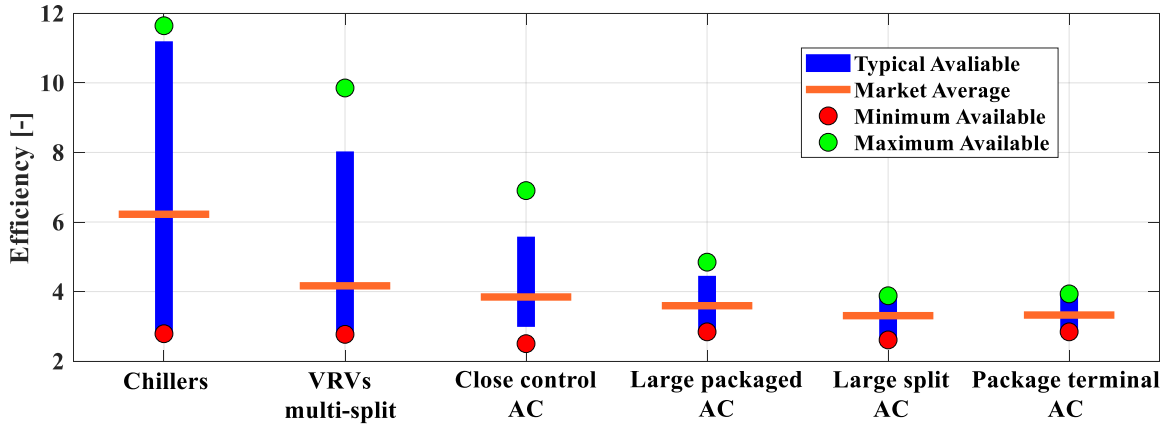


Figure 2.13. Energy efficiency values of available commercial air conditioning systems, according to [5], with minimum, maximum and average available on the market

For this reason, regulations aimed at the improvement of the energy efficiencies of air conditioning equipment in the market have been developed, such as the energy labelling [32] and eco-design [33] regulations. The energy labelling introduces a classification of products in energy classes from A+++ (the best) to G (the worst) updated every year, whereas eco-design fixes minimum energy performance standards (MEPS). As a matter of fact, Eco-design defines

the minimum seasonal efficiency depending on the type of systems between air space heating products, space cooling systems and high temperature process chillers, and distinguishing minimum values within two different threshold tiers, the first from 1st January 2018 and the second from 1st January 2021. In case of air-to-air heat pumps driven by an electric motor, except rooftop systems, the minimum seasonal efficiency for heating have been fixed to 137% in the second tier in heating mode, and to 189% in the second tier in cooling mode. Similar considerations have been done for air-to-water chillers and for water/brine to water chillers depending on the system rated cooling capacity. Minimum seasonal efficiencies within the 1st January 2021 for air heating and cooling heat pumps are reported in Table 2.4.

Table 2.4. Minimum seasonal efficiency to be guaranteed within the 1st January 2021 for different heating and cooling systems, according to the Eco-design regulation [33]

System Technology	$\eta_{s,h/c}$**[%]**
Air Heating Products	
Air-to-air heat pumps, driven by an electric motor, except rooftops heat pumps	137
Rooftop heat pumps	125
Air-to-air heat pumps, driven by an internal combustion engine	130
Cooling products	
Air-to-water chillers with a rated cooling capacity <400 kW, driven by an electric motor	161
Air-to-water chillers with a rated cooling capacity ≥400 kW, driven by an electric motor	179
Water/brine-to-water chillers with a rated cooling capacity <400 kW, driven by an electric motor	200
Water/brine-to-water chillers with a rated cooling capacity ≥400 kW and <1500 kW, driven by an electric motor	252
Water/brine-to-water chillers with a rated cooling capacity ≥1500 kW, driven by an electric motor	272
Air-to-water comfort chillers, when driven by an internal combustion engine	154
Air-to-air air conditioners, driven by an electric motor, except rooftop air conditioners	189
Rooftop air conditioners	138
Air-to-air air conditioners, driven by an internal combustion engine	167

Eco-design regulation also fixed the minimum information to provide in manufacturer datasheets regarding each category of the analysed system. Finally, the regulation defines standard conditions to carry out performance tests for each typology of system investigated, the part load ratio to consider in tests and number of hours in European heating and cooling seasons, for the evaluation of the seasonal performances.

2.2.4 Market data and future development

Number of heat pumps installed has largely increased along years. According to IEA [34] about 190 million heat pump units were in operation worldwide in buildings in 2021, which a quite steady rise of the global stock over the past few years. A record for the heat pump sales was registered also in Europe, with almost 17 million units installed in 2022. In Figure 2.14 is it shown the evolution of the heat pump stock and number of sales per year in the period from 2004 to 2020 according to the European Heat Pump Association (EHPA) Market Report 2022 [35], in which it can be noticed a number of units which is almost doubled between 2013 and 2021, and a number of units sold of 1.61 million units in 2021.

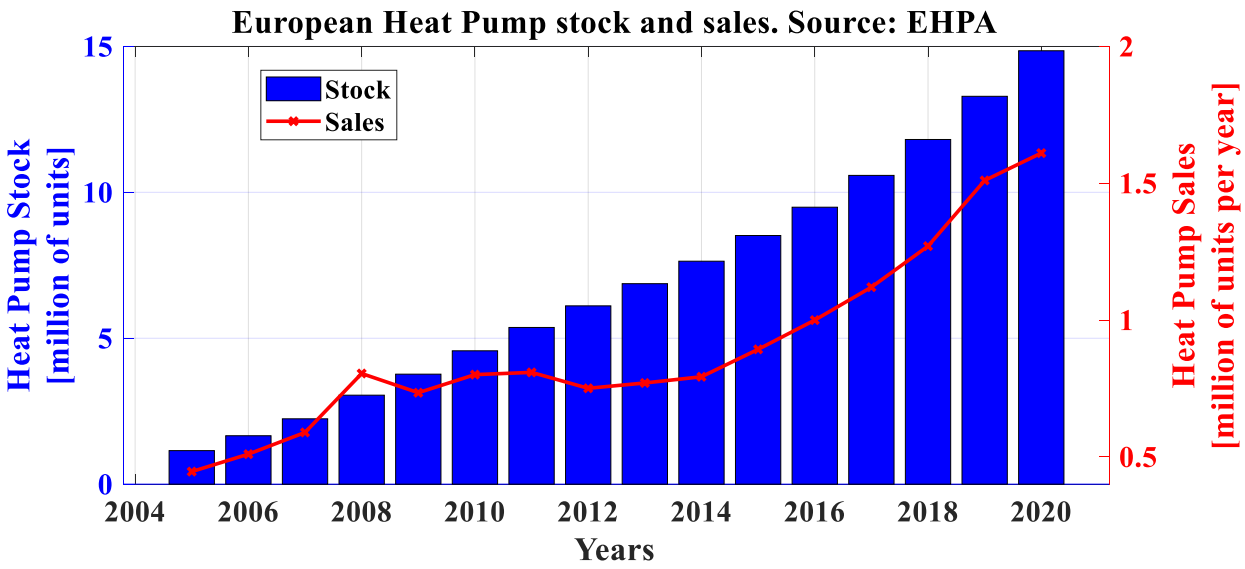


Figure 2.14. Heat pump stock (blue, left axis) and sales (red, right axis) in Europe, between 2004 and 2020 according to the EHPA Market Report 2022 [35]

In Figure 2.15 instead is represented the evolution of heat pump sales divided per typology between ground source, air-to-water and air-to-air. Whereas ground source heat pumps remained almost unchanged during years, a great evolution is registered especially for air-to-water heat pumps for heating and for reversible air-to-air for both heating and cooling purposes. The 87% of the European market volume was sold in only ten countries, with the three biggest European markets in 2020 that were France with 394k units sold, Italy with 233k units sold, and Germany with 140k units sold. France is characterized especially by air-to-water and air-to-air heat pumps for residential heating and hot water production, Italy by a predominance of reversible air-to-air heat pumps (due to a not negligible cooling load, especially in southern regions) and Germany by a balance of ground source and air-to-water systems.

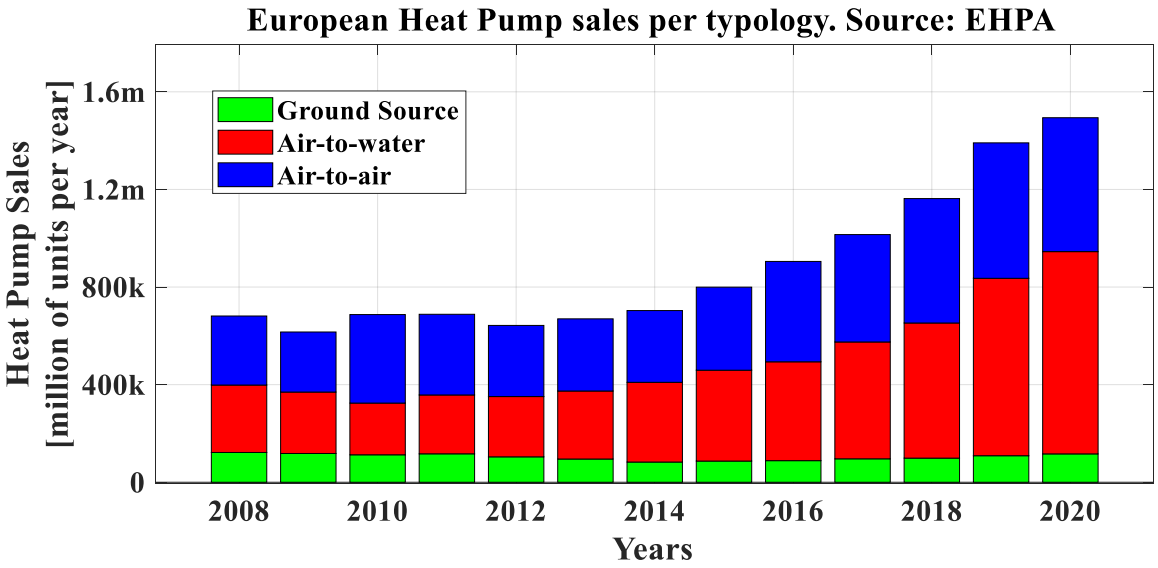


Figure 2.15. Heat Pump sales per typology among ground source, air to water and air to air, in Europe between 2008 and 2020 according to the EHPA Market Report 2022 [35]

Regarding future perspectives, a global heat pump stock rise to about 600 million units by 2030 is expected. For instance, in heating technology sales, whose percentages between 2010 and 2030 are shown in Figure 2.16 according to IEA [36], a percentage of heat pump development by 2030 of 20% is estimated, in an NZE scenario by 2050 defined by World Energy Outlook 2022 [13]. At the same time, a reduction of fossil fuel-based and of conventional electric equipment for heating to respectively 35% and 14% is also predicted.

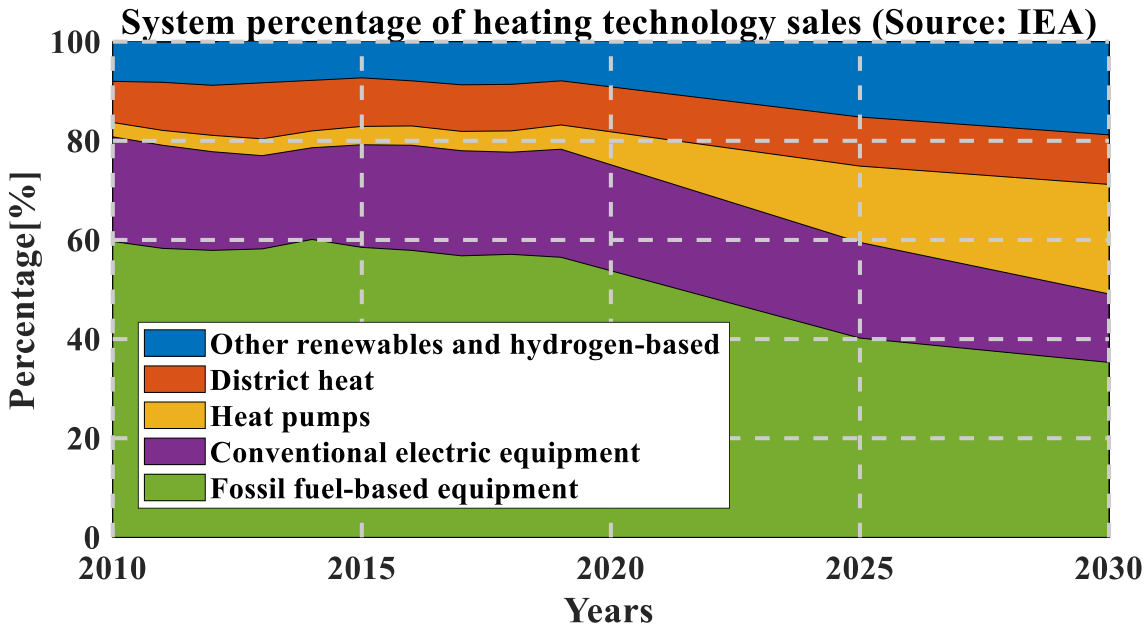


Figure 2.16. System percentage of heating technology sales in the world between 2010 and 2030 in an NZE scenario, according to [36]

2.2.5 Common faults

Heat pumps, especially after several hours of operations, may be subjected to failures which cause either machine downtime or performance degradation. According to Breuker and Braun [37], faults for vapor compression systems can be categorized in two groups: hard and soft failures. Hard faults are related to conditions which are not compatible with the continuous operation of the machines, therefore if the machine is not able to operate anymore, or if a condition of local thermohydrometric discomfort is registered by the user. These faults can occur abruptly, such as a compressor or a fan sudden failure, or as a consequence of an accumulation of other minor faults, in case of lack of maintenance. On the other hand, soft faults cause a degradation in performance, allowing the continuous operation of the system. For example, the accumulation of dust on heat exchanger surfaces, and a slight continuous refrigerant leakage does not compromise the machine operation but lead to an extra energy consumption. Usually, hard failures are more expensive since they need a component(s) replacement. However, the occurrence of hard faults is easier to detect compared with a soft fault, due to the operation stop of the machine caused by the failure, with the possibility of detection also with inexpensive measurements. On the other hand, if a soft fault remains unidentified for long periods of time, it can strongly affect the energy performance of the machine for a long time, increasing consequently the energy consumption and the running costs. Therefore, it is much interesting to understand if it is possible to develop intelligent strategies able to detect and diagnoses soft faults, from measured parameters on the machines. In this way it is possible to achieve an energy saving, avoiding that a soft fault is identified only if its severity reaches such a level to compromise the machine operation or the user comfort. This aspect is already discussed for high-capacity machines, in which the percentage cost of a monitoring system is quite low compared to the entire cost of the heat pump. Otherwise, in case of small capacity machines, a monitoring system, made up of cheap and non-invasive measurements, is of greater interest since it will allow to contain investment costs.

Most common typologies of soft faults registered on heat pumps are condenser and evaporator fouling or mass flow rate reduction, refrigerant leakage, refrigerant overcharge, compressor ageing or valve leakage, liquid line restriction, non-condensable gases in the refrigerant and less common others. A complete list of common hard and soft faults on heat pumps and air conditioning system is provided in Figure 2.17.

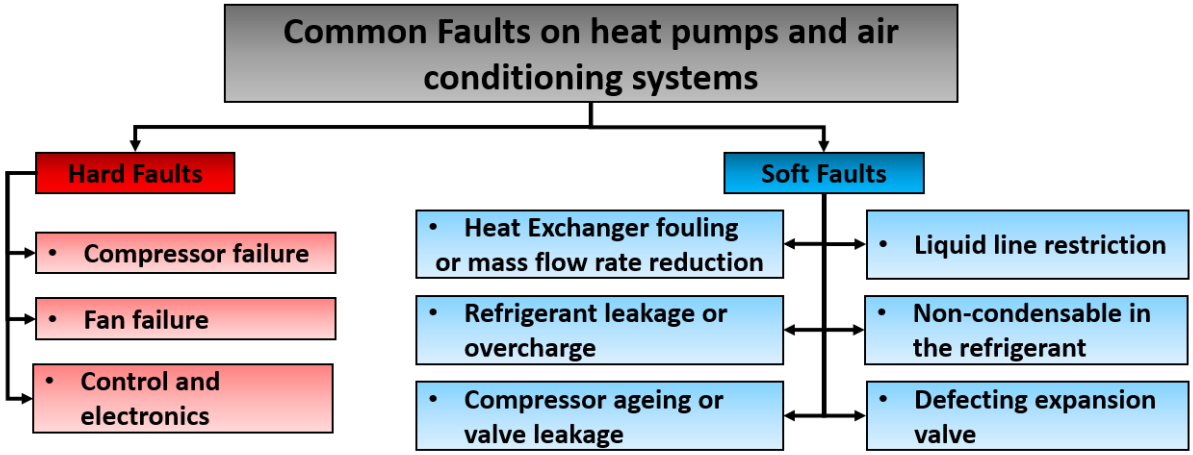


Figure 2.17. List of common faults on heat pumps and air conditioning systems, categorized in hard and soft faults

The effects of a soft fault on a measured parameter of the machine instead can be defined as symptoms, and common parameters mostly affected by faults are condensing and evaporating temperatures, evaporator outlet superheating, condenser outlet subcooling, coefficient of performance, power consumption of the compressor and heating/cooling capacity of the system. According to Mehrabi and Yuill [38], to analyse the cause-effect of each fault, the fault severity is measured by a Fault Intensity parameter (FI), defined depending on the fault typology, whereas the effect on symptoms is quantified by a Fault Impact Ratio (FIR) parameter, defined as the ratio between the measured quantity in faulty and in fault-free conditions. In the following sections, the phenomena for each of the common soft faults are presented.

2.2.5.1 Heat exchanger fouling

Heat exchanger fouling is defined as the accumulation or growth of particles on the surface of the heat exchanger coil, which can degrade the performance of the component. According to Sarfraz and Back [39], fouling phenomena can be divided into several types: particulate precipitate, chemical reaction, corrosion, biological and freezing fouling. For air cooled heat exchangers in HVAC applications, the main mechanisms which can occur are particulate, freezing and biological fouling [40] .

Particulate fouling is related to the accumulation of suspended particles in the air stream on the heat exchanger surfaces. As a matter of fact, in real installations of air source heat pumps (ASHPs), especially in the outdoor unit, is quite common the accumulation of particles, dust, debris, fibres and leaves. According to Inamdar et al. [41], particulate fouling can be divided in inertial impaction, gravitational settling, Brownian motion, the presence of turbulences, thermophoresis and electrophoresis, depending on the deposition mechanism. Additionally, several experimental evidences [42], [43] have observed that fouling mostly tends to

accumulate on the frontal face of the heat exchanger, with a level which gradually decreases passing from the front face to the rear face, according to visual inspections. The effect of this kind of fouling is to increase the pressure drop of the secondary fluid circuit, changing the coupling point between the pump/fan and the circuit and causing a mass flow rate reduction. According to Yang et al. [44], if the level of particulate deposition is at an initial state, in some cases heat transfer can be enhanced due to higher turbulences caused by dust accumulation. Otherwise, if the level of fouling is particularly high, it can also cause both a heat transfer reduction [45], and a penalization of the effective heat transfer surface. Biological fouling instead, sometimes referred as biofouling, is related to the growth of biological material in the fluid stream, especially in case of prolonged presence of water and poor air-circulation [39]. These particles stick on fin surfaces in a uniform way, so they have an influence both on pressure drop and on the heat transfer coefficient (HTC) [46]. Finally, freezing fouling or frosting occurs due to the freezing of condensing water on the heat transfer surfaces.

Regarding to the fouling evolution, according to Awais and Bhuiyan [47], the process is composed of several steps: initiation, transport, deposition, removal and ageing. Initiation refers to the incubation period before the fouling takes hold after a surface has been cleaned. In transport, fouling particles are transported to the surface by deposition processes mentioned above. Deposition instead refers to the attachment of particles on the heat transfer surface. After deposition process, some particles remain stuck on the surface, whereas others are detached by the fluid flow, with a rate of removal which depends on the deposition rate, until a stabilization is reached, when deposition and removal rates become equivalent. Finally, the ageing refers to physical or chemical changes, which may strengthen or weaken the deposit.

To test fouling, the fault is usually reproduced in literature by blocking the secondary fluid inlet. It is the case for instance of the work of Breuker and Braun [37], in which authors simulate uniform condenser fouling by blocking the condenser coil with uniformly spaced, vertical strips of paper, representing a kind of "build-up" of dust and debris on the face-front of the condenser, that causes both an air mass flow rate reduction and a loss of condenser heat transfer area available. In some studies, instead, the fouling is simulated by reducing the secondary fluid flow rate, which is representative also of heat exchanger mechanical component failures such as fans or pumps.

2.2.5.2 Improper refrigerant charge

According to the literature, a refrigerant charge fault is believed as one of the most common and expensive faults in vapor compression systems [48]. As a matter of fact, there is an

interaction between the charge level requested by a system and boundary conditions in which the system is operating. Therefore, a non-correct level of refrigerant charge may lead to several malfunctioning, and so to a performance degradation. An improper refrigerant charge fault occurs when the refrigerant level is too low or too high compared with that requested by the machine. The first case is referred as refrigerant undercharge, whereas the second is referred as refrigerant overcharge [49].

A refrigerant undercharge may happen both if a lower refrigerant charge than requested is employed during the first installation or a maintenance intervention, or if there is a point of leakage into the system pipeline. In the first case, the fault intensity remains the same, whereas in the second it increases until it becomes enough to cause a machine stop [45]. According to Francis et al. [50], over 1464 maintenance operation are recorded for refrigerant leakage in US supermarkets, most of them caused by pipe or joint failures, or leaking seals/glands/cores located in the compressor pack and in the high-pressure line. Often, small leakages are not found, with several recharging processes of plants which are carried out without explanation. In this sense, it is recommended to improve the system design, installation and maintenance of valves and pipes, in order to minimize leakages.

On the other hand, a refrigerant overcharge, differently from a refrigerant undercharge, is only related to an improper installation or maintenance operation by the technician. Refrigerant charge failures are typically experimentally simulated by changing the refrigerant charge amount of a plant. The fault intensity depends on the ratio between the actual and the rated charge of a specific system.

2.2.5.3 Non-condensable in the refrigerant

The presence of non-condensable in the refrigerant is a typical soft fault deriving from an improper refrigerant charge carried out during the first installation or with a maintenance intervention. As a matter of fact, it occurs when the circuit is not completely emptied during a refrigerant charge operation, as a result of the vacuum pump malfunctioning or of an improper operation by a technician [45]. Therefore, the unit begins to run with a mixture of air and refrigerant. Since air is non-condensable, it remains trapped in the high-pressure vapor line.

This kind of fault is usually artificially simulated by adding nitrogen gas in the system pipeline, in different quantities in order to study the effect of different fault intensities on the system performance.

2.2.5.4 Compressor valve leakage

One of the consequences of the compressor ageing is the bypass of refrigerant from the discharge to the suction line. This fault is associated with the suction and discharge valves of a reciprocating compressor, whose seals can break or wear down, causing a compressor valve leakage [45]. The same fault can be found also in scroll compressors, as radial and tangential leakage [51]. Between the compressor valves, if the discharge valve is worn out, some refrigerant from the high-pressure pipeline can go back to the compressor. Otherwise, if the fault is localized on the suction valve, high pressure refrigerant in the compressor during the compression phase can flow back to the suction line.

Furthermore, a similar leakage may occur outside the compressor, in a 4-way valve of a reversible heat pump, but they are classified as the same category of fault due to the same consequences.

In laboratory experiments, this kind of fault is simulated by placing a pipe between the inlet and the outlet of the compressor, with an adjustable 2-way valve in order to simulate different fault intensity levels.

2.2.5.5 Liquid line restriction

A liquid-line restriction occurs when solid particles accumulate on the refrigerant filter/dryer situated between the expansion valve and the condenser [49]. Solid debris are typically welding residuals, or clumps of oil deterioration. The particles clog up the filter increasing pressure drop and decreasing mass flow rate. In a laboratory this fault could be simulated by installing an adjustable valve in series with the expansion valve of the system considered.

2.2.5.6 Other faults

All the already mentioned faults are the most analysed in the literature. However, other unusual soft faults which may occur on vapor compression systems are: liquid compressor floodback, especially for systems with long compressor suction pipelines (e.g. VRF, Zhou et al. [52]), excess of oil and defective expansion valves [45].

2.3 Future opportunities for heat pumps

Among the future opportunities of heat pumps, these can be divided into the ones deriving from digitalization purposes and multi-source exploitation, in order to further reduce energy consumption of machines.

Digitalization leads to the employment of smart meters and measurements through IoT device, which can allow households to remotely control their heating and cooling equipment, to monitor energy consumption reducing costs [53]. The huge amount of data simultaneously collected by

an IoT interface from different machines [54] [55] can be used to train artificial intelligence (AI) and machine learning (ML) tools.

Regarding multi-source exploitation, heat pumps can exploit in an alternate way multiple sources, such as air, solar, ground, etc, in order to maximise system performance in each operating hours of machines. In this way an energy performance and a total cost saving can be achieved compared with traditional air source heat pumps. In this section both the future opportunities related to AI and ML tools, and multi-source exploitation are deepened.

2.3.1 Artificial intelligence and machine learning tools

AI and ML tools can be developed for several purposes in the heat pump sectors. Between them, ML model can be trained for fault detection, diagnosis and evaluation purposes (FDDE) [56], for energy performance and consumption prediction [57] [58], for optimization of new control strategies based on model predictive control (MPC) [59], and for intelligent defrost strategies.

2.3.1.1 Fault detection, diagnosis and evaluation strategies

A self-fault detection method, according to Isermann [60], should include the following steps: fault detection, fault diagnosis and fault evaluation. The fault detection refers to a deviation in the behaviour of the analysed system from normal operating conditions. The fault diagnosis indicates instead the identification phase of the typology of the fault occurred, distinguishing it from other kinds and categories of faults. Finally, a fault evaluation is able to identify the precise fault intensity level of the occurred fault, the corresponding performance degradation and to establish if the fault severity is such as to justify a maintenance operation [61]. All these steps described are not necessary to ensure that a fault detection method works properly, but undoubtedly several information may be lost if only one or two steps are carried out. For instance, if only the operation of fault detection (FD) is carried out, the sole information about the occurrence of an anomaly can be obtained, without extrapolating any information about the fault typology and intensity. On the other hand, if the two operations of fault detection and diagnosis (FDD) are carried out, indication about the occurrence of a fault and about its typology can be obtained, without obtaining any information about the fault(s) severity level.

Several other classifications of FDDE methods can be done. According to Yang et al. [62], FDDE methods can be divided into data-driven, grey box and rule-based methods, depending on the typology for the resolution model employed. Similarly, Zhao et al. [63] classified fault detection methods for buildings in data driven-based and knowledge driven-based. The first class, based especially on ML tools or on statistical methods, is in turn divided depending on the identification models, such as classification models (one or multiclass), regression black-

box models (such as artificial neural network) or unsupervised learning tools (such as clustering). The second class instead is composed of non-artificially intelligence (AI) based methods and can be divided in rule-based and model-based. Between the non-AI methods, physics-based model (white box) employs physical principles and laws to carry out the identification of a fault, whereas grey box can be considered as a hybrid between a data-driven and physic-based approach. The complete classification of FDDE tools according to Zhao et al. [63] is presented in Figure 2.18.

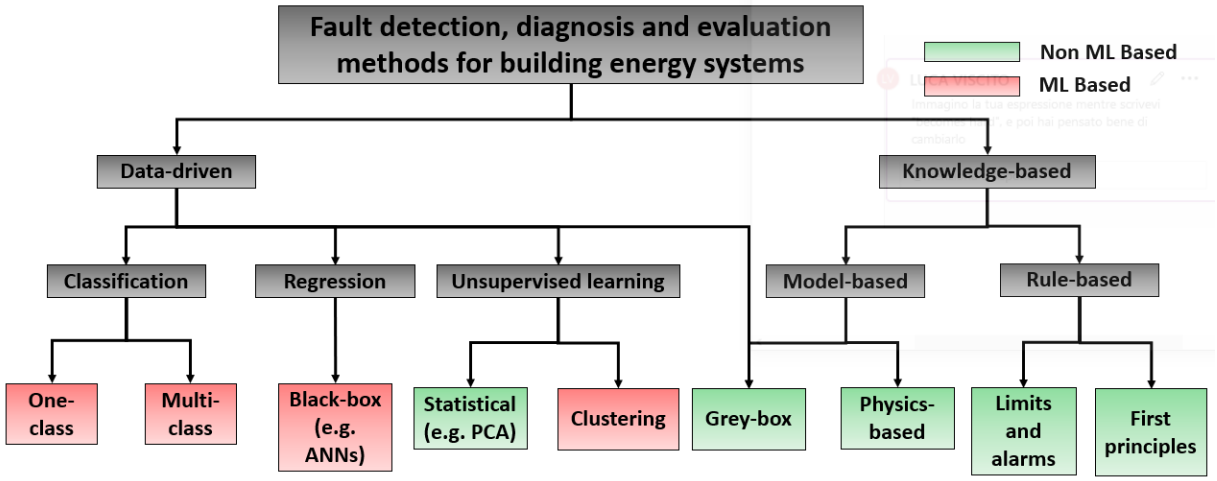


Figure 2.18. Classification of FDDE methods according to Zhao et al. [63]

Each category of FDDE methods has its own advantages and disadvantages. With data-driven methods, due to their ability to learn from available past data, high fault prediction accuracies are achieved, without any physical knowledge of the machine dynamics, Furthermore, they could work properly also in case of incomplete datasets and sensor missing [64], [65]. On the other hand, these models can be used only on the system for which they are calibrated [66], and they need a huge amount of data for the training phase [56] that, if experimentally obtained, will represent an important cost. They tend to degrade prevision performance if input data differs too much from the training dataset [58] and the connection between the physical effect caused by a fault remains unrelated. Furthermore, if multiple simultaneous faults occur, they can lead to similar effects on the machine measured variables, leading to misclassification or misinterpretation. Through physics-based model, instead, it is possible to make a physical direct link between causes and effects on performance of faults [67]. In addition, they can be applied also to different kinds of systems, being therefore more generalizable. However, they usually require higher computational time than calibrated data-driven approaches, and sometimes they still required a calibration in order to satisfy high prediction performance requirements. To overcome the problem of the huge amount of data needed for data-driven models, these datasets

can be generated also by calibrated physics-based methods, limiting experimental activities and achieving savings in terms of time and cost. In the end, the use of data-driven approach could be interesting if low calculation time is needed [68], and if only incomplete datasets are available for FDDE purposes.

2.3.1.2 Energy performance prediction, optimization and control

With AI and ML, an opportunity observed by several works of the literature is to make energy performance and consumption predictions based on measured data. Some of the literature manuscripts have been reviewed in Citarella et al. [68]. Most of these works are calibrated on case study or experimental activities data and employs several inputs such as boundary conditions of ambient or ground temperature, temperatures of a water source/sink, operation time, relative humidity and other weather data to predict COP depending on the system analysed [69], [70] [71]. Among them, only the work of Mathioulakis et al. [72] tried to develop an artificial neural network (ANN) to predict not only the system COP but also its heating capacity, energy consumption and water condenser outlet temperature, for an air-to-water heat pumps considering as inputs the boundary conditions of evaporator air inlet and condenser water inlet temperatures.

Several other works used AI and ML algorithm to carry out system optimization and predictive controls. As a matter of fact, actual controllers used in refrigeration and air conditioning equipment are based on thermostatic or PID logics, which both suffers of non-linearity and time delays during transient operations. Therefore, having a model predictive control (MPC) based on AI and calibrated on field data can overcome the limits of standard controllers. For instance, Ekren et al. [73] compared PID and fuzzy-logic with ANN based controllers on a R134a water chiller, obtaining a lower energy consumption with the ANN of respectively 8.1% and 6.6% compared with the two others, especially due to the lowest response time to external perturbations. Other works, instead [74], [75] optimize the operation schedule of multiple chiller systems with black-box based controllers, obtaining a minimum of operational costs.

Finally, ML models can be used to make frosting prediction and demand defrost optimization. However, these studies are still low and mostly applied to refrigeration systems than heat pumps.

2.3.1.3 New business model

Digitalization, big data, AI and ML tools can be used not only to guarantee a cost reduction. As a matter-of-fact, digitalization created a universal interconnected space, offering new ways of service and customization of products, by integrating physical and digital systems with

advanced technologies [53]. Software-enabled service platforms will guarantee a help towards a correct system design and schedule of maintenance, and can be used also to simulate the behaviour of heating and cooling systems before their effective installation. Specifically regarding heat pumps, a new business model is being studied, in order to convert heating and cooling from machines to services, where the end users pay for the delivery of the kWh of heating and cooling, and not for the machine and electric energy purchase. Service providers in this case must not sell a product, but a complete package consisting of hardware, software, support, maintenance services, and in addition must take charge of the electric energy purchase. In this way, tools able to simulate the behaviour of machines, predict the occurrence of a fault, predict energy consumption and performance could be very interesting for provider service companies, in order to achieve higher cost savings and guaranteeing at the same time the service continuity. This approach is sometimes already applied to large capacity systems, but it will be applied also for residential and commercial small size machines.

2.3.2 Options of multi-source integrations for traditional heat pumps

As clarified before, traditional heat pumps can be integrated with other energy sources, with the scope of exploiting alternative sources in order to increase system performance and decrease energy consumption. Other sources apart from the air such as sun, ground, water, waste heat and others can be used. Therefore, the following alternative systems are analysed in this section: ground source heat pumps, solar assisted heat pumps, water source, sewage and waste heat recovery heat pumps and others.

2.3.2.1 Ground source heat pumps

Ground source, or geothermal heat pumps (GSHPs) use an external heat exchanger made of copper or plastic tubes buried in the ground [76]. This kind of heat pumps led to the possibility of exploiting a higher quality source, thanks to the soil temperature, which can be more stable and different from the external. Figure 2.19 shows the ground temperature evolution with depth into the ground, according to Aydin et al. [77], in which it can be noticed that the ground temperature becomes more stable and less dependent from the season as quick as the depth increases. Therefore, in heating mode, it may happen that the soil has a higher temperature than the external ambient one and it becomes more convenient to evaporate through the ground than through air, whereas in cooling season it may happen that the external temperature is higher than the soil one, leading to a more convenient condensation underground.

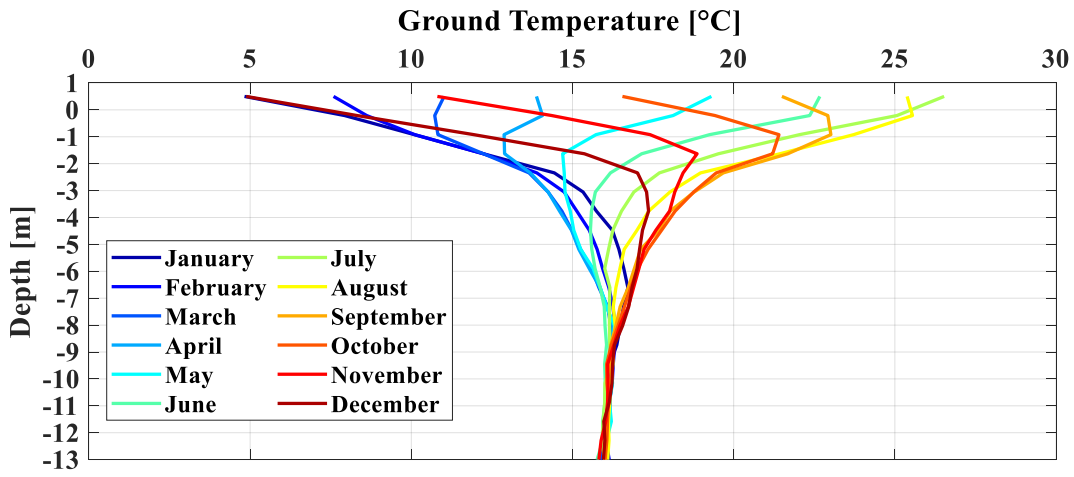


Figure 2.19. Ground temperature distribution depending on the depth and on the month of the year. Source: Aydin et al. [77]

Ground source heat pumps can be categorized based on the circuitry, in open-loop and closed loop. Open-loop systems extract and reject water from groundwater resources such as aquifers, and therefore they need wells to withdraw water from the ground. However, the availability is sometimes limited, and in some countries, they can be some regulations about the usage of groundwaters. Closed-loop systems instead employ a closed circuitry entirely buried in the soil. These can be divided into DX and IDX systems, depending on if directly refrigerant or a water-glycol mixture flows in pipes. Despite the first are characterized by higher performances, due to a higher need of refrigerant charge amounts and due to severe regulations in terms of maximum refrigerant leakage, their number has been reduced along the years. Moreover, closed-loop systems can be further categorized depending on the buried pipeline disposition, if in horizontal trenches or in vertical boreholes. Horizontal ground source heat pumps require more space for the individual site, and usually the depth of the trenches is around 1-2 m, otherwise vertical system boreholes can reach around 100-150 m in depth. Therefore, vertical systems may achieve higher performance due to the more constant ground temperature at a higher depth but are usually more expensive than horizontal ground source heat pumps. A summary of the GSHP classification, with some examples of the system schemes, are reported in Figure 2.20.

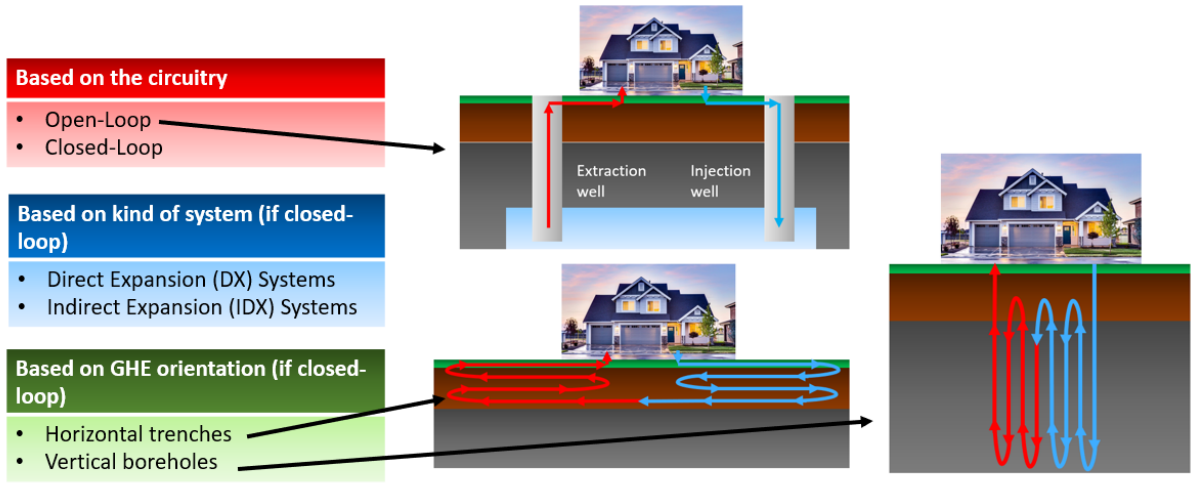


Figure 2.20. Ground source heat pump classification based on the circuitry, on the kind of system and on the GHE orientation (left). Representation of open-loop, horizontal trenches and vertical boreholes systems (right)

Despite all the advantages presented of a ground source heat pump, one of the main disadvantages is related to their installation, which can be more disruptive and expensive rather than a traditional heat pump. As a matter of fact, both horizontal and vertical systems require heavy mechanical interventions, and this led to an increase in installation costs of such systems. Prices usually depend on the volume of the dig to be made and may vary between 40 and 65 $ per m^3 of removed ground [78]. Moreover, a GSHP if used only in heating or cooling season, may affect the temperature of the ground surrounding the pipes. In fact, if the ground is not able to recover the heat extracted or dissipate the heat received, its temperature can change over years causing a performance reduction after several years of operations. Therefore, an accurate study of the ground morphology and physical properties is required before a ground source heat pump installation.

To solve problems related to soil thermal imbalance, defined as the difference between the annual heat rejection and extraction from the ground [79], other kinds of hybrid ground source heat pumps (HGSHPs) can be employed [80]. GSHPs in heating mode can be integrated with fossil fuels, to satisfy the heating load peak, with solar energy and waste heat, as shown in the next section. Otherwise, in cooling mode, the coupling with ice storages or cooling towers can be advantageous. In both cases, the integration of thermal storages, both sensible and PCM type can reduce thermal problems of the soil.

2.3.2.2 Solar assisted heat pumps

Solar assisted heat pumps (SAHPs) can exploit the solar source in different ways to increase system performance of traditional heat pumps. SAHPs are typically employed for domestic hot

water production in warm-climate countries and for space-heating in cold-climate countries [81].

The solar source and SAHPs indeed can be employed in different ways through different typologies of solar collectors [76] integrated in traditional systems. A first classification is based on the kind of solar source, whether photovoltaic or thermal. Solar photovoltaic collectors produce electricity which can be used to feed traditional electric air-source heat pumps, representing a saving of the effective consumption of the machine, whereas thermal solar collectors produce heat which can be used to improve performances. Even if it is quite easy to imagine a photovoltaic integration to a traditional heat pump, the same cannot be said for solar thermal integration, due to the large availability of possible schematics. Thermal solar systems can be categorized between DX and IDX systems [82]. In the first case, refrigerant flows directly into solar collectors which act as an evaporator, whereas in the second case a heat transfer fluid, water or a water/glycol mixture, flows in solar collectors and the refrigerant evaporation occurs in an external heat exchanger. DX systems show promising performance for heating purposes, but the number of hours in which the solar source is exploited can be low due to the effect of a non-constant solar radiation intensity, and the absence of a thermal energy storage located on the source side [81]. Better performances are instead obtained for the domestic hot water production, as shown in Chow et al. [83], due to a more stable energy demand along the entire year. Based on the connection between the heat pump and the solar source, IDX system instead can be further categorized in series, parallel and dual source configurations. In series systems the solar collector produces hot water, which directly flows into the heat pump evaporator. In the parallel configuration instead, both a traditional air source heat pump and the solar source operates in parallel to charge a storage tank in order to satisfy user needs. Finally, a dual source configuration is a hybrid between series and parallel, by using two evaporators, through external air or water by the sun. In this case in some schemes the solar collector pipes can likewise be connected directly with the user. The whole classification of SAHPs, with some schematic examples reported in Chu and Cruickshanks [82], is shown in Figure 2.21.

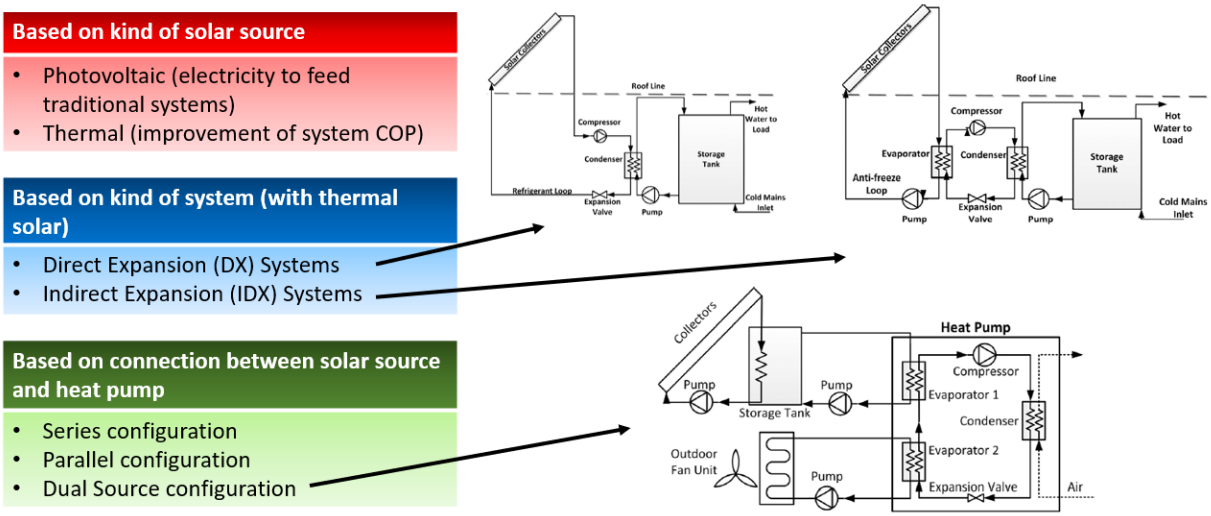


Figure 2.21. Solar assisted heat pump classification based on the kind of solar source, on the kind of system and on the connection between the solar source and the heat pump (left). Representation of DX and IDX systems and of a dual source configuration. Source: Chu and Cruickshanks [82]

Regarding the possibility of a multi-source integration, according to Lazzarin [84] both geothermal and air-source heat pumps could be integrated with a solar source, especially in colder climates. In this way, it becomes possible to alternatively exploit up to three sources, using the best operating modes which guarantee the highest system actual performance depending on external conditions. Finally, future developments of such systems will consider the integration of innovative thermal storages, such as PCMs, or to complicate the system layout through the integration of other multiple renewable energy sources such as wind, solar photovoltaic etc.

2.3.2.3 Water source waste heat recovery and sewage heat pumps

A possible source exploitable by the heat pump is related to a water reservoir, if the water source has a more favourable temperature condition than the external air used in traditional air-source heat pumps. Various typologies of water source heat pumps (WSHPs) can be used [85] such as river, sea, lake water and groundwater (already categorized as open-loop ground source heat pumps). It is obvious that these kinds of machines are developed only for large capacities, between 100 kW and 10 MW, and only if the system is closer to a water reservoir such as a lake or a river. Usually, WSHPs can be categorized based on the kind of water reservoir, between the typologies mentioned before, and based on the water intake system between open-loop, pumping-well and closed loop. In open loop systems, both the withdrawal and injection points are situated in the water reservoir. In this case, a water screening and filtering is required, in order to avoid the entering of biological organisms and other substances. Closed-loop systems instead employ an immersed heat exchanger in the water reservoir, without any requirements of filtering or screening. The most used heat exchanger typologies for these

applications are flat-plane or spiral-helical tube. Finally, the pumping-well system employs an immersed pump in the wet-sump pit of a seashore as withdrawal point, and the water reservoir as injection point. In this way, both advantages given by soil and water temperatures can be achieved and, since the soil has a higher temperature than the water reservoir during the heating season, these systems can be used to improve stability, reliability and energy efficiency for heating in cold climates.

Also, these systems may cause thermal imbalance of the reservoir if thermal extraction and discharge are too different each other. Moreover, regulations usually fix the limits for the temperature difference between the water withdrawal and injection in lakes or rivers. For instance, the Italian regulations (D. Lgs 152/06 [86]) set the maximum variation between upstream and downstream of the injection point temperatures in rivers must not overcome 3 °C, whereas for lakes the discharge temperature must not overcome 30 °C, with a maximum temperature increment of 3 °C over 50 m far from the injection point.

In addition, this kind of heat pump can exploit the heat source coming from a waste heat for power or production plants. As a matter of fact, a significant amount of low-grade waste heat with a temperature between 45 and 60 °C is available from cooling towers and distillation processes [87]. Since the source is usually already at a high temperature (over 30 °C) the recovery of the waste heat is employed to feed other industrial processes at a high temperature over 100 °C, with the employment of high temperature heat pumps [88]. Finally, there are also several promising WSHPs, which exploit thermal energy recovered from urban untreated sewage, with heating and cooling purposes [89].

PART 1

3. Faults, effects on energetic performance and possibility of fault detection, diagnosis and evaluation

3.1 Effect of soft fault on system performance: state of the art

In this section a review about works dealing with the analysis of soft fault and their effect on measured parameters and performances of the machines is provided.

Several works from literature are reported in Table 3.1 and are categorized depending on the typology of system studied, methods employed, and faults investigated.

Table 3.1. State of the art regarding the effect of soft faults on performances and measured parameters of the machines, divided per Application/system studied, method, fault investigated and analysis of simultaneous faults

Author	Application/System studied	Method*	Fault investigated**	Effect of simultaneous faults
Breuker and Braun [37]	10 kW Rooftop	Exp.	RL	No
Comstock and Braun [90]	316 kW Chiller (ASHRAE 1043-RP) [91]	Exp.	CF, CSF, DEV, ESF, EO, NC, RL, RO	No
Grace et al. [92]	R404A 4 kW Chiller	Exp.	RL, RO	No
Qureshi and Zubair [93]	R22 5 kW Split	PB mod.	CF, EF	No
Qureshi and Zubair [94]	R22 5 kW Split	PB mod.	CF, EF	No
Qureshi and Zubair [95]	R22 5 kW Split	Exp.	CF	No
Du et al. [96]	R410A 8.8 -10.6 kW Split. 10.5-17.6 kW Rooftop	MP mod.	CSF, CVL, ESF, RL, RO	No
Mehrabi and Yuill [38]	Different systems, capacities, and fluids	Exp.	RL, RO	No
Mehrabi and Yuill [97]	Different systems, capacities, and fluids	Exp.	CSF, CVL, ESF, LL, NC	No
Kim et al. [49], [98]	44 kW Rooftop	PB mod.	CF, LL, NC, RL, RO	No
Mehrabi and Yuill [99]	Fin and tube condensers	Exp.	CF	No
Noel et al. [100]	R134a ASHP	Exp.	CSF, ESF, RL, RO	No
Hu et al. [101]	R410A 14 kW Split	Exp.	ESF, LL, NC, RL, RO	No
Hu et al. [102], [103]	R410A 14 kW Split	Exp.	ESF, LL, NC, RL, RO	Yes
Bellanco et al. [45]	Propane 10 kW water heat pump	Exp.	CVL, EF, LL, RO	No
Zhou et al. [52]	R410A 15.5 kW VRF	Exp.	CSF, ESF, NC, RL, RO	Yes

*Exp: Experimental; MP: Multivariate polynomial; Mod: Model; PB: Physics-based

**CF: Condenser fouling; CSF: Condenser secondary flow error; CVL: Compressor Valve Leakage; DEV: defective expansion valve; EF: Evaporator fouling; EO: Excess oil; ESF: Evaporator secondary flow error; HPLB: High pressure pipeline blockage; LL: Liquid Line Restriction; NC: Non-condensable in the refrigerant; RL: Refrigerant leakage; RO: Refrigerant overcharge

The following comments try to generalize the fault effects on measured parameters for all the kinds of systems analysed, based on experimental observations of the literature. However, these effects could be more or less marginal depending on the system analysed. For instance, effects of faults can be mitigated by the presence of a thermostatic expansion valve (TXV) compared with a fixed orifice (FXO) as expansion device, or by the presence of a liquid receiver as accumulation point for refrigerant charge.

Most of the analysed faults in literature are heat exchangers fouling and improper refrigerant charge. Regarding condenser fouling, all works analysing this fault agreed that the main influenced symptoms are the condensing pressure and temperature, which both increase with fault severity. The increased compressor lift increases the electricity consumption, whereas the increased evaporator inlet quality causes a cooling capacity reduction. On the other hand, the refrigerant mass flow rate seems not to be significantly affected by condenser fouling.

Regarding evaporator fouling, from all the experimental evidence it results that the most affected variables are evaporating temperature and pressure, which decrease with the increase in fault severity. No significant influences on the enthalpy at the evaporator inlet can be noticed. For FXO equipped systems, the reduced evaporator temperature causes a reduction of the compressor inlet density, leading to a mass flow rate reduction and an increase of outlet evaporator superheating.

Concerning the effect of the refrigerant undercharge or leakage, as shown in literature works, usually the most influenced parameters are outlet evaporator superheating and outlet condenser subcooling, depending on the system analysed. A refrigerant leakage causes both a reduction of evaporating and condensing temperatures. Furthermore, for FXO equipped systems, the outlet evaporator superheating increases, causing a mass flow rate reduction. In order to adapt the requested refrigerant charge by the system depending on boundary conditions, a refrigerant leakage causes a reduction of the subcooling, and may cause in case of strong fault intensity a two-phase condition at the expansion valve inlet. All these aspects results in a system performance reduction. However, in case of an accumulation point presence, a refrigerant leakage fault significantly affects the system performance only in case of no accumulation points, or if the undercharge is so strong that the receiver becomes empty.

Regarding the presence of a refrigerant overcharge, the effects on variables are typically opposite to the ones caused by refrigerant leakage. As a matter of fact, for FXO systems, refrigerant outlet evaporator superheating decreases, whereas outlet condenser subcooling increases with the increase of the refrigerant charge. Both evaporating and condensing

temperatures increase. According to experiments, refrigerant charge levels above the nominal values slightly affect the capacity of the machines, whereas they cause a COP penalization. However, the refrigerant overcharge fault becomes significant only in case of absence of an accumulation point for refrigerant charge, or if the overcharge is so strong that the level overcomes the receiver capacity. For TXV equipped systems, instead, the effect of improper refrigerant charge is quite mitigated compared with FXO systems, until the valve reaches its actuation limits between all open or closed. For instance, in case of refrigerant leakage, if the valve becomes fully open, it is not able to control evaporator superheating anymore, which rises uncontrollably.

Several experimental works analyze the effect of the presence of non-condensable gases in the refrigerant, and the main symptom is an increase of pressure difference between the high- and low-pressure levels, which in turn causes an increase of power consumption of the compressor. According to Comstock et al. [90], the presence of only 1% (by mass) of air makes a chiller completely unusable. The increase of condensing temperature causes a large increase of outlet condenser subcooling. Therefore, a reduction both of capacity and COP of the system is manifested in experimental apparatuses, increasing the fault intensity level.

Liquid line restriction, according to works of the literature, causes a restriction in the liquid line after the condenser, therefore it causes a mass flow rate reduction, with all related consequences. For FXO equipped systems, inlet compressor superheat increases, whereas for system employing TXVs, the effect is almost negligible for small fault severities, due to the capacity of the valve to compensate the restriction by changing its opening percentage. However, when the valve becomes fully open, both the cooling capacity and the COP rapidly decrease with the increase of fault intensity.

According to works of Bellanco et al. [45], Du et al. [96] and Mehrabi and Yuill [97], the flow bypass between the compressor discharge and suction, due to by a compressor valve leakage, causes a lower mass flow rate than the fault-free value. This tends to affect the capacity of the system mainly, and variables such as compressor electrical power, evaporator superheating and condenser subcooling seems to be almost unaffected, especially for TXV equipped systems.

Regarding other faults, excess of oil and defective expansion valve have been studied only by Comstock et al. [90], for a centrifugal chiller. According to the authors, excess oil causes an increase of outlet condenser subcooling, of the condenser approach temperature, of the oil sump and feed temperatures, whereas a defective expansion valve causes especially problems in control evaporator superheating or condenser subcooling.

Finally, among all the works of the literature, only few of them (Hu et al. [102], [103] and Zhou et al. [52]) analyse the effect of simultaneous faults on system performance and on the thermodynamic cycle of the heat pump. Hu et al. [102], [103] analysed up to four simultaneous occurring faults, studying the effect of the overlapping on cooling capacity and COP. Similarly, Zhou et al. [52] analyse the effect on performances and measured pressures and temperatures of simultaneous faults up to three.

3.2 Case study: residential air-to-air heat pump for domestic heating and cooling

In this chapter, the analysis of a residential reversible air-to-air heat pump for domestic heating and cooling, published in Pelella et al. [104], [105], is presented. The main aim of this work is to investigate the effects of soft faults on these kinds of machines. The system is composed of an internal and an external unit. The external unit has a scroll compressor, a fin-and-tube heat exchanger used as a condenser or evaporator respectively in cooling and heating operating modes, a liquid receiver and a thermostatic expansion valve for the heating mode. The internal unit has a fin-and-tube heat exchanger used as an evaporator or condenser respectively in cooling and heating mode, and a thermostatic expansion valve for the cooling mode. The system can be reverted with the employment of a 4-way valve, able to invert the refrigerant flow direction in heat exchangers. For instance, in Figure 3.1 the machine scheme plant is represented in cooling mode, with the refrigerant flowing from the compressor to the outside condenser. Then, passing through the liquid receiver, the refrigerant reaches the expansion valve and the evaporator in the internal unit, before to return back to the compressor. Both thermostatic valves operate to maintain a fixed value for the evaporator superheating, whereas the liquid receiver can guarantee in normal operation an expansion valve always fed with saturated liquid. On/off valves are instead used to guarantee the correct inversion of the cycle.

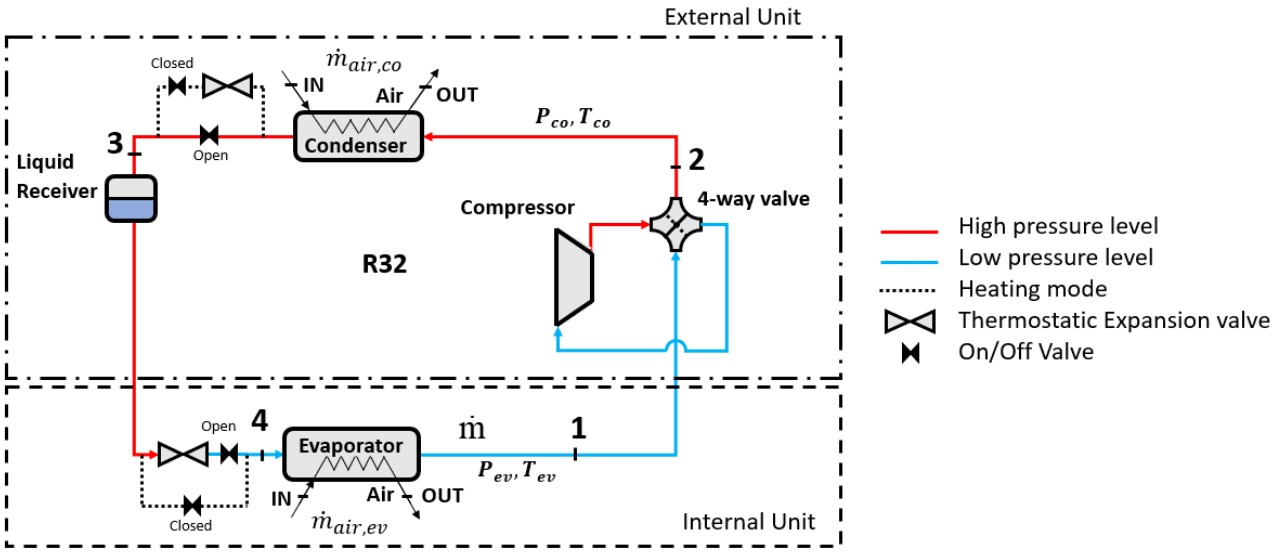


Figure 3.1. Schematic and piping of the residential air source heat pump studied in Pelella et al. [104] for domestic heating and cooling

3.2.1 Component models in normal operations

All models provided in this section have been implemented in MATLAB [106], with the aim of Refprop 9.1 [107] for thermodynamic properties evaluation. Therefore, the sub-models have been coupled to simulate the behaviour of the entire system.

3.2.1.1 Scroll compressor

Regarding the compressor, the mass flow rate and the electrical energy consumptions are evaluated with the following expressions:

$$\dot{m}_{comp} = \rho_{in} \cdot \eta_v \cdot \frac{n}{60} \cdot K_3 \tag{3.1}$$

$$\dot{W}_{el} = \frac{\dot{m}_{comp} \cdot (h_{out,comp,is} - h_{in,comp})}{\eta_g} \tag{3.2}$$

ρ_{in}, n, K_3 are respectively the refrigerant density at the inlet, the rotational speed and the displacement of the compressor, whereas $h_{out,comp,is}$ and $h_{in,comp}$ are respectively the iso-entropic outlet and inlet enthalpies of the compressor. η_v and η_g are the volumetric and global efficiencies, which are obtained from a fitting process from manufacturer data, as done in Botticella et al. [108], and through the model of Navarro-Peris et al. [109] Further details on the calibration process are given in section 3.2.4.

3.2.1.2 Thermostatic Expansion Valve

Regarding the expansion process in the thermostatic valve, all the dissipations are considered after the throat section, where the valve is designed to cause a fluid detachment so that to avoid any pressure recovery. Therefore, for the first part of the valve body, from the inlet to the throat

section, the process is considered iso-entropic. Assuming equal pressures between the outlet and the throat sections of the valve, the following expression has been used for the evaluation of valve mass flow rate.

$$\dot{m}_{valve} = \xi \cdot \rho_{in} \cdot K_4 \cdot \sqrt{\frac{2 \cdot \bar{v}_{in-out,is} \cdot (p_{in} - p_{out})}{\left(\frac{\rho_{in}^2}{\rho_{out,is}^2} \cdot K_5 - 1\right)}} \tag{3.3}$$

$p_{in}, p_{out}, \rho_{in}, \rho_{out,is}$ are respectively the valve inlet and iso-entropic outlet pressures and densities, $\bar{v}_{in-out,is}$ is the mean specific volume along the iso-entropic process between the input and throat sections, whereas ξ is the percentage of the valve opening. K_4 and K_5 are instead two calibration coefficients calibrated on experiments or manufacturer data. It can be noticed that, according to experiments, a choked flow is considered to avoid the evaluation of the effective speed of sound, when the valve mass flow causes a valve choking. The results of the calibration procedure are provided in section 3.2.4.

3.2.1.3 Fin-and-tube heat exchangers

The modelling of heat exchangers is divided into two steps: the geometrical and the heat transfer characterization. Regarding the geometrical modelling, the main geometrical features have been evaluated according to Shah and Sekulic [110], with overall dimensions such as length, width, height, internal and external tube diameters which have been used to evaluate the number of fins, number of rows, number of tube per row, external and internal heat transfer surfaces. Both heat exchangers have been considered with plain fins.

For each row, the tube length is divided into several infinitesimal control volumes. For each of them the overall conductance is evaluated according to the following equation:

$$dUA = \frac{1}{dR_{c,int} + dR_k + dR_{c,ext}} \tag{3.4}$$

$$dR_{c,int} = \frac{1}{HTC_{refr} \cdot A_{int,hex}} \tag{3.5}$$

$$dR_k = \frac{ln\left(\frac{d_{ext}}{d_{int}}\right)}{2\pi k L} \tag{3.6}$$

$$dR_{c,ext} = \frac{1}{HTC_{air} \cdot A_{ext,hex}} \tag{3.7}$$

The model considers convection thermal resistances in the refrigerant and air sides ($dR_{c,int}, dR_{c,ext}$), and conductive heat transfer through the metal (dR_k). Temperatures and enthalpies of refrigerant and air are integrated over the entire length of the tube. Therefore,

another row is added, and the calculation continues up to the effective heat transfer surface, as also presented in the work of Botticella et al. [108]. Regarding the heat transfer characterization, for the evaluation of the HTC several correlations from the literature are used. For refrigerant, prediction methods of Gungor and Winterton [111] for flow boiling, that was seen to perform well for R32 [112], Shah [113] for flow-condensation and Dittus-Boelter [114] for superheated vapor are employed. The air-side HTC is instead obtained with Wang and Chi [115] correlation for plain fins. The external heat transfer surface considers a fin efficiency evaluated through Schmidt approximation [116]. Finally, the coupling between fans and heat exchanger coils was solved to evaluate the effective air mass flow rate and air pressure drop across fin-and-tube heat exchanger coils, through fan characteristic curves reported in section 3.2.4.1, and fixing the geometric free-flow area of the heat exchanger.

3.2.1.4 Refrigerant Charge

The refrigerant charge has been evaluated considering the two contributions of single phase (vapor and liquid) and two-phase charges:

$$m_{tot} = m_{sp} + m_{tp} \tag{3.8}$$

For two-phase flow in the heat exchanger tubes, the refrigerant charge is obtained by using the following expression:

$$dm_{tp} = S[\rho_L(1-\alpha) + \rho_V\alpha]dz \tag{3.9}$$

S is the cross-sectional surface of the tube, whereas $\alpha = V_V/V_{tot}$ is the volumetric void fraction, which has been evaluated through Rouhani – Axelsson correlation [117]. For single phase sections, the following equation is employed:

$$dm_{sp} = \rho\, Sdz \tag{3.10}$$

For the evaluation of the total amount of refrigerant charge into the system, only the amount of charge in the heat exchangers and in the liquid line is considered. The refrigerant of the compressor line has been instead neglected.

3.2.2 Fault modelling

3.2.2.1 Refrigerant leakage

To identify the refrigerant leakage intensity level, a parameter called fault intensity (FI) is employed, which is directly related to measurable quantities applied in a laboratory experiment or in a numerical simulation. In case of refrigerant leakage, according to Yuill and Braun, the fault intensity can be defined as follow.

$$FI_{leak} = \frac{m_{nominal} - m_{actual}}{m_{nominal}} \cdot 100 \quad (3.11)$$

The nominal value of refrigerant charge considered for the system studied is assumed equal to the maximum value requested in all the simulated operating conditions. In all other conditions, the liquid receiver is used as an accumulation point to store the exceeded refrigerant charge. A refrigerant leakage faulty condition of the machine is considered only when the liquid receiver becomes empty, when the valve starts to be fed with saturated vapor. Hence, the lower density of the refrigerant at the valve inlet causes a valve flow chocking. This phenomenon leads to a variation in the coupling fluid-dynamic point between the compressor and the valve, causing both a mass flow rate and an evaporation temperature reduction. All the consequences of these aspects are further described in the results. Furthermore, the phenomenon is considered equal for both heating and cooling operating modes.

3.2.2.2 Heat exchangers fouling

Between all the typologies of heat exchanger fouling previously mentioned, for the cooling mode only particulate type of fouling is considered in this analysis, due to the operating temperatures that prevent the formation of frost on heat exchanger fins on the internal unit, and the difficult conditions in which biofouling takes hold. In heating mode, instead, frosting on the external unit has been neglected, since if low temperature conditions occur, frosting can cause a relative fast performance degradation which can be identified by dedicated defrosting systems, which are not the object of the study of this work. Figure 3.2 shows the heat exchanger elementary geometry, in case respectively of clean surfaces, external and internal heat exchanger fouling. Regarding the heat pump external unit fouling process, according to several experimental evidences [42] [43], the accumulation of particulate dust in the condenser is considered only along the frontal face area of the heat exchanger occupied by the first row of tubes, with a uniform dust distribution along the first-row fins which could be considered in an initial phase. With the progress of dust accumulation, it can happen that several elementary cells of the heat exchanger become completely closed by dust, causing an almost zero local velocity and then heat transfer in those zones, as shown in Figure 3.2(b). From a computational point of view, this aspect could be simulated with a penalization of the free-flow surface for the air passage across the heat exchanger coils, and two different air flow velocities in clean and fouled zones have been considered. This methodology is in accordance with the experimental approach used by Breuker and Braun [37], mentioned in section 2.2.5.1 to artificially simulate fouling on fin-and-tube heat exchangers.

Similarly to refrigerant leakages, a fault intensity factor for the external heat exchanger fouling is defined as follows. The same penalization factor is also considered for the heat transfer surface.

$$FI_{foul,ext} = \frac{S_{free-flow,foul}}{S_{free-flow,clean}} \cdot 100 \tag{3.12}$$

Regarding the internal unit, generally it is provided with an air filter plugged with dust, installed to guarantee the indoor air quality and to reduce fouling effects on the heat exchanger, according to Yang et al. [44]. Therefore, most of the fouling accumulates on the top surface of the filter, reducing the free-flow area and therefore the air flow rate through the evaporator, as shown in Figure 3.2(c). From a computational point of view the fault has been modelled considering an internal unit air flow-rate reduction. Likewise, this methodology is in accordance with the experimental approach used by Breuker and Braun [37], to artificially recreate the fault in a laboratory environment. In this work, a fault intensity factor for internal fin-and-tube heat exchanger fouling is defined as:

$$FI_{foul,int} = \frac{\dot{V}_{free-flow,foul}}{\dot{V}_{free-flow,clean}} \cdot 100 \tag{3.13}$$

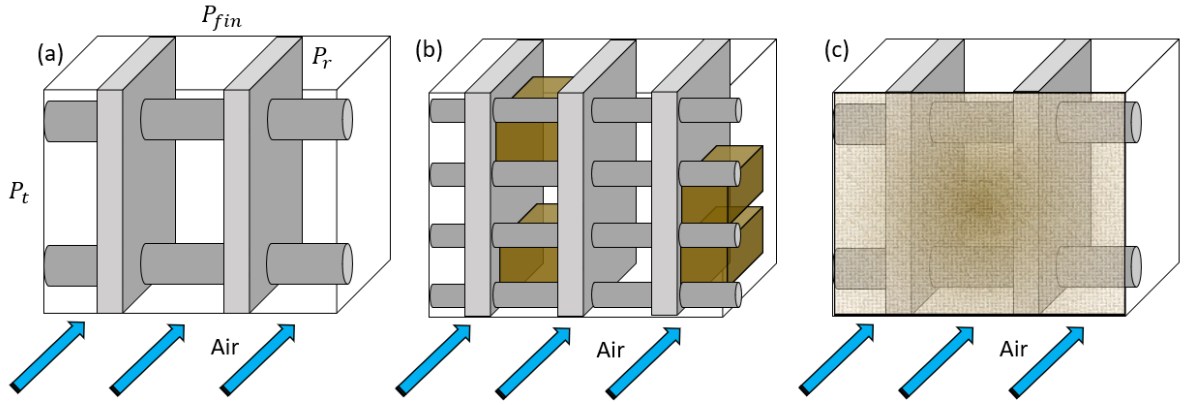


Figure 3.2. Elementary geometry of a fin-and-tube heat exchanger considered in the paper of Pelella et al. [104].(a) Clean surfaces. (b) Condenser fouling: presence of dust along fins for the first row. (c) Evaporator fouling : presence of dust only on the face-front filter

3.2.3 Resolution algorithm

To simulate the entire behaviour of the machine, all the previously described sub-models have been coupled together employing a resolution algorithm. The refrigerant at the condenser outlet is considered saturated liquid in normal operation, and it is in two-phase conditions in case of refrigerant leakage, whereas the expansion valve is designed to control a fixed value for the

evaporator superheating, guaranteeing in normal operating conditions the same mass flow rate of the compressor. The following steps are performed:

1. Values for the indoor temperature T_{indoor}, the condensing temperature T_{co}, and the inlet valve vapor quality $x_{in,valve} \geq 0$ are fixed. Therefore, the internal and external heat exchanger fouling fault intensity parameters ($FI_{foul,int}, FI_{foul,ext}$) are fixed too.
2. Mass flow rates of compressor and valve depending on evaporating temperature are estimated from models presented in sections 3.2.1.1 and 3.2.1.2. The maximum value for the opening percentage of the expansion valve is considered ($\xi = 1$) as a first attempt. Therefore, from the coupling between the two components, the effective evaporating temperature and mass flow rate are evaluated.
3. Effective air mass flow rate through heat exchangers is evaluated through the fluid-dynamic coupling between heat exchangers coils and fans.
4. An iterative procedure on the outlet refrigerant evaporator superheating, for the resolution of evaporator heat transfer is carried out. With a first attempt value, thermodynamic states of the machine are solved, and thermal, electrical powers and COP are evaluated through energy balances presented below:

$$\dot{Q}_{ev} = \dot{m} \cdot \left(h_{out,ev} - h_{in,ev}\right) \tag{3.14}$$

$$\dot{W}_{fan} = \frac{\Delta p_{air} \cdot \dot{V}_{air}}{\eta_{fan}} \rightarrow \eta_{fan} = 0.65 \tag{3.15}$$

$$\dot{W}_{comp} = \dot{m} \cdot \left(h_{out,comp} - h_{in,comp}\right) \tag{3.16}$$

$$COP = \frac{\dot{Q}_{ev}}{(\dot{W}_{comp} + \dot{W}_{fan})} \tag{3.17}$$

   The fan efficiency is set to 0.65, which is a common value for low-budget heat exchanger fans. Iterations terminate when a convergence on the evaporator thermal powers evaluated between heat transfer law and first thermodynamic principles is reached. The evaporator superheating solution is then found.
5. If the superheating solution found in point 4 is higher than the target superheating, the valve will remain completely open resulting to be unable to control superheating. If the superheating solution is lower than the target value, the valve will reduce its opening percentage to control superheating. Therefore, steps 2, 3 and 4 are repeated with a lower value of opening percentage of the valve ξ until the superheating solution coincides with the target.
6. Once the iteration in point 4 is concluded, another iteration on the inlet air temperature of the condenser to solve the heat transfer in the condenser is carried out. Iterations

conclude when condenser thermal power evaluated from the heat transfer equation is equal to the one obtained with the energy balance.

7. Refrigerant charges in the condenser, evaporator, and liquid line are finally evaluated.

A flowchart of the resolution algorithm is provided in Figure 3.3.

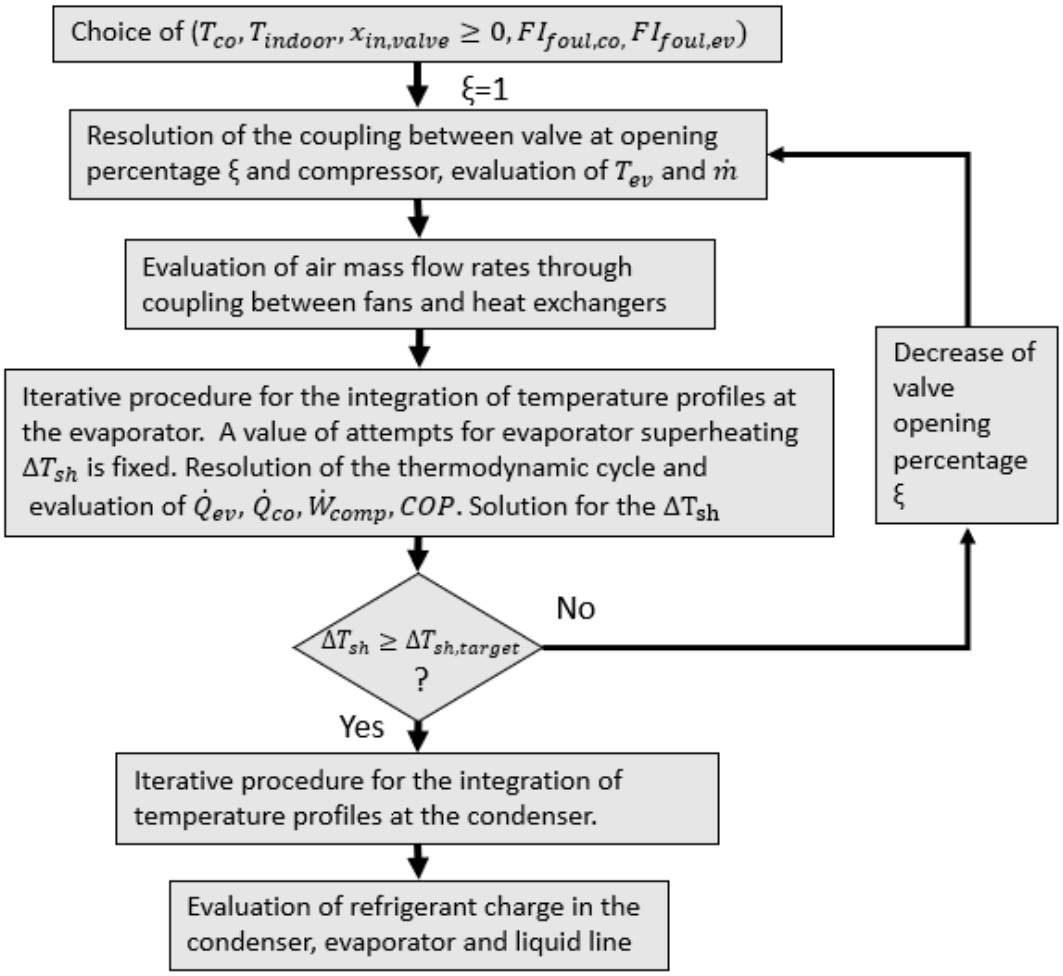


Figure 3.3. Steps for the resolution algorithm of the model presented in Pelella et al. [104], both in normal and in faulty operating conditions

Simultaneous faults have been simulated by choosing in both cases different values for fault intensities for the external and internal heat exchanger fouling. Moreover, two different performance maps have been generated, in order to simulate the presence or absence of a refrigerant leakage fault, one for $x_{in,valve} = 0$ which is used in case of available refrigerant charge higher than the one requested by the system, and the other one for $x_{in,valve} > 0$ in case of a strong refrigerant leakage that causes the liquid receiver emptying.

3.2.4 Case study data and model calibration

It should be clarified that, at the current state of the art, there are no data or experiments in literature obtained by imposing the same type of faults of this work, analyzing the same systems and the effect on performance degradation. For that reason, the main purpose of the analysis is to estimate the variation of the seasonal performance parameters once a certain fault (type and intensity) or combined faults are imposed, analysing trends occurring in a specific case study more than providing exact and reliable numerical results.

Therefore, it is reasonable that calibrating all the sub-models is a good expedient to guarantee satisfactory results within the aim of this investigation. Calibrations of the sub-model are then reported in this section, whereas faults represent assigned parameters, thus changing only the boundary conditions of the model and no other terms related to phenomenological equations that would require instead a dedicated calibration.

3.2.4.1 Case study

The developed model is applied to a specific case study of a domestic air-to-air heat pump, characterized by a rated cooling capacity of 2.6 kW, R32 as refrigerant fluid employed, which is largely used for these kind of systems as already discussed in section 2.2.2.1, and a rated evaporator superheating of 7 °C. Heat exchanger geometric characteristics, with other parameters of the machine, are reported in Table 3.2. These parameters have been chosen accordingly to typical values for small capacities domestic air conditioning applications, considering the assigned rated cooling capacity.

Table 3.2. Case study rated characteristics of a 2.6 kW residential heat pump, and geometrical features of the heat exchangers

Parameter	**Machine**	
Cooling Capacity (27-35 °C) [kW]	2.6	
Working fluid	R32	
Rated evaporator superheating (°C)	7.0	
Liquid line length (m)	0.5	
Rated refrigerant charge (g)	660	
Compressor rated speed (rpm)	1140	
	Internal Unit	**External Unit**
Dimensions [m] (Length x Width x Height)	0.55 x 0.17 x 0.16	0.8 x 0.4 x 0.51
Number of circuits – rows – tubes per row	4 – 9 – 8	4 – 2 – 26
Longitudinal tube pitch [m]	0.02	0.02
Transverse tube pitch [m]	0.02	0.02
Fin pitch [mm]	2	2
Fin thickness [mm]	0.3	0.3
Tube diameter [mm]	7	7
Tube thickness [mm]	0.5	0.5
Tube thermal conductivity [$Wm^{-1}K^{-1}$]	386 (Copper)	
Fin thermal conductivity [$Wm^{-1}K^{-1}$]	204 (Aluminium)	

The air mass flow rate in the internal heat exchanger is provided by a tangential blower, whereas an axial fan is employed for the air circulation across the external heat exchanger. Characteristic curves for both fans used for this case study, coupled with heat exchanger coils curves for both evaporator and condenser, are presented in Figure 3.4.

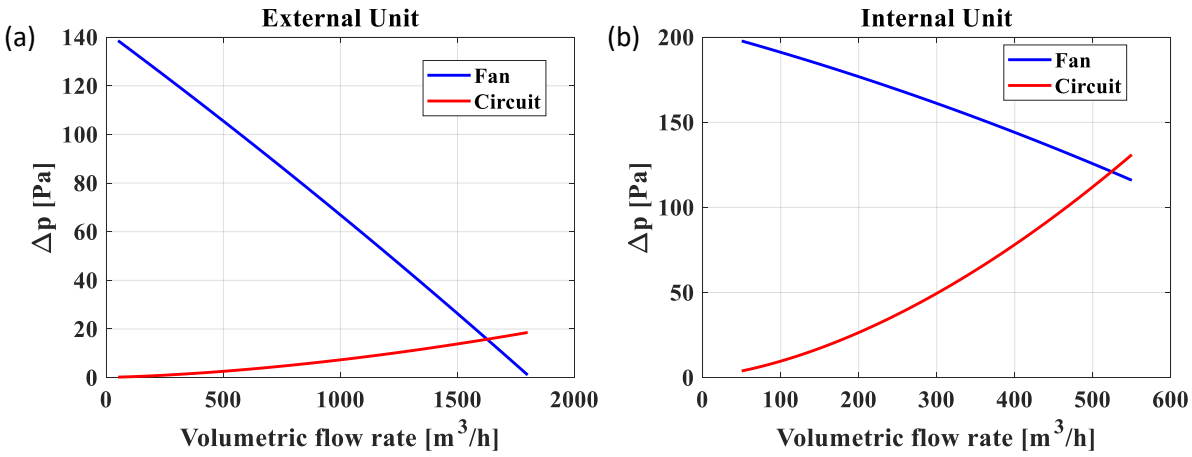


Figure 3.4. Fans characteristic curves on the static pressure drop - volumetric flow rate diagram, and coupling with characteristic curves of heat exchanger coils, in case of absence of fouling. (a) Axial fan of the external unit. (b) Tangential blower of the internal unit

3.2.4.2 Compressor model calibration

Regarding compressor model, data from manufacturer data catalogues have been taken, in terms of values of cooling capacity and electrical power of the compressor depending on evaporating, and condensing temperatures. For the evaluation of model calibration parameters for compressor mass flow rate and global efficiency, several experimental points are used, some of which situated on the borders and others in the middle of the functioning map of the compressor in terms of upper and lower limits of evaporating and condensing temperatures. For all these points, values of experimental mass flow rate and global efficiency are evaluated through energy balances and simulating a vapor compression system. All the remaining points are used for validation. The compressor overall efficiency model is calibrated for different intervals of inlet compressor density. Figure 3.5(a) represents a comparison between model and catalogue experimental points for the volumetric efficiency of the compressor depending on compression ratio, whereas Figure 3.5(b) shows the results in terms of global efficiency. Different colours indicate several values for refrigerant inlet compressor density, which ranges from 16 to 42 kg/m^3. The goodness of the model is further verified in terms of mean absolute percentage error (MAPE), mean relative percentage error (MRPE) and percentage of experimental points predicted with errors falling into $\pm 10\%$ error band. MAPE and MRPE expressions are reported in the nomenclature.

Results show that the compressor model can predict its volumetric efficiency with a MAPE of 1.53%, a MRPE of -0.36%, with all experimental points falling into the $\pm 10\%$ error band. The global efficiency is instead predicted with a MAPE of 3.60%, a MRPE of -0.95% and with the 94.2% of experimental point falling into the $\pm 10\%$ error band.

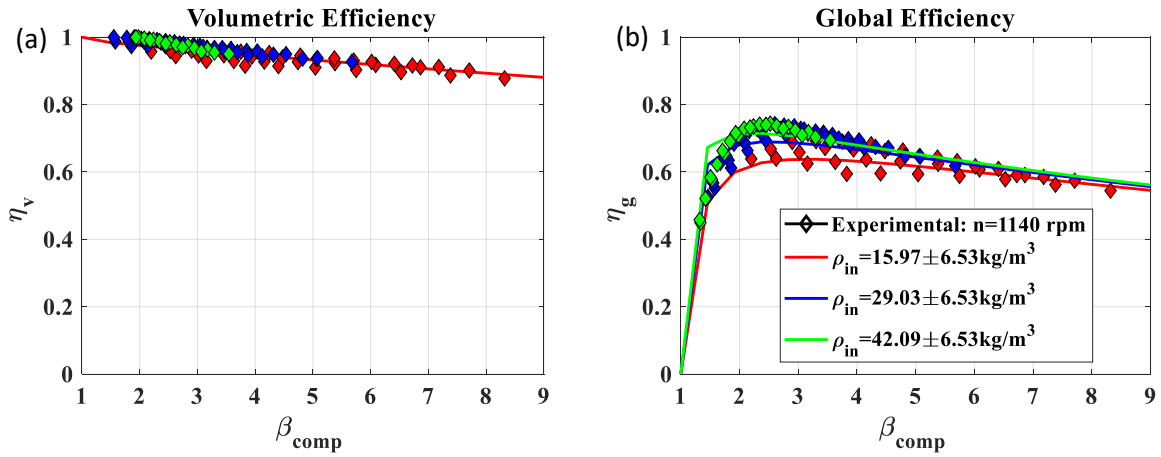


Figure 3.5. Calibration curves for volumetric (a) and global (b) compressor efficiencies depending on the compression ratio and on inlet compressor densities, and comparison with manufacturer data

3.2.4.3 Valve model calibration

Regarding the thermostatic expansion valve, also in this case data from manufacturer data catalogues have been collected in terms of cooling capacity depending on evaporating temperature and pressure drop across the valve. Several experimental points equally distributed in the operating functioning map of the valve have been used to calibrate the model parameters, whereas all the others have been employed for validation. Figure 3.6 shows the accuracy of the valve model in predicting experimental data. The values obtained for MAPE and MRPE are respectively 9.8%, and -8.6%, with approximately the 60% of experimental point falling into the $\pm$10% error band.

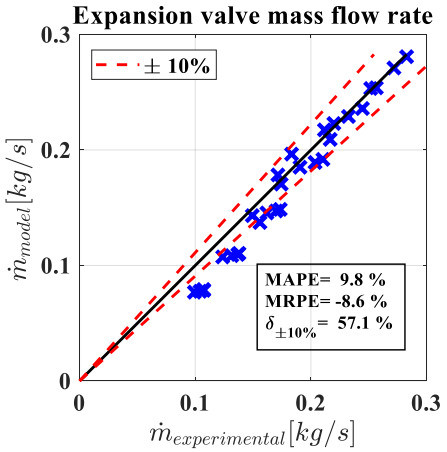


Figure 3.6. Validation of the valve mass flow rate model, and comparison with manufacturer data

3.2.5 Result in cooling mode

Here, results about the small-capacity system for residential air conditioning case study working in cooling mode are presented. The latent load of the user has been neglected since residential applications usually are characterized by a low crowding index, so a negligible humidity

production. Therefore, with no significant air renewal, the air conditioning system will operate at constant specific humidity after a short transient period. In cooling mode, the rated refrigerant charge of the machine is assumed to be equal to the maximum value requested by the system with an ambient temperature of 40 °C, which is approximately 660 g. In these sections the following results of the cooling mode are presented: performance maps depending on fault intensities, the effect of the soft faults investigated on the thermodynamic cycle of the machine, and finally dynamic simulations.

3.2.5.1 Performance maps of the case study

2D maps of the coefficient of performance depending on ambient temperature and fault intensities are provided in Figure 3.7 for cooling mode and for a fixed indoor temperature of 26 °C. Figure 3.7(a) shows a 2D contour plot of COP in case of evaporator fouling, with the fault intensity ranging from 0 to 40%. As expected, COP decreases with the increase of ambient temperature and evaporator fouling intensity. The air mass flow rate decreasing through the evaporator causes higher temperature differences, so a lower evaporating temperatures considering the same indoor temperature. COP values and evaporator fouling seem to be almost linear, with the slope almost not affected by the fault intensity, with the fault intensity ranging from 0 to 40%. Figure 3.7(b) shows COP values depending on ambient temperature and condenser fouling, with the fault intensity ranging from 0 to 40%. Similarly to the evaporator fouling case, COP values decrease with the increase of the fouling intensity. As a matter of fact, the heat transfer surface penalization of the heat exchanger especially causes higher values of condensing temperatures with the same ambient temperature, causing therefore a COP degradation. Furthermore, the figure shows that the effect of condenser fouling becomes slightly higher for higher values of fault intensity. The rate of COP degradation with the occurrence of condenser fouling is similar to that seen for the evaporator. Finally, Figure 3.7(c) shows a COP performance map in case of refrigerant leakage, with fault intensity ranging between 0 and 60%. As expected, COP decreases for both higher ambient temperatures and higher refrigerant leakages. As a matter of fact, refrigerant leakages cause an increase of evaporator superheating due to the chocked flow through the valve, and the lower mass flow rate led to a reduced coupling evaporating temperature between the compressor and the valve. It can be noticed that for high intensities of leakage, values of COP become less dependent from ambient temperature, with a rate of COP degradation for refrigerant leakages which is slightly higher than the one in the case of heat exchangers fouling. Finally, a horizontal asymptote for COP can be identified for a nearly zero refrigerant leakage. This is related to the fact that the rated refrigerant charge of the system is assumed equal to the maximum requested by the system

analysed, which is at 40 °C. Therefore, in case of lower ambient temperatures due to the presence of an exceeded refrigerant charge stored in the liquid receiver, higher values of fault intensity are required to cause a malfunctioning of the system.

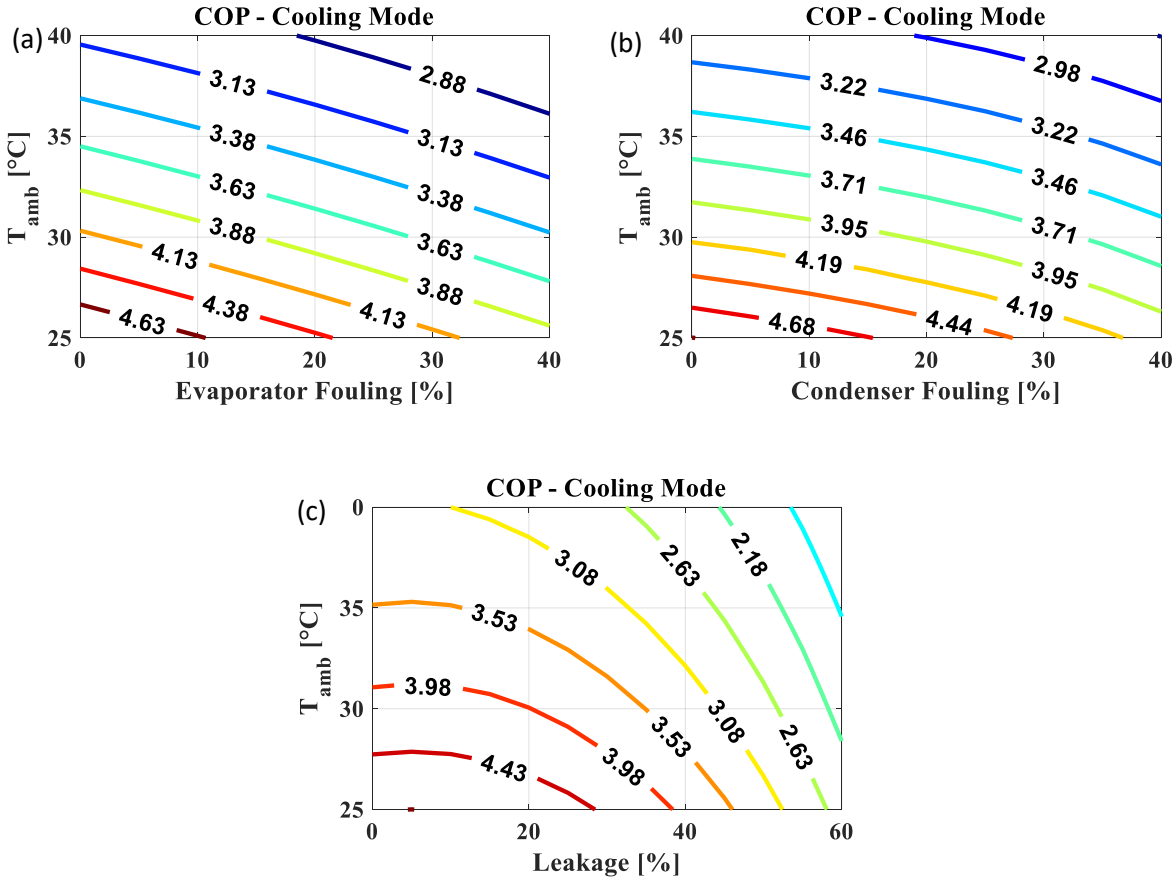


Figure 3.7. Performance maps in cooling mode in terms of COP value, depending on ambient temperature and fault intensities, for a fixed condition of the indoor temperature of 26 °C. (a) Evaporator fouling. (b) Condenser fouling. (c) Refrigerant leakage

Figure 3.8 shows a 3D map for the coefficient of performance depending on the fault intensities for each of the three kinds of fault analysed in this manuscript in case both of standalone and multiple simultaneous occurring faults. In this case the performance map is given in terms of COP penalization which is defined in this work as the difference between the COP for the fault-free and the faulty condition, divided by the COP related to the fault-free conditions.

$$COP_{penaliz} = \frac{COP_{fault-free} - COP_{faulty}}{COP_{fault-free}} \cdot 100 \qquad (3.18)$$

Figure 3.8(a) shows the map represented on the 3 dimensions, which shows COP degradation in case of three simultaneous occurring faults, obtained for fixed conditions of ambient and indoor temperature of respectively 35 °C and 26 °C, whereas Figure 3.8(b-d) are projections of Figure 3.8(a) related to conditions of two simultaneous occurring faults, respectively without

evaporator fouling ($FI_{ev} = 0$), without condenser fouling ($FI_{co} = 0$) and without refrigerant leakage ($FI_{leak} = 0$). In case of combined leakages and condenser fouling for the thresholds of $FI_{leak} > 15\%$ and $FI_{co} > 10\%$ (see Figure 3.8(b)), significant COP penalizations (at least 10%) occur. If both refrigerant leakages and evaporator fouling occur, the approximate thresholds for the same penalization are $FI_{leak} > 10\%$ and $FI_{ev} > 20\%$ (see Figure 3.8(c)). Finally, combining both evaporator and condenser fouling, the threshold for COP penalization at least about 10% can be found around the conditions $FI_{ev} > 15\%$ and $FI_{co} > 10\%$ (see Figure 3.8(d)).

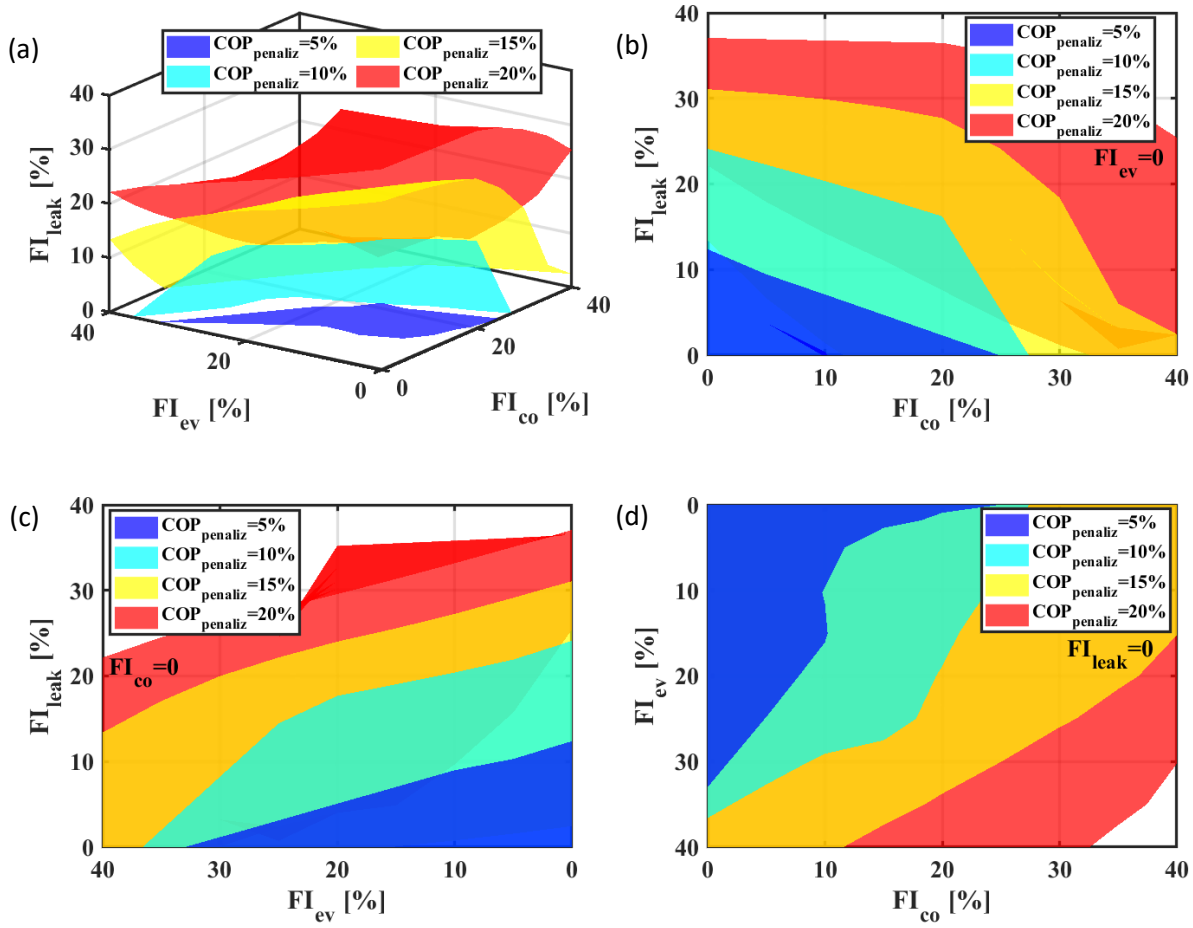


Figure 3.8. 3-D contour plot for COP depending on the three fault intensities, for ambient and indoor temperatures of respectively 35 °C and 26 °C (a). Projection of the 3-D plot considering the absence, respectively, of evaporator fouling ($FI_{ev} = 0$, b), of condenser fouling ($FI_{co} = 0$, c) and of refrigerant leakage ($FI_{leak} = 0$,d)

3.2.5.2 Effect of standalone faults on the thermodynamic cycle

After analysing the COP penalization caused by standalone fault, the effects of standalone faults on the thermodynamic cycle of the heat pump analysed are here presented. Several temperature – specific entropy diagrams are represented in Figure 3.9, in cooling mode and with indoor and ambient temperatures respectively of 26 °C and 35 °C, for standalone 40% refrigerant leakage, 40% condenser fouling and 40% evaporator fouling. In these diagrams, it is possible to estimate the temperature and pressure variations of a thermodynamic cycle related to a faulty condition, compared with a fault-free case.

For a 40% refrigerant leakage of the rated refrigerant charge of the system (Figure 3.9(a)) evaporating and condensing temperatures result to be 5.8 °C and 1.9 °C respectively lower than the fault-free case. The outlet temperature of the compressor rises of almost 25 °C, with air-temperature profiles which remain almost unchanged. On the other hand, the valve is no longer able to control evaporator outlet superheating, which rises of about 12.5 °C. This results in a cooling capacity 25.9% lower and a COP 24.7% lower compared with fault-free conditions. In case of a 40% condenser fouling (Figure 3.9(b)) the condensing temperature increases of approximately 5 °C, whereas the evaporating temperature remains unchanged compared with the fault-free case. The outlet compressor temperature instead increases of almost 10 °C. All these aspects led to a COP degradation of approximately 13%, whereas the cooling capacity seems to be almost not affected by the condenser fouling, with a negligible effect on the air temperature variation in the evaporator. This results in a difficult self-identification of condenser fouling by a user, also with high intensities, with the machine which can operate also for long periods of time in faulty conditions. On the other hand, the air temperature variation through the condenser coils slight increases due to the lower air mass flow rate, resulting from the fluid-dynamic coupling between the coil and the fan characteristic curves.

In case of 40% evaporator fouling (Figure 3.9(c)), the evaporating temperature becomes 5.7 °C lower than the fault-free case, whereas the outlet temperature of the compressor which rises of about 10 °C. Air temperature difference through the evaporator becomes almost 6 °C higher than the fault-free case, whereas air temperature difference through the condenser remains almost unaffected. A 40% evaporator fouling causes a performance degradation in terms of COP of almost 16.8%, with a cooling capacity decrease of approximately 16.5%. Therefore, due to the higher effect of evaporator fouling on cooling capacity, this kind of fault should be more easily identified by a user without any planned maintenance.

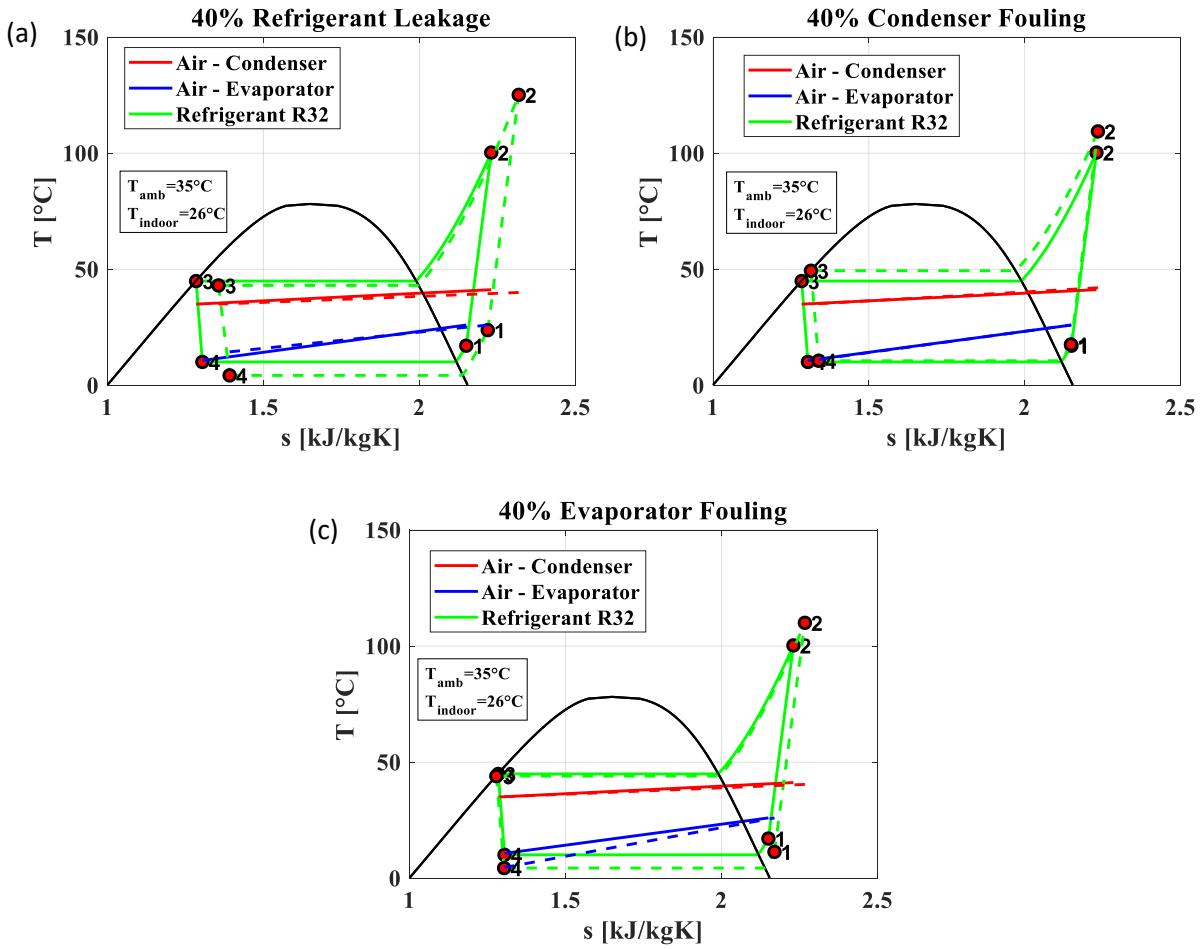


Figure 3.9. Temperature – specific entropy diagrams for fixed conditions of ambient and indoor temperature of 35 °C and 26 °C, obtained in case of a 40% refrigerant leakage (a), a 40% condenser fouling (b) and a 40% evaporator fouling (c). Solid and dashed lines are related respectively to fault-free and faulty thermodynamic cycles

All the numerical values for evaporating and condensing temperatures, outlet compressor temperature, outlet evaporator superheating, cooling capacity and COP, with respective variations with the fault-free case in brackets, are reported in Table 3.3. All the results presented in this section agree with the experimental evidence analysed in section 3.1.

Table 3.3. Values of measured parameters on the machine in cooling mode, in case of fault-free and faulty conditions, for fixed conditions of ambient and indoor temperature of 35 °C and 26 °C. In brackets are reported the differences between the faulty and fault-free specific cases

Operation (Difference with fault-free)	T_{ev} [°C]	T_{co} [°C]	$T_{out,comp}$ [°C]	ΔT_{sh} [°C]	$\Delta T_{air,co}$ [°C]	$\Delta T_{air,ev}$ [°C]	$\dot{Q}_{ev}$ [kW]	**COP**
Fault-free	10.1	44.9	100.3	7.0	6.2	15.3	2.55	3.57
40% Refrigerant Leakage	4.3 (-5.8 °C)	43.1 (-1.9 °C)	125.2 (+24.9 °C)	19.5 (+12.5°C)	5.0 (-1.2 °C)	11.6 (-3.7 °C)	1.89 (-25.9%)	2.69 (-24.7%)
40% Fouling Condenser	10.6 (+0.5 °C)	49.4 (+4.5 °C)	109.4 (+9.1 °C)	7.0 (0.0 °C)	7.0 (+0.8 °C)	14.8 (-0.5 °C)	2.47 (-3.13%)	3.10 (-13.2%)
40% Fouling Evaporator	4.4 (-5.7 °C)	44.0 (-0.9 °C)	110.0 (+9.7 °C)	7.0 (0.0 °C)	5.4 (-0.8 °C)	21.4 (+6.1 °C)	2.13 (-16.5%)	2.97 (-16.8%)

3.2.5.3 Effect of multiple simultaneous faults on the thermodynamic cycle of the machine

Each kind of fault may have different effects on the thermodynamic cycle. It could happen that a combination of different faults causes similar effects on some measured parameters. In Figure 3.10, thermodynamic cycles in cases of fault-free, standalone, and simultaneously occurring faults are presented, for ambient and indoor temperatures fixed respectively to 35 °C and 26 °C. As a matter of fact, each kind of fault may have different effects on measured parameters of the cycle, and simultaneous faults can create a superposition, causing a reduction or an enhancement of the effect caused by faults. Figure 3.10(a) shows the effect of a 40% condenser fouling, in a standalone condition (solid green line), combined with a 40% evaporator fouling (dashed magenta line) and a 30% refrigerant leakage (dashed blue line). Similarly, Figure 3.10(b) shows the effect of a 40% evaporator fouling, in a standalone condition (solid green line), combined with a 40% condenser fouling (dashed magenta line) and a 30% refrigerant leakage (dashed blue line). Figure 3.10(c) instead represents the effect of a standalone 30% refrigerant leakage (solid green line) combined with a 40% evaporator fouling (dashed magenta line) and a 30% refrigerant leakage (dashed blue line). All these thermodynamic cycles are then compared with the one derived from a fault-free case (solid red line). Finally, Figure 3.10(d) shows the thermodynamic cycle deriving from the combination of all of the analysed faults, with the considered fault intensities, and compares it with the fault-free case. Numerical values in terms of evaporating and condensing temperatures, outlet compressor temperature,

evaporator superheating, and corresponding values of mass flow rate, COP and cooling capacity penalizations are provided in Table 3.4.

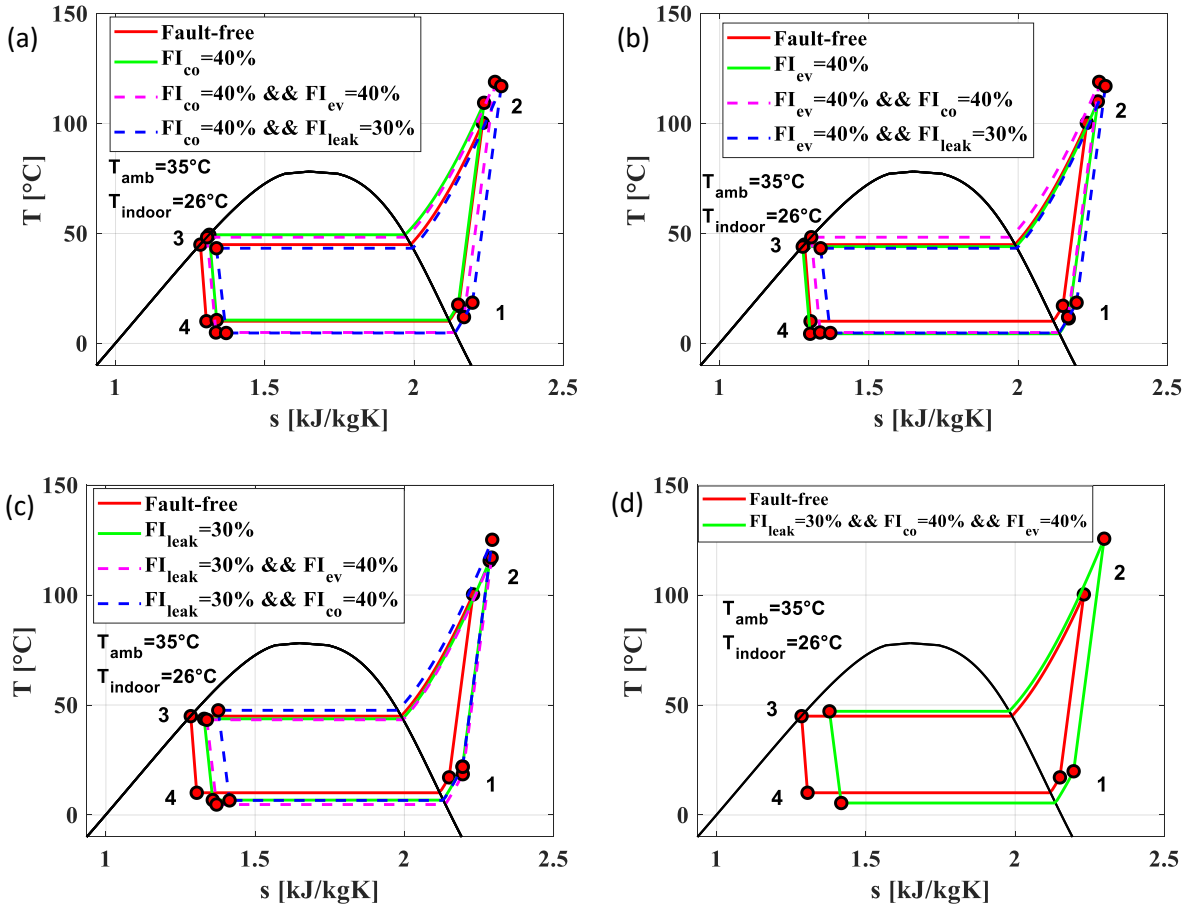


Figure 3.10. Temperature – specific entropy diagrams in case of multiple simultaneous faults, for fixed conditions of ambient and indoor temperature of 35 °C and 26 °C. 40% condenser fouling (a), 40% evaporator fouling (b) and 30% refrigerant leakage (b) reported respectively standalone (green solid lines) or combined with another fault (coloured dashed lines), and simultaneous combination of all the three faults analysed (d). In all cases the fault-free thermodynamic cycles are represented with red solid lines

The combination of evaporator and condenser fouling causes respectively a lower evaporating temperature compared to the standalone condenser fouling case and a higher condensing temperature compared to the standalone evaporator fouling case, according to the previous section. This causes a higher COP penalization of about 26.5%, compared with the one in case of standalone condenser and evaporator fouling conditions, respectively of 17% and 13%.

The combination of evaporator fouling and refrigerant leakage causes instead a higher reduction of condensing temperature compared to standalone faults. Regarding evaporating temperature two different effects can be observed. As a matter of fact, both faults cause an evaporating temperature reduction, according to the previous section. However, the huge reduction of mass flow rate caused by the valve chocking, and the corresponding reduction of cooling capacity caused by the combination of faults led to a reduction in the average temperature difference at

the evaporator, which causes an increase of evaporating temperature with the same boundary conditions. These aspects result in an evaporating temperature which seems not to be particularly affected by the combination of these two faults, causing a COP penalization of about 22%, still greater than the two standalone faulty conditions considered.

The combination of condenser fouling and refrigerant leakage instead causes a contrasting effect on the condensing temperature, with an increase led by the condenser fouling and a decrease led by the refrigerant leakage. In this case, the condensing temperature increase is of about 3 °C compared to the fault-free case, which is lower to the increase caused by a standalone condenser fouling. On the other hand, the refrigerant leakage causes a huge reduction of the evaporating temperature, which is almost not affected by a standalone condenser fouling, causing a COP penalization which is about 27%, higher than the two standalone faulty conditions.

Finally, a combination of all the three fault conditions investigated causes different combinations of effects on measured parameters, not easily describable, and these effects cause a penalization in cooling capacity and COP of respectively 26% and 32%. All the results obtained and previously described agree with the experimental evidence from the literature, presented in section 3.1.

Table 3.4. Effect of standalone and simultaneous faults on measured variables of the machine. The differences are reported in brackets for each specific case

Fault imposed (Difference with fault-free)	T_{ev} [°C]	T_{co} [°C]	$T_{out.comp}$ [°C]	ΔT_{sh} [°C]	$\dot{m}$ [kg/s]	$\dot{Q}_{ev}$ [kW]	COP
Fault-free	10.1	44.9	100.3	7.0	0.0106	2.55	3.55
40% Evaporator Fouling	4.4 (-5.7°C)	44.0 (-0.9°C)	110.0 (+9.7°C)	7.0 (+0.0°C)	0.0089 (-16.0%)	2.13 (-16.5%)	2.96 (-16.9%)
40% Condenser Fouling	10.6 (+0.5°C)	49.4 (+4.5°C)	109.4 (+9.1°C)	7.0 (+0.0°C)	0.0108 (+1.9%)	2.47 (-3.1%)	3.09 (-13.2%)
30% Refrigerant leakage	6.8 (-3.3°C)	43.7 (-1.2°C)	115.7 (+15.4°C)	15.3 (+8.3°C)	0.0091 (-14.2%)	2.17 (-14.9%)	3.06 (-13.8%)
40% Evaporator Fouling + 40% Condenser Fouling	5.0 (-5.1°C)	48.3 (+3.4°C)	118.9 (+18.6°C)	7.0 (+0.0°C)	0.0090 (-15.1%)	2.08 (-18.4%)	2.62 (-26.5%)
30% Refrigerant leakage + 40% Evaporator Fouling	4.8 (-5.3°C)	43.3 (-1.6°C)	117.0 (+16.7°C)	13.8 (+6.8°C)	0.0086 (-18.9%)	1.98 (-22.4%)	2.78 (-21.9%)
30% Refrigerant leakage + 40% Condenser Fouling	6.6 (-3.5°C)	47.6 (+2.7°C)	125.1 (+24.8°C)	15.3 (+8.3°C)	0.0090 (-15.1%)	2.05 (-19.6%)	2.60 (-26.8%)
30% Refrigerant leakage + 40% Evaporator Fouling+ 40% Condenser Fouling	5.4 (-4.7°C)	47.1 (+2.2°C)	125.6 (+25.3°C)	14.4 (+7.4°C)	0.0087 (-17.9%)	1.90 (-25.5%)	2.44 (-31.6%)

3.2.5.4 Assumption and boundary conditions for dynamic simulations

The model developed and the performance maps obtained are employed to carry out a dynamic simulation of the case study analysed, in order to investigate the behaviour of the heat pump along an expected lifetime of 12 years. In this section several assumptions made for the dynamic simulations are presented, and then results for cooling mode are provided. Due to the slow variation of the external temperature, a quasi-steady-state simulation process is carried out, considering a timestep of 1 hour. An air-conditioned room with a global thermal conductivity of 150 W/K is considered, in order to have a system which is oversized to guarantee the cooling load request by the user at each temperature level. This aspect is better clarified in Figure 3.11, in which the cooling thermal power provided by the machine and requested by the user is represented depending on the ambient temperature. It is worth to notice that the bivalent temperature is over 40°C, and in all conditions the machine is able to satisfy the user load.

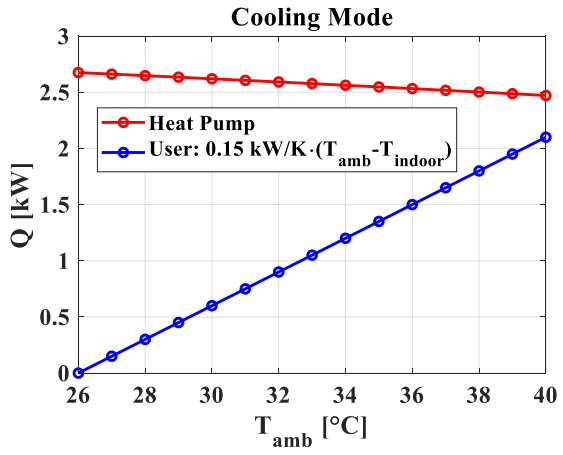


Figure 3.11 Cooling load provided by the machine (red) and requested by the user (blue) depending on the external ambient temperature

The internal target temperature of the air-conditioned environment is fixed equal to 26 °C. Furthermore, the dynamic behaviour of the case study system has been analysed for 3 different typical climate conditions of: Naples in Italy, Miami in the USA, and Shanghai in China, with climatic data according to software TRNSYS [118], and considering the machine operating in cooling mode only for months between May and September. These cities have been chosen because they are all characterized by temperature peaks over 30 °C and humidity peaks over 70% during the summer season. The number of bins depending on ambient temperature, and temperature evolution along the working months are reported in Figure 3.12. The patched area in light blue refers to the number of hours with an external temperature higher than the indoor temperature of 26 °C.

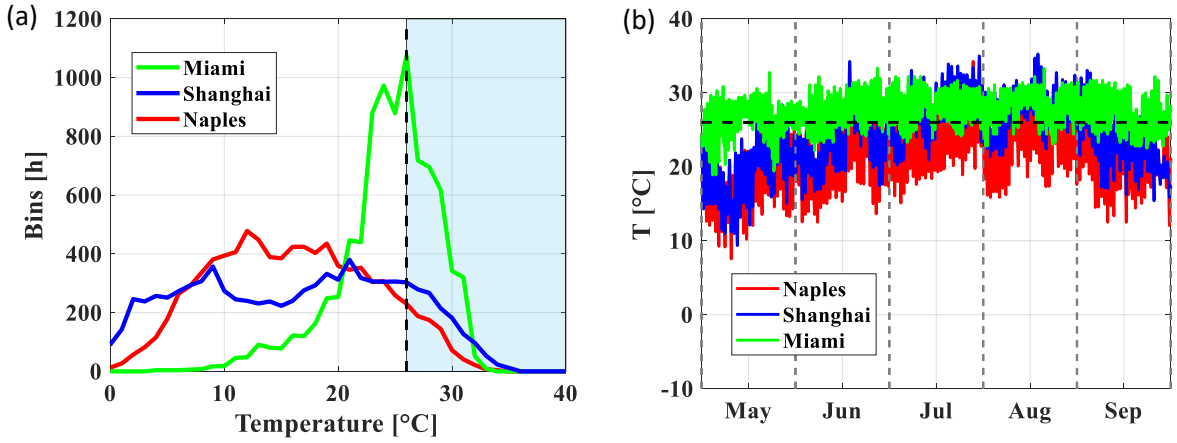


Figure 3.12. Number of operating hours vs. external temperature (a) and external temperature evolution in months between May and September (b), for the climate conditions of Naples, Miami and Shanghai

The machine has been considered turned on only when the external temperature rises above the internal target temperature of 26 °C. Therefore, annual operating hours for each of the climate conditions investigated are reported in Table 3.5. It can be noticed that Naples has the lowest number of working hours, Miami the highest, whereas Shanghai has the highest temperature values compared to the other two cities, and a number of working hours intermediate between Naples and Miami.

Table 3.5. Number of operating hours for which the external temperature rises above 26 °C, for climate conditions of Naples, Miami and Shanghai

Annual operating hours of the machine		
Naples	**Miami**	**Shanghai**
748	2444	1378

Several scenarios in terms of fault evolution are simulated, considering different kinds of service maintenance to reset ordinary conditions of the machine. In detail, the following scenarios have been analysed and combined each other:

- Fault-free case: no refrigerant leakages, no condenser fouling, and no evaporator fouling occur along the entire lifetime of the machine.
- Linear growth of refrigerant leakage (RL), with a maximum slope of 20% (RLmax) per year ($\cong 132\ g/year$). For all the simulations carried out, as refrigerant leakage slope values of RLmax, the half (1/2 RLmax, 66 g/year), ad a quarter of it (1/4 RLmax, 33 g/year) have been employed. RLmax has been chosen according to the percentage range of emission declared by the 24th IIR Informatory Note on Refrigeration Technology [29] and reported in Table 2.2. System plants are usually characterized by a positive pressure depending on the kind of refrigerant employed, with always a sonic motion for leakage holes, also when the system is not operating. For that reason, the refrigerant leakage has

been considered linear and continuous, independently from the on/off current operating mode and from the actual level of system charge.

- Growth of condenser fouling (CF). Due to the phenomenology of dust accumulation described in section 2.2.5.1, the fouling evolution has been modelled through a hyperbolic tangent trend [47], fixing the maximum value of fault intensity reachable and the number of hours to reach the 90% of the maximum value. In case of condenser fouling a maximum value for free-flow area penalization (CFmax) of 40% has been chosen, whereas a number of 2000 hours to reach the 90% of CFmax has been selected. CFmax has been chosen according to the maximum value of free-flow area penalization investigated by Chen and Braun [119]. Furthermore, due to the fact that dust is drawn to the heat exchanger surface by fans, fouling increases only when the machine is turned on, thus becoming dependent on the effective system working hours. For all the simulations carried out, the maximum value of condenser fouling fault intensity (CFmax), the half (1/2 CFmax) and a quarter (1/4 CFmax) have been considered.
- Growth of evaporator fouling (EF). The same fault evolution considered for condenser fouling has been adopted. The maximum value for air flow-rate penalization (EFmax) of 40% have been considered, slightly higher than the value experimented by Breuker and Braun [37], whereas a number of hours of 3000 has been considered as the time to reach 90% of the maximum fault intensity. A higher value has been chosen compared to the condenser unit, because we suppose a faster dust accumulation for the external unit, especially due to its greater exposure with the external environment. For all simulations, the maximum evaporator fouling fault intensity (EFmax), the half (1/2 EFmax) and a quarter (1/4 CFmax) have been selected.

An example of faults evolution along time is provided in Figure 3.13, for a refrigerant leakage of 20% per year, a maximum condenser fouling of 40% and a maximum evaporator fouling of 20%.

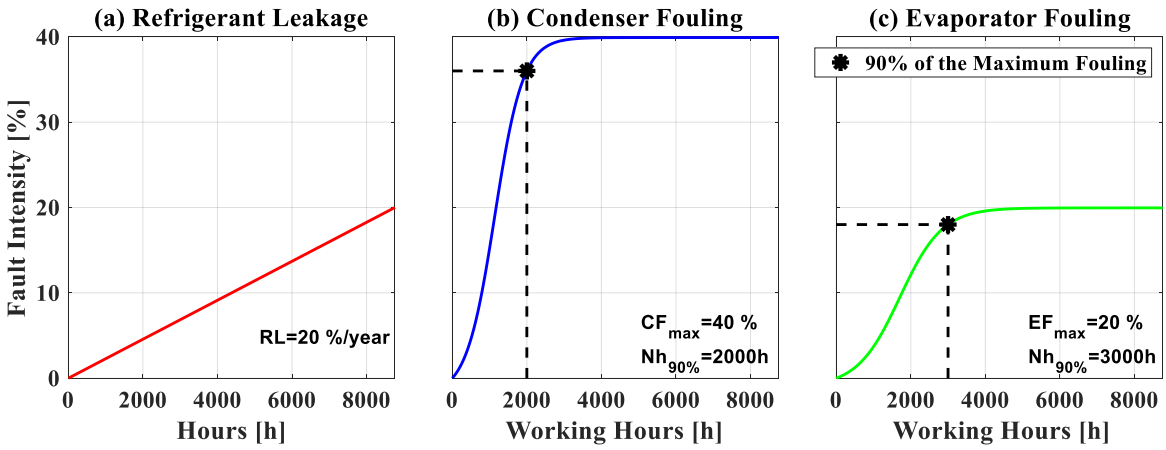


Figure 3.13. Example of fault intensity evolution along one year, in case of a 20%/year refrigerant leakage (a), a maximum condenser fouling of 40%, with the 90% reached in 2000h(b) and a maximum evaporator fouling of 20%, with the 90% reached in 3000h. The 90% limit is represented by the black dashed lines

All the considered fault evolution levels are combined, and 64 different combinations, both of standalone and simultaneous faults, have been obtained. For each of them, different scenarios of maintenance are simulated, in order to establish a resolution strategy for each of the occurring faults:

- Not ordinary maintenance. The maintenance operation is carried out by the user only when he/she realises that the machine is not operating properly anymore and has a lack of comfort. Numerically, this situation occurs when the machine is not able to satisfy more than the 10% of the cooling load requested by the user. In this occasions, all fault intensity values are numerically returned to zero (extraordinary maintenance), and every single fault is solved.
- Ordinary maintenance every 4 years. After 4 years of functioning every fault is solved.
- Ordinary maintenance every 2 years. After 2 years of functioning every fault is solved.
- Ordinary maintenance every year. After 1 years of functioning every fault is solved.

For all the simulations carried out, the two key performance parameters of seasonal coefficient of performance (SCOP) and total equivalent warming impact (TEWI) are evaluated along the entire lifetime of the machine, assumed equal to 12 years. The SCOP index has been already defined in section 2.2.3.2, whereas TEWI represents instead the sum of the two different direct and indirect contributes for global warming and has been evaluated according to the IIR Guideline for Life Cycle Climate Performance [120]. The indirect contribute has been evaluated considering a fixed emission factor f_{ee} for the electricity production equal to 0.49 kg_{CO_2}/kWh. Moreover, the COP variation with the partialization of the machine is neglected, and the following expressions are used. It is worth notice that $W_{el,tot}$ has to be converted in kWh.

$$SCOP = \frac{\sum_{t=1}^{n} Q_{user,t}}{\sum_{t=1}^{n} W_{el,t}} = \frac{\sum_{t=1}^{n} Q_{user,t}}{\sum_{t=1}^{n} \frac{Q_{user,t}}{COP_t}} \quad (3.19)$$

$$TEWI = m_{leak} \cdot GWP + \frac{W_{el,tot}}{3600} \cdot f_{ee} \quad (kgCO_{2,equiv}) \quad (3.20)$$

3.2.5.5 SCOP and TEWI results for the simulated scenarios

Figure 3.14(a,b) shows an example of the COP dynamic evolution, respectively for scenarios of not planned and every 2 years maintenance operations, in case of Naples climate conditions. In this case, a leakage growth rate of 1/2 RLmax, a maximum level for the condenser fouling of CFmax and a maximum threshold for the evaporator fouling of 1/2 EFmax are considered. The fault intensities evolution along the lifetime of the machine can be observed in Figure 3.14(c, d) in the two maintenance scenarios previously mentioned. In both cases, grey dots represent the COP evolution in the ideal scenario, without the presence of the three faults investigated.

In case of a not planned maintenance, the user realises about the fault only when the COP values are nearly zero, which occurs in this case in approximately 8 years. In this case SCOP assumes a value of 2.23, which is 47.2% lower than the ideal scenario (SCOP=4.24), whereas TEWI assumes a value of 1.170 $tCO_{2,equiv}$, which is about 240% higher than the ideal scenario (TEWI=0.347 $tCO_{2,equiv}$). This rise is especially related to the direct contribution caused by refrigerant leakage in a non-ideal scenario. In case of an ordinary maintenance every two years, instead, the refrigerant leakage fault intensity never exceeds the 20% level, whereas both condenser and evaporator fouling fault intensities never reach their maximum values, remaining below respectively 10% and 30%. In this case the SCOP value becomes closer to the ideal case, with a SCOP which assumes a value of 3.94, only 7% lower than the ideal case. On the other hand, TEWI becomes 0.910 $tCO_{2,equiv}$, approximately 22% lower than the not-planned maintenance scenario.

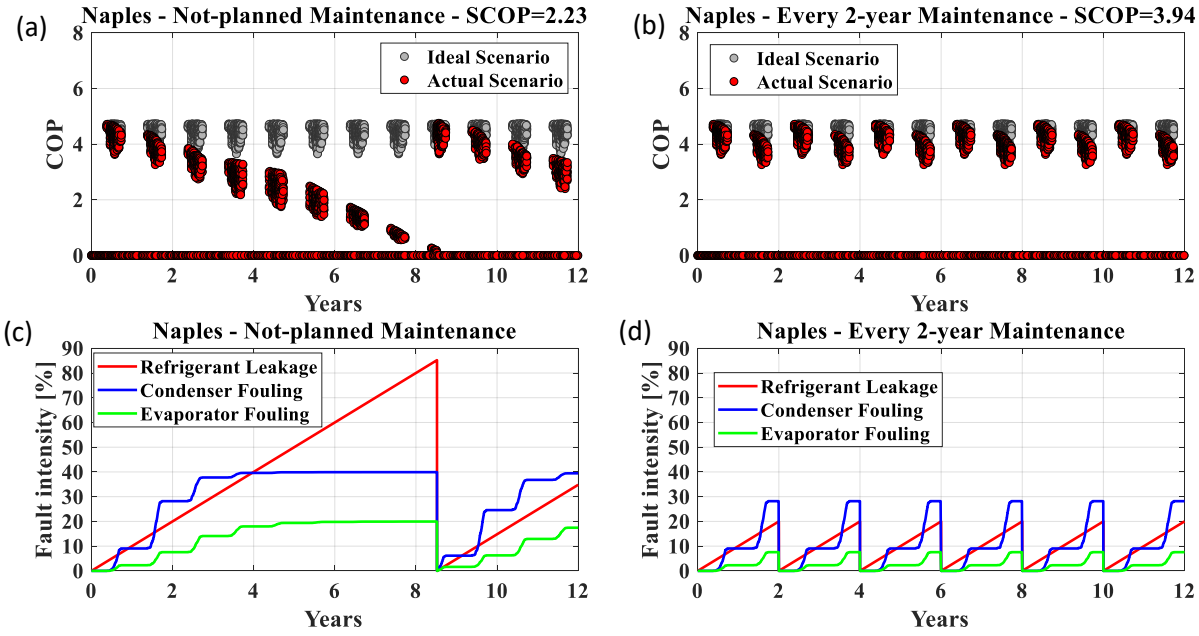


Figure 3.14. COP evolution (a, b) and corresponding fault intensities evolution (c, d) along the entire machine lifetime in cooling mode for Naples climate conditions, for a 10%/year refrigerant leakage, a maximum condenser fouling of 40% and a maximum evaporator fouling of 20%, in case of a not-planned (a, c) and every two years (b, d) maintenance scenarios.

Results in terms of SCOP, TEWI and number of performed maintenance interventions, for all the climate conditions, maintenance strategies investigated are reported in the following tables. Table 3.6 shows the results for a not-planned maintenance by the user, whereas Table 3.7, Table 3.8 and Table 3.9 report the 64 combination results for scenarios of organized maintenance, respectively every 4 years, 2 years and 1 year.

Table 3.6. Results in terms of SCOP, TEWI and number of maintenance interventions in cooling mode, for all the 64 possible combinations of fault intensities evolutions, for climate conditions of Naples, Miami and Shanghai, and for a not-planned maintenance scenario

Not planned maintenance by User												
Test	Fault Evolution			Naples			Miami			Shanghai		
	Refrigerant Leakage (RL)	Condenser Fouling (CF)	Evaporator Fouling (EF)	SCOP	TEWI [t_{CO2}]	Ninterv.	SCOP	TEWI [t_{CO2}]	Ninterv.	SCOP	TEWI [t_{CO2}]	Ninterv.
1	0	0	0	4.24	0.347	0	4.22	1.296	0	4.11	0.869	0
2	0	1/4 CFmax	0	4.13	0.356	0	4.10	1.334	0	4.00	0.893	0
3	0	1/2 CFmax	0	4.02	0.366	0	3.98	1.375	0	3.89	0.919	0
4	0	CFmax	0	3.69	0.398	0	3.62	1.512	0	3.55	1.005	0
5	0	0	1/4 EFmax	4.11	0.358	0	4.07	1.346	0	3.97	0.900	0
6	0	1/4 CFmax	1/4 EFmax	4.00	0.367	0	3.95	1.384	0	3.86	0.924	0
7	0	1/2 CFmax	1/4 EFmax	3.90	0.377	0	3.84	1.425	0	3.76	0.950	0
8	0	CFmax	1/4 EFmax	3.58	0.410	0	3.50	1.564	0	3.44	1.037	0
9	0	0	1/2 EFmax	3.97	0.370	0	3.91	1.398	0	3.83	0.933	0
10	0	1/4 CFmax	1/2 EFmax	3.88	0.379	0	3.81	1.436	0	3.73	0.957	0
11	0	1/2 CFmax	1/2 EFmax	3.78	0.389	0	3.71	1.477	0	3.63	0.983	0
12	0	CFmax	1/2 EFmax	3.48	0.423	0	3.38	1.620	0	3.33	1.072	0
13	0	0	EFmax	3.63	0.405	0	3.51	1.559	0	3.47	1.029	0
14	0	1/4 CFmax	EFmax	3.55	0.414	0	3.43	1.597	0	3.40	1.051	0
15	0	1/2 CFmax	EFmax	3.47	0.424	0	3.34	1.638	0	3.33	1.074	0
16	0	CFmax	EFmax	3.28	0.448	0	3.19	1.715	0	3.15	1.136	0
17	1/4 RLmax	0	0	3.37	0.704	0	3.35	1.899	0	3.26	1.362	0
18	1/4 RLmax	1/4 CFmax	0	3.25	0.719	0	3.25	1.953	0	3.16	1.396	0
19	1/4 RLmax	1/2 CFmax	0	3.13	0.736	0	3.13	2.016	0	3.05	1.436	0
20	1/4 RLmax	CFmax	0	2.95	0.765	0	2.89	2.158	0	2.82	1.534	0
21	1/4 RLmax	0	1/4 EFmax	3.26	0.717	0	3.24	1.958	0	3.16	1.396	0
22	1/4 RLmax	1/4 CFmax	1/4 EFmax	3.17	0.730	0	3.15	2.005	0	3.07	1.429	0
23	1/4 RLmax	1/2 CFmax	1/4 EFmax	3.07	0.745	0	3.05	2.059	0	2.98	1.466	0
24	1/4 RLmax	CFmax	1/4 EFmax	2.84	0.784	0	2.78	2.239	0	2.72	1.577	0
25	1/4 RLmax	0	1/2 EFmax	3.16	0.733	0	3.11	2.027	0	3.06	1.435	0
26	1/4 RLmax	1/4 CFmax	1/2 EFmax	3.08	0.743	0	3.04	2.065	0	2.98	1.465	0
27	1/4 RLmax	1/2 CFmax	1/2 EFmax	3.00	0.756	0	2.97	2.111	0	2.89	1.501	0
28	1/4 RLmax	CFmax	1/2 EFmax	2.73	0.805	0	2.65	2.334	0	2.62	1.626	0
29	1/4 RLmax	0	EFmax	2.96	0.763	0	2.89	2.161	0	2.83	1.526	0
30	1/4 RLmax	1/4 CFmax	EFmax	2.85	0.782	0	2.78	2.235	0	2.74	1.569	0
31	1/4 RLmax	1/2 CFmax	EFmax	2.73	0.805	0	2.66	2.327	0	2.63	1.622	0
32	1/4 RLmax	CFmax	EFmax	2.54	0.844	0	2.46	2.489	0	2.44	1.727	0
33	1/2 RLmax	0	0	2.56	1.095	1	2.59	2.601	1	2.57	1.868	1
34	1/2 RLmax	1/4 CFmax	0	2.52	1.102	1	2.49	2.674	1	2.54	1.887	1
35	1/2 RLmax	1/2 CFmax	0	2.48	1.111	1	2.44	2.713	1	2.49	1.910	1
36	1/2 RLmax	CFmax	0	2.38	1.136	1	2.31	2.841	1	2.35	1.994	1
37	1/2 RLmax	0	1/4 EFmax	2.52	1.102	1	2.48	2.681	1	2.53	1.890	1
38	1/2 RLmax	1/4 CFmax	1/4 EFmax	2.49	1.108	1	2.42	2.732	1	2.49	1.908	1
39	1/2 RLmax	1/2 CFmax	1/4 EFmax	2.46	1.116	1	2.38	2.764	1	2.45	1.931	1
40	1/2 RLmax	CFmax	1/4 EFmax	2.34	1.147	1	2.22	2.923	1	2.30	2.024	1
41	1/2 RLmax	0	1/2 EFmax	2.47	1.112	1	2.39	2.756	1	2.48	1.917	1
42	1/2 RLmax	1/4 CFmax	1/2 EFmax	2.45	1.117	1	2.36	2.779	1	2.45	1.935	1
43	1/2 RLmax	1/2 CFmax	1/2 EFmax	2.36	1.138	1	2.33	2.806	1	2.41	1.956	1
44	1/2 RLmax	CFmax	1/2 EFmax	2.23	1.171	1	2.15	2.997	1	2.25	2.059	1
45	1/2 RLmax	0	EFmax	2.36	1.135	1	2.29	2.850	1	2.38	1.973	1
46	1/2 RLmax	1/4 CFmax	EFmax	2.33	1.144	1	2.24	2.901	1	2.33	2.002	1
47	1/2 RLmax	1/2 CFmax	EFmax	2.28	1.156	1	2.18	2.967	1	2.27	2.039	1
48	1/2 RLmax	CFmax	EFmax	2.16	1.190	1	2.05	3.113	1	2.14	2.129	1
49	RLmax	0	0	2.51	1.624	2	2.47	3.179	2	2.59	2.364	2
50	RLmax	1/4 CFmax	0	2.47	1.633	2	2.45	3.195	2	2.50	2.403	2
51	RLmax	1/2 CFmax	0	2.44	1.638	2	2.39	3.246	2	2.41	2.443	2

52	RLmax	CFmax	0	2.36	1.659	2	2.28	3.353	2	2.28	2.517	2
53	RLmax	0	1/4 EFmax	2.48	1.628	2	2.45	3.194	2	2.45	2.418	2
54	RLmax	1/4 CFmax	1/4 EFmax	2.44	1.638	2	2.41	3.228	2	2.41	2.442	2
55	RLmax	1/2 CFmax	1/4 EFmax	2.35	1.654	2	2.34	3.282	2	2.38	2.457	2
56	RLmax	CFmax	1/4 EFmax	2.25	1.680	2	2.20	3.427	2	2.23	2.550	2
57	RLmax	0	1/2 EFmax	2.38	1.645	2	2.37	3.257	2	2.40	2.445	2
58	RLmax	1/4 CFmax	1/2 EFmax	2.06	1.737	2	2.34	3.282	2	2.40	2.444	2
59	RLmax	1/2 CFmax	1/2 EFmax	2.35	1.653	2	2.31	3.312	2	2.35	2.473	2
60	RLmax	CFmax	1/2 EFmax	2.52	1.613	2	2.13	3.500	2	2.22	2.550	2
61	RLmax	0	EFmax	2.35	1.651	2	2.29	3.329	2	2.34	2.479	2
62	RLmax	1/4 CFmax	EFmax	2.45	1.629	2	2.23	3.391	2	2.31	2.494	2
63	RLmax	1/2 CFmax	EFmax	2.21	1.684	2	2.16	3.467	2	2.24	2.540	2
64	RLmax	CFmax	EFmax	2.06	1.729	2	2.04	3.597	2	2.09	2.637	2

Table 3.7. Results in terms of SCOP, TEWI and number of maintenance interventions in cooling mode, for all the 64 possible combinations of fault intensities evolutions, for climate conditions of Naples, Miami and Shanghai, and for an ordinary every 4 year maintenance scenario

Ordinary maintenance every 4 years												
Test	**Fault Evolution**			**Naples**			**Miami**			**Shanghai**		
	Refrigerant Leakage (RL)	**Condenser Fouling (CF)**	**Evaporator Fouling (EF)**	**SCOP**	**TEWI [t_{CO2}]**	**Ninterv.**	**SCOP**	**TEWI [t_{CO2}]**	**Ninterv.**	**SCOP**	**TEWI [t_{CO2}]**	**Ninterv.**
1	0	0	0	4.24	0.347	3	4.22	1.296	3	4.11	0.869	3
2	0	1/4 CFmax	0	4.19	0.351	3	4.11	1.331	3	4.02	0.889	3
3	0	1/2 CFmax	0	4.13	0.356	3	4.00	1.368	3	3.92	0.911	3
4	0	CFmax	0	4.00	0.368	3	3.67	1.492	3	3.64	0.980	3
5	0	0	1/4 EFmax	4.21	0.349	3	4.09	1.340	3	4.00	0.892	3
6	0	1/4 CFmax	1/4 EFmax	4.16	0.353	3	3.98	1.375	3	3.91	0.913	3
7	0	1/2 CFmax	1/4 EFmax	4.11	0.358	3	3.88	1.412	3	3.82	0.934	3
8	0	CFmax	1/4 EFmax	3.97	0.370	3	3.56	1.537	3	3.56	1.005	3
9	0	0	1/2 EFmax	4.19	0.351	3	3.95	1.385	3	3.90	0.917	3
10	0	1/4 CFmax	1/2 EFmax	4.14	0.355	3	3.85	1.420	3	3.81	0.937	3
11	0	1/2 CFmax	1/2 EFmax	4.09	0.360	3	3.76	1.457	3	3.73	0.959	3
12	0	CFmax	1/2 EFmax	3.95	0.372	3	3.45	1.585	3	3.47	1.030	3
13	0	0	EFmax	4.14	0.355	3	3.60	1.521	3	3.63	0.984	3
14	0	1/4 CFmax	EFmax	4.09	0.359	3	3.52	1.556	3	3.56	1.003	3
15	0	1/2 CFmax	EFmax	4.04	0.364	3	3.44	1.593	3	3.49	1.023	3
16	0	CFmax	EFmax	3.91	0.376	3	3.28	1.669	3	3.30	1.081	3
17	1/4 RLmax	0	0	4.14	0.622	3	4.11	1.597	3	4.01	1.157	3
18	1/4 RLmax	1/4 CFmax	0	4.09	0.626	3	4.01	1.631	3	3.92	1.177	3
19	1/4 RLmax	1/2 CFmax	0	4.03	0.631	3	3.91	1.667	3	3.83	1.199	3
20	1/4 RLmax	CFmax	0	3.90	0.644	3	3.60	1.788	3	3.56	1.271	3
21	1/4 RLmax	0	1/4 EFmax	4.12	0.624	3	3.98	1.642	3	3.90	1.182	3
22	1/4 RLmax	1/4 CFmax	1/4 EFmax	4.06	0.629	3	3.88	1.677	3	3.82	1.202	3
23	1/4 RLmax	1/2 CFmax	1/4 EFmax	4.01	0.634	3	3.78	1.715	3	3.73	1.224	3
24	1/4 RLmax	CFmax	1/4 EFmax	3.88	0.646	3	3.48	1.839	3	3.47	1.296	3
25	1/4 RLmax	0	1/2 EFmax	4.09	0.626	3	3.84	1.691	3	3.79	1.209	3
26	1/4 RLmax	1/4 CFmax	1/2 EFmax	4.04	0.631	3	3.75	1.728	3	3.71	1.230	3
27	1/4 RLmax	1/2 CFmax	1/2 EFmax	3.98	0.636	3	3.65	1.767	3	3.63	1.252	3
28	1/4 RLmax	CFmax	1/2 EFmax	3.85	0.648	3	3.36	1.893	3	3.38	1.323	3
29	1/4 RLmax	0	EFmax	4.04	0.631	3	3.50	1.829	3	3.52	1.282	3
30	1/4 RLmax	1/4 CFmax	EFmax	3.99	0.635	3	3.42	1.868	3	3.44	1.304	3
31	1/4 RLmax	1/2 CFmax	EFmax	3.94	0.640	3	3.33	1.908	3	3.37	1.327	3
32	1/4 RLmax	CFmax	EFmax	3.81	0.653	3	3.09	2.039	3	3.15	1.401	3
33	1/2 RLmax	0	0	3.89	0.912	3	3.86	1.950	3	3.76	1.483	3
34	1/2 RLmax	1/4 CFmax	0	3.83	0.918	3	3.76	1.988	3	3.67	1.506	3
35	1/2 RLmax	1/2 CFmax	0	3.76	0.924	3	3.66	2.030	3	3.58	1.532	3
36	1/2 RLmax	CFmax	0	3.65	0.937	3	3.37	2.158	3	3.32	1.611	3
37	1/2 RLmax	0	1/4 EFmax	3.86	0.914	3	3.73	2.002	3	3.66	1.509	3
38	1/2 RLmax	1/4 CFmax	1/4 EFmax	3.80	0.920	3	3.64	2.039	3	3.58	1.532	3

39	1/2 RLmax	1/2 CFmax	1/4 EFmax	3.74	0.926	3	3.54	2.079	3	3.49	1.558	3
40	1/2 RLmax	CFmax	1/4 EFmax	3.62	0.939	3	3.24	2.225	3	3.22	1.642	3
41	1/2 RLmax	0	1/2 EFmax	3.84	0.917	3	3.58	2.062	3	3.55	1.540	3
42	1/2 RLmax	1/4 CFmax	1/2 EFmax	3.78	0.922	3	3.50	2.096	3	3.47	1.562	3
43	1/2 RLmax	1/2 CFmax	1/2 EFmax	3.72	0.928	3	3.42	2.135	3	3.39	1.588	3
44	1/2 RLmax	CFmax	1/2 EFmax	3.60	0.942	3	3.09	2.304	3	3.12	1.680	3
45	1/2 RLmax	0	EFmax	3.78	0.922	3	3.31	2.187	3	3.31	1.613	3
46	1/2 RLmax	1/4 CFmax	EFmax	3.73	0.927	3	3.22	2.235	3	3.23	1.639	3
47	1/2 RLmax	1/2 CFmax	EFmax	3.68	0.933	3	3.11	2.292	3	3.14	1.671	3
48	1/2 RLmax	CFmax	EFmax	3.55	0.948	3	2.87	2.441	3	2.92	1.758	3
49	RLmax	0	0	2.15	1.732	3	2.19	3.503	3	2.16	2.642	3
50	RLmax	1/4 CFmax	0	2.15	1.732	3	2.17	3.532	3	2.14	2.651	3
51	RLmax	1/2 CFmax	0	2.15	1.732	3	2.13	3.570	3	2.12	2.665	3
52	RLmax	CFmax	0	2.11	1.745	3	2.05	3.671	3	2.03	2.734	3
53	RLmax	0	1/4 EFmax	2.15	1.731	3	2.16	3.529	3	2.14	2.651	3
54	RLmax	1/4 CFmax	1/4 EFmax	2.15	1.731	3	2.14	3.553	3	2.12	2.662	3
55	RLmax	1/2 CFmax	1/4 EFmax	2.15	1.732	3	2.12	3.583	3	2.10	2.677	3
56	RLmax	CFmax	1/4 EFmax	2.11	1.746	3	2.00	3.729	3	2.00	2.758	3
57	RLmax	0	1/2 EFmax	2.15	1.732	3	2.12	3.575	3	2.11	2.670	3
58	RLmax	1/4 CFmax	1/2 EFmax	2.15	1.732	3	2.11	3.589	3	2.10	2.680	3
59	RLmax	1/2 CFmax	1/2 EFmax	2.15	1.733	3	2.09	3.611	3	2.08	2.694	3
60	RLmax	CFmax	1/2 EFmax	2.10	1.747	3	1.95	3.796	3	1.97	2.783	3
61	RLmax	0	EFmax	2.14	1.735	3	2.08	3.624	3	2.08	2.693	3
62	RLmax	1/4 CFmax	EFmax	2.14	1.735	3	2.03	3.685	3	2.05	2.720	3
63	RLmax	1/2 CFmax	EFmax	2.14	1.736	3	1.98	3.758	3	2.00	2.752	3
64	RLmax	CFmax	EFmax	2.10	1.749	3	1.89	3.886	3	1.91	2.831	3

Table 3.8. Results in terms of SCOP, TEWI and number of maintenance interventions in cooling mode, for all the 64 possible combinations of fault intensities evolutions, for climate conditions of Naples, Miami and Shanghai, and for an ordinary every 2 year maintenance scenario

Ordinary maintenance every 2 years												
Test	**Fault Evolution**			**Naples**			**Miami**			**Shanghai**		
	Refrigerant Leakage (RL)	**Condenser Fouling (CF)**	**Evaporator Fouling (EF)**	**SCOP**	**TEWI [t_{CO2}]**	**Ninterv.**	**SCOP**	**TEWI [t_{CO2}]**	**Ninterv.**	**SCOP**	**TEWI [t_{CO2}]**	**Ninterv.**
1	0	0	0	4.24	0.347	6	4.22	1.296	6	4.11	0.869	6
2	0	1/4 CFmax	0	4.20	0.350	6	4.13	1.326	6	4.04	0.883	6
3	0	1/2 CFmax	0	4.17	0.353	6	4.03	1.358	6	3.97	0.899	6
4	0	CFmax	0	4.09	0.360	6	3.74	1.462	6	3.78	0.944	6
5	0	0	1/4 EFmax	4.21	0.349	6	4.12	1.330	6	4.05	0.882	6
6	0	1/4 CFmax	1/4 EFmax	4.18	0.352	6	4.02	1.360	6	3.98	0.896	6
7	0	1/2 CFmax	1/4 EFmax	4.14	0.355	6	3.93	1.393	6	3.92	0.912	6
8	0	CFmax	1/4 EFmax	4.06	0.362	6	3.66	1.497	6	3.73	0.957	6
9	0	0	1/2 EFmax	4.19	0.351	6	4.01	1.365	6	3.99	0.895	6
10	0	1/4 CFmax	1/2 EFmax	4.15	0.354	6	3.92	1.395	6	3.93	0.910	6
11	0	1/2 CFmax	1/2 EFmax	4.12	0.357	6	3.83	1.427	6	3.86	0.925	6
12	0	CFmax	1/2 EFmax	4.04	0.364	6	3.57	1.534	6	3.68	0.971	6
13	0	0	EFmax	4.14	0.355	6	3.74	1.464	6	3.86	0.926	6
14	0	1/4 CFmax	EFmax	4.11	0.358	6	3.66	1.494	6	3.80	0.940	6
15	0	1/2 CFmax	EFmax	4.07	0.361	6	3.59	1.526	6	3.74	0.955	6
16	0	CFmax	EFmax	3.99	0.368	6	3.42	1.602	6	3.56	1.002	6
17	1/4 RLmax	0	0	4.21	0.616	6	4.20	1.571	6	4.09	1.141	6
18	1/4 RLmax	1/4 CFmax	0	4.18	0.619	6	4.10	1.601	6	4.02	1.155	6
19	1/4 RLmax	1/2 CFmax	0	4.14	0.622	6	4.01	1.632	6	3.95	1.170	6
20	1/4 RLmax	CFmax	0	4.06	0.629	6	3.73	1.734	6	3.76	1.216	6
21	1/4 RLmax	0	1/4 EFmax	4.19	0.618	6	4.09	1.606	6	4.03	1.154	6
22	1/4 RLmax	1/4 CFmax	1/4 EFmax	4.15	0.621	6	4.00	1.636	6	3.96	1.169	6
23	1/4 RLmax	1/2 CFmax	1/4 EFmax	4.12	0.624	6	3.91	1.668	6	3.90	1.184	6

24	1/4 RLmax	CFmax	1/4 EFmax	4.04	0.631	6	3.64	1.770	6	3.71	1.229	6
25	1/4 RLmax	0	1/2 EFmax	4.16	0.620	6	3.98	1.643	6	3.96	1.168	6
26	1/4 RLmax	1/4 CFmax	1/2 EFmax	4.13	0.623	6	3.89	1.674	6	3.90	1.182	6
27	1/4 RLmax	1/2 CFmax	1/2 EFmax	4.09	0.626	6	3.80	1.706	6	3.84	1.198	6
28	1/4 RLmax	CFmax	1/2 EFmax	4.01	0.633	6	3.55	1.808	6	3.66	1.243	6
29	1/4 RLmax	0	EFmax	4.11	0.624	6	3.70	1.746	6	3.82	1.201	6
30	1/4 RLmax	1/4 CFmax	EFmax	4.08	0.627	6	3.62	1.777	6	3.76	1.216	6
31	1/4 RLmax	1/2 CFmax	EFmax	4.04	0.630	6	3.55	1.810	6	3.70	1.231	6
32	1/4 RLmax	CFmax	EFmax	3.97	0.637	6	3.32	1.915	6	3.54	1.277	6
33	1/2 RLmax	0	0	4.14	0.889	6	4.11	1.864	6	4.01	1.424	6
34	1/2 RLmax	1/4 CFmax	0	4.10	0.892	6	4.03	1.893	6	3.95	1.439	6
35	1/2 RLmax	1/2 CFmax	0	4.06	0.895	6	3.94	1.924	6	3.88	1.455	6
36	1/2 RLmax	CFmax	0	3.98	0.903	6	3.67	2.026	6	3.69	1.501	6
37	1/2 RLmax	0	1/4 EFmax	4.11	0.891	6	4.01	1.899	6	3.95	1.438	6
38	1/2 RLmax	1/4 CFmax	1/4 EFmax	4.08	0.894	6	3.92	1.929	6	3.89	1.453	6
39	1/2 RLmax	1/2 CFmax	1/4 EFmax	4.04	0.897	6	3.83	1.962	6	3.82	1.468	6
40	1/2 RLmax	CFmax	1/4 EFmax	3.96	0.905	6	3.57	2.066	6	3.64	1.515	6
41	1/2 RLmax	0	1/2 EFmax	4.09	0.893	6	3.90	1.937	6	3.89	1.452	6
42	1/2 RLmax	1/4 CFmax	1/2 EFmax	4.05	0.896	6	3.81	1.969	6	3.83	1.467	6
43	1/2 RLmax	1/2 CFmax	1/2 EFmax	4.01	0.900	6	3.72	2.003	6	3.76	1.483	6
44	1/2 RLmax	CFmax	1/2 EFmax	3.94	0.907	6	3.47	2.109	6	3.58	1.530	6
45	1/2 RLmax	0	EFmax	4.03	0.898	6	3.64	2.038	6	3.75	1.486	6
46	1/2 RLmax	1/4 CFmax	EFmax	4.00	0.901	6	3.56	2.072	6	3.69	1.502	6
47	1/2 RLmax	1/2 CFmax	EFmax	3.97	0.904	6	3.48	2.107	6	3.63	1.518	6
48	1/2 RLmax	CFmax	EFmax	3.89	0.912	6	3.25	2.215	6	3.46	1.565	6
49	RLmax	0	0	3.88	1.446	6	3.86	2.484	6	3.76	2.017	6
50	RLmax	1/4 CFmax	0	3.84	1.450	6	3.77	2.517	6	3.69	2.034	6
51	RLmax	1/2 CFmax	0	3.80	1.454	6	3.68	2.554	6	3.62	2.053	6
52	RLmax	CFmax	0	3.72	1.462	6	3.44	2.660	6	3.44	2.106	6
53	RLmax	0	1/4 EFmax	3.86	1.448	6	3.75	2.526	6	3.70	2.032	6
54	RLmax	1/4 CFmax	1/4 EFmax	3.82	1.452	6	3.67	2.557	6	3.64	2.049	6
55	RLmax	1/2 CFmax	1/4 EFmax	3.78	1.456	6	3.59	2.592	6	3.57	2.068	6
56	RLmax	CFmax	1/4 EFmax	3.70	1.465	6	3.32	2.715	6	3.38	2.123	6
57	RLmax	0	1/2 EFmax	3.83	1.451	6	3.63	2.573	6	3.64	2.048	6
58	RLmax	1/4 CFmax	1/2 EFmax	3.79	1.454	6	3.57	2.602	6	3.58	2.065	6
59	RLmax	1/2 CFmax	1/2 EFmax	3.76	1.458	6	3.49	2.635	6	3.51	2.083	6
60	RLmax	CFmax	1/2 EFmax	3.67	1.467	6	3.19	2.781	6	3.32	2.143	6
61	RLmax	0	EFmax	3.78	1.456	6	3.43	2.664	6	3.51	2.084	6
62	RLmax	1/4 CFmax	EFmax	3.75	1.459	6	3.34	2.705	6	3.45	2.102	6
63	RLmax	1/2 CFmax	EFmax	3.71	1.463	6	3.25	2.753	6	3.39	2.122	6
64	RLmax	CFmax	EFmax	3.63	1.472	6	3.02	2.881	6	3.20	2.183	6

Table 3.9. Results in terms of SCOP, TEWI and number of maintenance interventions in cooling mode, for all the 64 possible combinations of fault intensities evolutions, for climate conditions of Naples, Miami and Shanghai, and for an ordinary every year maintenance scenario

Ordinary maintenance every year												
Test	Fault Evolution			Naples			Miami			Shanghai		
	Refrigerant Leakage (RL)	Condenser Fouling (CF)	Evaporator Fouling (EF)	SCOP	TEWI [t_{CO2}]	Ninterv.	SCOP	TEWI [t_{CO2}]	Ninterv.	SCOP	TEWI [t_{CO2}]	Ninterv.
1	0	0	0	4.24	0.347	12	4.22	1.296	12	4.11	0.869	12
2	0	1/4 CFmax	0	4.23	0.348	12	4.16	1.317	12	4.08	0.875	12
3	0	1/2 CFmax	0	4.22	0.349	12	4.09	1.339	12	4.05	0.881	12
4	0	CFmax	0	4.19	0.351	12	3.90	1.403	12	3.99	0.894	12
5	0	0	1/4 EFmax	4.23	0.348	12	4.17	1.314	12	4.09	0.873	12
6	0	1/4 CFmax	1/4 EFmax	4.22	0.348	12	4.10	1.335	12	4.06	0.879	12
7	0	1/2 CFmax	1/4 EFmax	4.21	0.349	12	4.03	1.357	12	4.04	0.885	12
8	0	CFmax	1/4 EFmax	4.18	0.351	12	3.85	1.421	12	3.98	0.898	12
9	0	0	1/2 EFmax	4.22	0.348	12	4.11	1.331	12	4.07	0.877	12
10	0	1/4 CFmax	1/2 EFmax	4.21	0.349	12	4.05	1.352	12	4.04	0.883	12
11	0	1/2 CFmax	1/2 EFmax	4.20	0.350	12	3.98	1.375	12	4.02	0.889	12
12	0	CFmax	1/2 EFmax	4.18	0.352	12	3.80	1.440	12	3.96	0.902	12
13	0	0	EFmax	4.21	0.350	12	4.00	1.370	12	4.03	0.885	12
14	0	1/4 CFmax	EFmax	4.19	0.351	12	3.93	1.391	12	4.01	0.891	12
15	0	1/2 CFmax	EFmax	4.18	0.351	12	3.87	1.413	12	3.98	0.898	12
16	0	CFmax	EFmax	4.16	0.353	12	3.70	1.480	12	3.92	0.911	12
17	1/4 RLmax	0	0	4.24	0.614	12	4.22	1.563	12	4.11	1.136	12
18	1/4 RLmax	1/4 CFmax	0	4.23	0.614	12	4.16	1.584	12	4.08	1.142	12
19	1/4 RLmax	1/2 CFmax	0	4.22	0.615	12	4.09	1.606	12	4.05	1.148	12
20	1/4 RLmax	CFmax	0	4.19	0.617	12	3.90	1.669	12	4.00	1.161	12
21	1/4 RLmax	0	1/4 EFmax	4.23	0.614	12	4.17	1.580	12	4.09	1.140	12
22	1/4 RLmax	1/4 CFmax	1/4 EFmax	4.22	0.615	12	4.10	1.601	12	4.06	1.146	12
23	1/4 RLmax	1/2 CFmax	1/4 EFmax	4.21	0.616	12	4.03	1.623	12	4.04	1.152	12
24	1/4 RLmax	CFmax	1/4 EFmax	4.18	0.618	12	3.85	1.687	12	3.98	1.165	12
25	1/4 RLmax	0	1/2 EFmax	4.22	0.615	12	4.11	1.599	12	4.07	1.144	12
26	1/4 RLmax	1/4 CFmax	1/2 EFmax	4.21	0.616	12	4.04	1.620	12	4.04	1.150	12
27	1/4 RLmax	1/2 CFmax	1/2 EFmax	4.20	0.617	12	3.98	1.642	12	4.02	1.156	12
28	1/4 RLmax	CFmax	1/2 EFmax	4.18	0.619	12	3.80	1.705	12	3.96	1.169	12
29	1/4 RLmax	0	EFmax	4.20	0.616	12	3.98	1.641	12	4.03	1.152	12
30	1/4 RLmax	1/4 CFmax	EFmax	4.19	0.617	12	3.92	1.662	12	4.01	1.158	12
31	1/4 RLmax	1/2 CFmax	EFmax	4.18	0.618	12	3.86	1.684	12	3.98	1.164	12
32	1/4 RLmax	CFmax	EFmax	4.16	0.620	12	3.69	1.748	12	3.92	1.178	12
33	1/2 RLmax	0	0	4.21	0.882	12	4.20	1.837	12	4.09	1.408	12
34	1/2 RLmax	1/4 CFmax	0	4.20	0.883	12	4.13	1.858	12	4.06	1.414	12
35	1/2 RLmax	1/2 CFmax	0	4.19	0.884	12	4.07	1.880	12	4.03	1.420	12
36	1/2 RLmax	CFmax	0	4.17	0.886	12	3.88	1.943	12	3.97	1.433	12
37	1/2 RLmax	0	1/4 EFmax	4.20	0.883	12	4.14	1.855	12	4.07	1.412	12
38	1/2 RLmax	1/4 CFmax	1/4 EFmax	4.19	0.884	12	4.08	1.876	12	4.04	1.418	12
39	1/2 RLmax	1/2 CFmax	1/4 EFmax	4.18	0.885	12	4.01	1.898	12	4.01	1.424	12
40	1/2 RLmax	CFmax	1/4 EFmax	4.16	0.887	12	3.83	1.961	12	3.95	1.437	12
41	1/2 RLmax	0	1/2 EFmax	4.20	0.884	12	4.08	1.874	12	4.05	1.416	12
42	1/2 RLmax	1/4 CFmax	1/2 EFmax	4.18	0.885	12	4.02	1.895	12	4.02	1.422	12
43	1/2 RLmax	1/2 CFmax	1/2 EFmax	4.17	0.886	12	3.96	1.917	12	3.99	1.428	12
44	1/2 RLmax	CFmax	1/2 EFmax	4.15	0.888	12	3.78	1.980	12	3.93	1.441	12
45	1/2 RLmax	0	EFmax	4.18	0.885	12	3.96	1.916	12	4.01	1.425	12
46	1/2 RLmax	1/4 CFmax	EFmax	4.17	0.886	12	3.90	1.937	12	3.98	1.431	12
47	1/2 RLmax	1/2 CFmax	EFmax	4.16	0.887	12	3.84	1.960	12	3.95	1.437	12
48	1/2 RLmax	CFmax	EFmax	4.13	0.889	12	3.67	2.023	12	3.90	1.450	12
49	RLmax	0	0	4.14	1.422	12	4.11	2.398	12	4.01	1.958	12
50	RLmax	1/4 CFmax	0	4.12	1.423	12	4.05	2.418	12	3.98	1.964	12
51	RLmax	1/2 CFmax	0	4.11	1.424	12	3.99	2.438	12	3.95	1.970	12

52	RLmax	CFmax	0	4.09	1.426	12	3.82	2.500	12	3.90	1.984	12
53	RLmax	0	1/4 EFmax	4.13	1.423	12	4.06	2.415	12	3.99	1.962	12
54	RLmax	1/4 CFmax	1/4 EFmax	4.12	1.424	12	4.00	2.436	12	3.96	1.968	12
55	RLmax	1/2 CFmax	1/4 EFmax	4.10	1.425	12	3.94	2.457	12	3.93	1.975	12
56	RLmax	CFmax	1/4 EFmax	4.08	1.427	12	3.77	2.519	12	3.88	1.988	12
57	RLmax	0	1/2 EFmax	4.12	1.424	12	4.01	2.433	12	3.97	1.967	12
58	RLmax	1/4 CFmax	1/2 EFmax	4.11	1.425	12	3.94	2.454	12	3.94	1.973	12
59	RLmax	1/2 CFmax	1/2 EFmax	4.10	1.426	12	3.88	2.477	12	3.92	1.979	12
60	RLmax	CFmax	1/2 EFmax	4.07	1.428	12	3.72	2.540	12	3.86	1.992	12
61	RLmax	0	EFmax	4.10	1.425	12	3.89	2.475	12	3.93	1.975	12
62	RLmax	1/4 CFmax	EFmax	4.09	1.426	12	3.83	2.497	12	3.91	1.981	12
63	RLmax	1/2 CFmax	EFmax	4.08	1.427	12	3.77	2.520	12	3.88	1.988	12
64	RLmax	CFmax	EFmax	4.06	1.429	12	3.60	2.586	12	3.82	2.001	12

Table 3.10 is obtained instead as an extract from the previous tables, considering in case of Naples climate conditions the standalone maximum severities for each of the three faults analysed.

The number of maintenance interventions oscillates between 0 and 2 in case of a not planned maintenance scenario, whereas for 4-year, 2-year and 1-year ordinary maintenance scenarios, they become respectively 3, 6 and 12.

Generally, the SCOP decreases and the TEWI index increases with the rise of fault intensities levels. For instance, in case of not-planned maintenance and a standalone condenser and evaporator fouling faults with maximum intensities of CFmax (test 4) and EFmax (test 13), the SCOP assumes values of respectively 3.69 and 3.63, approximately 14% lower than the ideal case (test 1). In case of a refrigerant leakage with a leakage rate of RLmax, instead (test 49), SCOP decreases to 2.51, which is approximately 41% lower than the fault-free scenario. Regarding the environmental impact, the TEWI values are mainly affected by refrigerant leakages, especially due to the direct contribution, whereas heat exchanger fouling slightly affect the TEWI only in its indirect contribution related to the extra-consumption of the machine. For instance, in case of Naples, the TEWI increases from 0.347 $tCO_{2,equiv}$ to 1.624 $tCO_{2,eq}$ passing from the fault-free case to the scenario with a standalone refrigerant leakage, whereas for respectively standalone condenser and evaporator fouling faults, the TEWI increases of approximately 15% and 17% respectively compared with the fault-free scenario.

Considering the ordinary maintenance scenarios, higher values of SCOP and TEWI can be obtained, closer to the ones assumed in the fault-free cases. For instance, in case of a 4-year ordinary maintenance, SCOP values for standalone condenser and evaporator fouling faults become respectively 8% and 14% higher compared to the not-planned maintenance scenarios. On the other hand, for refrigerant leakage, the SCOP is slightly lower than the not-planned maintenance case, 2.15 against 2.51, especially due to different evolution stories of faults and a limited convenience of this kind of maintenance in this case. Finally, in case of an ordinary

maintenance every year, SCOP values for standalone refrigerant leakage, condenser and evaporator fouling faults become respectively 65%, 14% and 16% higher than the corresponding cases in a not-planned maintenance scenario. Similar considerations could be done also for TEWI values.

Table 3.10. Extract of the previous tables for Naples climate conditions, and considering the fault free case and the standalone maximum value for each of the fault intensities considered

Test	Fault Evolution			Naples		
	Refrigerant Leakage (RL)	**Condenser Fouling (CF)**	**Evaporator Fouling (EF)**	**SCOP**	**TEWI [$t_{CO2.equiv}$]**	**Ninterv.**
1	0	0	0	4.24	0.347	0
Not planned maintenance by User						
4	0	CFmax	0	3.69	0.398	0
13	0	0	EFmax	3.63	0.405	0
49	RLmax	0	0	2.51	1.624	2
Ordinary maintenance every 4 years						
4	0	CFmax	0	4.00	0.368	3
13	0	0	EFmax	4.14	0.355	3
49	RLmax	0	0	2.15	1.732	3
Ordinary maintenance every 2 years						
4	0	CFmax	0	4.09	0.360	6
13	0	0	EFmax	4.14	0.355	6
49	RLmax	0	0	3.88	1.446	6
Ordinary maintenance every year						
4	0	CFmax	0	4.19	0.351	12
13	0	0	EFmax	4.21	0.350	12
49	RLmax	0	0	4.14	1.422	12

Considering all these aspects, the results from Table 3.6, Table 3.7, Table 3.8 and Table 3.9 show higher SCOP values for Naples and Miami compared to Shanghai in fault-free operation. On the other hand, a higher number of operating working hours of the machine, typical of Miami and Shanghai climate conditions, means more time spent by the machine operating faulty, and so it gives a higher contribution to performance degradations. Furthermore, heat exchanger fouling growths depend strongly by the number of effective working hours of the machine. For this reason, the performance penalizations obtained in case of not planned

maintenance operations compared with the fault free scenario are typically higher for the city of Miami and Shanghai, compared with Naples. Several exceptions (for instance test 33) can be explained as the fact that more operating hours mean also higher probability for a user to self-identify the ongoing fault. TEWI is especially affected by the energy consumptions of the machine, which depend in turn on working hours. Therefore, lower values are obtained for Naples and higher values for Miami, whereas for Shanghai it assumes intermediate values between Naples and Miami.

In case of an organized pre-planned maintenance, higher performances of the machine are generally obtained with a higher number of interventions. Figure 3.15(a-c) shows the percentage of all the 64 combinations shown in tables, in which the SCOP penalization is higher respectively than 5%, 10% and 15%. Results are provided for every maintenance strategy, and different colours refer to the three climate conditions investigated. In case of SCOP penalization over 15% (Figure 3.15(a)), a 4-year maintenance operation is able to halve the number of the penalized scenarios for the city of Naples, whereas for Miami and Shanghai at least a planned maintenance every 2 years is required to reach a 50% percentage. In case of SCOP penalization over 10% (Figure 3.15(b)), similar considerations could be done for the cities of Naples and Shanghai, whereas for the city of Miami even a every 2 years planned maintenance is not able to reduce to 50% the penalized cases. Finally, in case of SCOP penalization over 5% (Figure 3.15(c)), a 2-years planned maintenance can guarantee a reduction of penalized scenarios to 50% only for the city of Naples, whereas respectively for Miami and Shanghai at least a 1 year maintenance should be provided.

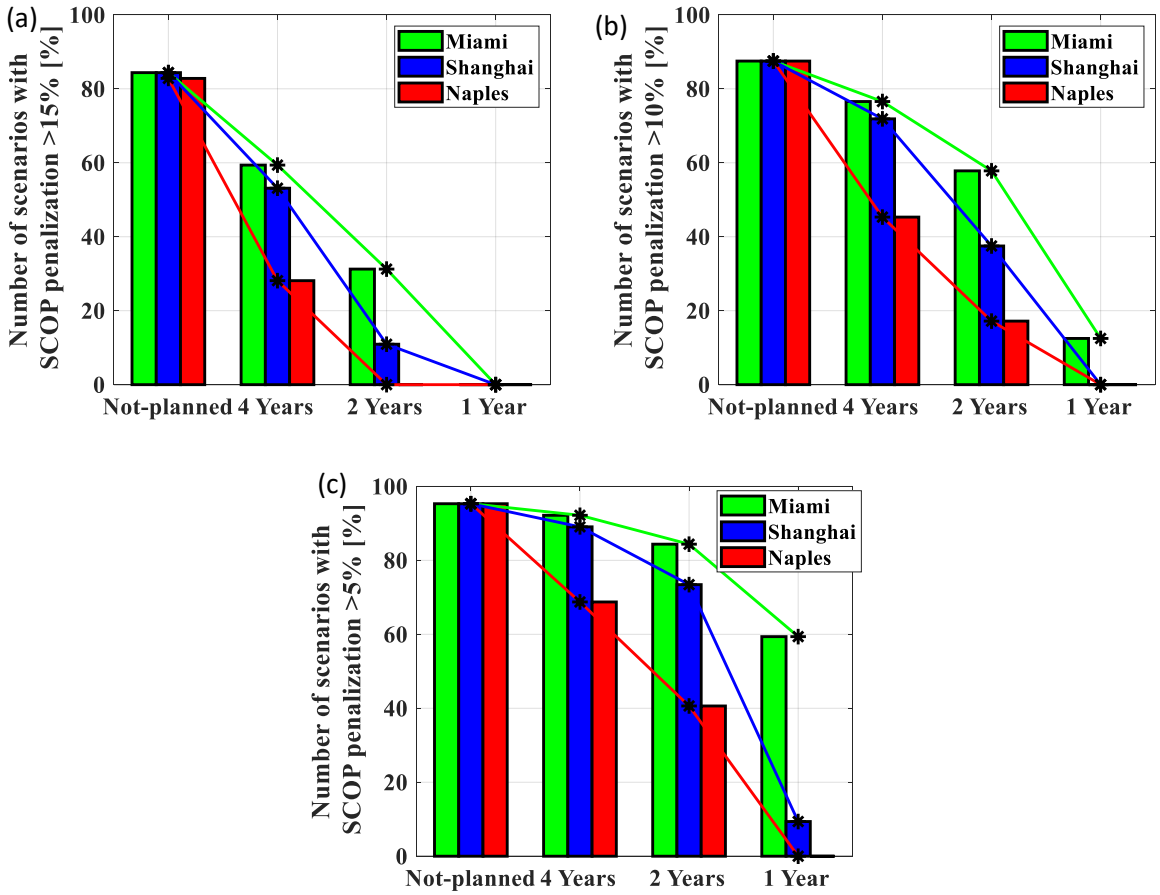


Figure 3.15. Percentages of scenario for which SCOP results to be penalized more than 15% (a), 10% (b) and 5% (c), for the cooling mode, depending on the climate condition and on the maintenance scenario investigated

Therefore, better seasonal performances of the machine can be reached by increasing the number of maintenance intervention, with the possibility of reducing the number of SCOP penalized scenarios. However, an increased number of interventions means higher maintenance costs, and the real risk is to perform maintenance operations also when is not necessary. As a matter of fact, when the level of fault is low, a maintenance operation becomes not useful, and the corresponding advantage in terms of system recovery could be marginal. This aspect refers also to the fact that each of the simulated combinations of faults and fault severities may not have the same probability of occurrence, as simulated in this work.

3.2.6 Results in heating mode

In this section the performance maps are reported, with the effect of standalone and combined faults on the thermodynamic cycle of the heat pump and the study of the dynamic behaviour of the machine along its entire lifetime, related to a machine operating in heating mode. The system analysed is the same already studied for the cooling mode, except that the external heat exchanger is now used as the evaporator and the internal heat exchanger as the condenser.

Therefore, further indications about system data and assumptions can be found in previous sections.

3.2.6.1 Performance maps of the case study

Here results for COP performance maps depending on ambient temperature and percentage of fault intensities are provided in Figure 3.16 for the three faults analysed in this thesis, for a fixed indoor temperature of 20 °C. As expected, in all cases, the COP increases with the increase of the ambient temperature.

Figure 3.16(a) represents COP values in case of fouling for the external unit fouling, used as evaporator in heating mode, with a fault intensity ranging from 0 to 40%. Differently to what analysed in cooling mode, in this case it seems that fouling affects the system performance only for higher ambient temperatures and fault intensities. For instance, in case of an ambient temperature of -10 °C, evaporator fouling almost does not influence COP, which remains approximately equal to 3.05. Figure 3.16(b) represents instead a COP performance map obtained in case of fouling for the internal unit, used as condenser in heating mode, with a fault intensity between 0 and 40%. In this case, the effect of fouling on performance degradation is higher compared to the evaporator fouling, and quite similar to what already observed in cooling mode. As a matter of fact, the COP decreases almost linearly with fouling for lower values of the fault intensity, with a decreasing rate which increases for higher fault intensities. Likewise, the evaporator fouling and condensing fouling effects seem to be higher at higher ambient temperatures. Finally, Figure 3.16(c) represents a COP contour obtained for refrigerant leakage in a range between 0 and 60%. Similarly to what already observed for the cooling mode, COP decreases with the increase of refrigerant loss in the system analyzed, with a decrease rate that largely increases for higher leakage values.

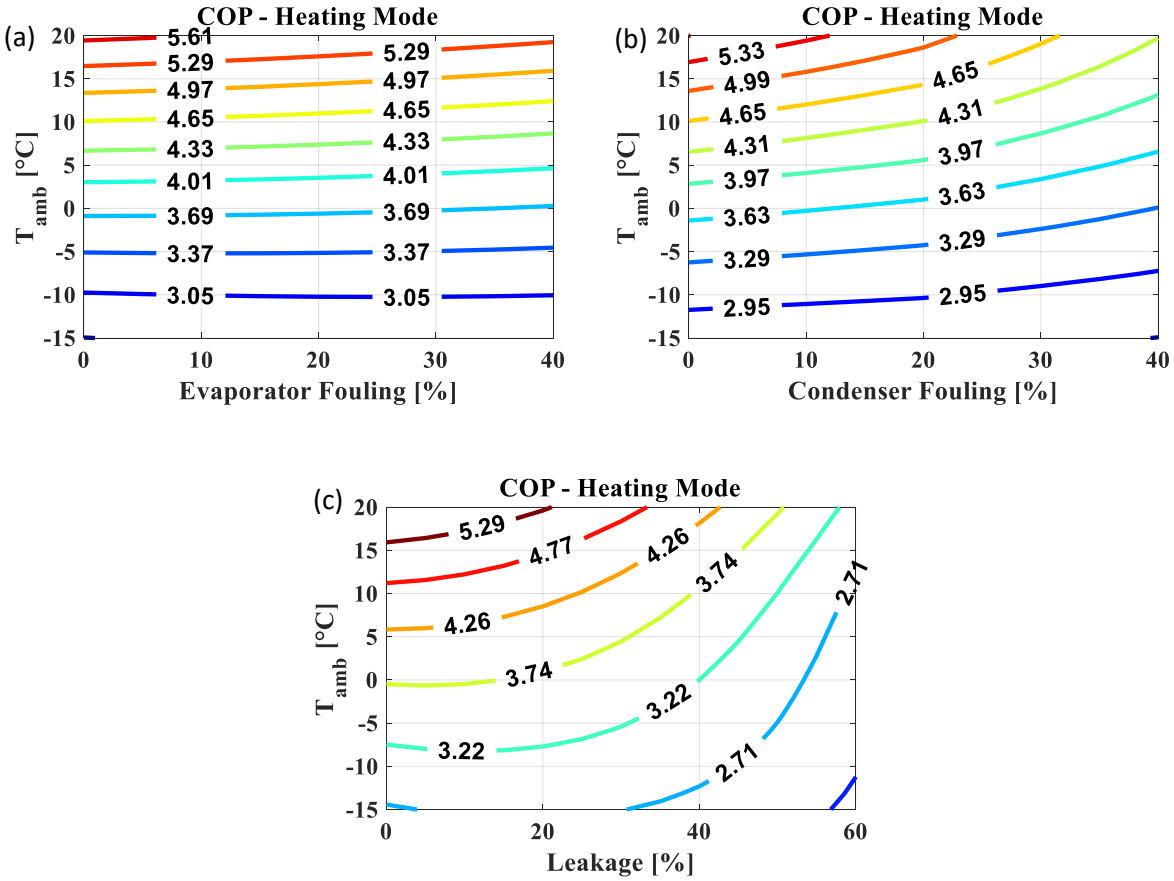


Figure 3.16. Performance maps in heating mode in terms of COP value, depending on ambient temperature and fault intensities, for a fixed condition of the indoor temperature of 20 °C. (a) Evaporator fouling. (b) Condenser fouling. (c) Refrigerant leakage

3.2.6.2 Effect of standalone and combined faults on the thermodynamic cycle

As already analysed for the cooling mode, soft faults influence on the measured parameters of the thermodynamic cycle of the machine is here presented also for the heating mode. Figure 3.17 shows on T-s diagrams a comparison between faulty and fault-free thermodynamic cycles, obtained for fixed boundary conditions related ambient and indoor temperatures, respectively equal to 7 °C and 20 °C.

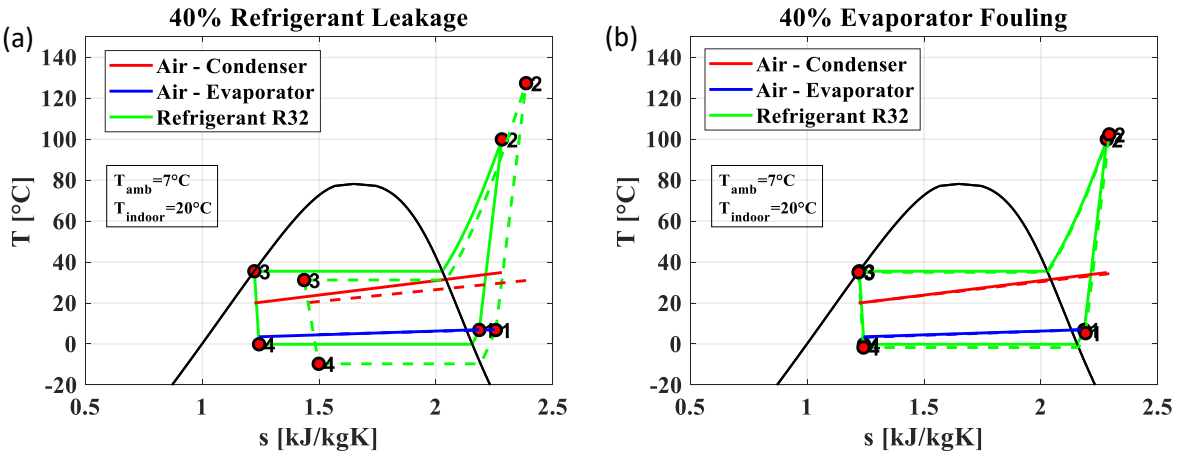
For a 40% refrigerant leakage condition (Figure 3.17(a)), evaporating and condensing temperatures result to be respectively 9.6 °C and 4.3 °C lower than the fault-free case. Outlet compressor temperature becomes 27.4 °C higher, whereas outlet evaporator superheating rises of about 10 °C. This results in a heating capacity which becomes about 38% lower, and a COP penalization of approximately 42%. These results are in accordance with the ones obtained for cooling mode.

For a 40% condenser fouling (Figure 3.17(b)), the condensing temperature is strongly affected, resulting to be about 7.0 °C higher than the fault-free case, whereas the evaporating temperature

seems to be almost unaffected. The increased condensing temperature causes a rise of the outlet compressor temperature of about 17 °C. Although the condenser fouling causes a reduction of the mass flow rate of the internal unit, it seems that it affects especially the air temperature difference at the condenser, which rises of 12.5 °C, whereas heating capacity remains almost unaffected. Otherwise, the COP decreases of approximately 21% if compared with the fault-free case.

In case of a 40% evaporator fouling (Figure 3.17(c)), in accordance with the previous section, the thermodynamic cycle seems to be almost unaffected by that kind of fault. As a matter of fact, the most influenced variables are the evaporating temperature, which decreases of 1.6 °C and the outlet compressor temperature, which increases of 2.4 °C. Definitely, heating capacity and COP decrease of respectively 3.9% and 4.2%.

Finally, in case of a combination of all the three faults analysed, with the same fault intensity level of 40% (Figure 3.17(d)), different variations can be noticed deriving from the effect overlapping from each kind of fault, as also observed in cooling mode. For instance, the presence of both refrigerant leakage and evaporator fouling enhances the evaporator temperature reduction, which becomes of approximately 12 °C lower. Similar consideration could be done also for the outlet compressor temperature, which rises of about 50 °C. On the other hand, the contrasting effects of refrigerant leakage and condenser fouling make the condensing temperature almost unchanged, with a decrease of only 1 °C. Definitely, the combination of faults causes a heating capacity reduction of 45% and a COP reduction of about 60% compared to the fault-free case.



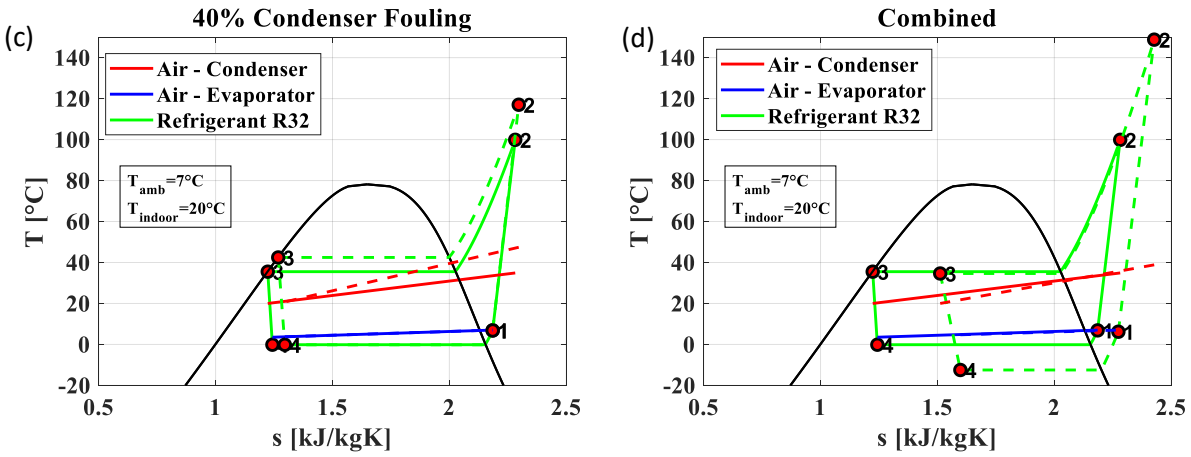


Figure 3.17. Temperature – specific entropy diagrams for fixed conditions of ambient and indoor temperature of 7 °C and 22 °C, obtained in case of a 40% refrigerant leakage (a), a 40% condenser fouling (b), a 40% evaporator fouling (c), and combined a 40% for all the fault intensities(d). Solid and dashed lines are related respectively to fault-free and faulty thermodynamic cycles

All the numerical values for evaporating and condensing temperatures, outlet compressor temperature, outlet evaporator superheating, condenser and evaporator air temperature differences, heating capacity and COP are reported in Table 3.11.

Table 3.11. Values of measured parameters on the machine in heating mode, in case of fault-free and faulty conditions, for fixed conditions of ambient and indoor temperature of 7 °C and 20 °C. The differences between the faulty and fault-free specific cases are reported in brackets.

Operation (Difference with fault-free)	T_{ev} [°C]	T_{co} [°C]	$T_{out,comp}$ [°C]	ΔT_{sh} [°C]	$\Delta T_{air,co}$ [°C]	$\Delta T_{air,ev}$ [°C]	$\dot{Q}_{co}$ [kW]	**COP**
Fault-free	-0.1	35.5	99.9	7	14.9	3.5	2.58	3.35
40% Refrigerant Leakage	-9.7 (-9.6°C)	31.2 (-4.3°C)	127.3 (+27.4°C)	16.5 (+9.7°C)	11.0 (-3.9°C)	2.4 (-1.1°C)	1.61 (-37.6%)	1.93 (-42.4%)
40% Fouling Condenser	-0.2 (-0.1°C)	42.5 (+7.0°C)	117.0 (+17.1°C)	7 (+0.0°C)	27.4 (+12.5°C)	3.3 (-0.2°C)	2.56 (-0.8%)	2.65 (-20.9%)
40% Fouling Evaporator	-1.7 (-1.6°C)	35.0 (-0.5°C)	102.3 (+2.4°C)	7 (+0.0°C)	14.3 (-0.6°C)	3.8 (+0.3°C)	2.48 (-3.9%)	3.21 (-4.2%)
40% Fault intensity every fault combined	-12.5 (-12.4°C)	34.6 (-0.9°C)	148.8 (+48.9°C)	18.7 (+11.7°C)	18.8 (+3.9°C)	2.3 (-1.2°C)	1.42 (-45.0%)	1.41 (-57.9%)

3.2.6.3 Dynamic simulations

As already done in cooling mode, the dynamic behaviour of the machine is analysed also in heating mode, along a 12 year lifetime. For this analysis, an air-conditioning environment characterized by a global conductance of 55 W/m^{2}K is chosen to have a bivalent temperature of -10 °C. For lower ambient temperatures, an integration is considered in order to satisfy the remaining part of user load. The machine is considered operating in heating mode between the months of October and April. Furthermore, for this analysis, three different climate conditions have been investigated: New York in USA, Beijing in China and Vienna in Austria. Temperature values have been collected from TRNSYS Software database [118], and number of bins and temperature evolutions along the operating winter months are reported in Figure 3.18. From Figure 3.18(a) it can be noticed that Vienna and New York climate conditions are characterized by a large number of hours in which the temperature oscillates between 0 and 20 °C, whereas the coldest temperatures are reached for Beijing, with a considerable number of hours for which the ambient temperature drops below 0 °C. Same consideration could be done also in Figure 3.18(b), with few hours reaching minimum temperatures of -15 °C for climates of New York and Beijing.

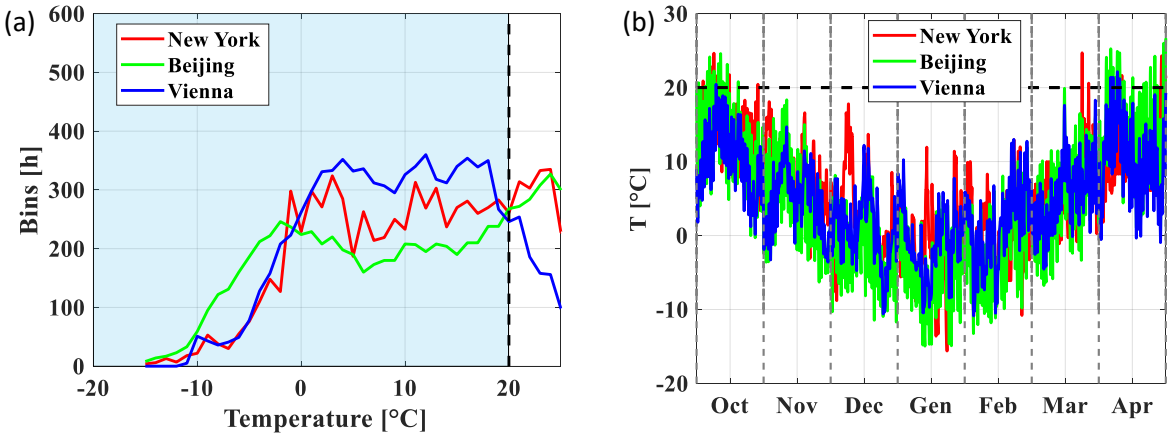


Figure 3.18. Number of operating hours vs. external temperature (a) and external temperature evolution in months between October and April (b), for the climate conditions of New York, Beijing and Vienna

The machine is considered operating whenever the ambient temperature drops below 20 °C. Number of operating hours of the machine for each of the climate conditions investigated are reported in Table 3.12. Although it seems from previous graphs that Vienna has the highest temperatures between the climate conditions investigated, it has also the highest number of working hours. Similar numbers are instead obtained for the cities of New York and Beijing.

Table 3.12. Number of operating hours for which the external temperature drops below 20 °C, for climate conditions of New York, Beijing and Vienna

Annual operating hours of the machine		
New York	**Beijing**	**Vienna**
6387	5967	7613

The same scenarios already simulated in cooling modes in terms of refrigerant leakage rate (0, ¼ RL_{max}, ½ RL_{max}, RL_{max}) and maximum values for condenser (0, ¼ CF_{max}, ½ CF_{max}, CF_{max}) and evaporator (0, ¼ EF_{max}, ½ EF_{max}, EF_{max}) fouling processes have been adopted also in the heating mode. Values assumed by RL_{max}, CF_{max} and EF_{max} have been previously defined in section 0. For the internal and external units, a number of hours to reach the 90% of the maximum dust accumulation of respectively 5000 and 3000 working hours have been considered. Furthermore, the same maintenance scenarios used for cooling mode of not-planned, ordinary every 4 years, 2 years and 1 year are adopted. For each maintenance scenario, a total of 64 cases has been obtained combining the different fault intensities, and for each of them the corresponding SCOP and TEWI values are evaluated.

Figure 3.19 (a, b) shows an example of COP evolution along the 12-year lifetime of the machine, in case of not planned (Figure 3.19(a)) and every two-year maintenance scenarios (Figure 3.19(b)). Results are obtained for a refrigerant leakage rate of ½ RL_{max}, a maximum value for evaporator fouling of ½ EF_{max} and for condenser fouling of ¼ CF_{max}. In grey, instead, the COP evolution is shown for the ideal fault-free case. The evolution of the fault intensity is reported in Figure 3.19 (c, d) for the two maintenance scenarios investigated. Similarly to the cooling mode, in case of a not planned maintenance scenario, the user realises about the fault only after about 8 years when values for COP become almost zero. In this case, the refrigerant leakage has reached a value of about 80%, whereas both condenser and evaporator fouling have reached their maximum value. The SCOP is equal to 3.01, about 25% lower than the ideal case (3.98). With every two-year maintenance, the level of leakage never exceeds 20%, with a COP that never drops below approximately 3. In this case, the SCOP value is about 3.88. which is 29% higher than the not-planned maintenance scenario and closer to the ideal case.

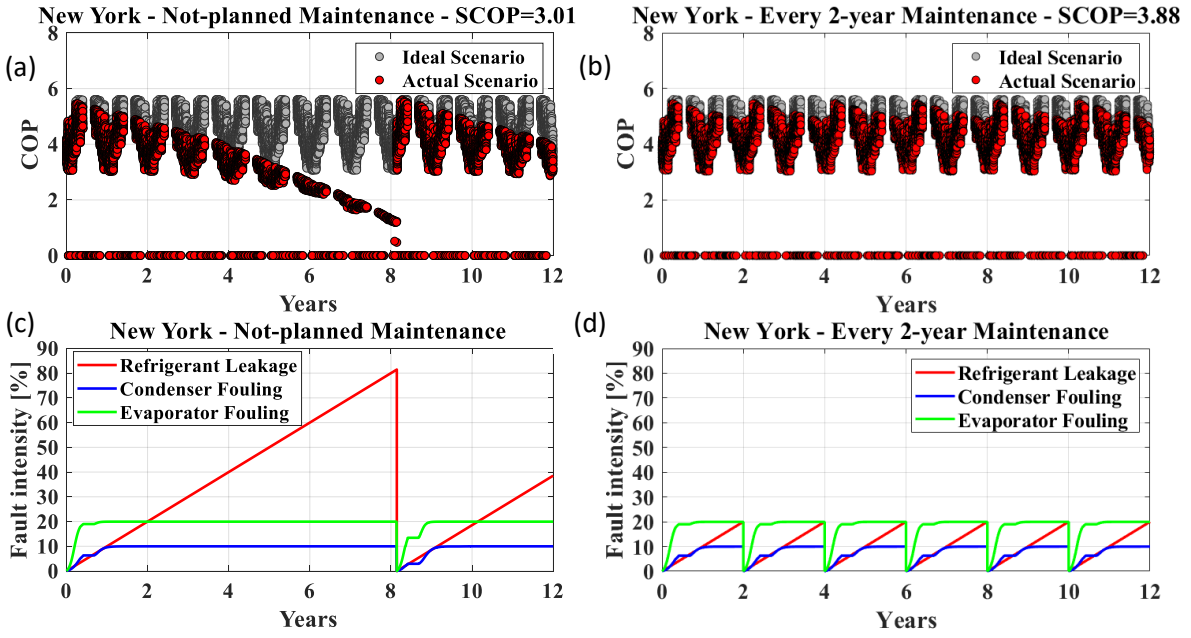


Figure 3.19. COP evolution and corresponding fault intensities evolution along the entire machine lifetime in heating mode for New York climate conditions, for a 10%/year refrigerant leakage, a maximum condenser fouling of 10% and a maximum evaporator fouling of 20%, in case of a not-planned (a) and every two years (b) maintenance scenarios

Results in terms of SCOP, TEWI and number of maintenance interventions occurring during the entire lifetime of the machine are reported in the following tables for all the 64 aforementioned combinations and for all the maintenance scenarios. Table 3.13 shows the results for a not planned maintenance, whereas Table 3.14, Table 3.15 and Table 3.16 show the results in case of ordinary maintenance, respectively every 4, 2 and 1 year.

Table 3.13. Results in terms of SCOP, TEWI and number of maintenance interventions in heating mode, for all the 64 possible combinations of fault intensities evolutions, for climate conditions of New York, Beijing and Vienna, and for a not-planned maintenance scenario

Not planned maintenance by User												
Test	Fault Evolution			New York			Beijing			Vienna		
	Refrigerant Leakage (RL)	Condenser Fouling (CF)	Evaporator Fouling (EF)	SCOP	TEWI [t_{CO2}]	Ninterv.	SCOP	TEWI [t_{CO2}]	Ninterv.	SCOP	TEWI [t_{CO2}]	Ninterv.
1	0	0	0	3.98	6.19	0	3.78	7.01	0	3.98	6.95	0
2	0	1/4 CFmax	0	3.88	6.36	0	3.69	7.17	0	3.88	7.13	0
3	0	1/2 CFmax	0	3.78	6.53	0	3.60	7.34	0	3.78	7.32	0
4	0	CFmax	0	3.46	7.13	0	3.33	7.94	0	3.46	8.00	0
5	0	0	1/4 EFmax	3.97	6.21	0	3.77	7.02	0	3.97	6.96	0
6	0	1/4 CFmax	1/4 EFmax	3.87	6.37	0	3.69	7.18	0	3.87	7.14	0
7	0	1/2 CFmax	1/4 EFmax	3.77	6.54	0	3.60	7.35	0	3.77	7.33	0
8	0	CFmax	1/4 EFmax	3.46	7.13	0	3.33	7.95	0	3.45	8.00	0
9	0	0	1/2 EFmax	3.97	6.22	0	3.77	7.03	0	3.96	6.98	0
10	0	1/4 CFmax	1/2 EFmax	3.87	6.38	0	3.68	7.19	0	3.86	7.16	0
11	0	1/2 CFmax	1/2 EFmax	3.77	6.55	0	3.60	7.36	0	3.76	7.35	0
12	0	CFmax	1/2 EFmax	3.46	7.14	0	3.33	7.95	0	3.45	8.01	0
13	0	0	EFmax	3.90	6.32	0	3.72	7.11	0	3.90	7.09	0
14	0	1/4 CFmax	EFmax	3.81	6.47	0	3.64	7.26	0	3.81	7.26	0
15	0	1/2 CFmax	EFmax	3.72	6.63	0	3.57	7.42	0	3.72	7.43	0
16	0	CFmax	EFmax	3.43	7.20	0	3.31	8.01	0	3.42	8.08	0
17	1/4 RLmax	0	0	3.44	7.35	0	3.34	8.09	0	3.42	8.26	0
18	1/4 RLmax	1/4 CFmax	0	3.40	7.44	0	3.29	8.20	0	3.39	8.33	0
19	1/4 RLmax	1/2 CFmax	0	3.35	7.55	0	3.24	8.33	0	3.35	8.43	0
20	1/4 RLmax	CFmax	0	3.10	8.14	0	3.03	8.88	0	3.09	9.14	0
21	1/4 RLmax	0	1/4 EFmax	3.40	7.43	0	3.30	8.16	0	3.38	8.35	0
22	1/4 RLmax	1/4 CFmax	1/4 EFmax	3.37	7.50	0	3.27	8.25	0	3.36	8.40	0
23	1/4 RLmax	1/2 CFmax	1/4 EFmax	3.33	7.58	0	3.22	8.36	0	3.33	8.47	0
24	1/4 RLmax	CFmax	1/4 EFmax	3.07	8.22	0	3.01	8.94	0	3.06	9.22	0
25	1/4 RLmax	0	1/2 EFmax	3.36	7.53	0	3.27	8.24	0	3.34	8.46	0
26	1/4 RLmax	1/4 CFmax	1/2 EFmax	3.34	7.56	0	3.24	8.31	0	3.33	8.48	0
27	1/4 RLmax	1/2 CFmax	1/2 EFmax	3.32	7.62	0	3.20	8.40	0	3.31	8.52	0
28	1/4 RLmax	CFmax	1/2 EFmax	3.04	8.30	0	2.98	9.02	0	3.02	9.32	0
29	1/4 RLmax	0	EFmax	3.25	7.78	0	3.17	8.47	0	3.23	8.74	0
30	1/4 RLmax	1/4 CFmax	EFmax	3.24	7.79	0	3.15	8.52	0	3.23	8.73	0
31	1/4 RLmax	1/2 CFmax	EFmax	3.22	7.82	0	3.12	8.60	0	3.22	8.75	0
32	1/4 RLmax	CFmax	EFmax	2.95	8.53	0	2.90	9.22	0	2.94	9.57	0
33	1/2 RLmax	0	0	2.93	8.37	1	2.92	8.83	1	2.94	9.33	1
34	1/2 RLmax	1/4 CFmax	0	3.06	8.05	1	2.99	8.63	1	3.05	9.00	1
35	1/2 RLmax	1/2 CFmax	0	3.03	8.13	1	2.96	8.73	1	3.03	9.07	1
36	1/2 RLmax	CFmax	0	2.83	8.66	1	2.79	9.22	1	2.82	9.70	1
37	1/2 RLmax	0	1/4 EFmax	2.91	8.42	1	2.91	8.86	1	2.92	9.39	1
38	1/2 RLmax	1/4 CFmax	1/4 EFmax	3.04	8.09	1	2.97	8.66	1	3.03	9.05	1
39	1/2 RLmax	1/2 CFmax	1/4 EFmax	3.01	8.15	1	2.94	8.75	1	3.01	9.10	1
40	1/2 RLmax	CFmax	1/4 EFmax	2.74	8.92	1	2.73	9.41	1	2.74	9.97	1
41	1/2 RLmax	0	1/2 EFmax	2.89	8.46	1	2.89	8.89	1	2.90	9.44	1
42	1/2 RLmax	1/4 CFmax	1/2 EFmax	3.01	8.14	1	2.95	8.71	1	3.01	9.11	1
43	1/2 RLmax	1/2 CFmax	1/2 EFmax	3.02	8.12	1	2.93	8.77	1	3.00	9.14	1
44	1/2 RLmax	CFmax	1/2 EFmax	2.69	9.06	1	2.69	9.51	1	2.69	10.11	1
45	1/2 RLmax	0	EFmax	2.82	8.64	1	2.83	9.06	1	2.83	9.65	1
46	1/2 RLmax	1/4 CFmax	EFmax	2.85	8.56	1	2.82	9.06	1	2.84	9.59	1
47	1/2 RLmax	1/2 CFmax	EFmax	2.87	8.49	1	2.82	9.06	1	2.88	9.47	1
48	1/2 RLmax	CFmax	EFmax	2.66	9.14	1	2.66	9.58	1	2.66	10.20	1
49	RLmax	0	0	2.92	8.43	2	2.88	8.83	2	2.89	9.42	2
50	RLmax	1/4 CFmax	0	2.84	8.60	2	2.77	9.09	2	2.81	9.61	2
51	RLmax	1/2 CFmax	0	2.83	8.61	2	2.76	9.12	2	2.81	9.61	2

52	RLmax	CFmax	0	2.65	9.14	2	2.61	9.58	2	2.62	10.23	2
53	RLmax	0	1/4 EFmax	2.89	8.44	2	2.87	8.80	2	2.86	9.43	2
54	RLmax	1/4 CFmax	1/4 EFmax	2.81	8.67	2	2.76	9.12	2	2.79	9.65	2
55	RLmax	1/2 CFmax	1/4 EFmax	2.82	8.63	2	2.75	9.15	2	2.79	9.64	2
56	RLmax	CFmax	1/4 EFmax	2.65	9.12	2	2.64	9.47	2	2.64	10.15	2
57	RLmax	0	1/2 EFmax	2.87	8.50	2	2.84	8.86	2	2.84	9.50	2
58	RLmax	1/4 CFmax	1/2 EFmax	2.78	8.74	2	2.74	9.16	2	2.77	9.71	2
59	RLmax	1/2 CFmax	1/2 EFmax	2.81	8.66	2	2.73	9.18	2	2.78	9.68	2
60	RLmax	CFmax	1/2 EFmax	2.69	9.01	2	2.68	9.35	2	2.66	10.07	2
61	RLmax	0	EFmax	2.79	8.70	2	2.78	9.04	2	2.75	9.73	2
62	RLmax	1/4 CFmax	EFmax	2.75	8.81	2	2.78	9.02	2	2.78	9.66	2
63	RLmax	1/2 CFmax	EFmax	2.72	8.90	2	2.67	9.35	2	2.71	9.86	2
64	RLmax	CFmax	EFmax	2.65	9.11	2	2.64	9.44	2	2.63	10.15	2

Table 3.14. Results in terms of SCOP, TEWI and number of maintenance interventions in heating mode, for all the 64 possible combinations of fault intensities evolutions, for climate conditions of New York, Beijing and Vienna, and for an ordinary every 4 year maintenance scenario

Ordinary maintenance every 4 years												
Test	**Fault Evolution**			**New York**			**Beijing**			**Vienna**		
	Refrigerant Leakage (RL)	**Condenser Fouling (CF)**	**Evaporator Fouling (EF)**	**SCOP**	**TEWI [t_{CO2}]**	**Ninterv.**	**SCOP**	**TEWI [t_{CO2}]**	**Ninterv.**	**SCOP**	**TEWI [t_{CO2}]**	**Ninterv.**
1	0	0	0	3.98	6.19	3	3.78	7.01	3	3.98	6.95	3
2	0	1/4 CFmax	0	3.89	6.34	3	3.70	7.15	3	3.89	7.11	3
3	0	1/2 CFmax	0	3.80	6.49	3	3.62	7.31	3	3.79	7.29	3
4	0	CFmax	0	3.51	7.03	3	3.37	7.84	3	3.50	7.89	3
5	0	0	1/4 EFmax	3.97	6.21	3	3.77	7.02	3	3.97	6.96	3
6	0	1/4 CFmax	1/4 EFmax	3.88	6.35	3	3.69	7.16	3	3.88	7.13	3
7	0	1/2 CFmax	1/4 EFmax	3.79	6.50	3	3.62	7.32	3	3.79	7.30	3
8	0	CFmax	1/4 EFmax	3.51	7.03	3	3.37	7.85	3	3.50	7.90	3
9	0	0	1/2 EFmax	3.97	6.22	3	3.77	7.03	3	3.96	6.98	3
10	0	1/4 CFmax	1/2 EFmax	3.88	6.36	3	3.69	7.17	3	3.87	7.14	3
11	0	1/2 CFmax	1/2 EFmax	3.79	6.51	3	3.61	7.32	3	3.78	7.31	3
12	0	CFmax	1/2 EFmax	3.50	7.04	3	3.37	7.85	3	3.50	7.91	3
13	0	0	EFmax	3.91	6.31	3	3.73	7.10	3	3.90	7.08	3
14	0	1/4 CFmax	EFmax	3.83	6.45	3	3.65	7.24	3	3.82	7.23	3
15	0	1/2 CFmax	EFmax	3.74	6.59	3	3.58	7.38	3	3.74	7.39	3
16	0	CFmax	EFmax	3.48	7.10	3	3.35	7.90	3	3.47	7.97	3
17	1/4 RLmax	0	0	3.97	6.41	3	3.77	7.22	3	3.97	7.16	3
18	1/4 RLmax	1/4 CFmax	0	3.88	6.55	3	3.69	7.36	3	3.88	7.32	3
19	1/4 RLmax	1/2 CFmax	0	3.79	6.70	3	3.62	7.51	3	3.79	7.50	3
20	1/4 RLmax	CFmax	0	3.51	7.23	3	3.37	8.04	3	3.50	8.09	3
21	1/4 RLmax	0	1/4 EFmax	3.96	6.43	3	3.76	7.23	3	3.96	7.18	3
22	1/4 RLmax	1/4 CFmax	1/4 EFmax	3.87	6.56	3	3.69	7.37	3	3.87	7.34	3
23	1/4 RLmax	1/2 CFmax	1/4 EFmax	3.79	6.71	3	3.61	7.52	3	3.78	7.51	3
24	1/4 RLmax	CFmax	1/4 EFmax	3.51	7.23	3	3.37	8.05	3	3.50	8.10	3
25	1/4 RLmax	0	1/2 EFmax	3.94	6.45	3	3.75	7.25	3	3.94	7.21	3
26	1/4 RLmax	1/4 CFmax	1/2 EFmax	3.86	6.58	3	3.68	7.39	3	3.86	7.36	3
27	1/4 RLmax	1/2 CFmax	1/2 EFmax	3.78	6.73	3	3.61	7.53	3	3.77	7.53	3
28	1/4 RLmax	CFmax	1/2 EFmax	3.50	7.24	3	3.37	8.05	3	3.50	8.11	3
29	1/4 RLmax	0	EFmax	3.87	6.57	3	3.70	7.35	3	3.87	7.35	3
30	1/4 RLmax	1/4 CFmax	EFmax	3.81	6.68	3	3.64	7.47	3	3.80	7.47	3
31	1/4 RLmax	1/2 CFmax	EFmax	3.73	6.81	3	3.57	7.61	3	3.72	7.62	3
32	1/4 RLmax	CFmax	EFmax	3.47	7.30	3	3.35	8.11	3	3.46	8.18	3
33	1/2 RLmax	0	0	3.83	6.84	3	3.65	7.64	3	3.81	7.65	3
34	1/2 RLmax	1/4 CFmax	0	3.75	6.97	3	3.59	7.77	3	3.75	7.78	3
35	1/2 RLmax	1/2 CFmax	0	3.68	7.10	3	3.52	7.91	3	3.68	7.92	3
36	1/2 RLmax	CFmax	0	3.44	7.57	3	3.32	8.37	3	3.43	8.46	3

37	1/2 RLmax	0	1/4 EFmax	3.79	6.90	3	3.63	7.69	3	3.78	7.72	3
38	1/2 RLmax	1/4 CFmax	1/4 EFmax	3.73	7.01	3	3.57	7.81	3	3.72	7.83	3
39	1/2 RLmax	1/2 CFmax	1/4 EFmax	3.66	7.13	3	3.51	7.94	3	3.66	7.95	3
40	1/2 RLmax	CFmax	1/4 EFmax	3.42	7.61	3	3.30	8.40	3	3.41	8.51	3
41	1/2 RLmax	0	1/2 EFmax	3.75	6.97	3	3.60	7.75	3	3.73	7.80	3
42	1/2 RLmax	1/4 CFmax	1/2 EFmax	3.70	7.06	3	3.55	7.86	3	3.69	7.88	3
43	1/2 RLmax	1/2 CFmax	1/2 EFmax	3.65	7.16	3	3.49	7.98	3	3.64	7.98	3
44	1/2 RLmax	CFmax	1/2 EFmax	3.40	7.65	3	3.29	8.44	3	3.38	8.56	3
45	1/2 RLmax	0	EFmax	3.64	7.17	3	3.51	7.94	3	3.62	8.02	3
46	1/2 RLmax	1/4 CFmax	EFmax	3.60	7.24	3	3.46	8.04	3	3.59	8.09	3
47	1/2 RLmax	1/2 CFmax	EFmax	3.55	7.33	3	3.41	8.16	3	3.55	8.18	3
48	1/2 RLmax	CFmax	EFmax	3.34	7.79	3	3.24	8.57	3	3.32	8.72	3
49	RLmax	0	0	2.91	9.01	3	2.86	9.56	3	2.89	10.05	3
50	RLmax	1/4 CFmax	0	2.91	9.02	3	2.85	9.60	3	2.89	10.05	3
51	RLmax	1/2 CFmax	0	2.90	9.04	3	2.83	9.66	3	2.88	10.07	3
52	RLmax	CFmax	0	2.71	9.62	3	2.68	10.15	3	2.69	10.73	3
53	RLmax	0	1/4 EFmax	2.89	9.08	3	2.84	9.60	3	2.86	10.13	3
54	RLmax	1/4 CFmax	1/4 EFmax	2.89	9.06	3	2.83	9.63	3	2.87	10.10	3
55	RLmax	1/2 CFmax	1/4 EFmax	2.89	9.06	3	2.82	9.66	3	2.87	10.09	3
56	RLmax	CFmax	1/4 EFmax	2.69	9.68	3	2.66	10.21	3	2.67	10.81	3
57	RLmax	0	1/2 EFmax	2.86	9.16	3	2.82	9.67	3	2.83	10.23	3
58	RLmax	1/4 CFmax	1/2 EFmax	2.87	9.11	3	2.81	9.71	3	2.85	10.16	3
59	RLmax	1/2 CFmax	1/2 EFmax	2.88	9.09	3	2.81	9.72	3	2.86	10.12	3
60	RLmax	CFmax	1/2 EFmax	2.67	9.75	3	2.64	10.27	3	2.64	10.88	3
61	RLmax	0	EFmax	2.78	9.37	3	2.75	9.86	3	2.75	10.46	3
62	RLmax	1/4 CFmax	EFmax	2.80	9.29	3	2.75	9.84	3	2.78	10.37	3
63	RLmax	1/2 CFmax	EFmax	2.82	9.24	3	2.76	9.83	3	2.80	10.30	3
64	RLmax	CFmax	EFmax	2.60	9.95	3	2.58	10.43	3	2.58	11.10	3

Table 3.15. Results in terms of SCOP, TEWI and number of maintenance interventions in heating mode, for all the 64 possible combinations of fault intensities evolutions, for climate conditions of New York, Beijing and Vienna, and for an ordinary every 2 year maintenance scenario

Ordinary maintenance every 2 years												
Test	**Fault Evolution**			**New York**			**Beijing**			**Vienna**		
	Refrigerant Leakage (RL)	**Condenser Fouling (CF)**	**Evaporator Fouling (EF)**	**SCOP**	**TEWI [t_{CO2}]**	**Ninterv.**	**SCOP**	**TEWI [t_{CO2}]**	**Ninterv.**	**SCOP**	**TEWI [t_{CO2}]**	**Ninterv.**
1	0	0	0	3.98	6.19	6	3.78	7.01	6	3.98	6.95	6
2	0	1/4 CFmax	0	3.91	6.32	6	3.71	7.13	6	3.90	7.09	6
3	0	1/2 CFmax	0	3.83	6.44	6	3.65	7.26	6	3.82	7.24	6
4	0	CFmax	0	3.59	6.87	6	3.44	7.69	6	3.57	7.74	6
5	0	0	1/4 EFmax	3.97	6.21	6	3.77	7.02	6	3.97	6.96	6
6	0	1/4 CFmax	1/4 EFmax	3.90	6.33	6	3.71	7.14	6	3.89	7.10	6
7	0	1/2 CFmax	1/4 EFmax	3.82	6.45	6	3.64	7.27	6	3.81	7.25	6
8	0	CFmax	1/4 EFmax	3.58	6.88	6	3.44	7.69	6	3.57	7.75	6
9	0	0	1/2 EFmax	3.97	6.22	6	3.77	7.03	6	3.96	6.98	6
10	0	1/4 CFmax	1/2 EFmax	3.89	6.34	6	3.70	7.15	6	3.89	7.11	6
11	0	1/2 CFmax	1/2 EFmax	3.82	6.46	6	3.64	7.27	6	3.81	7.26	6
12	0	CFmax	1/2 EFmax	3.58	6.89	6	3.44	7.70	6	3.57	7.75	6
13	0	0	EFmax	3.92	6.30	6	3.73	7.09	6	3.91	7.07	6
14	0	1/4 CFmax	EFmax	3.85	6.41	6	3.67	7.21	6	3.84	7.20	6
15	0	1/2 CFmax	EFmax	3.78	6.53	6	3.61	7.33	6	3.77	7.34	6
16	0	CFmax	EFmax	3.55	6.94	6	3.42	7.75	6	3.54	7.81	6
17	1/4 RLmax	0	0	3.98	6.39	6	3.78	7.21	6	3.98	7.15	6
18	1/4 RLmax	1/4 CFmax	0	3.91	6.51	6	3.71	7.33	6	3.90	7.29	6
19	1/4 RLmax	1/2 CFmax	0	3.83	6.64	6	3.65	7.46	6	3.82	7.44	6
20	1/4 RLmax	CFmax	0	3.59	7.07	6	3.44	7.89	6	3.57	7.94	6
21	1/4 RLmax	0	1/4 EFmax	3.97	6.41	6	3.77	7.22	6	3.97	7.16	6

22	1/4 RLmax	1/4 CFmax	1/4 EFmax	3.90	6.52	6	3.71	7.34	6	3.89	7.30	6
23	1/4 RLmax	1/2 CFmax	1/4 EFmax	3.82	6.65	6	3.64	7.46	6	3.81	7.45	6
24	1/4 RLmax	CFmax	1/4 EFmax	3.58	7.08	6	3.44	7.89	6	3.57	7.94	6
25	1/4 RLmax	0	1/2 EFmax	3.96	6.42	6	3.77	7.23	6	3.96	7.18	6
26	1/4 RLmax	1/4 CFmax	1/2 EFmax	3.89	6.53	6	3.70	7.34	6	3.89	7.31	6
27	1/4 RLmax	1/2 CFmax	1/2 EFmax	3.82	6.66	6	3.64	7.47	6	3.81	7.46	6
28	1/4 RLmax	CFmax	1/2 EFmax	3.58	7.09	6	3.44	7.90	6	3.57	7.95	6
29	1/4 RLmax	0	EFmax	3.91	6.50	6	3.73	7.29	6	3.91	7.27	6
30	1/4 RLmax	1/4 CFmax	EFmax	3.85	6.61	6	3.67	7.40	6	3.84	7.39	6
31	1/4 RLmax	1/2 CFmax	EFmax	3.78	6.73	6	3.61	7.53	6	3.77	7.53	6
32	1/4 RLmax	CFmax	EFmax	3.55	7.14	6	3.42	7.94	6	3.54	8.01	6
33	1/2 RLmax	0	0	3.97	6.61	6	3.77	7.42	6	3.97	7.36	6
34	1/2 RLmax	1/4 CFmax	0	3.90	6.73	6	3.71	7.54	6	3.89	7.50	6
35	1/2 RLmax	1/2 CFmax	0	3.82	6.85	6	3.64	7.66	6	3.82	7.64	6
36	1/2 RLmax	CFmax	0	3.59	7.27	6	3.44	8.09	6	3.57	8.14	6
37	1/2 RLmax	0	1/4 EFmax	3.96	6.62	6	3.76	7.43	6	3.96	7.38	6
38	1/2 RLmax	1/4 CFmax	1/4 EFmax	3.89	6.74	6	3.70	7.55	6	3.88	7.52	6
39	1/2 RLmax	1/2 CFmax	1/4 EFmax	3.81	6.86	6	3.64	7.67	6	3.81	7.66	6
40	1/2 RLmax	CFmax	1/4 EFmax	3.58	7.28	6	3.44	8.09	6	3.57	8.14	6
41	1/2 RLmax	0	1/2 EFmax	3.94	6.65	6	3.75	7.45	6	3.94	7.41	6
42	1/2 RLmax	1/4 CFmax	1/2 EFmax	3.88	6.76	6	3.69	7.56	6	3.87	7.54	6
43	1/2 RLmax	1/2 CFmax	1/2 EFmax	3.81	6.88	6	3.63	7.68	6	3.80	7.67	6
44	1/2 RLmax	CFmax	1/2 EFmax	3.58	7.29	6	3.44	8.10	6	3.56	8.15	6
45	1/2 RLmax	0	EFmax	3.88	6.76	6	3.70	7.55	6	3.87	7.54	6
46	1/2 RLmax	1/4 CFmax	EFmax	3.82	6.85	6	3.65	7.64	6	3.82	7.64	6
47	1/2 RLmax	1/2 CFmax	EFmax	3.76	6.96	6	3.60	7.76	6	3.75	7.77	6
48	1/2 RLmax	CFmax	EFmax	3.55	7.35	6	3.41	8.15	6	3.53	8.22	6
49	RLmax	0	0	3.83	7.24	6	3.65	8.05	6	3.81	8.05	6
50	RLmax	1/4 CFmax	0	3.77	7.34	6	3.59	8.16	6	3.75	8.16	6
51	RLmax	1/2 CFmax	0	3.70	7.46	6	3.53	8.28	6	3.69	8.28	6
52	RLmax	CFmax	0	3.51	7.83	6	3.37	8.63	6	3.49	8.72	6
53	RLmax	0	1/4 EFmax	3.79	7.29	6	3.62	8.09	6	3.77	8.12	6
54	RLmax	1/4 CFmax	1/4 EFmax	3.74	7.38	6	3.57	8.19	6	3.73	8.21	6
55	RLmax	1/2 CFmax	1/4 EFmax	3.69	7.48	6	3.52	8.30	6	3.68	8.30	6
56	RLmax	CFmax	1/4 EFmax	3.49	7.87	6	3.36	8.67	6	3.47	8.77	6
57	RLmax	0	1/2 EFmax	3.75	7.36	6	3.59	8.16	6	3.73	8.20	6
58	RLmax	1/4 CFmax	1/2 EFmax	3.72	7.42	6	3.55	8.24	6	3.70	8.26	6
59	RLmax	1/2 CFmax	1/2 EFmax	3.68	7.50	6	3.51	8.33	6	3.67	8.33	6
60	RLmax	CFmax	1/2 EFmax	3.47	7.91	6	3.34	8.70	6	3.44	8.82	6
61	RLmax	0	EFmax	3.65	7.55	6	3.50	8.34	6	3.62	8.42	6
62	RLmax	1/4 CFmax	EFmax	3.62	7.60	6	3.47	8.42	6	3.60	8.46	6
63	RLmax	1/2 CFmax	EFmax	3.59	7.67	6	3.43	8.51	6	3.58	8.52	6
64	RLmax	CFmax	EFmax	3.40	8.04	6	3.29	8.82	6	3.38	8.97	6

Table 3.16. Results in terms of SCOP, TEWI and number of maintenance interventions in heating mode, for all the 64 possible combinations of fault intensities evolutions, for climate conditions of New York, Beijing and Vienna, and for an ordinary every year maintenance scenario

Ordinary maintenance every year												
Test	**Fault Evolution**			**New York**			**Beijing**			**Vienna**		
	Refrigerant Leakage (RL)	**Condenser Fouling (CF)**	**Evaporator Fouling (EF)**	**SCOP**	**TEWI [t_{CO2}]**	**Ninterv.**	**SCOP**	**TEWI [t_{CO2}]**	**Ninterv.**	**SCOP**	**TEWI [t_{CO2}]**	**Ninterv.**
1	0	0	0	3.98	6.19	12	3.78	7.01	12	3.98	6.95	12
2	0	1/4 CFmax	0	3.93	6.27	12	3.74	7.08	12	3.93	7.04	12
3	0	1/2 CFmax	0	3.89	6.35	12	3.69	7.16	12	3.87	7.14	12
4	0	CFmax	0	3.75	6.58	12	3.58	7.40	12	3.72	7.44	12
5	0	0	1/4 EFmax	3.98	6.20	12	3.77	7.02	12	3.97	6.96	12
6	0	1/4 CFmax	1/4 EFmax	3.93	6.28	12	3.73	7.09	12	3.92	7.05	12
7	0	1/2 CFmax	1/4 EFmax	3.88	6.36	12	3.69	7.17	12	3.87	7.15	12
8	0	CFmax	1/4 EFmax	3.74	6.59	12	3.57	7.41	12	3.71	7.44	12
9	0	0	1/2 EFmax	3.97	6.22	12	3.77	7.02	12	3.97	6.97	12
10	0	1/4 CFmax	1/2 EFmax	3.92	6.29	12	3.73	7.10	12	3.91	7.06	12
11	0	1/2 CFmax	1/2 EFmax	3.87	6.37	12	3.69	7.18	12	3.86	7.16	12
12	0	CFmax	1/2 EFmax	3.74	6.60	12	3.57	7.41	12	3.71	7.45	12
13	0	0	EFmax	3.93	6.27	12	3.74	7.07	12	3.93	7.04	12
14	0	1/4 CFmax	EFmax	3.89	6.34	12	3.70	7.15	12	3.88	7.13	12
15	0	1/2 CFmax	EFmax	3.84	6.42	12	3.66	7.22	12	3.83	7.22	12
16	0	CFmax	EFmax	3.71	6.64	12	3.55	7.45	12	3.69	7.50	12
17	1/4 RLmax	0	0	3.98	6.39	12	3.78	7.20	12	3.98	7.15	12
18	1/4 RLmax	1/4 CFmax	0	3.94	6.47	12	3.74	7.28	12	3.93	7.24	12
19	1/4 RLmax	1/2 CFmax	0	3.89	6.55	12	3.69	7.36	12	3.87	7.34	12
20	1/4 RLmax	CFmax	0	3.75	6.78	12	3.58	7.60	12	3.72	7.64	12
21	1/4 RLmax	0	1/4 EFmax	3.98	6.40	12	3.77	7.21	12	3.97	7.16	12
22	1/4 RLmax	1/4 CFmax	1/4 EFmax	3.93	6.48	12	3.73	7.29	12	3.92	7.25	12
23	1/4 RLmax	1/2 CFmax	1/4 EFmax	3.88	6.55	12	3.69	7.37	12	3.87	7.35	12
24	1/4 RLmax	CFmax	1/4 EFmax	3.74	6.79	12	3.57	7.60	12	3.71	7.64	12
25	1/4 RLmax	0	1/2 EFmax	3.97	6.41	12	3.77	7.22	12	3.97	7.17	12
26	1/4 RLmax	1/4 CFmax	1/2 EFmax	3.92	6.49	12	3.73	7.30	12	3.91	7.26	12
27	1/4 RLmax	1/2 CFmax	1/2 EFmax	3.87	6.56	12	3.69	7.38	12	3.86	7.36	12
28	1/4 RLmax	CFmax	1/2 EFmax	3.74	6.80	12	3.57	7.61	12	3.71	7.65	12
29	1/4 RLmax	0	EFmax	3.93	6.47	12	3.74	7.27	12	3.93	7.24	12
30	1/4 RLmax	1/4 CFmax	EFmax	3.89	6.54	12	3.70	7.34	12	3.88	7.33	12
31	1/4 RLmax	1/2 CFmax	EFmax	3.84	6.62	12	3.66	7.42	12	3.83	7.42	12
32	1/4 RLmax	CFmax	EFmax	3.71	6.84	12	3.55	7.65	12	3.69	7.70	12
33	1/2 RLmax	0	0	3.98	6.59	12	3.78	7.40	12	3.98	7.34	12
34	1/2 RLmax	1/4 CFmax	0	3.93	6.67	12	3.74	7.48	12	3.93	7.44	12
35	1/2 RLmax	1/2 CFmax	0	3.89	6.74	12	3.69	7.56	12	3.87	7.53	12
36	1/2 RLmax	CFmax	0	3.75	6.98	12	3.58	7.80	12	3.72	7.83	12
37	1/2 RLmax	0	1/4 EFmax	3.97	6.60	12	3.77	7.41	12	3.97	7.36	12
38	1/2 RLmax	1/4 CFmax	1/4 EFmax	3.93	6.67	12	3.73	7.49	12	3.92	7.45	12
39	1/2 RLmax	1/2 CFmax	1/4 EFmax	3.88	6.75	12	3.69	7.57	12	3.87	7.54	12
40	1/2 RLmax	CFmax	1/4 EFmax	3.74	6.99	12	3.57	7.80	12	3.71	7.84	12
41	1/2 RLmax	0	1/2 EFmax	3.97	6.61	12	3.77	7.42	12	3.97	7.37	12
42	1/2 RLmax	1/4 CFmax	1/2 EFmax	3.92	6.68	12	3.73	7.49	12	3.92	7.46	12
43	1/2 RLmax	1/2 CFmax	1/2 EFmax	3.87	6.76	12	3.69	7.57	12	3.86	7.56	12
44	1/2 RLmax	CFmax	1/2 EFmax	3.74	6.99	12	3.57	7.81	12	3.71	7.85	12
45	1/2 RLmax	0	EFmax	3.93	6.68	12	3.74	7.47	12	3.92	7.44	12
46	1/2 RLmax	1/4 CFmax	EFmax	3.89	6.74	12	3.71	7.54	12	3.88	7.52	12
47	1/2 RLmax	1/2 CFmax	EFmax	3.84	6.81	12	3.67	7.61	12	3.83	7.61	12
48	1/2 RLmax	CFmax	EFmax	3.71	7.04	12	3.55	7.85	12	3.69	7.90	12
49	RLmax	0	0	3.97	7.01	12	3.77	7.81	12	3.97	7.76	12
50	RLmax	1/4 CFmax	0	3.92	7.08	12	3.73	7.89	12	3.92	7.85	12
51	RLmax	1/2 CFmax	0	3.88	7.15	12	3.69	7.96	12	3.87	7.94	12

52	RLmax	CFmax	0	3.74	7.38	12	3.57	8.20	12	3.72	8.23	12
53	RLmax	0	1/4 EFmax	3.96	7.02	12	3.76	7.83	12	3.96	7.78	12
54	RLmax	1/4 CFmax	1/4 EFmax	3.91	7.09	12	3.72	7.90	12	3.91	7.87	12
55	RLmax	1/2 CFmax	1/4 EFmax	3.87	7.17	12	3.68	7.97	12	3.86	7.96	12
56	RLmax	CFmax	1/4 EFmax	3.74	7.39	12	3.57	8.20	12	3.71	8.24	12
57	RLmax	0	1/2 EFmax	3.94	7.06	12	3.75	7.85	12	3.94	7.82	12
58	RLmax	1/4 CFmax	1/2 EFmax	3.90	7.11	12	3.72	7.91	12	3.90	7.89	12
59	RLmax	1/2 CFmax	1/2 EFmax	3.86	7.18	12	3.68	7.99	12	3.85	7.97	12
60	RLmax	CFmax	1/2 EFmax	3.73	7.40	12	3.57	8.21	12	3.71	8.25	12
61	RLmax	0	EFmax	3.88	7.14	12	3.70	7.95	12	3.87	7.93	12
62	RLmax	1/4 CFmax	EFmax	3.85	7.20	12	3.67	8.00	12	3.84	7.99	12
63	RLmax	1/2 CFmax	EFmax	3.81	7.26	12	3.64	8.06	12	3.80	8.06	12
64	RLmax	CFmax	EFmax	3.70	7.45	12	3.55	8.25	12	3.68	8.31	12

On these results similar comments to the cooling mode can be made. In fault-free conditions cities of New York and Vienna present similar values of SCOP, whereas slightly lower values are obtained for Beijing. As expected, in each case the SCOP values decrease with the increases of fault intensities, and increases with the rise of the number of maintenance interventions, which depends on the number of times a user realise about the fault and on the maintenance strategy adopted.

Finally, similar to what already done in cooling mode, the percentages of the 64 scenarios for which values of SCOP are penalized above 15%, 10% and 5%, are reported in barplots of Figure 3.20, for all the climate conditions and maintenance strategies investigated. Regarding the 15% threshold (Figure 3.20(a)), it can be noticed that a 4 year planned maintenance can reduce significantly the percentage of penalized scenarios, passing from approximately 60-70% of the total for a not-planned maintenance to about 20%. For a maximum penalization of 10% (Figure 3.20(b)), a 2-year maintenance strategy led almost to zero penalized scenarios for climate conditions of New York, whereas the percentage remains about 20% for cities of Beijing and Vienna. Finally, considering the threshold of 5% for SCOP penalization (Figure 3.20(c)), a 1 year organized maintenance can guarantee a reduced percentage of penalized scenarios until approximately 20% for all the climate conditions investigated.

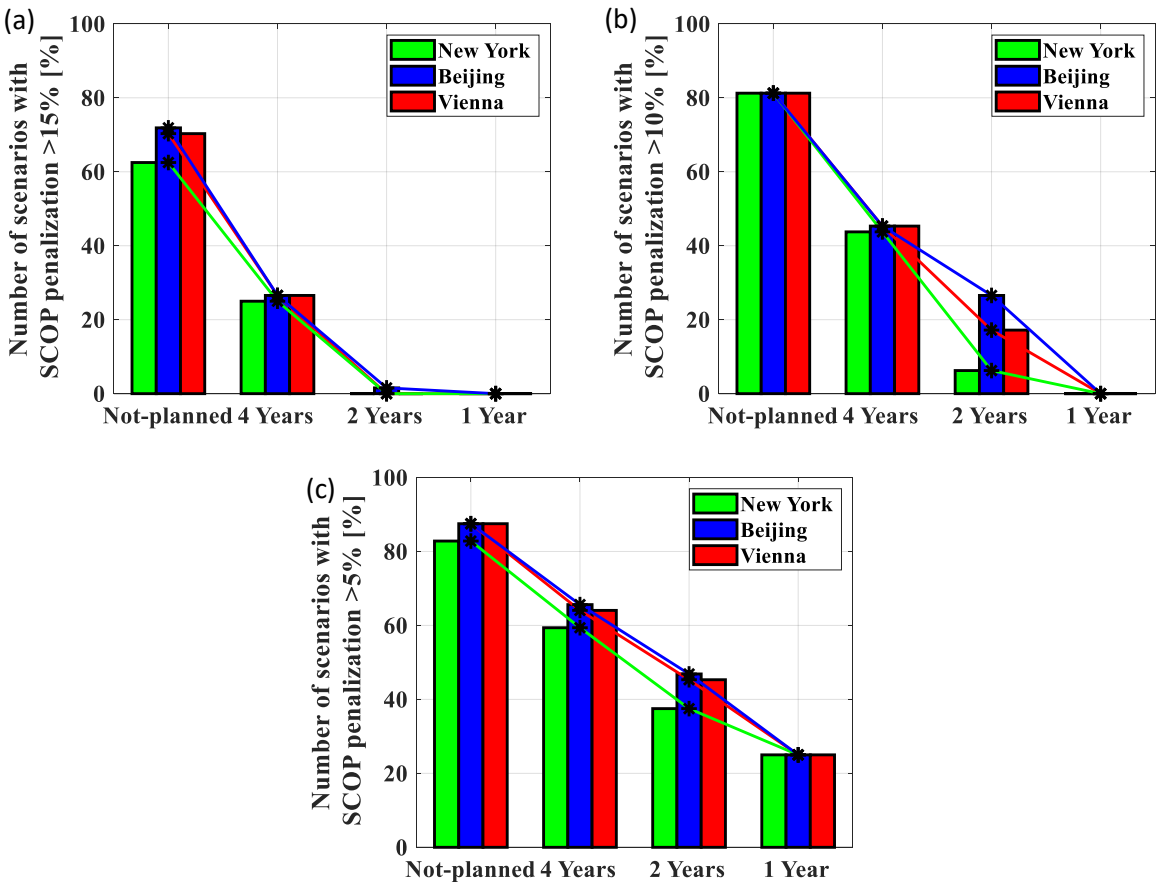


Figure 3.20. Percentages of scenario for which SCOP results to be penalized more than 15% (a), 10% (b) and 5% (c), for the heating mode, depending on the climate condition and on the maintenance scenario investigated

3.3 Possibility of fault detection, diagnosis and evaluation for residential heat pumps

Results of the work published by Pelella et al. [121] are presented in this paragraph. The main target is to study the possibility of a fault detection, diagnosis and evaluation for residential heat pumps, answering two different questions.

- When simultaneous faults occur, does it exist a bijective relation between pressure/temperature measurement and the determination of both COP and fault intensities values, for small capacity heat pumps?
- What is the influence of the instrumental uncertainty on both the univocal fault detection, and on the univocal fault diagnosis and evaluation, in the evaluation of the fault intensities?

In this section, the physic-based model presented previously is used to create a large database (step 1) representing real operating conditions of the machine, fixing different boundary conditions. As a matter of fact, the calibrated model is employed as a virtual experimental test bench from which data could be collected. However, the numerical approach results to be

cheaper than the experimental, in terms of time and cost, especially for the creation of large databases.

All the thermodynamic cycles obtained through the model are then compared in terms of pressures and temperatures (step 2), both with the only fault-free cycle and with all the others deriving from faulty conditions. In this way, it is possible to establish if from cheap measurements, characterized by a certain value of uncertainty, it is possible only to detect a fault, to trace its typology and fault intensity, through a look-up table or an AI tool. A graphical scheme of the two steps described is shown in Figure 3.21.

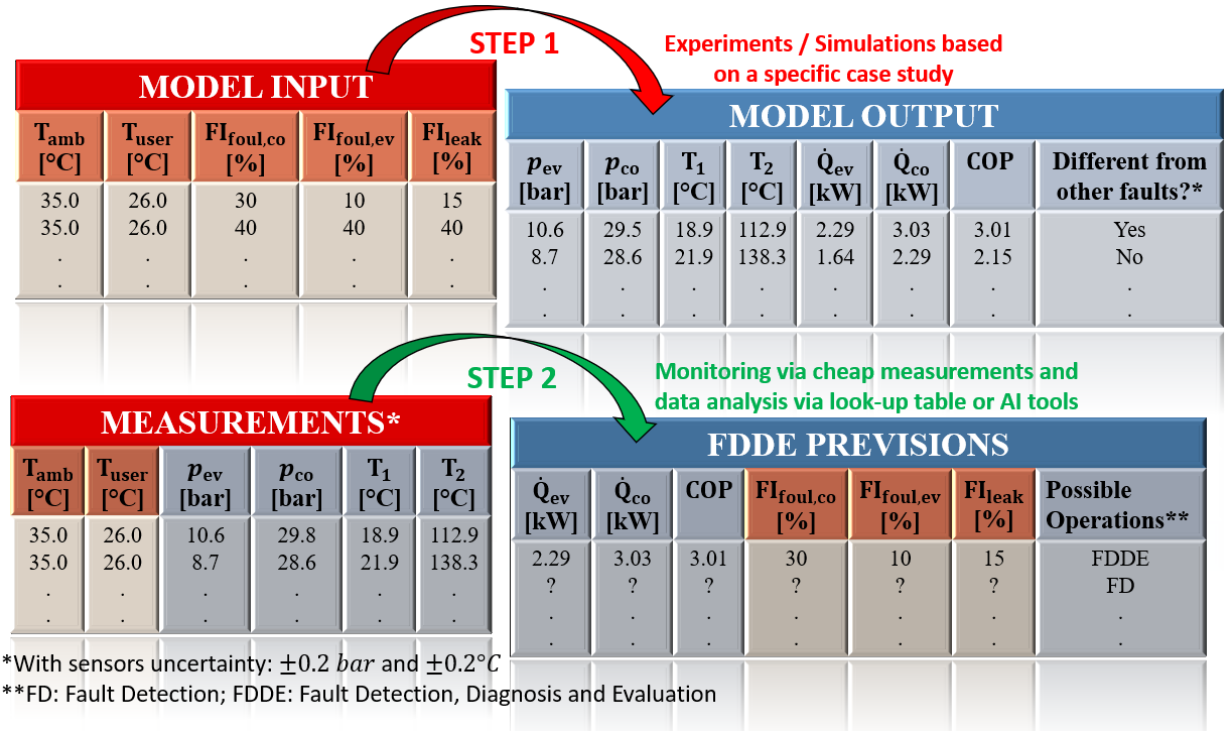


Figure 3.21. Graphical scheme for the two steps carried out in this work. The first is to generate data of thermodynamic cycles through the physics-based model and compared each other, the second is to understand if from this data it is possible to trace back to the cycle and detect, diagnoses and/or evaluate a fault

To carry out this analysis, the same case study previously analysed has been treated, operating in cooling mode. However, similar results could be extrapolated for the heating mode.

3.3.1 State of the art of FDDE

Several works dealing with fault detection, diagnosis and evaluation tools applied to heat pumps and air-conditioning equipment are available in the literature. Some of these are reported in

Table 3.17 and have been partially presented in the work of Citarella et al. [68]. Manuscripts are sorted on the system studied among chillers, VRF, air-to-air and air-to-water heat pumps, on the method employed between ML based or physics-based model, on the typology of fault investigated, and on the presence of simultaneous faults.

Table 3.17. State of the art of FDDE works, divided per Application/System studied, method, fault investigate and presence of simultaneous faults

Author	Application/System studied	Method*	Fault investigated**	Presence of simultaneous faults	Notes
Choi et al. [122]	316 kW Chiller (ASHRAE 1043-RP) [91]	ML mod. Based on exp.	CF, CSF, EF, ESF, RL	No	
Tassou and Grace [123]	R404A 4 kW Chiller	ML mod. Based on exp.	RL, RO	No	
Navarro-Esbri et al. [124]	WSHP Chiller	ML mod. Based on exp.	RL	No	
Zogg et al. [125]	8 kW GSHP	ML mod. Based on exp.	CF, CSF, EF, ESF	No	
Namburu et al. [126]	316 kW Chiller (ASHRAE 1043-RP) [91]	ML mod. Based on exp.	CF, CSF, EO, ESF, NC, RL, RO	No	Selection of best feature subset
Han et al. [127]	316 kW Chiller (ASHRAE 1043-RP) [91]	ML mod. Based on exp.	CF, CSF, EO, ESF, NC, RL, RO	No	Selection of best feature subset
Han et al. [128]	316 kW Chiller (ASHRAE 1043-RP) [91]	ML mod. Based on exp.	CSF, ESF	Yes	
Sun et al. [129]	R404A 2kW ASHP	ML mod. Based on exp.	CF, EF, NC, RL	No	
Cai et al. [130]	Generic GSHP	ML mod. Based on exp.	CF, CVL, DEV, EF, HPLB, NC, RO, RL,	Yes	Integration of observed information
Wang and Gao [131]	316 kW Chiller (ASHRAE 1043-RP) [91]	ML mod. Based on exp.	CF, ESF, NC, RL	No	
Yan et al. [132]	316 kW Chiller (ASHRAE 1043-RP) [91]	ML mod. Based on exp.	CF, CSF, ESF, NC, RL	No	
Eom et al. [133]	30 kW multi-split	ML mod. Based on exp.	RL	No	

Chen et al. [134] [135]	R410A 28 kW VRF	ML mod. Based on exp.	LCF	No	
Hwang et al. [136]	R410A 4.12kW Split	ML mod. Based on exp.	RL	No	
Kim and Braun [137]	R410A 14 kW Rooftop	PB mod. Based on exp.	CF, CVL, DEV, EF, RL, RO	Yes	Definition of virtual sensors to monitor fault evolutions
Yan et al. [138]	316 kW Chiller (ASHRAE 1043-RP) [91]	ML mod. Based on exp.	CF, CSF, EO, ESF, NC, RL, RO	No	
Zhang et al. [139]	316 kW Chiller (ASHRAE 1043-RP) [91]	ML mod. Based on exp.	CF, CSF, EO, ESF, NC, RL, RO	No	
Kim and Lee [140]	Several Split and Rooftop	PB mod. Based on exp.	CF, RL	Yes	Definition of virtual sensors to monitor fault evolutions

*Exp: Experimental; ML: Machine Learning Based; Mod: Model; PB: Physics-based

**CF: Condenser fouling; CSF: Condenser secondary flow error; CVL: Compressor Valve Leakage; DEV: defective expansion valve; EF: Evaporator fouling; EO: Excess oil; ESF: Evaporator secondary flow error; HPLB: High pressure pipeline blockage; LCF Liquid compressor floodback; LL: Liquid Line Restriction; NC: Non-condensable in the refrigerant; RL: Refrigerant leakage; RO: Refrigerant overcharge

Most of the faults analysed in literature are problems related to condenser and evaporator fouling or air flow rate reductions, and refrigerant leakage, whereas several works also analyse the presence of non-condensable in the refrigerant loop. Common input data are variables of pressures, temperatures and mass flow rates, both for refrigerant and secondary fluids [68]. Other observed information by operators such as vibrations, pungent smell, too much foam, grease stains in wiped joint and no stoppage of the compressor have been integrated in the FDD strategy developed by the work of Cai et al. [130]. Moreover, works of Namburu et al. [126] and Han et al. [127] in addition carried out optimizations to select the best feature input subset in order to maximise the prediction performance. Finally, between all the analysed faults, only four of them develop FDDE strategies considering the occurrence of multiple simultaneous faults.

From the presented state of the art, it can be noticed that the literature lacks of physic-based approaches. The main reason is that ML tools employed for FDD purposes are usually developed without a deep physical knowledge of the processes. One of the exceptions are the works of Kim and Braun [137] and Kim and Lee [140], which introduced the concept of virtual sensors. The main idea is to decouple and extrapolate features calculated from several other measurements, which becomes the unique identification of a certain kind of fault. The authors divided virtual sensors in three categories: sensor-level, component-level and system-level. The sensor-level virtual sensors can be used to replace traditional real measurements using other low-cost instrumentation. For instance, to evaluate saturation pressure, the authors employed cheaper measurement of saturation temperature. The component level provides sensors able to monitor the behaviour of single components, using physics-based models for each component in order to isolate a specific kind of fault. Particularly, the authors employed a compressor virtual sensor able to evaluate the mass flow rate and electric power consumption depending on condensing and evaporating temperature, through expressions calibrated on manufacturer data. These two values are then compared with the mass flow rate evaluated through an energy balance on the compressor and with the actual measured electric consumption by a smart meter. Therefore, if the deviations rise above a certain threshold, a fault on the compressor (e.g. ageing, wear, compressor valve leakage) can be suddenly identified. Regarding heat exchangers, a virtual sensor for the evaluation of air volumetric flow rate has been developed, comparing energy balances refrigerant and air sizes on the heat exchanger coils. In this case a heat exchanger fault (e.g. fouling or mass flow rate reduction) can be isolated by comparing the evaluated flow rate with rated values of the heat exchanger for a given speed setting. However, this method requires the measurement of the speed frequency for each heat exchanger fan,

which is not always possible in small capacity systems. Finally, the system level provides virtual sensors able to evaluate performances of the entire systems, in terms of actual refrigerant charge, capacity and COP. Refrigerant charge has been evaluated through the model of Li and Braun [141], whereas capacity and COP from energy balances on the system analysed. However, the virtual refrigerant charge sensor requires a calibration on the specific system analysed.

3.3.2 Faults analyzed and methodology

Among all the possible common faults analyzed in literature, in this work it has been chosen to analyse only refrigerant leakages, external and internal heat exchanger fouling. As a matter of fact, several faults such as a liquid line blockage, an unsuitable refrigerant charge and the presence of incondensable gases can produce a negative influence on the thermodynamic cycle and on system performance of the machine almost immediately after its installation, and therefore can be usually detected in a short time (2-3 weeks), and then these faults can be avoided if all the installation procedures are carried out properly, with a depth training of the installation and maintenance operators. Therefore, for this kind of fault an in-depth FDD analysis can be avoided, whereas is has more sense for all the other faults, which require instead a longer period to be identified. However, regarding compressor ageing or malfunctioning (such as compressor valve leakage problems), its detection is possible with independent equations on the component, and therefore it is possible to isolate that fault from other damages through the employment of virtual sensors, as observed by Kim and Braun [137] and presented in section 3.3.1. Also, a heat exchanger fouling can be easily detected by a measurement of the air mass flow rate by an operator, but the main aim of this section is to understand if it is possible to use only cheap, easy and automatic measuring equipment, such as pressure and temperature sensors, in order to detect, diagnose and evaluate such kinds of faults. An early detection of refrigerant leakages, instead, would result in a saving in time and costs deriving from useless maintenance operations.

For these reasons, a measuring instrumentation composed only by pressure transducers and temperature sensors has been equipped on the system case study. Particularly, 2 temperature sensors and 2 pressure transducers have been considered at the compressor inlet and outlet to measure refrigerant evaporating and condensing pressures and temperatures. In addition, other two sensors have been installed, in order to measure the air ambient and indoor temperatures. Figure 3.22 shows the position on the scheme plant for each of the measurement sensors employed.

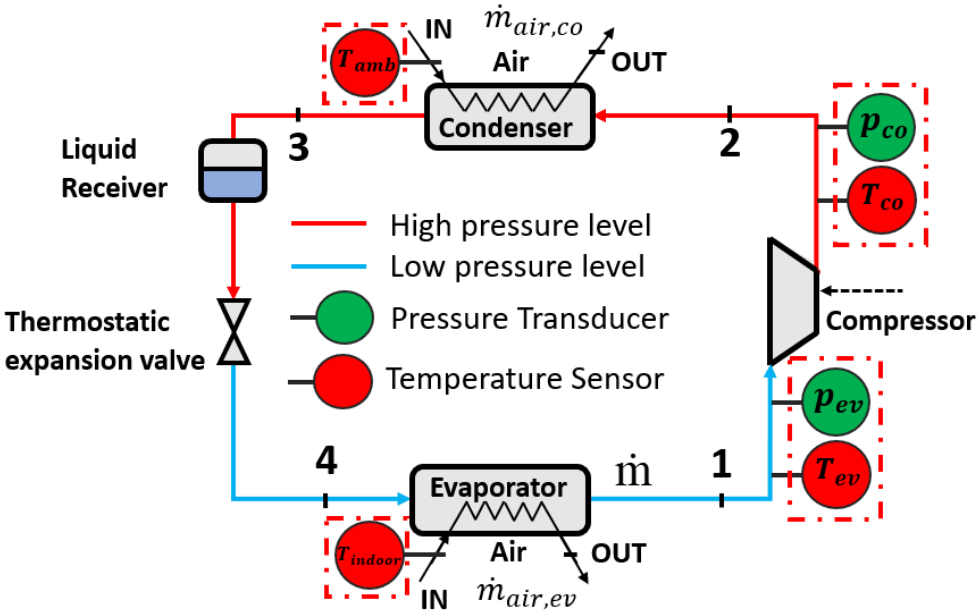


Figure 3.22. Indication of the number and the position of pressure and temperature sensors employed in the FDDE processes

For simplicity, the following results are obtained for fixed boundary conditions typical for space cooling of ambient and indoor temperatures respectively of 35 °C and 26 °C. Neglecting these measures, and considering the other sensors installed, a range of uncertainty for pressure and temperature transducers (unc_P, unc_T) has been fixed. Therefore, the performance penalization of an occurred faulty condition can be detected only if the following conditions are verified:

$$\begin{aligned} &\left|p_{ev,faulty} - p_{ev,fault-free}\right| > unc_p \;\; || \;\; \left|p_{co,faulty} - p_{co,fault-free}\right| > unc_p \;\; || \\ &\left|T_{in,comp,faulty} - T_{in,comp,fault-free}\right| > unc_T \;\; || \\ &\left|T_{out,comp,faulty} - T_{out,comp,fault-free}\right| > \; unc_T \end{aligned} \tag{3.21}$$

In other words, a faulty condition can be detected only if the corresponding thermodynamic cycle has at least one variable differing from the one of the fault-free cycle more than the instrumental uncertainty. However, this condition is not sufficient to diagnose a certain kind of fault and precisely identify its fault intensity. As a matter of fact, it is necessary to compare the faulty cycle not only with the fault-free cycle, but with the measured variables from all the other faulty conditions, with at least one of the following conditions which must be verified:

$$\begin{aligned} &\left|p_{ev,faulty,i} - p_{ev,faulty,others}\right| > unc_p || \left|p_{co,faulty,i} - p_{co,faulty,others}\right| > unc_p \\ &|| \;\; \left|T_{in,comp,faulty,i} - T_{in,comp,faulty,others}\right| > unc_T \;\; || \\ &\left|T_{out,comp,faulty,i} - T_{out,comp,faulty,others}\right| > \; unc_T \end{aligned} \tag{3.22}$$

3.3.3 Results: fault detection

Regarding the possibility of an only detection of an anomaly, Figure 3.23 shows a 3-D patched surface, with the fault intensities of the three faults analysed as axes. Each square is coloured only if its four edges correspond to a faulty detectable condition, therefore if at least one of the conditions presented in equations 3.18 and 3.19 is respected. The color scale instead refers to the average COP penalization of the faulty cycles corresponding to the four edges of each square. These figures are obtained with a 5% step on each of the fault intensities analysed, and for different instrumental uncertainties. For quite high and unrealistic measuring equipment uncertainties of ±3 bar and ±3 °C (Figure 3.23(a)), it happens that fouling intensities lower than 20% and refrigerant leakages lower than 15% cannot be detected. Otherwise, with more common instrumental uncertainties of ±1 bar and ±1 °C (Figure 3.23(b)) each fault whose intensity rises above 10% can be detected, leaving all the undetectable conditions characterized by a COP penalization lower than 5%. This value could be further reduced with increasing sensor accuracy, up to 2% with uncertainties of ±0.2 bar and ±0.2 °C.

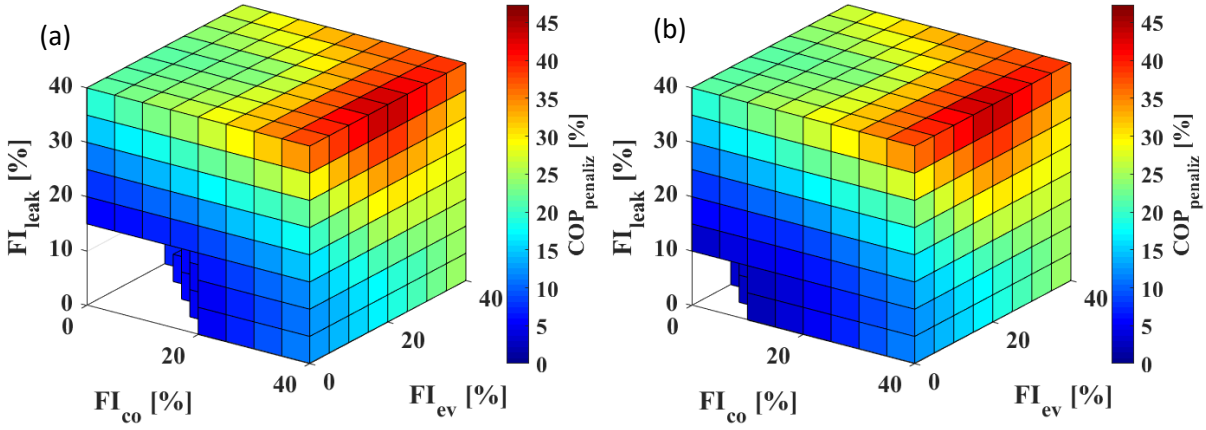


Figure 3.23. Fault detection domain depending on fault intensities analysed. Instrumental uncertainties of ±3 bar & ±3 °C (a) and of ±1 bar & ±1 °C (b)

3.3.4 Results: fault diagnosis and evaluation

Regarding the fault diagnosis and evaluation of a certain kind of fault, the results about the identification domain and the first identification surface are presented. Similarly as before, in the identification domain a square is coloured only if its four edges are related to uniquely identified thermodynamic cycles (condition presented in equation 3.22), with empty spaces related to the combination of not uniquely identifiable faults. For each of the analysed cases, a percentage of the diagnosed fault index ψ can be defined as the ratio between the number of patched squares and the total.

$$\psi = \frac{N_{square,patched}}{N_{square,total}} \tag{3.23}$$

On the other hand, the first identification surface is defined as the first surface in the domain, in which the intensity of each fault is uniquely identified, assuming a certain fault evolution path starting from the origin (fault-free case). Moreover, in this section two different aspects regarding the detection, diagnosis and evaluation of a fault are analysed: the first is the accuracy of monitoring sensors and the second is the fault severity step at which each fault can be univocally identified. It has to be clarified that the sensor accuracy must be smaller for smaller fault severity steps, in order to have an acceptable identification dominium, as better clarified later.

Figure 3.24(a) represents the domain obtained with a 10% fault severity step and for fixed uncertainties of ±1 bar and ±0.7 °C. In this case, the percentage of the diagnosed fault ψ is 45.8%. Figure 3.24(b) is obtained by rotating the first image by 90 degrees and highlights the first identification surface. Similarly as the only fault detection case, the color scale is proportional to the average COP penalization of the cycles corresponding to the four edges of the square. The first intercepted surface in this case is the closest possible to the free fault case since any damage is immediately identified reaching a fault intensity of 10%. Therefore COP penalization is limited under 6-7%. However, if this alarm is ignored and the fault evolution goes through the first identification surface, there can be some empty zones of the domain in which it is not anymore possible to uniquely identify the fault.

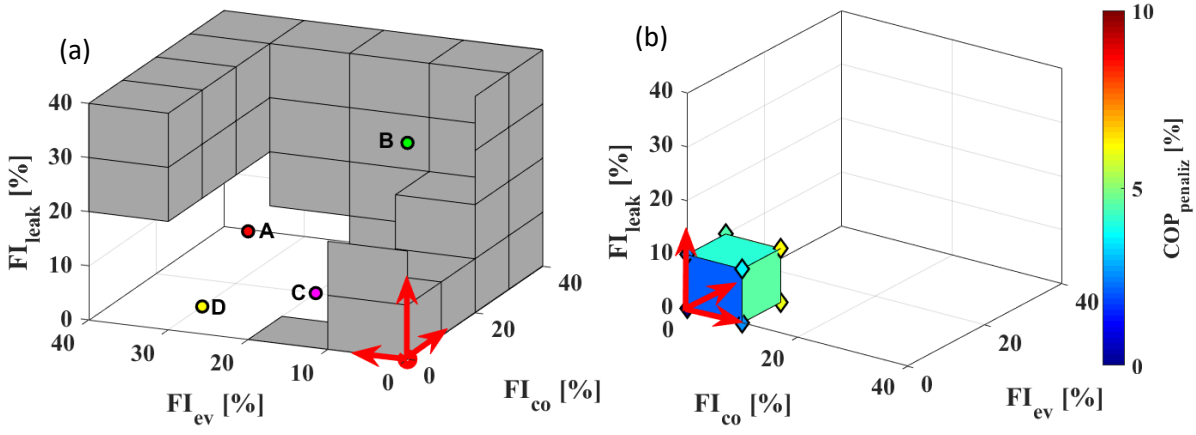


Figure 3.24. Fault diagnosis and evaluation domain depending on fault intensities, for an identification step of 10% and for uncertainties of ±1 bar and ±0.7 °C. (a) Entire domain. (b) First identification surface rotated by 90° and COP penalization for each point. Point A, B, C and D are further investigated in Figure 3.25 and Table 3.18

To better understand what happens inside the dominium, four points inside it named as A, B, C and D characterized by different values of fault intensities are analysed in detail. Figure 3.25

shows the thermodynamic cycles on the temperature-specific entropy diagram for the selected points, whereas Table 3.18 represents similar thermodynamic cycles to each of the points analysed of the dominium. Point A is characterized by a refrigerant leakage of 20%, an evaporator fouling of 20% and no condenser fouling. The thermodynamic cycle is found similar to other two faulty conditions characterized by the same refrigerant leakage, a condenser fouling of 10%, and an evaporator fouling respectively equal to 10% and 20%, as presented in Figure 3.25(a). This aspect is related to the fact that most of the conditions related to the empty domain of the previous figure are often related to close fault severities, not easily identifiable with the measurement instrumentation at disposal. If a higher refrigerant leakage fault severity is considered, the number of similar thermodynamic cycles could rise, as shown in Figure 3.25(b). Point B is characterized by a 40% refrigerant leakage and the absence of heat exchanger fouling. All the similar cycles are characterized by the same refrigerant leakage and different condenser fouling up to 10% and evaporator fouling up to 20%. This aspect is related to the fact that, with high values of refrigerant leakage fault intensity, the thermal capacities of condenser and evaporator decrease, and the heat exchangers start to behave as if they had infinite surface. Therefore, the effect of heat exchanger fouling could be more difficult to identify for high refrigerant leakage rates. Point C, whose thermodynamic cycle is presented in Figure 3.25(c), is characterized by a condenser and evaporator fouling at the 20% level, and by no refrigerant leakages. This condition has two similar cycles, characterized by a higher refrigerant leakage of 10%, and it highlights that in case of non-zero refrigerant leakage it may happen that, despite the thermostatic valve is fed with saturated vapor, with its possible oversizing it is still able to control the evaporator superheating. Therefore, the evaporating pressure and mass flow rate are almost the same, and the consequent thermodynamic cycle results to have similar pressures and temperatures compared with the fault-free case. It only differs by the higher inlet enthalpy of the thermostatic valve, not controllable with conventional and non-invasive measurements. A more evident case related to the previously discussed aspect can be noticed also for point D, as shown in Figure 3.25(d). In this case the cycle, characterized by a condenser fouling of 10%, evaporator fouling of 30% and no refrigerant leakages, can be confused with three other faulty conditions, characterized by a 10% refrigerant leakage, a condenser fouling from 0% to 20% and an evaporator fouling of 40%. In this case the high measure instrument uncertainty employed led to a mis-identification also for fouling conditions close to each other.

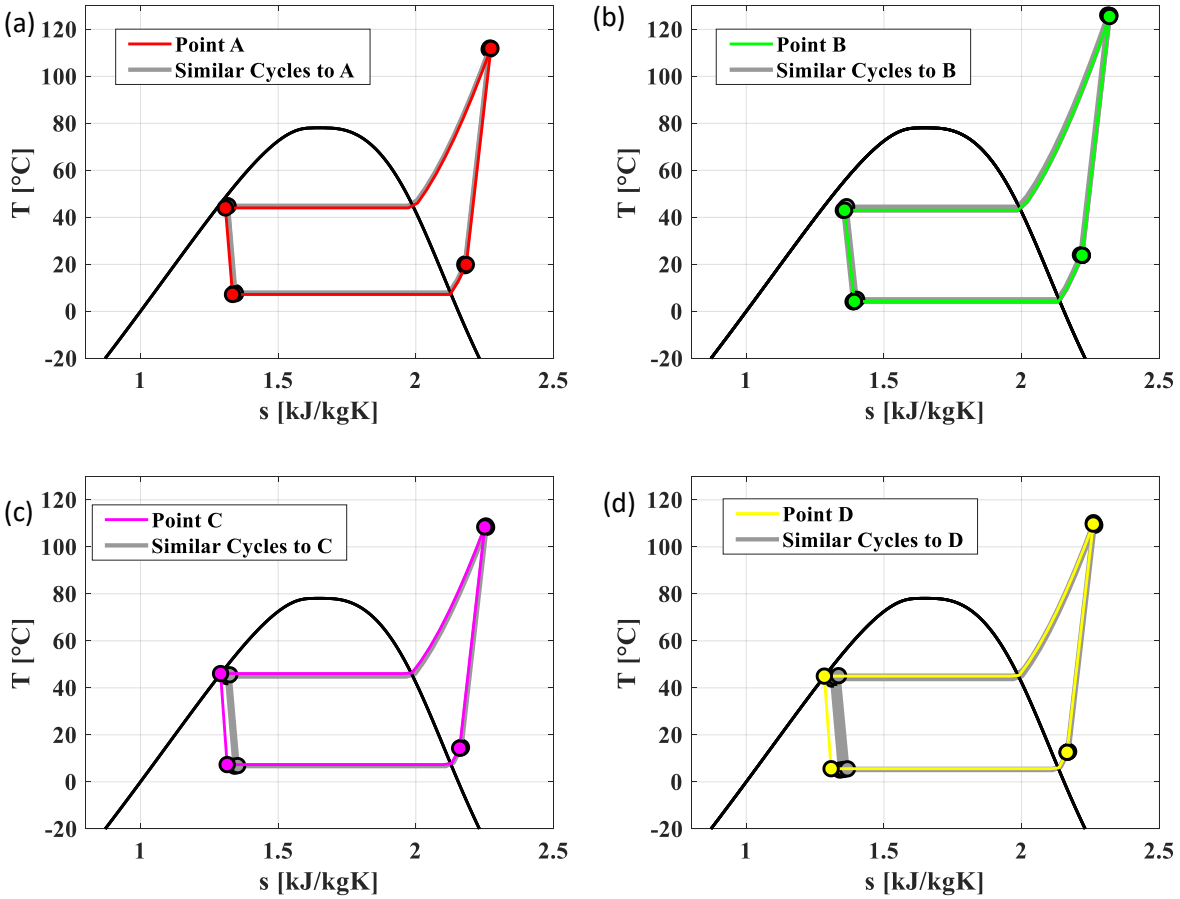


Figure 3.25. Temperature – specific entropy diagrams for condition A, B, C and D of Figure 3.24. (a) Point A: 20% refrigerant leakage and 20% evaporator fouling. (b) Point B: 40% refrigerant leakage. (c) Point C: 20% condenser fouling and 20% evaporator fouling. (d) Point D: 10% condenser fouling and 30% evaporator fouling. In all cases solid grey lines refer to similar thermodynamic cycles of other faulty conditions similar to the investigated points

Table 3.18. Fault conditions for points A, B, C, D and for similar thermodynamic cycle to each of the investigated points

Points	**Fault conditions of point (% - RL: Refrigerant Leakage CF: Condenser Fouling EF: Evaporator Fouling)**	**Fault conditions of similar cycles to point (% - RL: Refrigerant Leakage CF: Condenser Fouling EF: Evaporator Fouling)**
A	RL20CF0EF20	RL20CF10EF10 – RL20CF10EF20
B	RL40CF0EF0	RL40CF0EF10 – RL40CF0EF20 - RL40CF10EF20 -RL40CF20EF20
C	RL0CF20EF20	RL10CF10EF30 – RL10CF20EF30
D	RL0CF10EF30	RL10CF0EF40 – RL10CF10EF40 - RL10CF20EF40

At this point, the same analysis was carried out in Figure 3.26, for lower instrumental uncertainties of ±0.3 bar and ±0.5 °C. In this case the first identification surface remains unchanged (Figure 3.26(b)), whereas Figure 3.26(a) shows an almost complete full domain. As a matter of fact, almost every faulty thermodynamic cycle can be uniquely identified (except the one for refrigerant leakage of 40% and evaporator fouling from 0 to 20%), with an identification percentage ψ of 96.3%.

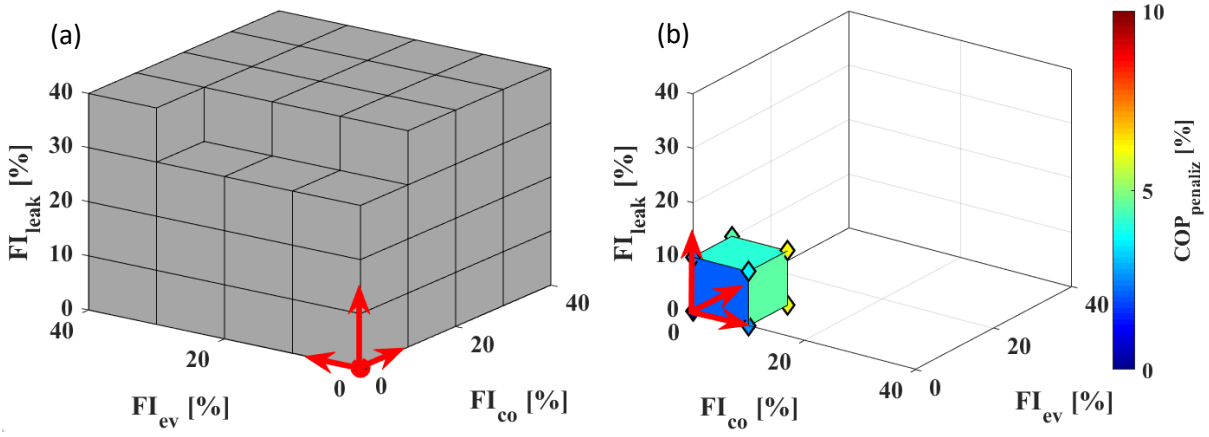


Figure 3.26. Fault diagnosis and evaluation domain depending on fault intensities, for an identification step of 10% and for uncertainties of ±0.3 bar and ±0.7 °C. (a) Entire domain. (b) First identification surface rotated by 90° and COP penalization for each point

Figure 3.27 represents the results in terms of the identification domain (Figure 3.27(a)) and first identification surface (Figure 3.27(b)) for a fault intensity step of 20%. In this case, higher instrumental uncertainties of ±1 bar and ±2.3 °C can be used to obtain an acceptable result in terms of first identification surface. Furthermore, as before, the first identification surface is the closest possible to the origin, with each kind of fault that can be uniquely detected if it reaches a fault intensity of 20%, limiting the maximum COP penalization to approximately 16%. If the alarm given by the first identification surface about the presence of a certain kind of fault is ignored, only in case of a 40% refrigerant leakage there can be further problems in the unique identification of the fault and of its level, as shown in Figure 3.27(a), because of the reduced effect of heat exchanger fouling, especially evaporator. In this case, the diagnosed fault percentage ψ is 69.4%.

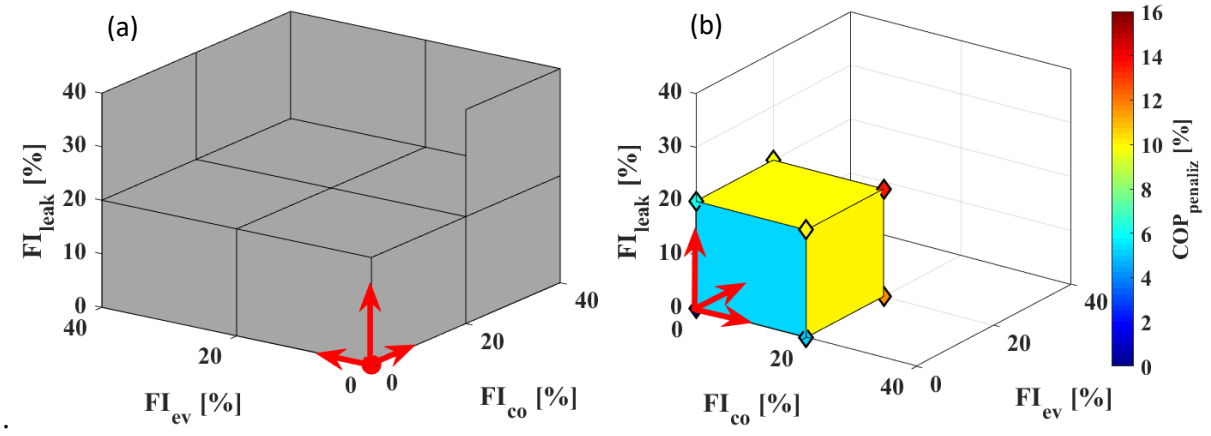


Figure 3.27. Fault diagnosis and evaluation domain depending on fault intensities, for an identification step of 20% and for uncertainties of ±1 bar and ±2.3 °C. (a) Entire domain. (b) First identification surface rotated by 90° and COP penalization for each point

Finally, a more stringent fault severity step of 5% is considered in Figure 3.28, for lower fixed values of measuring equipment uncertainties of 0.2 bar and 0.5 °C. The first identification surface in Figure 3.28(b) presents an empty zone for a refrigerant leakage less than 10%. This aspect is related to the presence of the liquid receiver in the system studied, so a refrigerant leakage of 5% does not cause any malfunctioning and any thermodynamic cycle modification, as already discussed before. If the first alarm is ignored, within the domain it can be several empty zones caused by non-adequate instrument uncertainties, as shown in Figure 3.28(a). Therefore, near faulty conditions in terms of similar fault intensities are likely to be mistaken each other, with an identification percentage factor ψ of approximately 47.3%.

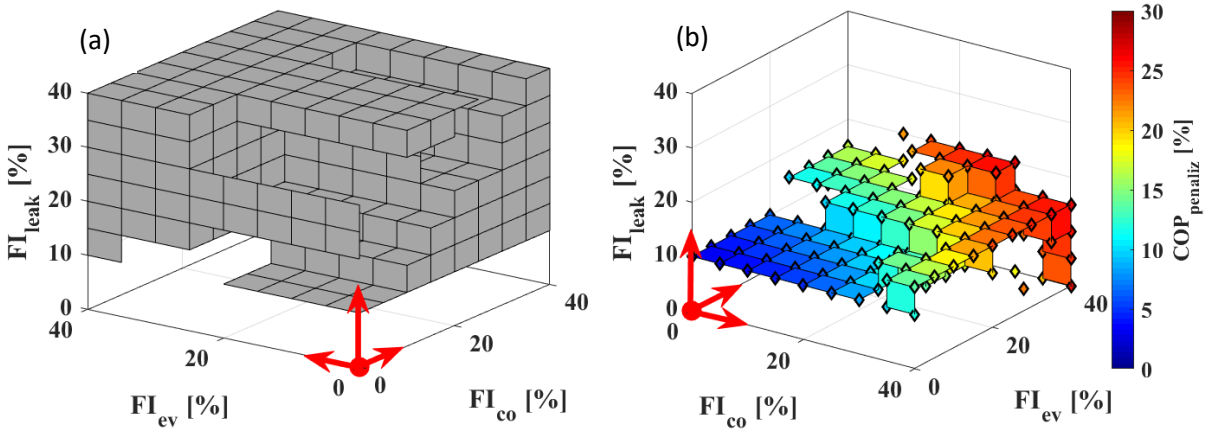


Figure 3.28. Fault diagnosis and evaluation domain depending on fault intensities, for an identification step of 5% and for uncertainties of ±0.2 bar and ±0.5 °C. (a) Entire domain. (b) First identification surface rotated by 90° and COP penalization for each point

Decreasing the measuring equipment uncertainty to ±0.2 bar and ±0.2 °C, it can be noticed from Figure 3.29(a) that the identification domain is almost completely patched (ψ of 71.9%). As before, also in this case for the liquid receiver there are several empty zones for a refrigerant

leakage less than 10%. Figure 3.29(b) shows the first identification surface closest to the origin for these conditions. In any case, using such a high accuracy is justified only when very small COP penalizations need to be avoided, and it becomes therefore less interesting from the industrial point of view.

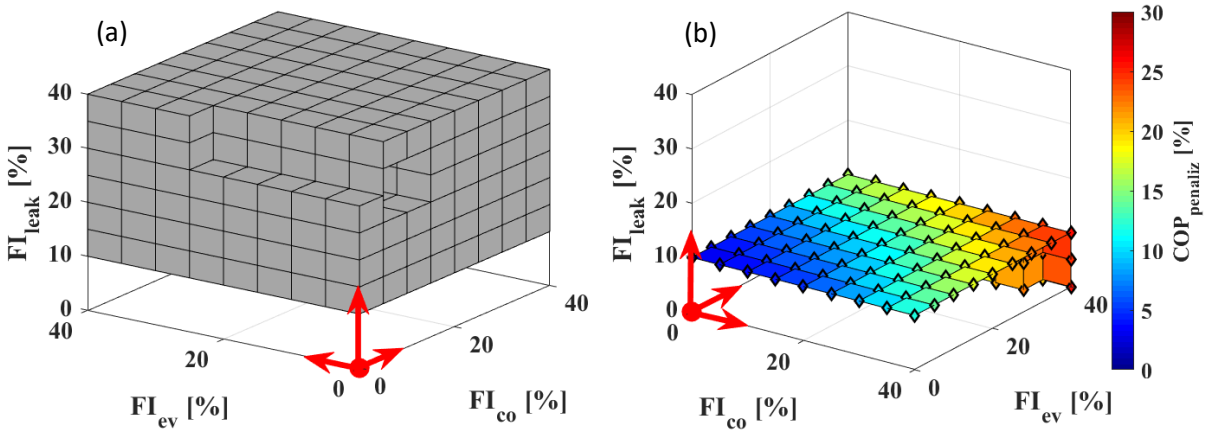


Figure 3.29. Fault diagnosis and evaluation domain depending on fault intensities, for an identification step of 5% and for uncertainties of ±0.2 bar and ±0.2 °C. (a) Entire domain. (b) First identification surface rotated by 90° and COP penalization for each point

3.3.5 Proof of concept of a ML FDDE tool implementation

In this section, some preliminary results for the implementation of a FDDE are reported, as proof of concept for all the observed aspects in previous sections. The developed tool is based on a ML approach. This analysis is currently partial, and further developments must be done in order to assess and compare ML tools with mechanistic physics-based model.

Data generated through the model are employed to calibrate three different AI tools predicting the fault severity of refrigerant leakage, condenser fouling and evaporator fouling faults. Input data considered are: external temperature, pressures and temperature at the inlet and outlet of the compressor (same employed in section), whereas the outputs are the fault intensities for each kind of investigated fault. The internal temperature is considered fixed to 26 °C, whereas a 5% fault intensity step is adopted, and data are used to train a quadratic support vector machine (SVM) classification method. Confusion matrixes for the three calibrated ML models, indicating the number of right and wrong classifications for each of the fault intensities investigated, are reported in Figure 3.30. Numbers on the major diagonal refer to the right classifications, whereas others indicate the differences between the effective and predicted results. In case of refrigerant leakages (Figure 3.30(a)), most of the misclassified cases belong to close faults conditions, especially between 0 and 5%, due to the compensation effect of the liquid receiver used in the system investigated. More misclassifications are present in case of

evaporator fouling (Figure 3.30(b)), with most of them also in this case belonging especially to close fault intensities conditions. Finally, better results in terms of performance prediction are obtained for condenser fouling intensity prediction (Figure 3.30(c)).

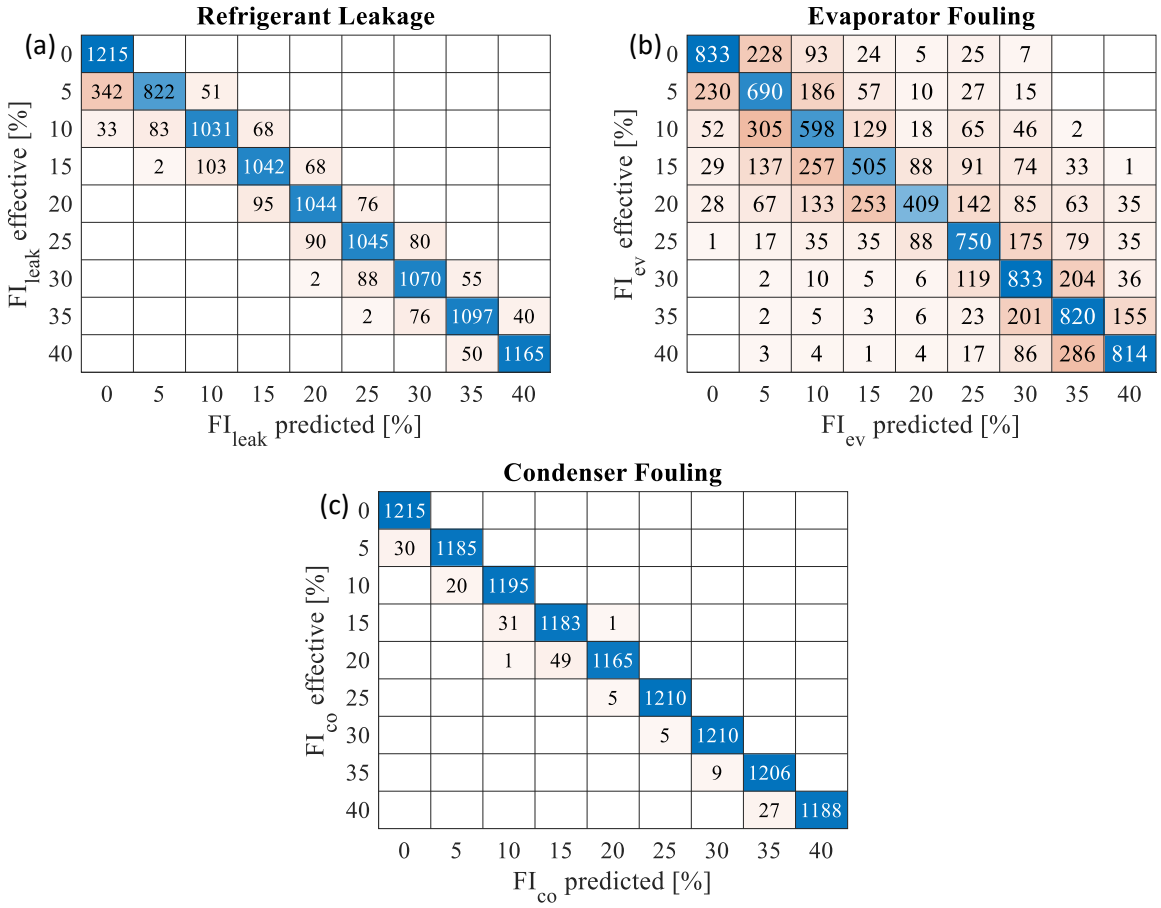


Figure 3.30 – Confusion matrixes for the ML based models in the prediction of refrigerant leakage (a), condenser fouling(b) and evaporator fouling (c)

As proof of concept of the ML FDDE tool, the three calibrated models have been applied to several fault evolution situation. Figure 3.31(a) shows the COP evolution in case of a 3%/year refrigerant leakage, a 40% maximum condenser fouling an no evaporator fouling, and . Figure 3.31(c) the comparison between fault intensities obtained with the physics-based approach (solid line) and with the ML based approaches (coloured dots). Indications about the mean absolute error of the fault intensities prediction between the two aforementioned approaches are also provided for each kind of fault. Similarly, Figure 3.31(b, d) shows a comparison obtained in case of a 40% maximum condenser fouling, a 40% maximum evaporator fouling and absence of refrigerant leakages. Results show that both the refrigerant leakage and the condenser fouling models are able to predict fault intensity values, with mean absolute errors lower than 1%. Regarding instead the less performing prediction model for evaporator fouling, the misclassification mainly occurs in case of huge refrigerant leakages, as shown in Figure

3.31(a) where a 40% refrigerant leakage led to a wrong identification of a 10% evaporator fouling. This result is in accordance with results presented in section 3.3.4 for which the effect of heat exchanger fouling is more difficult to identify in case of high leakages. Otherwise, in case of absence of refrigerant leakages, the evaporator fouling model is able to predict effective results with a MAE of approximately 1%.

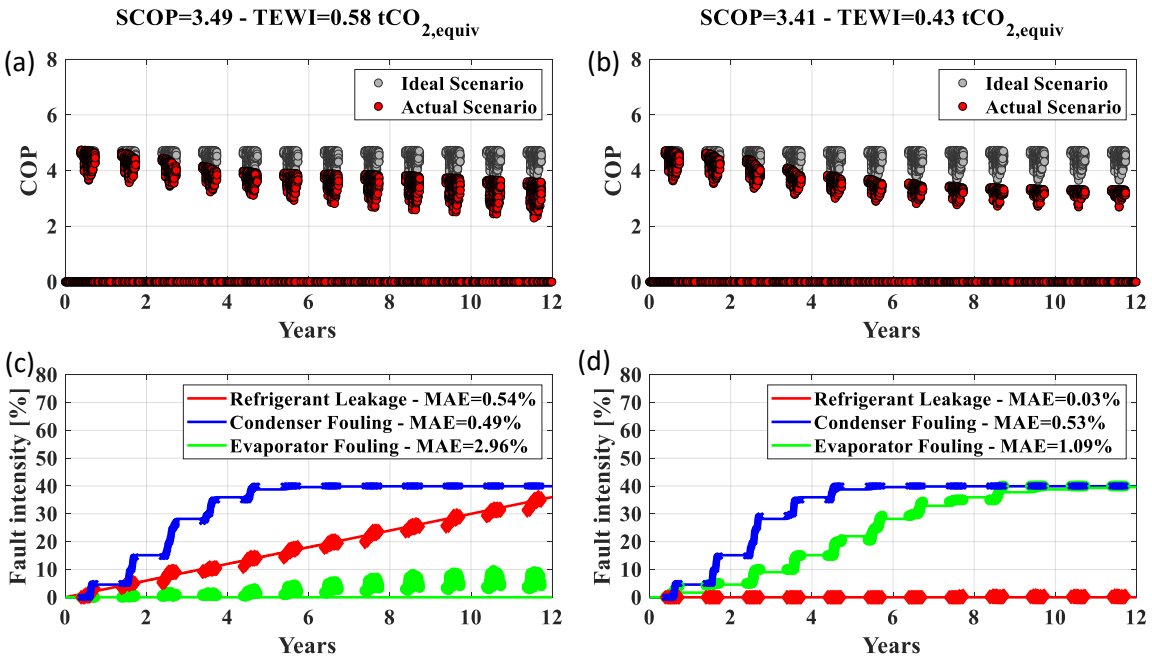


Figure 3.31. COP evolution and comparison between fault intensities predicted with the physics-based approach (solid lines) and the machine-learning based approach (coloured dots), with indications for the mean absolute errors. (a) 3%/year refrigerant leakage, 40% maximum condenser fouling and absence of evaporator fouling. (b) 40% maximum condenser fouling, 40% maximum evaporator fouling an absence of refrigerant leakage

However, it has to be clarified that this is only a preliminary analysis of a study that will be deepened in the future. As a matter of fact, this analysis does not consider the instrument uncertainties that, compatibly with the fault severity step adopted, will lead to higher mean absolute errors in the previsions.

3.4 Conclusions of Part 1

The principal quantitative conclusions and remarks from results of part 1, regarding the investigation of soft faults on a residential air source heat pump case study, are here provided.

- For cooling mode, in case of an external and internal temperatures of respectively 35 °C and 26 °C, a 40% refrigerant leakage causes a COP penalization of approximately 25%, a 40% condenser fouling of 13.2% and a 40% evaporator fouling of 16.8% than the fault-free case. For the same boundary conditions, in case of simultaneous refrigerant leakages and condenser fouling with fault intensities higher respectively than 15% and 10%, a COP penalization higher than 10% occurs. In case of simultaneous refrigerant

leakages and evaporator fouling, the same penalization is obtained for fault intensities higher respectively than 10% and 20%. Finally, for a combination of both condenser and evaporator fouling, the 10% COP penalization is reached for fault intensities at least equal to respectively 10% and 15% for the considered faults. In terms of the effect on measured variables, a 40% refrigerant leakage causes a decrease of evaporating temperature, increase of outlet evaporator superheating and outlet compressor temperature, respectively of 6 °C, 12.5 °C and 24.9 °C. A 40% condenser fouling causes a rise of the condensing and outlet compressor temperatures of respectively 5 °C and 10 °C, whereas an evaporator fouling causes a decrease of the evaporation temperature of 5.7 °C and a rise of the air temperature difference of 6.1 °C. Considering the overlapping effects of the faults investigated, the combination of evaporator and condenser fouling causes both a lower evaporating temperature and a higher condensing temperature compared to the fault free case. The combination of evaporator fouling and refrigerant leakages instead causes a higher condensing temperature reduction, compared with standalone faults, and a compensation effect caused by contrasting contributions for the evaporating temperature, which almost does not vary compared with fault-free conditions. Finally, the combination of condenser fouling and refrigerant leakages causes a contrasting effect on the condensing temperature, which rises in a slight way compared with a standalone condenser fouling.

- Regarding dynamic simulations in cooling mode, it is obtained that the SCOP decreases and the TEWI increases for higher fault severities and numbers of combined faults, for all the climate conditions investigated of Naples, Miami and Shanghai. Moreover, SCOP and TEWI become closer to the fault-free case with the increasing number of maintenance interventions. For all the investigated conditions, it is obtained a 4-year ordinary maintenance strategy can reduce to 50% the percentage of scenarios with SCOP penalized higher than 10%, whereas to obtain the same results for other climates, at least a every 2-year maintenance scenario for Shanghai and a every year maintenance interventions for Miami have to be adopted.
- For heating mode, and for fixed conditions of ambient and indoor temperatures of 7 °C and 20 °C, a COP penalization of 42.4% is obtained in case of 40% refrigerant leakage, a 21% penalization for a 40% condenser fouling and only a 4.2% degradation for 40% evaporator fouling. Combining all the three faults investigated considering a 40% fault intensity for all cases, almost a 60% degradation of COP is obtained. Regarding the effects on measured parameters on the machine, for the same boundary conditions, a

40% refrigerant leakage causes a decrease of evaporating and condensing temperature, of respectively 9.6 °C and 4.3 °C, and a rise of outlet compressor temperature and outlet evaporator superheating of respectively 27.4 °C and 9.7 °C. A 40% condenser fouling affects especially the condensing temperature and the superheating, which both increase of respectively 7 °C and 17 °C, whereas a 40% evaporator fouling causes a 1.6 °C reduction of the evaporation temperature, without significantly affect other measured variables. Combining the three fault intensities, both the evaporating temperature decrease, and the outlet compressor increase are enhanced by the overlapping of faults, whereas the condensing temperature remains almost unchanged compared with the fault-free case.

- Regarding dynamic simulations in heating mode, as the cooling mode, the SCOP decreases and the TEWI increases with the increase of the fault evolutions, the number of faults combined and with the decreasing of maintenance interventions, for the three climate conditions investigated of New York, Beijing and Vienna. In this case, it seems that a 4-year ordinary maintenance strategy is able to reduce the percentage of scenarios under 50% with SCOP penalizations higher than 10% for all climate conditions investigated, whereas this percentage becomes almost zero for New York, slight below 20% for Vienna and almost 30% for Beijing in case of maintenance interventions every 2 years.
- Regarding the sole determination of a system malfunctioning, a COP penalization between 5 and 10% can be detected with commercial and cheap pressure and temperature sensors, with uncertainties respectively of ± 1 bar and $\pm 1°C$, whereas lower penalizations (below 2%) can be detected for sensor uncertainties of ± 0.2 bar and ± 0.2 °C.
- Regarding a complete fault detection, diagnosis and evaluation process, this depends both on the fault severity step and on the measuring equipment uncertainty. In case of a fault severity step of 10% and sensor uncertainties of ± 1 bar and ± 0.7 °C, the first unique identification surface is the closest to the fault-free case, but there are several zones in the fault intensities dominium in which fault combinations could not be specifically identified and evaluated. Almost all the combinations (96.3%), instead, can be uniquely identified in case of sensor uncertainties of ± 0.3 bar and ± 0.5 °C. By reducing the fault severity step to 5%, the closest first identification surface is obtained only in case of uncertainties of ± 0.2 bar and ± 0.2 °C. However, due to the presence of the liquid receiver, there are several conditions characterized by a refrigerant leakage

lower than 10% that remain unidentified also for restricted values of the measuring equipment uncertainties.

- Finally, three FDDE ML based models are developed to predict intensities for the three faults investigated, and results shows mean absolute errors lower than 1% for the prediction of refrigerant leakage and condenser fouling with a 5% fault intensity step, whereas less performances but a MAE still lower than 3% are instead obtained for the evaporator fouling prediction model.

PART 2

4. Integration of traditional heat pump with renewable energy sources

4.1 Multi-source heat pumps: state of the art

Table 4.1 shows several works in literature dealing with the integration of multiple sources alternative to air for traditional air-source heat pumps, of the types already seen in section 2.3.2. These works are categorized considering different criteria. Based on the source exploited, studies are divided between air, ground, sun thermal (T), photovoltaic (PV) and other energy sources. Regarding the application, the division is made among space heating, space cooling, domestic hot water (DHW) production and others. Works are distinguished based on the typology of thermal storage employed, among none, water, PCM or soil, and based on if an indication of seasonal performance is provided, or a dynamic performance analysis is carried out. Another classification criteria used regards if a works carries out a comparison among different scheme plants or system technologies, in terms of system performance, feasibility, economic convenience etc. Moreover, the table highlights if a paper between the reviewed carries out an optimization for the system components, or if analyses the effect of sizing of one or more of them. Finally, the last three columns of the table refer to the description or the development of a control strategy for the system analysed, or if an economic analysis is carried out by the manuscript considered, to conclude in the end with a final note column.

Table 4.1. State of the art of multi-source heat pumps, divided per typology of energy source, application, type of thermal storage and other categories

Work	Source*	Application	Thermal storage	Dynamic performance analysis	Comparison with other scheme – technologies	Optimization of system components / Effect of sizing	System control strategy	Economic analysis	Notes
Comakli et al. [142]	Air + Sun(T)	Space heating	PCM	Yes	Yes	No	No	No	Experimental in Trabzon, Turkey
Trillat-Berdal et al. [143]	Ground + Sun(T)	Space heating, cooling, DHW	Water/ Soil	Yes	No	No	Yes	No	Experimental in a 180m^2 private residence
Han et al. [144]	Ground + Sun(T)	Space heating	PCM	Yes	No	No	Yes	No	Numerical
Chow et al. [83]	Sun(T)	DHW	Water	Yes	No	No	No	No	Numerical
Wang et al. [145]	Ground + Sun(T)	Space heating, cooling	Soil	No	No	No	Yes	No	Experimental in a detached house in Harbin, China
Sterling and Collins [146]	Sun(T)	DHW	Water	No	No	No	No	No	Numerical in TRNSYS [118]
Yumrutas and Unsal [147]	Sun(T)	Space heating	Water	Yes	No	Yes	No	No	Numerical
Arteconi et al. [148]	Ground	Space heating, cooling	Water	No	No	Yes	No	No	Experimental in office building
Liu et al. [89]	Water (Urban Sewage)	Space Heating	No	Yes	No	No	No	Yes	Experimental in Dalia, China
Verma and Murugesan [149]	Ground + Sun(T)	Space heating	No	No	No	Yes	No	No	Optimization with Taguchi method

Banister and Collins [150]	Sun(T)	DHW	Water	No	No	Yes	No	Experimental apparatus at University of Waterloo, Canada
Safa et al. [151]	Ground	Space heating, cooling	Water	Yes	No	Yes	No	Experimental + Numerical in TRNSYS
Zhu et al. [152]	Air + Ground	Space cooling	PCM	Yes	No	Yes	Yes	GHE in parallel with a cooling tower
Cai et al. [153], [154]	Air + Sun(T)	Space heating, cooling, DHW	Water	No	No	No	No	Experimental + Numerical
Ni et al. [155]	Air + Sun (T)	Space heating, cooling	PCM	No	No	Yes	No	Experimental
Croci et al. [156]	Air + Sun (PV+T)	Space heating, cooling, DHW	Water	Yes	No	No	No	Numerical
Starke et al. [157] [158]	Air + Sun (T)	Swimming Pool Heating	No	Yes	Yes	Yes	Yes	Numerical in TRNSYS
Corberan et al. [159]	Air + Ground	Space heating, cooling, DHW	No	Yes	No	No	No	Experimental. Boreholes in series with an air-coil
Kim et al. [160]	Ground	Space heating, cooling	Water	Yes	No	No	No	Numerical
Bamigbetan et al. [88]	Water (Waste Heat)	Industrial Heating	No	No	No	No	Yes	Experimental + Numerical of an HTHP
Dannemand et al. [161]	Sun (PV+T)	DHW	Water	Yes	No	Yes	No	Experimental in DTU, Denmark
Hervàs-Blasco et al. [162]	Water (Waste Heat)	DHW	Water	No	Yes	Yes	No	Numerical in TRNSYS
Plytaria et al. [163]	Sun (PV+T)	Space Heating	Water/ PCM	No	Yes	No	Yes	Numerical in TRNSYS

Shin et al. [164]	Ground	Space heating, cooling, DHW	Water	No	No	Yes	No	Propose a simultaneous heating and cooling system and focus on the operation strategy
Huang et al. [165]	Ground + Sun(T)	Space heating, cooling, DHW	Water	No	No	No	No	Experimental in Wangjapu, China + Numerical in TRNSYS
Kuthu et al. [166]	Sun(T)	DHW	PCM	Yes	No	Yes	No	Numerical
Ma et al. [167]	Sun(T)	Space heating	Water	No	Yes	Yes	No	Numerical in TRNSYS. Analyzed one-stage and two-stage schemes
Sun et al. [168]	Ground + Sun(T)	Space heating	Water	Yes	No	Yes	No	Experimental in Shandong, China
Wang et al. [169]	Air + Sun (T)	Space Heating	Water	Yes	No	Yes	No	Experimental + Numerical in TRNSYS
Zhou et al. [170]	Sun (PV+T)	Space heating	Water	Yes	No	No	No	Experimental + Numerical
Belmonte et al. [171]	Sun(T)	Space heating	Water/ PCM	Yes	Yes	No	No	Numerical in TRNSYS
Kosan and Aktas [172]	Sun (T)	Space heating	PCM	Yes	No	No	No	Experimental
Lei et al. [173]	Sun(T) + Air + Wind	Space heating	Water	No	No	No	No	Traditional vapor compression system with absorption heat pump. Theoretical
Li et al. [174]	Air + Sun (PV)	Space heating, cooling, DHW	Water	No	Yes	Yes	Yes	Numerical

Nasouri et al. [175]	Sun(T)	DHW	Water	No	No	Yes	No	Numerical. Pareto Optimization
Ural et al. [176]	Air heated by Sun	Space heating	Water	Yes	Yes	No	Yes	Experimental at University in Mugla, Turkey
Bulmez et al. [177]	Ground + Sun (PV+T)	Space heating, cooling	Water	Yes	No	No	Yes	Experimental in University of Transilvania, Romania
Kamazani and Aghanajafi [178]	Ground + Sun (PV+T)	Space heating, cooling	PCM	Yes	No	Yes	No	Numerical, Pareto optimization
Lee et al. [179]	Ground + Sun(T)	Space heating, DHW	Water	Yes	Yes	Yes	No	Numerical in TRNSYS
Yang et al. [180]	Air + Sun(T)	Space heating, DHW	Water	Yes	Yes	No	Yes	Numerical in TRNSYS

*Sun(T): Thermal solar collectors; Sun(PV): Photovoltaic solar collectors; Sun(PV+T): Both thermal and photovoltaic solar collectors

4.1.1 Energy source exploited

Regarding the source exploited, works can analyse one-source, two-sources or multi-sources solutions. The thermal solar source alone has been analysed by Chow et al. [83], Sterling and Collins [146], Yumrutas and Unsal [147], Banister and Collins [150], Kutlu et al. [166], Ma et al. [167], Belmonte et al. [171], Kosan and Aktas [172] and Nasouri et al. [175], whereas both thermal and photovoltaic collectors are employed in the works of Dannemand et al. [161], Plytaria et al. [163] and Zhou et al. [170]. Only ground source systems are instead studied by Arteconi et al. [148], Safa et al. [151], Kim et al. [160] and Shin et al. [164]. Finally, water source systems were studied by Bamigbetan et al. [88], Hervàs-Blasco et al. [162] in terms of waste heat recovery, and by Liu et al. [89] for urban sewage heat pumps. Regarding two-source exploitation, most of the studies analyse the integration of the solar source with air or ground. In case of both air and sun sources, most of the works deal with an alternative operation of the two operating modes (air/sun) (Cai et al. [154], Ni et al. [155]) depending on the system performance, whereas few others employ the two sources in parallel (Wang et al. [169]). Other works instead employ innovative PV-T collectors (Croci et al. [156]) or photovoltaic panels instead of traditional solar collectors (Li et al. [174]). Among the analyzed works, only Ural et al. [176] introduces innovative solar collectors able to pre-heat the air before its inlet into the heat pump evaporator. In case of ground and sun exploitation instead, they can be different connections between the two sources, with solar collectors that can be installed in series with geothermal heat exchanger (GHEs) and therefore used to increase temperature of the water coming from the ground (Verma and Murugesan [149], Huang et al. [165], Trillat-Berdal et al. [143], Sun et al. [168]), or in parallel (Wang et al. [145], Lee et al. [179]) in order to satisfy the user needs. Also in this case, there can be several works which employed innovative PV-T collectors integrated with the ground source, such as the works of Bulmez et al. [177] and of Kamazani and Aghanajafi [178]. Finally, between the reviewed works, only the ones of Zhu et al. [152] and of Corberan et al. [159] put together air and ground sources, in the first case with the employment of a ground heat exchanger and of a cooling tower alternatively operating, in the second case using ground boreholes situated in series with an air coil. The only work which considered more than two energy sources for a heat pump is the one of Lei et al. [173], which integrates a traditional air source heat pump with a wind turbine and solar collector, coupling the vapor compression system with an absorption heat pump and developing a complex layout for space heating.

4.1.2 Application and thermal storage typology

Regarding the system application, most of the reviewed papers analysed systems developed for space heating, space cooling and DHW purposes, either as alone or alternative supply, except for the particular cases given by work of Bamigbetan et al. [88] dealing with industrial heating purposes, and work of Starke et al. [157] [158] considering a swimming pool heating system. Regarding the typology of thermal storage employed, most of the works integrate their systems with water storage tank, and several works instead with a PCM thermal storage. A comparison between water and PCM thermal storage was carried out by Plytaria et al. [163], which obtains a slight increase in system performance and a high increase in investment cost by using PCM instead water, and by Belmonte et al. [171], for whom the performance rise itself is not so evident.

4.1.3 Dynamic performance and comparison between different schemes

Regarding the performance indication, several of the works reviewed only give an information about COP variation along a short period of time ([161], [65], [166], [170]), whereas other works deal with a detailed dynamic performance analysis. Moreover, performance indications are given by comparing different types of systems, technologies, and schematics.

Regarding systems exploiting solar source, the work of Croci et al. [156] obtained values of seasonal performances which are on average 50-60% higher than the only air mode. Similarly, Kosan et al. [172] obtained a heating COP on average 14% higher passing from an air source to a solar assisted heat pump. Regarding performance comparison between series, parallel and dual source configurations, Comakli et al. [142] obtained a seasonal COP which is 4.60 for a series system and 3.00 for a parallel configuration. Similarly, Yang et al. [180] obtained a higher yearly seasonal performance factor for a serial configuration of 5.5, and lower values for parallel and dual source configurations, respectively of 4.5 and 4.4, but the heat provision of the serial which is limited by the solar irradiance. Differently with other works instead, integrating sun and ground sources, the work of Lee et al. [179] obtained higher average COP of the heat pump for a parallel than a series configuration. Starke et al. [157] [158] instead compared a traditional air source heat pump with a solar assisted for the series, parallel and dual source configurations. Results show that the lowest seasonal performance factor is obtained for the air source heat pump between 2.5 and 4 depending on the heat pump scale factor, whereas the highest are obtained for a dual source configuration between 7 and 8. Results underline also that parallel systems are more convenient than series configuration for lower heat pump capacity. Finally, Ma et al. [167] compared two trans-critical CO_2 solar assisted heat pumps, in

a one-stage and two-stage configurations, with a traditional one-stage R410A. They obtained the highest performance for the two-stage CO_2 cycle, the lowest for the one-stage CO_2 cycle, and intermediate for the R410A system.

Regarding system employing the ground source instead, the work of Corberan et al. [159] compared seasonal performance factor between an only ground source and dual source systems, obtaining almost negligible differences between the two configurations. The effect of ground thermal imbalance on seasonal performance has been instead studied by Zhu et al. [152], which obtained a 20% penalization of system COP after 20 years of operation of the machine. The work of Lee et al. [179] instead obtained a mitigated effect of the thermal soil imbalance, if the system is integrated with solar collectors connected in series or parallel.

4.1.4 Optimization of system components and effect of design parameters

Among the reviewed papers, several works analyze the effect of some sizing parameters on system performances, whereas other few works deal with more complex system optimizations. For the solar source, the work of Nasouri et al. [175] carried out an optimization of the coefficient of performance and of the solar collector efficiency with a particle swarm optimization method, considering as input variables solar collector area and materials, compressor speed, condenser length, collector pipes diameter and thickness. Similarly, also considering the ground source, Kamazani and Aghanajafi [178] carried out a multi-objective optimization with a genetic algorithm (GA) of life-cycle costs and exergy efficiency, considering as input number and depth of boreholes, heating and cooling setpoints, condenser and evaporator lengths, collector tilt and azimuth angles, number of PV cells and batteries, tank volume and PCM percentage. COP was instead optimized by Verma and Murugesan [149], considering as inputs several parameters related to the ground heat exchanger and solar collectors.

Regarding works analysing the effect of sizing parameters on the system performance, the most investigated variables are the storage tank volume and the solar collector surface. The storage tank volume effect was analyzed by Ma et al. [167], which obtained a slight decrease of electricity consumption with the increase of the tank size. Similar considerations were also done by Li et al. [174], which obtained a small annual grid consumption by increasing both hot and cold tank sizes, and by Belmonte et al. [171], for which the effect of the storage tank size is almost negligible. For the seasonal storage used in Yumrutas and Unsal [147], a higher COP increase from approximately 5 to 6 is achieved by incrementing the tank volume from 100 to 300 m^3, until a saturation for the benefit deriving from the volume increase is reached. For

system exploiting the ground source, Arteconi et al. [148] obtained a negligible effect of the tank volume on energy consumption in winter mode and a high negative effect in summer mode. Regarding the ground imbalance effect instead, Huang et al. [165] discovered a higher soil temperature rise in 20 years for higher volumes of the storage tank investigated.

Solar collector surface effect was instead analyzed by Starke et al. [157], which obtained an SPF increase from 4 to almost 11.5 passing from a solar field area of 11m^2 to 143m^2. Similarly, Ma et al. [167] obtained a 20% average electricity consumption reduction by passing from 30m^2 to 90m^2 of solar collector surface. Lee et al. [179] obtained an increase of the system COP from 2.4 to 2.7 for a parallel configuration, and from 2.2 to 2.35 for a series configuration, passing from 2 to 10m^2 of solar collector surface, whereas for Plytaria et al. [163], COP increases from 5.7 to 6.3 by increasing the solar area from 10 to 25m^2. The effect of the compressor capacity is analyzed by Ma et al. [167], which obtain an optimal value to minimize the electricity consumption depending on the configuration investigated. The effect of the solar photovoltaic collector capacity is instead observed in Li et al. [121]. Finally, Arteconi et al. [148] studied the effect of several ground heat exchanger parameters such as length and number of boreholes.

4.1.5 System control strategies

Regarding the system control, most of the reviewed article presents the development of control strategy based on solar collector and storage tank temperatures, as done in Dannemand et al. [161], Li et al. [174], Yang et al. [180] and Wang et al. [169]. In system exploiting the ground source, the heat pump, circulating pumps and switching valves can be activated/deactivated depending on the differences between outlet ground and solar collectors temperatures, and tank temperatures, as done in Trillat-Berdal et al. [143], Shin et al. [164], and Sun et al. [168] . Lee et al. [179] developed two different control strategies based on tank and ground temperature for series and parallel configurations. Some other works instead employ also other external conditions in order to establish the operating mode of the system. Ma et al. [167] measured evaporation and water/glycol mixture temperatures and temperature difference of secondary fluid at the gas-cooler/condenser and at the evaporator. Wang et al. [145] decided the control logic of the system based on the specific period of the year, whereas Ni et al. [155] regulated differently depending on whether it is day, night, summer, and winter seasons. Meteorologic conditions have been considered in the control strategy of Kutlu et al. [166] and of Han et al. [144], whereas Hervàs-Blasco et al. [162] logic is based not only on temperatures and water level of the storage tank, but also on the number of starts of the heat pump. Between all the control logics investigated, only the ones of Zhu et al. [152] and Banister and Collins [150] are

oriented to find the optimal cooling storage ratio, to satisfy always the DHW request and to minimize the energy consumption of the entire system.

4.1.6 Economic analysis

For the economic analysis, several works in literature compare investment, operating and total costs of multi-source heat pumps with other technologies. Liu et al. [89] obtained that an urban sewage heat pump system has comparable operating costs of a coal-fired boiler, and lower operating costs of a gas-fired and oil-fired boilers. Similarly, Bamigbetan et al. [88] obtained that high temperature heat pumps for industrial heating are characterized by lower total costs of electric heater, and gas-boilers, with a rising convenience with the lifetime years of the machines increase. Regarding comparison between different schematics, Yang et al [180] compared costs for serial, parallel and dual source configurations, obtaining the lowest payback for the parallel, the highest for the serial and slightly higher than the parallel for the dual-source. Plytaria et al. [163] evaluated capital, operating and total costs for systems with and without PV-T collectors, and with and without a PCM storage tank, obtaining that in all cases the usage of PV-T panels and PCM does not guarantee lower total costs than the solution without. Similarly, Li et al. [174] compared capital, operation, maintenance and total costs for three different solutions, comparing a traditional system assumed as baseline with other two cases employing PV panels and a thermal storage tank. The authors obtained that the employment of photovoltaic panels and of the storage tank causes a strong reduction of operation costs, which are able to counterbalance the rise of capital investment given by the extra components, therefore a reduction of the total cost on a lifetime of 10 years. For ground systems, instead, Bulmez et al. [177] compared capital costs related to horizontal and vertical ground heat exchangers, considering the costs for load, excavation, pipes, heating cable, grouting and accessories.

Regarding the effect of design parameters on system costs, Zhu et al. [152] analysed investment, operating and total costs depending on the cooling storage ratio, defined as the ration between the tank capacity and the total cooling capacity, obtaining the minimum value of total costs for a cooling storage ratio of 40%. Similarly, Starke et al. [157] compared the life cycle saving depending on the solar field area and on the schematics, obtaining that for high solar collector surfaces only the parallel and the dual source configurations may have financial benefits. The solar collector surface effect on costs was analyzed also by Plytaria et al. [163], in which the increase of solar collector area is not able to guarantee a total cost reduction. Finally, between all the reviewed studies of the literature, only the work of Kamazani and Aghanajafi [178] dealt

with the effect of electricity prices changes on the levelized cost of energy and on the annual operating costs, obtaining less influence for system employing PV-T panels compared to traditional ground source heat pumps, and not a big influence instead by the employment of PCM thermal storage.

4.2 Case study 1: 5 kW direct expansion solar assisted heat pump for residential heating

To study the effective convenience of a solar source integrated in traditional heat pumps, a case study of a residential dual source (air-solar) heat pump used for domestic heating is here analyzed. In this section, results published in the paper of Mastrullo et al. [181] are presented. A detailed scheme plant of the system analyzed is provided in Figure 4.1. It is composed of two air fin-and-tube heat exchangers, situated respectively indoor for the condenser and outdoor for the evaporator, a scroll compressor, a liquid receiver, a thermostatic expansion valve, and a fixed number of thermal solar collectors. The evaporation may occur alternatively through air in the fin-and-tube evaporator, and through sun with refrigerant direct flowing into solar collectors, both in direct expansion configuration and depending on which operating mode gives the highest performance. For simplicity, the two operating modes will be referred as air and sun evaporations modes in this section. The switch between air and sun modes occurs through a three-way switch valve situated at the outlet of the expansion valve. Main rated characteristics of the system studied, in terms of heating capacity, outlet evaporator superheating and geometric attributes of heat exchangers and solar collectors, are reported in Table 4.2. Similarly to the system modelled in section 3.2, the model has been implemented in MATLAB [106], using REFPROP 9.1 [107] software for thermodynamic properties evaluation.

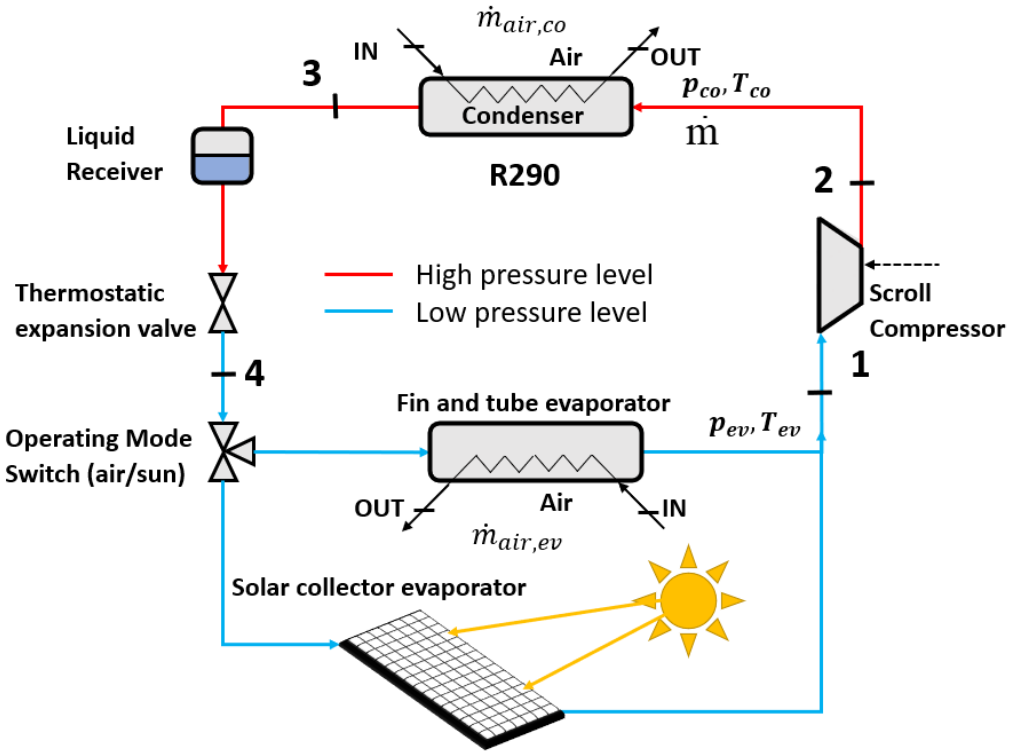


Figure 4.1. Schematic of the direct expansion solar assisted heat pump studied in Mastrullo et al. [181]

Table 4.2. Rated characteristics of the solar assisted heat pump studied in Mastrullo et al. [181], and geometrical characteristics of heat exchangers

Rated Characteristics		
Parameter	**Heat Pump**	
Heating Capacity (7-20 °C) [kW]	5.0	
Outlet evaporator superheating (°C)	7.0	
Working Fluid	R290 (propane)	
Fin-and-tube heat exchangers	**Internal Unit**	**External Unit**
Dimensions [m] (Length x Width x Height)	0.55 x 0.17 x 0.16	0.80 x 0.20 x 0.51
Number of circuits – rows – tubes per row	4 – 9 – 8	4 – 1 – 26
Air Mass Flow Rate [m^3/h]	2000	3000
Longitudinal and transverse tube pitches [m]	0.02	
Fin pitch [mm]	2	
Fin thickness [mm]	0.3	
Tube diameter[mm]	6	
Evaporator solar collector		
Surface [m^2/collector]	2.0	
Zero-loss efficiency η_0	0.755	
Effective heat transfer coefficient a_1 [W/m^2K]	7.745	
Second-order coefficient a_2 [W/m^2K^2]	0.015	

4.2.1 Model

The models for each component are firstly developed and then put together to simulate the behaviour of the entire system.

4.2.1.1 User Load

The requested user load is evaluated according to Commission Regulation (EU) 2016/2281 [33]:

$$\dot{Q}_{user} = \dot{Q}_{design} \cdot \frac{T_{amb} - T_{user}}{T_{design} - T_{user}} \tag{4.1}$$

T_{amb} is the actual ambient temperature, whereas $\dot{Q}_{design}$ is the load requested by the user corresponding to the external temperature of T_{design}. T_{user} is instead the indoor temperature of the user.

4.2.1.2 Scroll compressor, expansion valve and heat exchangers

Regarding the scroll compressor, the thermostatic expansion valve and the fin-and-tube heat exchangers, same approaches used for the system modelled in section 3.2 is employed. Models for each component are presented respectively in sections 3.2.1.1, 3.2.1.2 and 3.2.1.3.

4.2.1.3 Thermal solar collectors

Regarding the thermal solar collector model, the definition of panel efficiency is employed according to Hottel-Whiller-Bliss equation [182].

$$\eta_{col} = \eta_0 + a_1 \cdot x + a_2 \cdot G \cdot x^2 \quad \rightarrow \quad x = \frac{T_{ev} - T_{amb}}{G} \tag{4.2}$$

Coefficient η_0 is the zero-loss efficiency of the collector, representative of the optical losses of the panel, whereas a_1 and a_2 are respectively the first and second-order coefficients, used to evaluate thermal losses of the collector. $\eta_0, a_1$and a_2 are fixed according to manufacturer data, and values are reported in Table 4.2. Furthermore, the surface collector temperature is considered equal to the evaporation temperature, due to refrigerant flowing directly into solar collectors. An example of the solar collector efficiency evolution depending on the difference between ambient and evaporating temperature is provided in Figure 4.2, for several values of the solar radiation between 50 and 1000 W/m^2.

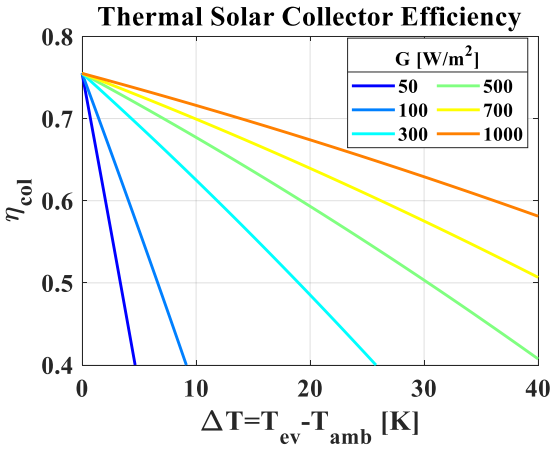


Figure 4.2. Example of thermal solar collector efficiency, according to Hottel-Whiller-Bliss equation [182], depending on the solar radiation and on the difference between the external ambient and the evaporation temperatures

Therefore, the solution for the ambient temperature related to a fixed evaporating temperature is iteratively found, by considering the convergence between the evaporating thermal power requested by the system and the available solar power at the collectors, according to the following expression.

$$\dot{Q}_{ev,requested} = \dot{m} \cdot (h_1 - h_4) = \dot{Q}_{ev,available} = \eta_{col} \cdot N_c \cdot G \cdot A_{col} \qquad (4.3)$$

4.2.2 Resolution algorithm

All the models for each of the system components are put together to simulate the behaviour of the entire system. Operational maps are obtained choosing several values for evaporating and condensing temperatures. For each of them, the thermodynamic conditions are firstly evaluated. Then, the refrigerant mass flow rate of the system is calculated through the compressor model, and electrical, thermal powers and COP are obtained through energy balances. An iterative procedure on the internal fin-and-tube condenser is carried out to evaluate the solution for the effective indoor temperature related to the couple of T_{co}, T_{ev} previously fixed. Finally, if the machine is operating in air mode the fin-and-tube evaporator is iteratively solved, to evaluate the effective ambient temperature corresponding to the fixed couple of T_{co}, T_{ev}. On the other hand, if the machine is operating in sun mode, the solar collector evaporator is solved. All the steps of the resolution algorithm employed are reported in Figure 4.3.

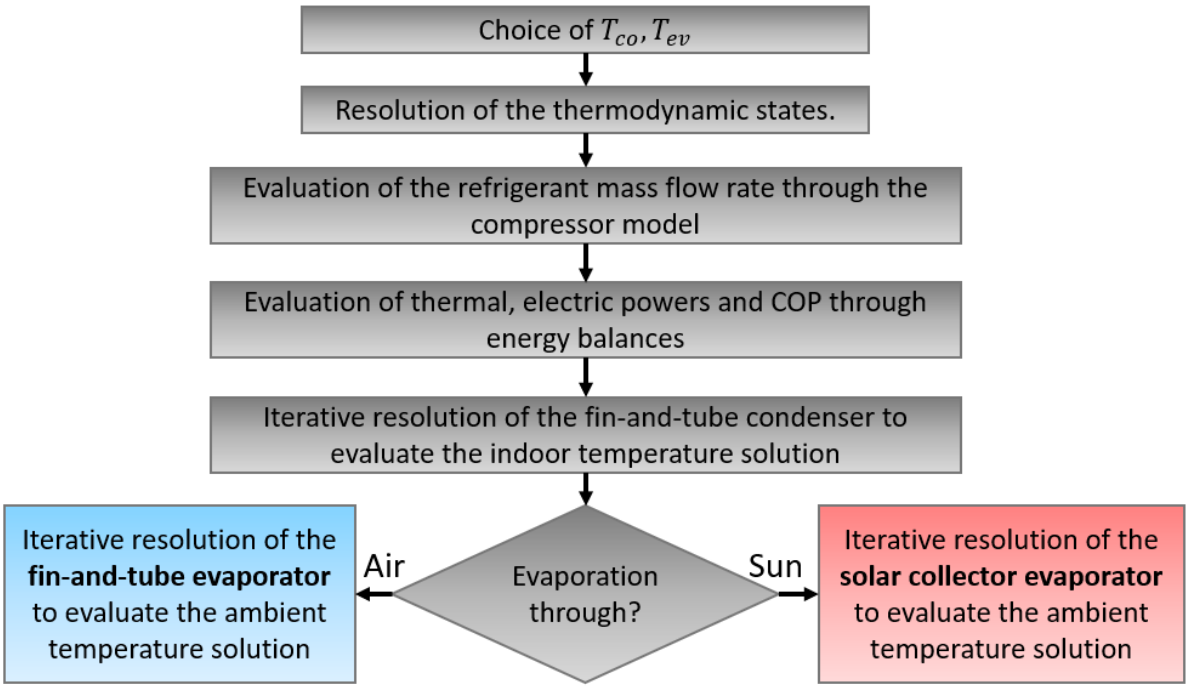


Figure 4.3. Steps of the resolution algorithm for the model of Mastrullo et al. [181]

Through the model and resolution algorithm analyzed, several values of evaporating and condensing temperature are investigated. In this way, two different functioning maps (one related to air evaporation and the other for sun evaporation) are obtained, and performance maps of COP can be obtained for both operating modes.

4.2.3 Control strategy development

Figure 4.4(a) represents the COP values depending on the ambient temperature, for respectively air-mode (dashed black lined) and sun mode (coloured lines) for different values of the solar radiation (G) between 100 and 1100 W/m^2, for fixed values of the indoor temperature of 20 °C and for 10 solar collectors. As expected, in both cases the COP increases with ambient temperature, whereas in case of sun mode the COP increases also with solar radiation. For instance, in case of an ambient temperature of 10 °C, the COP increases of approximately 38% passing from 100 to 300 W/m^2. Likewise, Figure 4.4(b) represents the COP values depending on the ambient temperature, for a number of solar panels between 2 and 15 and for a fixed solar radiation of 263 W/m^2. It can be noticed that COP increases also with the increase of solar panels. For instance, for a fixed ambient temperature of 10 °C, the COP increases of approximately 80% passing from 2 to 15 solar collectors.

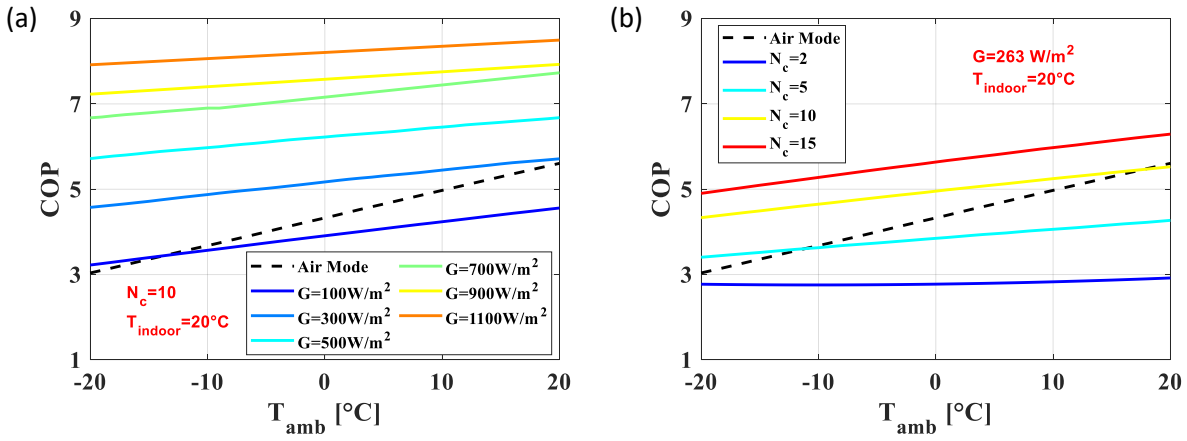


Figure 4.4. Performance maps in terms of COP values against ambient temperature in heating mode, for air (dashed black lines) and sun (coloured solid lines) evaporation modes, for a fixed indoor temperature of 20 °C. Effect of different solar radiations for 10 solar collectors (a) and effect of the number of solar collectors for a fixed solar radiation of 263 W/m^2(b)

Due to the different slopes of the COP curves in air and sun modes, for each value of the ambient temperature, it may happen that one or the other operating mode is the most convenient depending on the solar radiation. Therefore, by fixing the number of solar collectors, it is possible to identify a threshold for the solar radiation, above which it is more convenient for the machine to operate with an evaporation in solar collectors, and below which the air mode gives higher performance. In this way, the control unit of the machine switches from one to the other operating mode, in order to maximize the system performance. Curves of the solar irradiance threshold, depending on the ambient temperature and on the number of solar collectors, are reported in Figure 4.5. Results show that a higher number of solar collectors gives a lower limit above which the sun-mode is more convenient, by having fixed the ambient temperature. Furthermore, thresholds for solar radiation result to be higher for higher ambient temperatures, due to different slopes of performance curves in the two operating modes.

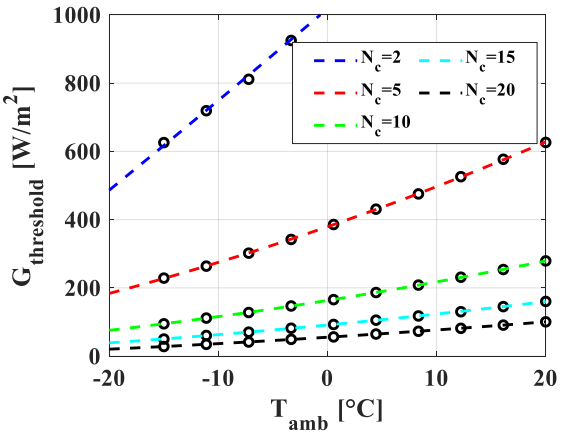


Figure 4.5. Solar radiation threshold, depending on the ambient temperature and the number of solar collectors, above which is more convenient to operate in sun mode, and below in air mode

4.2.4 Boundary conditions

Once the system control strategy is implemented to maximize the system performance, the dynamic behaviour of the heat pump is investigated in three different climate conditions of Naples, Berlin and Bergen. Climatic data have been obtained from the TRNSYS database [118]. Figure 4.6(a) shows the number of hours for each bin of temperature for the three climate conditions investigated, whereas Figure 4.6(b) represents the total horizontal radiation depending on the ambient temperature. As expected, climate of Naples is characterized by the highest ambient temperatures and solar radiation, with peaks up to 1000 W/m^2, whereas Berlin is characterized by lower solar radiation (max 900 W/m^2) and ambient temperatures. Finally, Bergen is characterized by the lowest value of solar radiation (max 800 W/m^2), and a huge number of hours for which the ambient temperature oscillates between -5 °C and 15 °C.

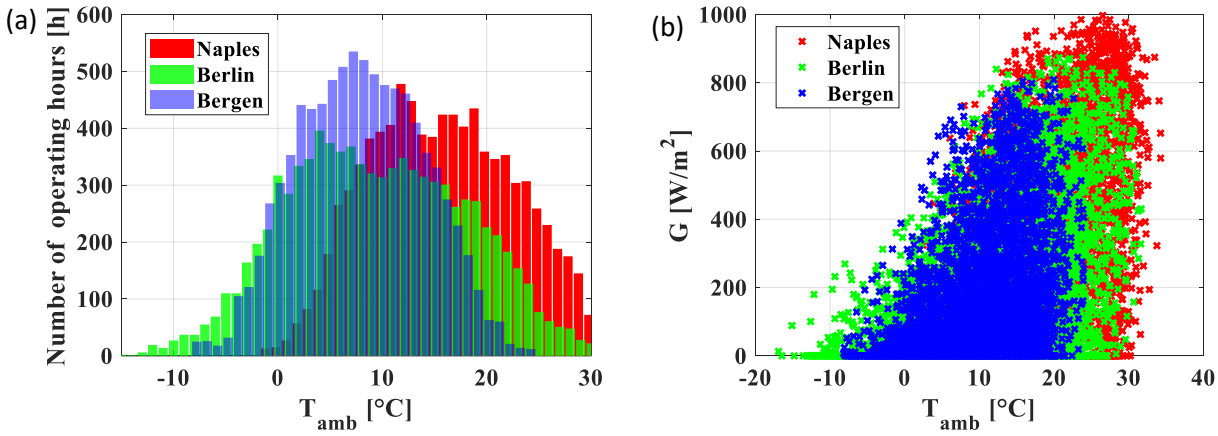


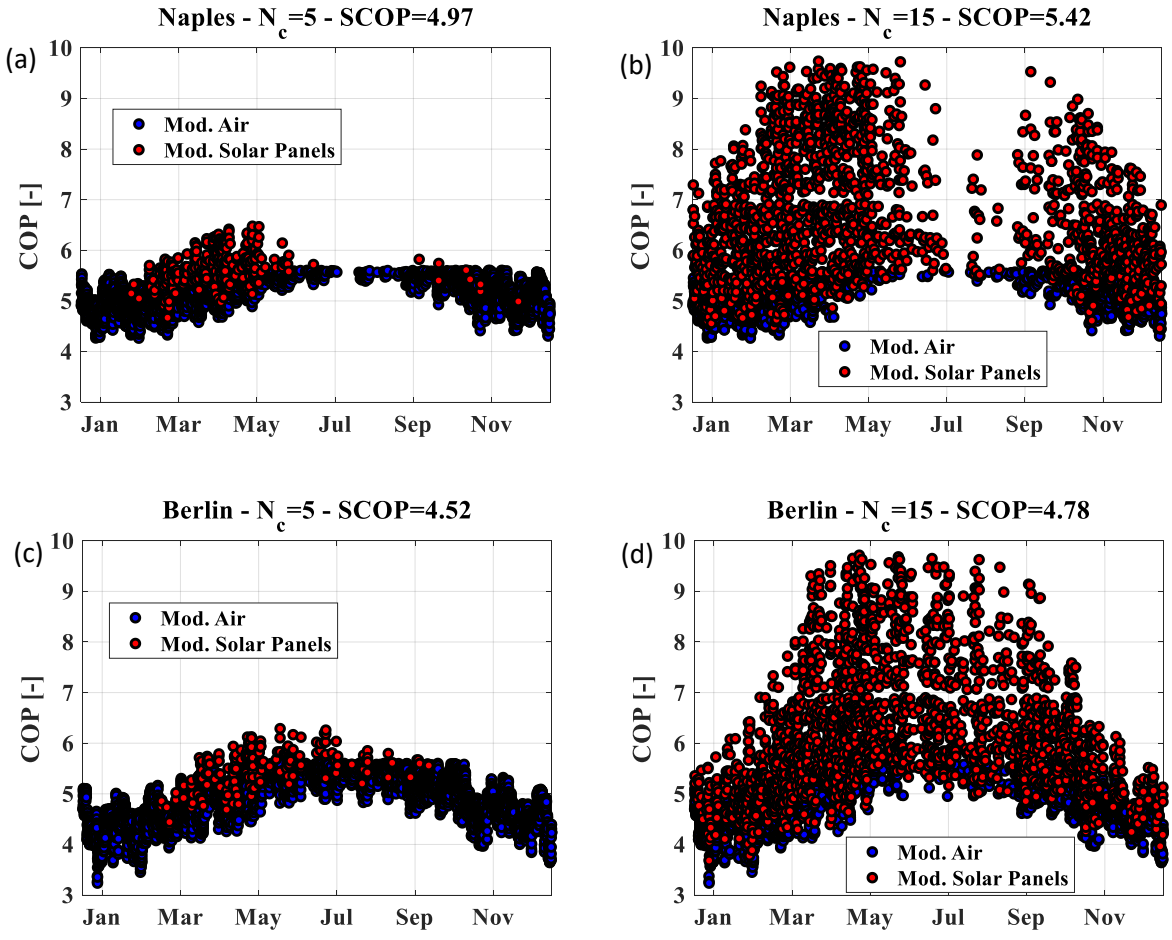
Figure 4.6. Number of operating hours (a) and solar radiation (b) vs. ambient temperature, for the climate conditions investigated of Naples, Berlin and Bergen, according to the TRNSYS meteorologic database [118]

Regarding the user, a typical user load of a commercial shop operating between 8am and 8pm is considered, to exploit the solar source as much as possible without the employment of a thermal storage. Therefore, the heat pump is considered turned on only if the ambient temperature drops below the indoor temperature, considered equal to 20 °C. For the user load evaluation through expression 4.1, $\dot{Q}_{design}$ and T_{design} are fixed respectively to 5 kW and -15 °C.

4.2.5 Results of dynamic simulations

Figure 4.7 shows the COP evolution along one entire simulation year, for all the climate conditions investigated. Operating hours in air mode are reported for both the air and sun modes, respectively in blue and red. Figure 4.7(a, c, e) are obtained for 5 solar collectors, whereas Figure 4.7(b, d, f) are related to 15 solar panels.

In case of Naples climate conditions, with 5 solar collectors, the sun mode operation hours are limited especially between the months of March and May, with the maximum COP values of 6.5 reached during the month of May. Furthermore, the machine operates in a very limited number of hours in summer months. With 15 solar collectors, higher COP values are reached, oscillating between 7 and 8 along the months of January and February, up to 9.5 in warmer months. Similar values are obtained for Berlin climate conditions, in which sun operating hours for 15 solar collectors are concentrated especially between the months of March and September. Finally, in case of Bergen for 5 solar collectors the machine operates in sun mode, especially between the months of April and August, with maximum values of approximately 6. Similarly, in case of 15 solar collectors, higher values of COP are obtained especially in warmer months, with a tighter time span compared with the cities of Naples and Berlin.



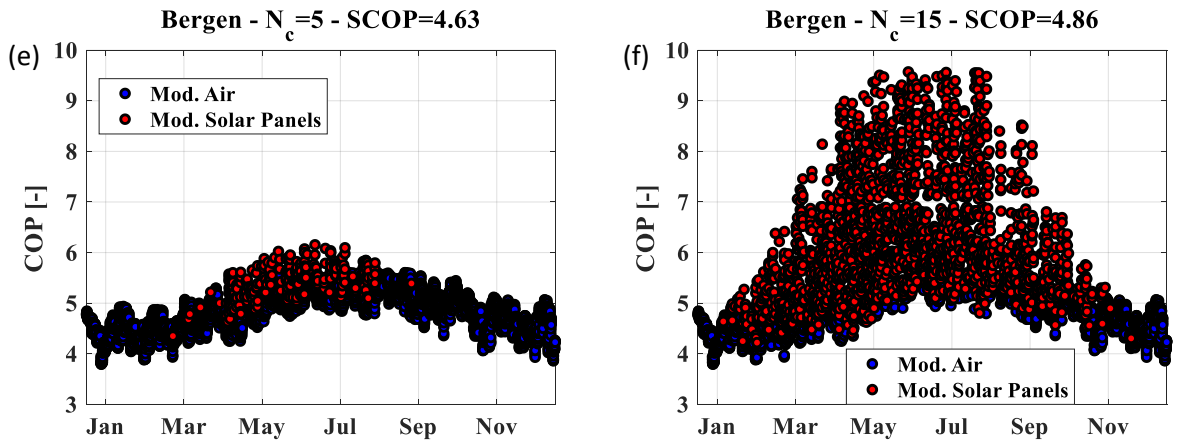


Figure 4.7. COP evolution along a year and valued of SCOP for a number of thermal solar collectors of 5 (a, c, e) and 15 (b, d, f), for the climate conditions of Naples (a, b), Berlin (c, d) and Bergen (e, f). Red points refer to the working hours of the heat pump operating in sun mode, whereas blue points are related to air evaporation working hours

The results in terms of working hours in air and sun evaporation modes, thermal energy requested by the user, electric energy consumption, seasonal coefficient of performance (SCOP), primary energy and total equivalent warming impact (TEWI), are reported in Table 4.3 for all the climate conditions investigated and for a number of solar collectors from 2 to 20. The SCOP is evaluated according to the Commission Regulation 2016/2281 [33], whereas TEWI according to the IIR Guideline for Life Cycle Climate Performance [120], as already done in section 0.

As expected, higher values of the SCOP are obtained for the warmer climate condition of Naples, whereas similar values are obtained for Berlin and Bergen. Regarding the number of hours operating in sun mode, it is never convenient to operate in sun mode with 2 solar collectors, with the SCOP that remains unchanged from the only-air configuration. With 5 solar collectors, the number of working hours in sun evaporation mode is still lower than that in air evaporation mode, whereas in case of 20 solar panels the number of hours in sun mode becomes almost 65% of the total working hours in Naples, 60% in Berlin and 50% in Bergen. Regarding instead the effect of the number of solar panels, it is influenced by two different aspects. As a matter of fact, higher performances could be achieved for climate conditions characterized by higher solar irradiance, but, on the other hand, these cities are also characterized by higher ambient temperatures, therefore having lower machine operating hours. Furthermore, usually high solar radiation hours are also characterized by lower thermal power requested by the user. Generally, between all these contrasting effects, it seems that the first is predominant, with higher performance enhancement from the sun source integration obtainable for warmer climates. As a matter of fact, the SCOP values result to be respectively 14.2%, 8.9% and 7.8%

higher for the climate conditions of Naples, Berlin and Bergen, passing from 2 to 20 solar collectors. Regarding primary energy and TEWI, the results are strongly affected by the average electricity production efficiency and the emission factor for each of the considered country. Indeed, the highest values are obtained for Germany, characterized by the lowest average electricity production efficiency and the highest equivalent emission factor, whereas the lowest values are obtained for Norway, in which most of the electric energy is nowadays produced by renewable sources. For Italy, instead, intermediate results between Germany and Norway are obtained.

Table 4.3. Numeric results of annual hours in air and sun modes, thermal and electric energy, SCOP, primary energy and TEWI depending on the number of solar collectors, for the three climate conditions investigated

Number of solar panels	**Annual hours in air-mode**	**Annual hours in sun-mode**	**Thermal energy [kWh/year]**	**Electric Energy [kWh/year]**	**SCOP**	**Primary Energy* [kWh/year]**	***TEWI* [kgCO_2]****
Naples							
2	2962	0	1823.8	368.6	4.95	769.5	1509.5
5	2700	262	1823.8	367.2	4.97	766.6	1503.9
10	1798	1164	1823.8	352.8	5.17	736.5	1445.1
15	1294	1668	1823.8	336.3	5.42	702.0	1377.7
20	1032	1930	1823.8	322.8	5.65	673.9	1322.7
Berlin							
2	3859	0	3966.1	878.1	4.52	1880.3	4009.7
5	3653	206	3966.1	877.0	4.52	1878.0	4004.9
10	2671	1188	3966.1	857.2	4.63	1835.5	3914.5
15	2033	1826	3966.1	830.1	4.78	1777.5	3790.8
20	1626	2233	3966.1	806.6	4.92	1727.1	3683.6
Bergen							
2	4632	0	4736.3	1024.0	4.63	1038.5	140.8
5	4367	265	4736.3	1021.9	4.63	1036.4	140.6
10	3433	1199	4736.3	1000.3	4.73	1014.5	137.7
15	2729	1903	4736.3	973.5	4.86	987.4	134.2
20	2253	2379	4736.3	949.9	4.99	963.4	131.1

*$\eta_{el} = 0.479$ $(Italy)$; $\eta_{el} = 0.467$ $(Germany)$; $\eta_{el} = 0.986$ $(Norway)$;

** Evaluated according to the IIR Guideline for Life Cycle Climate Performance, December 2015

4.2.6 Economic analysis

To understand if the advantage in terms of seasonal performances obtainable with the exploitation of the solar source influences costs, an economic analysis on the analyzed system is carried out. The main target is to identify the optimal configuration in terms of number of solar collectors that minimize the total costs of the systems in the two contributions of investment costs for the system purchase and of the operating costs of the machine. Investment costs are evaluated considering a fixed contribution for the heat pump of 233 €/kW, according to the Summerheat Publishable Report, 2009 [183], multiplied by the rated heating capacity of the machine of 5 kW, and the purchase cost for solar collectors, evaluated according to Ferreira et al. [184], with the following expression:

$$C_{col} = C_{ref} \cdot A_{ref} \cdot \left(\frac{A_{col}}{A_{ref}}\right)^{b_{solar}} \cdot \eta_0^{\gamma} \cdot a_1^{v} \cdot \frac{1}{DF} \ [€/year] \tag{4.4}$$

C_{ref}, A_{ref} are the reference collector cost and surface, equal to respectively 298.5 €/m^2 and 2.50 m^2, whereas b_{solar} is a scale coefficient equal to 0.5. γ and v are coefficient calibrated on real manufacturer data and are set respectively to 1.2 and -0.04, whereas DF is the discount factor evaluated considering a 12-year lifetime of the machine and a discount rate of 5%. Running costs are evaluated considering electricity specific costs given by the European Community [185], of 0.26 €/kWh, 0.37 €/kWh and 0.13 €/kWh respectively for Naples, Berlin and Bergen.

Results in terms of investment, operating and total costs are reported in Figure 4.8 as a function of the number of solar collectors, for respectively the climate conditions of Naples (Figure 4.8(a)), Berlin (Figure 4.8(b)) and Bergen (Figure 4.8(c)). Despite the investment costs depend only on the number of solar collectors and are increasing as expected, the operating costs depend also on the climate condition investigated. In fact, these are lower in the city of Naples and higher for Berlin due to the higher number of working hours of the second case. In Bergen, instead, the operating cost is intermediate between Naples and Berlin, due to the contrasting effect of higher number of hours but lower energy specific cost. Furthermore, the operating costs slight decrease with the increase of the solar collector, due to a higher performance and a lower energy consumption of the machine. In the end, in terms of total costs, it can be noticed that the minimum value is always obtained for an only-air system configuration without the employment of solar panels. As a matter of fact, it seems that, with the current scenario in terms of investment costs and energy prices, the advantages obtained in terms of energy saving with

the exploitation of the solar source are not balanced by the extra investment cost for solar collectors, for all the climate conditions investigated.

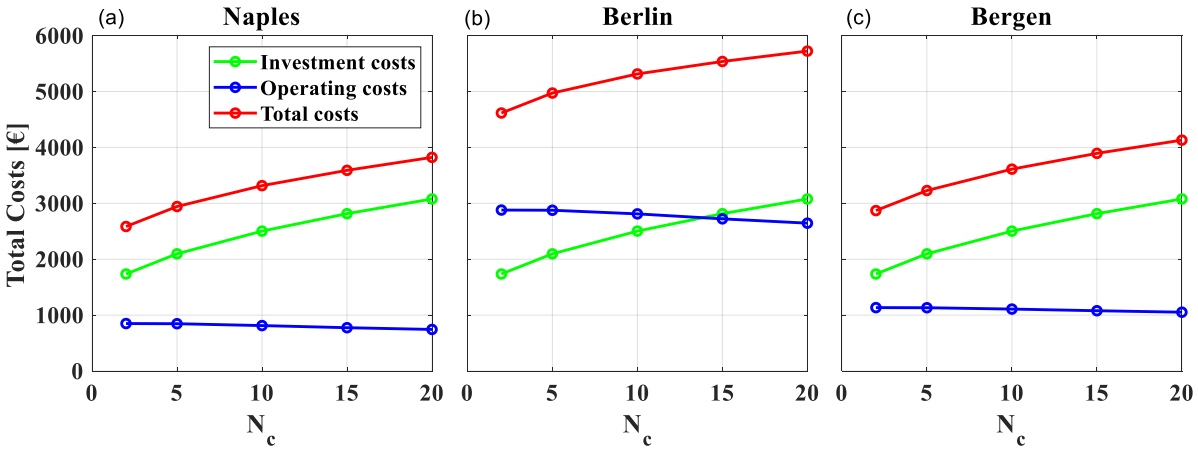


Figure 4.8. Investment, operating and total costs results depending on the number of thermal solar panels, for Naples (a), Berlin (b) and Bergen (c) climate conditions

Finally, the results of total costs are represented depending on the corresponding seasonal coefficient of performance in Figure 4.9(a), and the corresponding total equivalent warming impact in Figure 4.9(b). For each climate conditions the diamonds refer to the "only-air" configuration, whereas the circles, squares, triangles and stars are representative of respectively the conditions with 5, 10, 15 and 20 solar collectors. It can be noticed that, with the employment of solar collectors, higher total costs are always obtained compared with the only-air configuration if no incentives on investment costs or energy price are considered. Furthermore, the SCOP seems not to be particularly affected by a number of solar collectors lower than 10. Results in terms of TEWI instead are mainly affected by the electricity production efficiency and the emission factor for each country investigated.

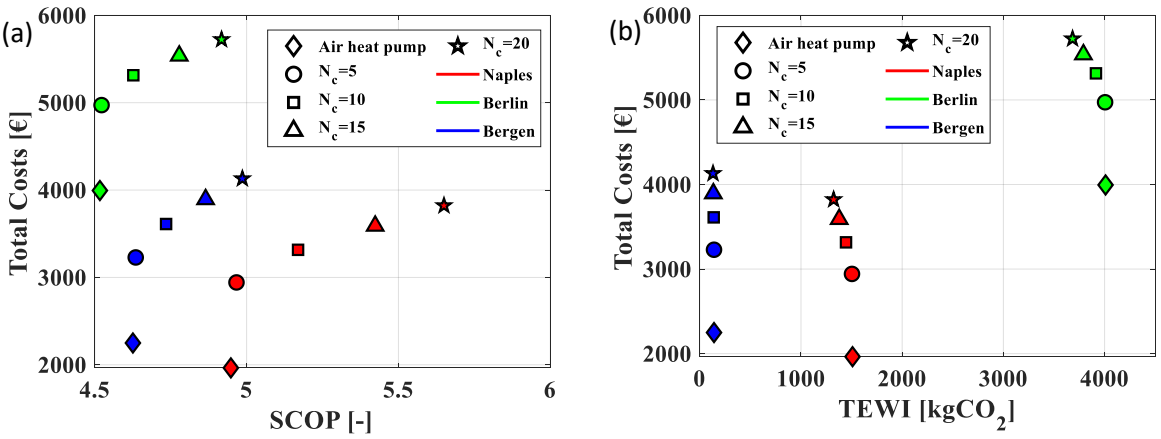


Figure 4.9. Total costs vs. SCOP (a) and vs. TEWI (b) for all the configurations and climate conditions investigated. The diamonds refer to the baseline configuration of a traditional air-to-air heat pump

Definitely, these results show that systems integrating the possibility of evaporation through the solar source seem to be currently thermodynamically but not economically convenient compared with traditional heat pumps. Nevertheless, more convenience could be obtained if different scenarios in terms of purchase cost and energy prices are analyzed, and if a thermal storage is employed, as will be analyzed in further sections.

4.3 Case study 2: 10 kW indirect expansion multi-source heat pump for residential heating

As a second case study, a 10 kW indirect expansion multi-source heat pump for residential heating, whose results are published in the works of Pelella et al. [186] [187], is analyzed in this section. The system is modelled to answer two different questions. The first target is to understand if it is convenient to integrate traditional heat pumps with other kinds of multiple energy sources, considering not only the solar source but also the ground one. The second aim is instead to identify if the employment of a thermal storage, if water type or PCM type, can guarantee an advantage in terms of decoupling the solar source availability and the energy request by the user.

4.3.1 Component model

A scheme plant for the system modelled is provided in Figure 4.10. The studied system is composed of three different loops: the solar loop (showed in red), heat pump loop (in green) and ground loop (in blue). The solar loop is composed of thermal solar collectors, a thermal storage tank, which can be sensible or latent, and a circulating pump, named P_1 in the schematic. The heat pump loop instead is composed of a scroll compressor, two evaporators, one fin and tube-type (in light blue) and one plate type (dark green), one fin-and-tube condenser and a thermostatic expansion valve, able to control evaporator outlet superheating. Finally, the ground loop is composed of a horizontal ground heat exchanger, and of a fixed speed circulation pump named P_2 in the scheme, which is shared with the solar source. The system is also equipped with photovoltaic solar panels, able to produce electric energy which can be stored in a battery, retailed to the grid and used to feed the heat pump and all the electric auxiliaries such as circulating pumps and the heat exchanger fan. All the electrical connections are reported in the scheme plant with dashed black lines. The heat pump employs propane as refrigerant fluid, whose pipelines are indicated in light-blue, whereas the heat transfer fluid in all the other parts of the system is water, whose pipelines are represented with continuous black lines. The storage tank is equipped with only one coil, through which charging and discharging processes may occur alternatively, due to the intervention of the two thee-way switching valve situated on the

tank pipeline branch. Other two- and three-way valves are employed to guarantee a correct feeding of the heat transfer fluids in the pipelines. Although the system analyzed seems to be very complex, it has to be clarified that this scheme is conceived to simulate different configurations between one-source, two-sources and three-sources exploitation, and it is not necessarily related to a real system. For instance, an only air source configuration can be considered if the solar collectors, the storage tank, the water evaporator and the ground heat exchanger are absent, with the heat pump evaporation which occurs through air. An only sun configuration can be simulated in case of absence of the ground heat exchanger and of the air evaporator, with the heat pump evaporation occurring through the water coming from the storage tank. An only-ground configuration instead occurs in case of absence of solar thermal collectors and the air evaporator, with the heat pump evaporation occurring through the water coming from the ground heat exchanger. For simplicity, the three operating modes will be referred as air, sun and ground evaporations in this section. Two-sources and three-sources configurations came from the combination of one-source schemes, considering the employment of several of the system components reported in Figure 4.10. Finally, a direct connection between the solar loop and the user allows the direct feeding of the user requested load through the solar radiation. The control strategy for the system analyzed is reported in the following section.

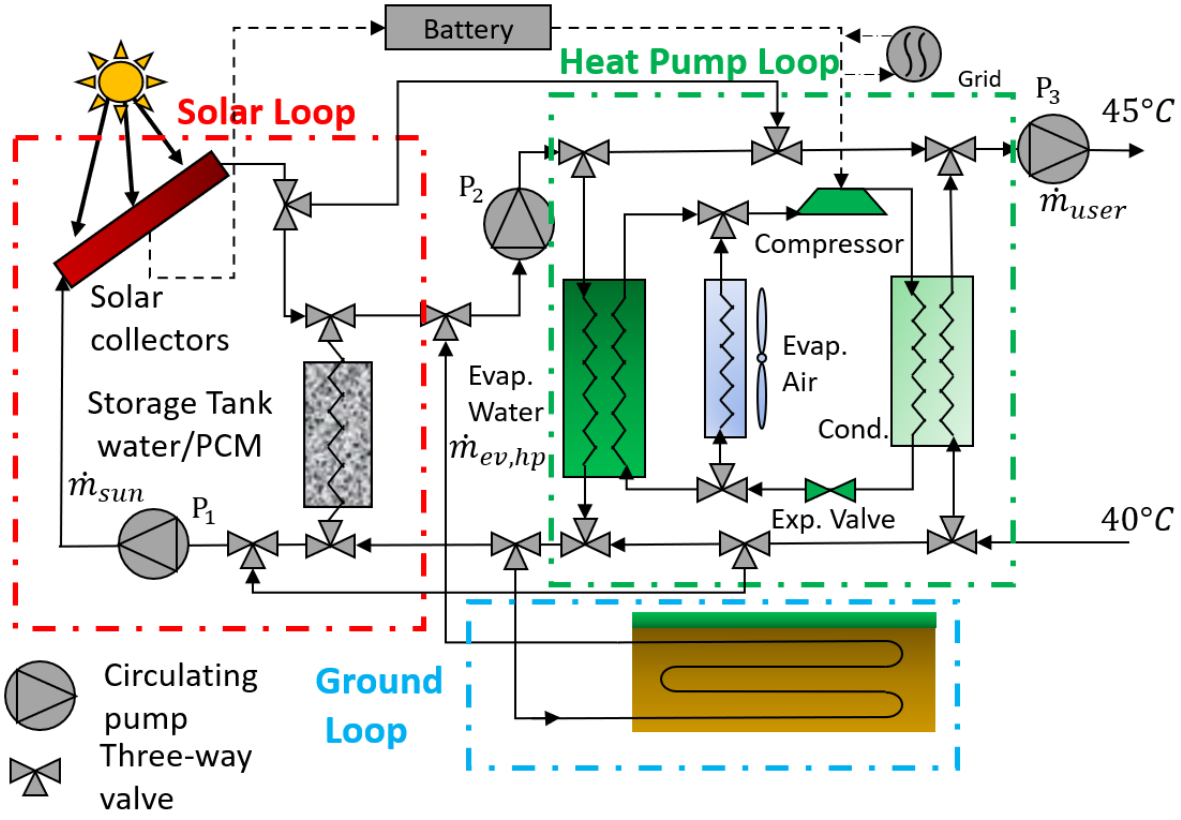


Figure 4.10. Schematic of the system analysed in Pelella et al. [186], conceived to simulate all the possible configurations of multi-source (sun, ground, air) heat pump considered

In the following sections, sub-models for each of the system components are presented, for each of the loops analyzed. For the heat pump loop, models for the compressor and the heat exchangers have been developed, whereas the expansion valve is considered well designed in order to guarantee the same mass flow rate of the compressor, and a fixed evaporator superheating of 7 °C. For the solar loop instead models for solar thermal and photovoltaic collectors, and for the storage tank have been developed.

4.3.1.1 User Load

Regarding the user load, its value is evaluated according to the Commission Regulation (EU) 2016/2281 [33], as already done in section 4.2.1.1. A 120-h moving average is considered to simulate the building inertia effect on the user load. In this way the user load results to be attenuated by the building inertia, therefore avoiding a useless oversize of the machine. An example of the instantaneous (black) and attenuated by the inertia of the building (red) user requested load is provided in Figure 4.11.

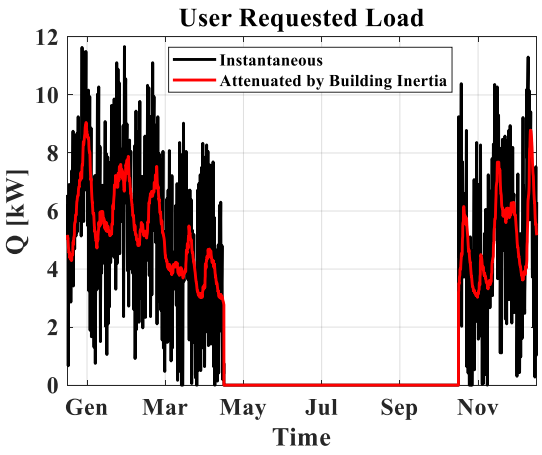


Figure 4.11. User requested load evolution along a year. Instantaneous evaluated through expression 4.1 (black line), and attenuated by building inertia (red line)

The thermal load is delivered though the circulating pump P_3, which varies the water mass flow rate in order to guarantee fixed values for supply and return water temperatures of respectively 45 °C and 40 °C.

4.3.1.2 Compressor and heat exchangers

For the compressor, the electrical power is evaluated similarly to what already done in section 3.2.1.1, with the compressor efficiency calibrated on manufacturer data. Regarding the mass flow rate, it is evaluated to always satisfy the thermal load requested by the user, in order to have a system well designed able to always satisfy the user needs and therefore adapting the compressor displacement and cost.

For the heat exchangers, both of fin-and-tube and plate types, the temperature profiles of both primary and secondary fluids are iteratively calculated considering a modified logarithmic mean temperature difference (F – LMTD) approach, using the following relation:

$$\dot{Q}_{hex} = F \cdot U \cdot A \cdot \Delta T_{ml} \tag{4.5}$$

The correction factor F depends on the coefficients R_1, R_2, P_1, P_2 defined respectively as:

$$R_1 = \frac{\dot{C}_1}{\dot{C}_2} = \frac{\Delta T_2}{\Delta T_1} \quad R_2 = \frac{\dot{C}_2}{\dot{C}_1} = \frac{\Delta T_1}{\Delta T_2} \tag{4.6}$$

$$P_1 = \frac{\Delta T_1}{\Delta T_{max}} = \frac{T_{1,in} - T_{1,out}}{T_{1,in} - T_{2,in}} \quad P_2 = \frac{\Delta T_2}{\Delta T_{max}} = \frac{T_{2,out} - T_{2,in}}{T_{1,in} - T_{2,in}} \tag{4.7}$$

$\Delta T_1, \Delta T_2$ and ΔT_{max} are respectively the inlet, outlet and maximum temperature differences of the analyzed heat exchangers. Expressions for the evaluation of factor F, according to Shah and Sekulic [110], are reported in Table 4.4, depending on the typology of heat exchanger investigated.

Table 4.4. Expressions for the evaluation of coefficient F of the equation 4.6, depending on the flow arrangement of the heat exchanger, according to Shah and Sekulic [110]

Flow Arrangement	Expression
Counterflow	$F = 1$
Parallelflow	$F = 1$
Crossflow (single-pass)	
Fluid 1 unmixed, fluid 2 mixed, stream asymmetric	$F = \frac{ln\left[(1-R_1P_1)/(1-P_1)\right]}{(R_1-1)ln\left[1+(1/R_1)ln\left(1-R_1P_1\right)\right]}$ $= \frac{ln\left[(1-R_2P_2)/(1-P_2)\right]}{(1-1/R_2)ln\left[1+R_2ln\left(1-P_2\right)\right]}$
Fluid 1 mixed, fluid 2 unmixed, stream asymmetric	$F = \frac{ln\left[(1-R_1P_1)/(1-P_1)\right]}{(1-1/R_1)ln\left[1+R_1ln\left(1-P_1\right)\right]}$ $= \frac{ln\left[(1-R_2P_2)/(1-P_2)\right]}{(R_2-1)ln\left[1+1/R_2ln\left(1-R_2P_2\right)\right]}$
1-2 TEMA E, shell fluid mixed stream symmetric	$F = \frac{D_1 ln\left[(1-R_1P_1)/(1-P_1)\right]}{(1-R_1)ln\frac{2-P_1(1+R_1-D_1)}{2-P_1(1+R_1+D_1)}}$ $= \frac{D_2 ln\left[(1-R_2P_2)/(1-P_2)\right]}{(1-R_2)ln\frac{2-P_2(1+R_2-D_2)}{2-P_2(1+R_2+D_2)}}$ Where $D_1 = (1+R_1^2)^{1/2}$ and $D_2 = (1+R_2^2)^{1/2}$
All exchangers with $R_1 = 0$ or ∞	$F = 1$

For the evaporator, the heat transfer surface is divided into the two contributes of evaporating and superheating surfaces, and for each of them, the F-LMTD method has been applied, considering averaged values for the heat transfer conductance.

$$A_{ev,tot} = A_{ev} + A_{sh} \tag{4.8}$$

$$A_{ev} = \frac{\dot{Q}_{ev}}{\overline{U}_{ev} \cdot \Delta T_{ml,ev} \cdot F} \qquad A_{sh} = \frac{\dot{Q}_{sh}}{\overline{U}_{sh} \cdot \Delta T_{ml,sh} \cdot F} \tag{4.9}$$

For the evaluation of $\overline{U}_{ev}$, the refrigerant HTC is evaluated through the correlation of Longo et al. [188] in case of a plate evaporator, and through the model of Gungor and Winterton [111] in case of a fin-and-tube evaporator. For the evaluation $\overline{U}_{sh}$, refrigerant HTC is instead calculated through the relation of Dittus and Boelter [114]. Water HTC is evaluated with the model of Martin [189], in case of a plate heat exchanger, whereas for a fin-and-tube heat

exchanger air HTC is calculated through Wang and Chi correlation [115] for plain fins. In all cases, pressure drops have been neglected. An example of evaporator temperature profiles, in case of water as secondary fluid, is provided in Figure 4.12(a).

For the condenser, the total heat transfer surface is split into the two contributions of condensing and de-superheating areas, similarly to the evaporator. Each contribution is evaluated as follows:

$$A_{co,tot} = A_{co} + A_{desh} \tag{4.10}$$

$$A_{co} = \frac{\dot{Q}_{co}}{\overline{U}_{co} \cdot DT_{ml,co} \cdot F} \qquad A_{desh} = \frac{\dot{Q}_{desh}}{\overline{U}_{desh} \cdot DT_{ml,desh} \cdot F} \tag{4.11}$$

$\overline{U}_{co}$ is evaluated considering the refrigerant HTC calculated through the Shah [113] correlation, whereas for $\overline{U}_{desh}$ refrigerant HTC is evaluated with the model of Dittus and Boelter [114]. Similarly, as before, water HTC is obtained with the model of Martin [189]. An example of condenser temperature profiles is provided in Figure 4.12(b).

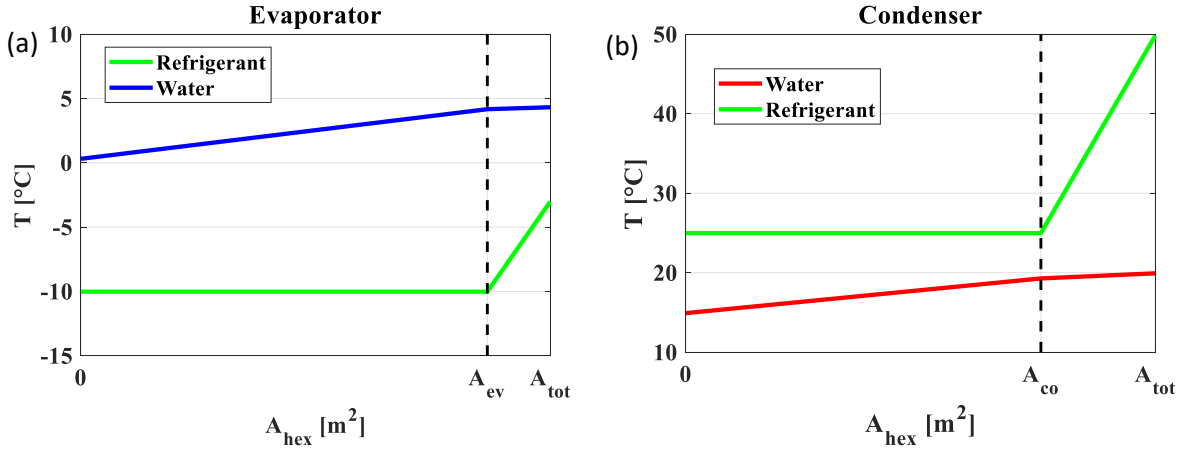


Figure 4.12. Temperature profiles at the evaporator (a) and at the condenser (b), depending on the heat transfer surfaces for evaporating, condensing, superheating and de-superheating

4.3.1.3 Ground heat exchanger

For the ground loop, it is assumed a horizontal infinite surface heat exchanger, in order to have the water outlet temperature equal to the ground temperature to a certain depth. The ground temperature is evaluated through the model of Krarti et al. [190], considering the following expression:

$$T_{ground,z} = T_{ground,z=0} \cdot exp\left(-\frac{z}{6}\right) \cdot sin\left(\omega \cdot t + \phi_s + \frac{z}{\delta}\right) \tag{4.12}$$

$T_{ground,z}$ and $T_{ground,z=0}$ are respectively the ground temperature at a certain depth z and superficial. ω is the period of the oscillation (1 year), ϕ_s is the delay between the external and

the ground temperature trend. $T_{ground,z=0}$ and ϕ_s are evaluated depending on external conditions of temperature, solar radiation, soil properties (density, specific heat, thermal conductivity), shading factor and humidity of the soil. Finally, δ is a coefficient depending on soil properties as well.

Therefore, the model gives a ground temperature as shift and attenuation of the external temperature, depending on solar radiation and other external factors. For instance, Figure 4.13 shows external conditions in terms of solar radiation, ambient and ground temperatures, for climate conditions of Naples, in which it can be noticed the delay and the attenuation between the black and green lines.

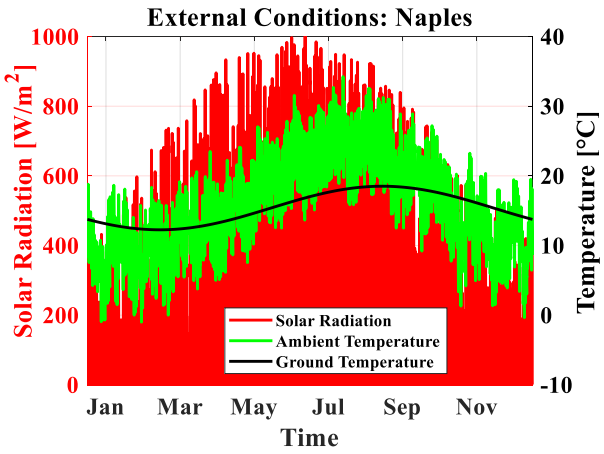


Figure 4.13. Evolution of ambient temperature (green line), solar radiation (red lined) and ground temperature (black line) evaluated with the model of Krarti et al. [138], for external climate conditions of Naples

4.3.1.4 Thermal and photovoltaic solar collectors

Regarding the thermal solar collectors, the definition of the solar panel efficiency (η_{pan}) according to Hottel – Whiller – Bliss [182] equation is used, as already done in section 4.2.1.3. Furthermore, it is assumed that the outlet temperature of the water from solar collectors is always equal to the temperature requested by the user, with the circulating pump P_1 able to vary accordingly the mass flow rate through thermal solar collectors.

Regarding the solar photovoltaic panels, a definition of solar panel efficiency has been introduced similarly to thermal collectors, according to Skoplaki and Palyvos [191]. Therefore, the available electrical power can be evaluated depending on solar radiation as:

$$\dot{W}_{el,pv} = G \cdot A_{pv} \cdot \eta_{pv} \tag{4.13}$$

Solar panel efficiency depends, in turn, on the actual solar radiation and on the surface temperature of the solar collector, and trends are usually fitted on manufacturer data depending on the solar panel technology. For instance, Figure 4.14 shows the observed trend for the

photovoltaic efficiency for a mono-crystalline solar collector, depending on solar radiation and for different number of surface temperature.

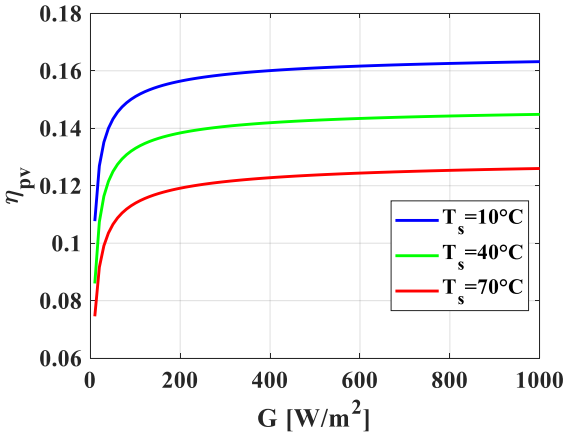


Figure 4.14. Example of photovoltaic solar collector efficiency, according to Skoplaki and Palyvos [191], depending on the solar radiation and on the surface temperature of the collector

A storage battery for the photovoltaic system has been considered as well. This component is modelled considering a charging process when the electrical energy from photovoltaic collectors is available, and a discharging process when the electric energy is used to feed the heat pump or the system auxiliaries. All kinds of electrical losses are neglected in this work.

4.3.1.5 Storage Tank

For the storage tank, a water/water or water/PCM encapsulated heat storage is considered. Therefore, the component is modelled with the approach of Zsembinszki et al. [192] [193]. The elementary geometry presented by the authors is shown in Figure 4.15, and it is composed of three different layers: the first refers to the heat transfer fluid (HTF, water in this case), the second is the wall and the third could be water or PCM depending on if the considered thermal storage is sensible or latent. The last two layers are divided into several elements depending on the number of nodes chosen for each layer. Therefore, a certain number of elementary geometries are considered, to reach a fixed certain value of the storage tank volume.

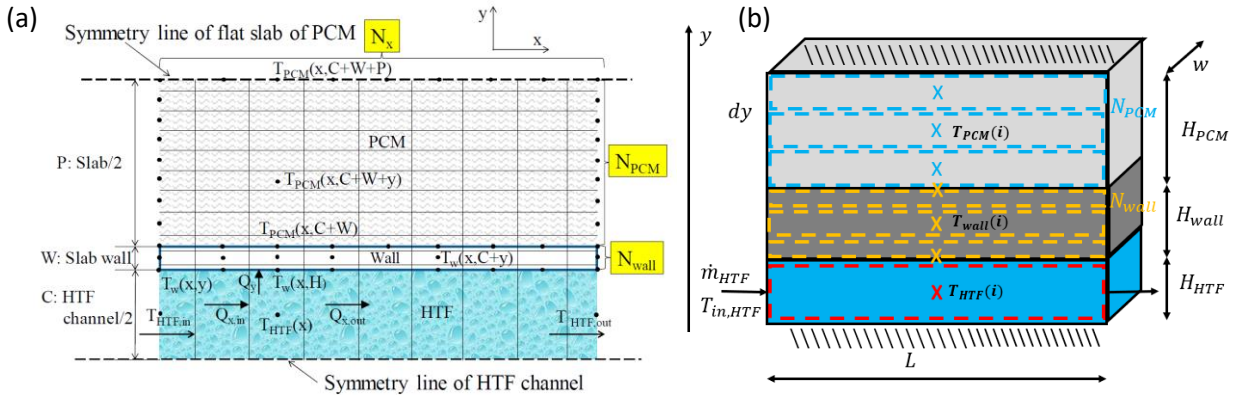


Figure 4.15. Elementary geometry of the PCM storage tank model of Zsembinszki et al. [192], [193] (a) and for the 1D version of the model employed in this work (b)

In case of a water thermal storage, thermodynamic properties depending only on temperature are considered. In case of employment of a PCM instead, a constant density and thermal conductivity have been assumed. Furthermore, fixed values for the specific heat are considered in a temperature range far from the melting point, whereas in proximity to the melting point an adequate specific heat curve has been adopted, according to PCM manufacturer data [194]. An example of the specific heat curve depending on the actual PCM temperature is shown in Figure 4.16, for a melting temperature of 25 °C.

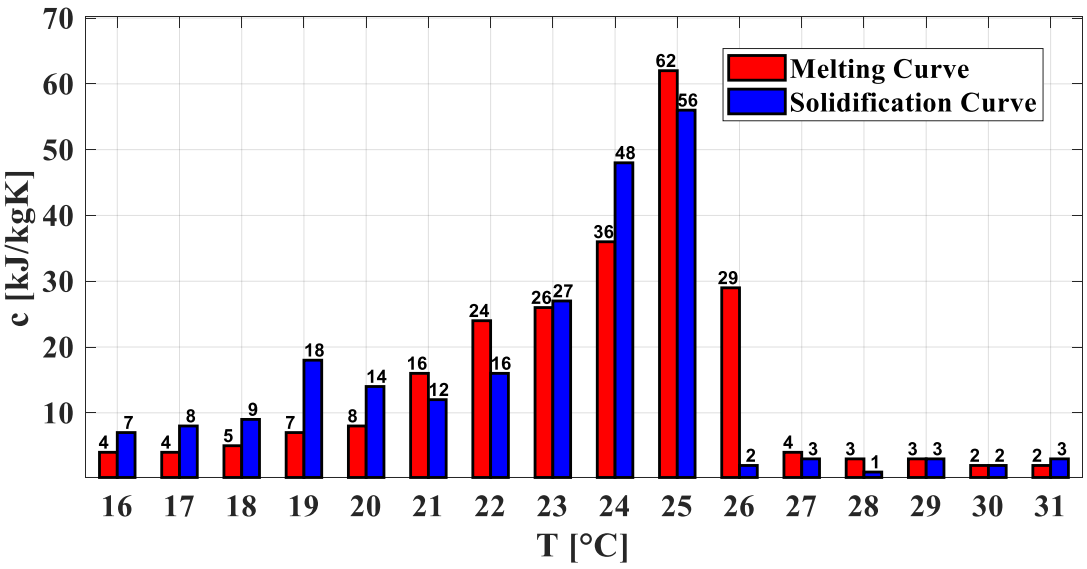


Figure 4.16. Specific heat capacity for the considered PCM material depending on the temperature level, in case of a melting temperature of 25 °C, according to PCM manufacturer data [141]. Melting and solidification curves are respectively reported in red and blue

A simplified version of the literature model, implicit and 1D along the y-direction is implemented in this work. In this specific case, the elementary geometry is shown in Figure 4.15(b). As further shown in section 4.3.5, it is demonstrated that the differences in terms of the yearly energy consumption and of the seasonal coefficient of performance between the 2D

validated model and the 1D version are less than 2.5%, with the 1D model which is able to guarantee a 30 second average time saving. Energy balances equations in an implicit form for generic control volumes i, related respectively to HTF, wall and PCM layers and indicated in Figure 4.15(b), are the following:

$$\left(h_{HTF}A + \frac{2k_{HTF}A}{H_{HTF}}\right)\left[T_{wall}(1,t) - T_{HTF}(t)\right] + \dot{m}_{HTF}c_{HTF}\left[T_{in,HTF} - T_{HTF}(t)\right] = m_{HTF}c_{HTF}\frac{\left[T_{HTF}(t+1) - T_{HTF}(t)\right]}{d\theta} \quad (4.14)$$

$$\frac{k_{wall}A}{dy_{wall}}\left[T_{wall}(i-1,t) + T_{wall}(i+1,t) - 2T_{wall}(i,t)\right] = dm_{wall}c_{wall}\frac{\left[T_{wall}(i,t+1) - T_{wall}(i,t)\right]}{d\theta} \quad (4.15)$$

$$\frac{k_{PCM}A}{dy_{PCM}}\left[T_{PCM}(i-1,t) + T_{PCM}(i+1,t) - 2T_{PCM}(i,t)\right] = dm_{PCM}c_{PCM}\frac{\left[T_{PCM}(i,t+1) - T_{PCM}(i,t)\right]}{d\theta} \quad (4.16)$$

4.3.2 System control strategy

A system control strategy is developed in order to establish in which operating mode the machine should operate, in order to maximize the system performance. Although the system may assume different configurations depending on the components employed, in this section the more general control strategy is described, considering therefore a system in its most complete configuration. The whole control strategy is shown in Figure 4.17.

A first level of the control strategy aims to manage the water mass flow rates related to the user side and to the solar loop. Regarding the user, the water mass flow rate is adjusted to have 40-45 °C as return and supply temperatures to the user if a thermal load is requested, otherwise the mass flow rate becomes zero. Similarly, regarding the solar loop, if a solar radiation is available, the collector mass flow rate is adjusted to have the same supply temperature of 45 °C to the user. Furthermore, the solar collector circulation pump P_1 is stopped if the temperature of the bottom part of the tank overcomes 40 °C, symptom of a completely charged storage system.

At this point, once user and solar mass flow rates are evaluated, the two thermal loads are compared each other. If the available solar thermal power is enough to satisfy the user needs, the user water flow rate $\dot{m}_{user}$ is taken directly by solar collectors, with the heat pump not operating, whereas the remaining part, equal to ($\dot{m}_{col}$-$\dot{m}_{user}$), is used to charge the storage tank through the opening of the three-way valves on the tank pipeline branch. Otherwise, if the solar thermal power is not able to satisfy all the user requested load, the remaining part ($\dot{Q}_{user}$-$\dot{Q}_{sun}$) is supplied by the heat pump, which is turned on. The second part of the control strategy aims to establish in which mode the heat pump should operate to maximize the system performance. As a matter of fact, if the COP in air evaporation mode is higher than the one in water evaporation mode, or the water temperature drops below 6 °C, in order to avoid freezing

problems in pipelines, the heat pump operates in air evaporation mode. Otherwise, the heat pump may operate in sun or in ground mode, depending on if the return temperature from the ground is higher or lower than the temperature of the storage tank. Finally, if the heat pump operates in sun evaporation mode, water returns from the user to the storage tank, which is discharged.

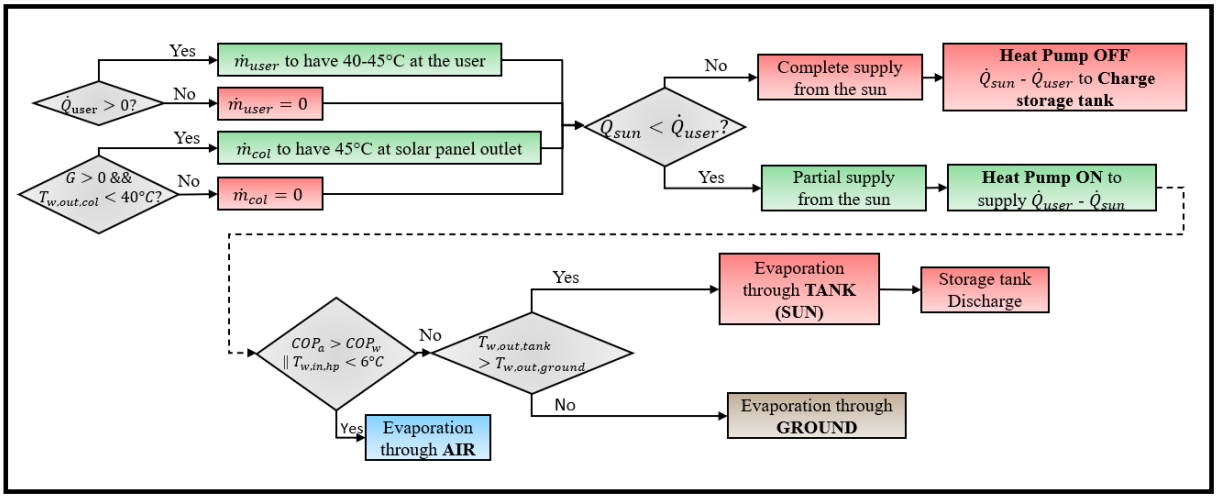


Figure 4.17. System control strategy for the solar loop, the user loop and the heat pump

Another control strategy, which operates in parallel with the one described above, is developed for the photovoltaic system and the storage battery, and it is shown in Figure 4.18. Particularly, during the charging process, which occurs only for a nonzero photovoltaic power, if the state of charge (SOC) of the battery is full, then the system is able to sell the exceeded energy to the grid, otherwise the energy is stored in the battery. In case of discharging, with the energy delivered to the heat pump or other electric appliances, if the SOC of the battery is empty, the energy is withdrawn from the grid, otherwise the energy of the battery is used.

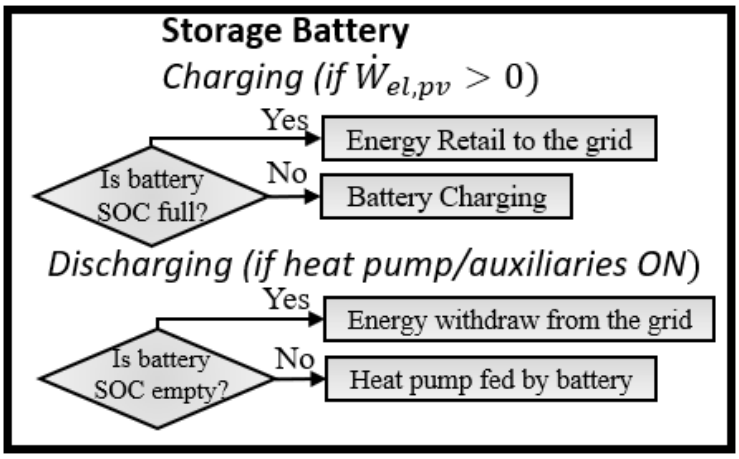


Figure 4.18. System control strategy for the storage battery

4.3.3 Resolution algorithm

To match all the described sub-models and therefore to simulate the behaviour of the entire system, a resolution algorithm is developed. All the steps reported in Figure 4.19 consider the most general system configuration, so employing all the components analyzed. The model has been implemented in MATLAB [106], and thermodynamic properties have been evaluated through REFPROP [107]. Considering as inputs the external temperature and solar radiation of a certain timestep t, and fixing initial conditions, firstly the user model is solved to evaluate the requested load. If available, photovoltaic panels are solved to evaluate the produced electric energy, and consequently the battery model is solved in charging mode. Similarly, the solar thermal available load is evaluated through the thermal collectors model. At this point, if the available thermal solar power is higher than the load requested by the user, the storage tank mode is solved in charge mode to evaluate temperatures at t+1 timestep. Otherwise, the ground model is employed to evaluate the ground temperature evolution if the geothermal heat exchanger (GHE) is present. Therefore, the heat pump is solved in all the operating modes between sun, air and ground evaporation, selecting the one which gives the highest value for COP. Only if the sun mode gives the highest COP, the storage tank model is solved in discharge mode. Finally, the energy consumptions for all the employed components between the heat pump and electric auxiliaries, the energy productions, withdraws and retails with the grid have been evaluated at the timestep t, before passing to solve the next timestep. The electric storage battery model is solved in discharge mode if the photovoltaic system is employed.

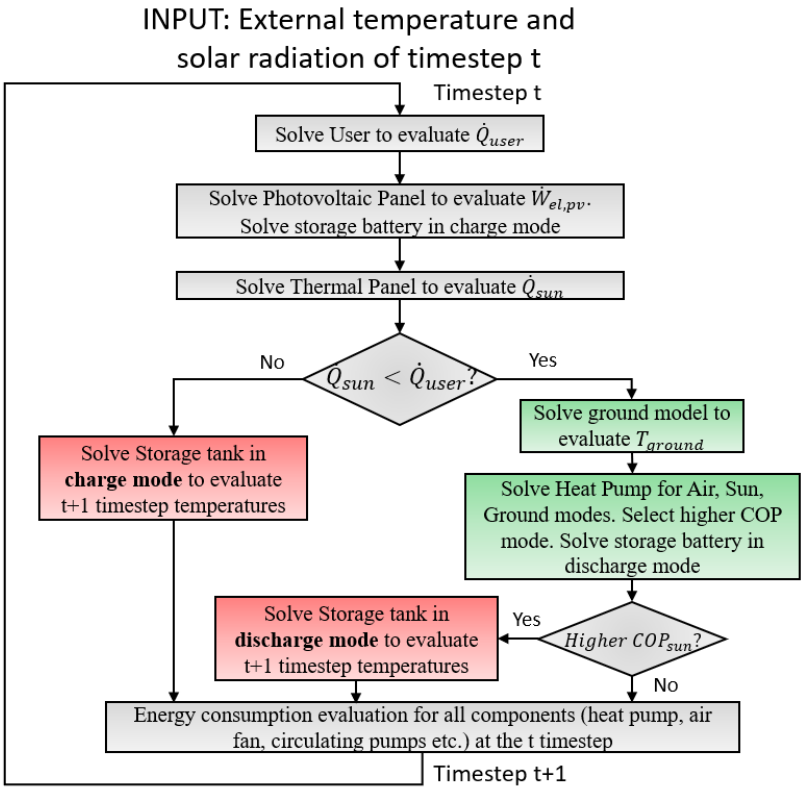


Figure 4.19. Steps for the resolution algorithm used to simulate the entire system, coupling single component models of Pelella et al. [186]

4.3.4 Case study, boundary conditions and optimization data

4.3.4.1 Case study data and boundary conditions

The model is applied to a case study for domestic space heating. Main data and characteristics of the system analyzed are reported in Table 4.5. For the PCM material, properties such as specific heat, density and thermal conductivity, both within and outside the melting zone, have been collected from manufacturer data [194].

Table 4.5. Main rated characteristics of the case study, and simulation data

Parameter	Value	Parameter	Value
$\dot{Q}_{design}[kW]$	10	$z_{ground}[m]$	2
$T_{design}[°C]$	-5	$T_{indoor}[°C]$	20
$\dot{V}_{ev,a}[m^3/h]$	2000	$\dot{m}_{ev,w}[kg/s]$	0.30
$T_{w,in,user}[°C]$	45	$T_{w,out,user}[°C]$	40
η_{fan}	0.65	η_{pump}	0.80
L/H_{tank}	3	$\rho^*_{PCM}[kg/m^3]$	880
$c^{**}_{PCM}[kJ/kgK]$	2	$k^*_{PCM}[W/mK]$	0.2
Number of hours considered per simulation [h]	8760	Simulation step [h]	1
*Considered constant for all the temperature range ** Constant only outside the melting range temperature			

Regarding the climate conditions, the three standard ones decided by the European Community of Athens, Strasbourg and Helsinki have been considered for dynamic simulations. For all of them, the number of operating winter months for the analyzed heat pump is chosen to cover approximately the 80% of the hours in which the external temperature drops below the indoor temperature of 20 °C. In this way, the heating season for the climate conditions of Athens has been considered between the months of November and April, whereas in Strasbourg and Helsinki between the months of September and May. Values of the number of operating hours and solar radiation depending on the ambient temperature are provided in Figure 4.20(a) and Figure 4.20(b) respectively, according to TRNSYS meteorologic database. Finally, for climates of Athens, Strasbourg and Helsinki, evaluated annual average ground temperatures are respectively equal to 14.4 °C, 8.7 °C and 3.9 °C.

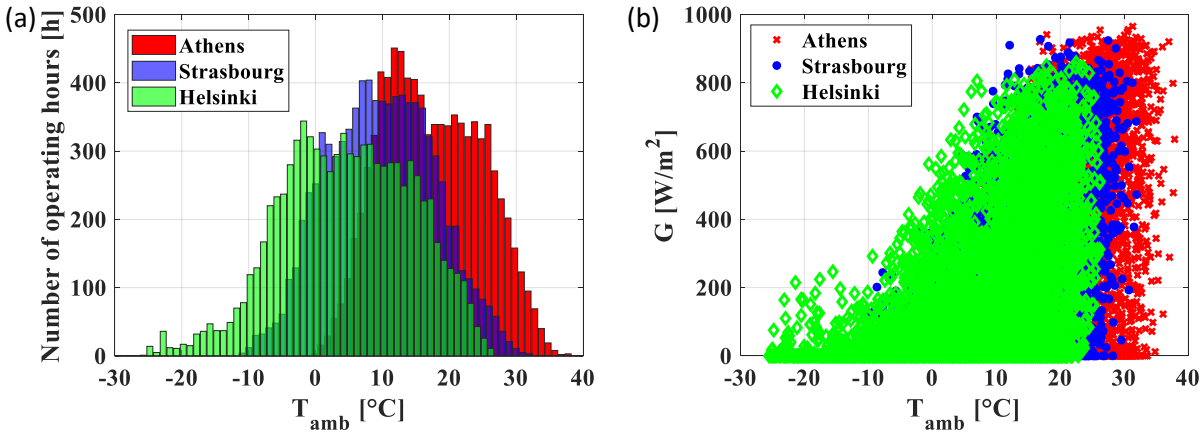


Figure 4.20. Number of operating hours (a) and solar radiation (b) vs. ambient temperature, for the climate conditions investigated of Athens, Strasbourg and Helsinki, according to TRNSYS meteorologic database [118]

4.3.4.2 Optimization variables: decisional parameters and objective functions.

A multi-objective optimization is carried out on the system analyzed, studying all the possible system configurations to maximize the system performance and minimize the investment costs. A total of 12 decisional variables are chosen as inputs of the optimization for the multi-source heat pump presented in this work: the storage tank volume, the solar thermal collector surface, the solar photovoltaic collector surface, the heat exchanger heat transfer surfaces (both for the two air and water evaporators, and for the water condenser), the electric battery capacity, presence or absence of a GHE, the type of storage tank (if sensible or latent), the PCM melting temperature (if the PCM is present), different technologies of solar thermal and photovoltaic collectors.

The two chosen objective functions are the seasonal coefficient of performance (SCOP) to maximize, and the investment cost to minimize, defined in this case as follow:

$$SCOP = \frac{\sum_{i=1}^{N_{hours}} \dot{Q}_{user,i}}{\sum_{i=1}^{N_{hours}} (\dot{W}_{comp,i} + \dot{W}_{pump,i} + \dot{W}_{fan,i})} \tag{4.17}$$

$$C_{inv} = \sum_{j=1}^{N_{components}} C_{component,i} \quad [€] \tag{4.18}$$

$\dot{Q}_{user,i}$ is the requested thermal power by the user, whereas $\dot{W}_{comp,i}$, $\dot{W}_{pump,i}$ and $\dot{W}_{fan,i}$ are the electric powers respectively of the compressor, circulation pumps and heat exchanger fan. $C_{component,i}$, instead, is the investment cost for each component of the system analyzed.

The choice of using investment costs as an objective function, instead of the total costs or net present value, is to give an indication to the machine installer of the maximum reachable seasonal performance depending on how much he is willing to spend in terms of capital costs. Furthermore, using both SCOP and net present value as objective functions of the optimization,

the process would have been too much addressed to the thermodynamic point of view, losing partly the real economic sense of the optimization.

The range intervals for each of the considered optimization variables are reported in Table 4.6.

Table 4.6. List of decisional variables with relative variation ranges, and objective functions employed in the work of Pelella et al. [186]

Decisional variables	
Storage Tank Volume $V_{tank} = [0\ 50\ 100\ 300\ 500]\ l$	Type of storage tank Water/PCM
Solar thermal collector surface area $A_{col} = [0\ 5\ 10\ 15\ 20]\ m^2$	Solar photovoltaic panels surface area $A_{pv} = [0\ 5\ 10\ 15\ 20]\ m^2$
Water evaporator heat transfer surface area* $A_{w,ev} = \left[0, \frac{1}{3}A_{max,ev,w}, \frac{2}{3}A_{max,ev,w}, A_{max,ev,w}\right]\ m^2$	PCM melting temperature $T_{melt,PCM} = [20\ 30\ 40]\ °C$
Water condenser heat transfer surface area* $A_{wat,co} = \left[\frac{1}{4}A_{max,co,w}, \frac{1}{2}A_{max,co,w}, \frac{3}{4}A_{max,co,w}, A_{max,co,w}\right]\ m^2$	Solar thermal collector type Without glass (1), plastic (2), flat-plane (3), and vacuum tube (4)
Air evaporator heat transfer surface area* $A_{ev,a} = \left[0, \frac{1}{4}A_{max,ev,a}, \frac{1}{2}A_{max,ev,a}, A_{max,ev,a}\right] m^2$	Solar photovoltaic panels type Amorphous (1), CIGS (2), CdTe (3), polycrystalline (4), monocrystalline (5), HIT (6)
Geothermal heat exchanger (GHE) Yes/No	Electric Storage Battery Capacity $C_{batt} = [0\ 1\ 3\ 6]\ kWh;$
Objective functions	
Seasonal coefficient of performance (SCOP) To maximize	Investment cost (C_{inv}) To minimize
*Maximum heat transfer surface areas for which the pinch-point in temperature profiles is 0.5 °C $A_{max,ev,w} = 0.76\ m^2;\ A_{max,co,w} = 1.17\ m^2;\ A_{max,ev,a} = 39.54\ m^2$	

Values for the storage tank volumes, the battery capacity, the solar thermal and photovoltaic collector surface are chosen according to common domestic sizes. The maximum values for heat exchanger heat transfer surfaces instead are selected in order to have a 0.5 °C pinch-point in temperature profiles and considering equally spaced intervals. Particularly, for the evaporator, the pinch point is evaluated as the difference between the outlet temperature of the secondary fluid and the evaporating temperature. On the other hand, for the condenser the

minimum difference between temperature profiles is situated after the de-superheating phase. In simulations, a thermal power equal to the design value is used to evaluate the maximum heat transfer surfaces. Regarding thermal and photovoltaic collector technology, an increasing number of decisional variables refers to better technologies in terms of higher collector efficiencies and higher capital costs. For thermal collectors, four typologies are investigated among: without glass, plastic, flat-plane and vacuum tube, whereas as regards photovoltaic collectors, six technologies are investigated among: amorphous, copper indium gallium (di)selenide (CIGS), Cadmium telluride (CdTe), polycrystalline, monocrystalline and heterostructure with intrinsic thin layer (HIT). Efficiency curves and specific costs for each of the technologies analyzed are reported in section 4.3.5.3. Between all the analyzed combinations, only feasible ones are considered in the optimization.

4.3.4.3 Optimization tools

To conduct this optimization, a brute-force research could be not suitable. In fact, by combining all the values assumed by the decisional variables presented above, the number of possible configurations for the system analyzed are approximately 10 million. Therefore, considering on average a simulation time of 3-4 min for each combination, the total simulation time would be excessively high and therefore not affordable. Different optimization tools must therefore be employed. Particularly, in this work a Latin Hypercube Sampling (LHS) method has been adopted to carry out a sensibility analysis, and a genetic algorithm (GA) to find out the optimal non-dominated solutions.

LHS is a type of sampling procedure of Monte Carlo analysis [195]. It can be viewed as a compromise between a random sampling, where each sample is generated in a random way independently of all other sample elements, and a stratified sampling, which provides a way to specify a subset from which sample elements will be selected. LHS divides variables into ranges, and one value is randomly selected from each interval. Therefore, a more ranged uniform dominium is selected, and more stable and exhaustive results are produced, by using an LHS instead other methods.

GA instead is a computational method built on the biological evolution, based on the idea that a population of individuals evolves under natural selection [196]. A first population of individuals is created, and among them some will be fitter than others (giving better solutions). The differences between them are then used to select a new set of individuals for the following timestep. During this phase, called selection, a new set of candidate solution is created, by copying the best individuals and deleting the worst. Moreover, in the selection process, copies

are not exact, but it can be a probability of mutation (random flips of bins) and crossover (exchange of corresponding parts of strings between two individuals). Each cycle of evaluation and selections the fitness of the population tends to improve, until a certain tolerance is reached. In this way the number of combinations analyzed to find optimal solutions can be significantly reduced. The risk of using a GA is to converge in proximity of local and non-global optimum, especially if the parameters of the algorithm are not chosen in a suitable way. Therefore, in this work a GA has been employed, considering as operating parameters a population size of 50, a crossover fraction of 0.7 and a tolerance of 10^{-3}, as suggested by the MATLAB optimization tool.

4.3.4.4 Cost functions

To evaluate investment costs for single components, employed in equation 4.19, different cost function from the literature have been implemented. These functions are reported in Table 4.7, for the compressor, heat exchangers, solar thermal and photovoltaic collectors, the storage battery, the storage tank and circulating pumps. Other component prices such as two- and three-way valves, pipelines, connections have been neglected. For operating costs, energy prices depending on the countries investigated are considered, whereas maintenance and other cost contributions are neglected. For the thermal storage, two different cost functions for sensible and latent storage tank are employed, using in the first case a well-known reference, and in the second case a function fitted on manufacturer data. Both depend on the storage tank volume. Finally, for the GHE an extra cost of 1500€ is considered, in order to consider both investment and installation costs. This value has been estimated by data reported in Zhou et al. [197].

Table 4.7. List of cost functions employed in Pelella et al. [186] for each of the system components

Component	Cost Function	Notes	Reference	Component	Cost Function	Notes	Reference
Compressor	$52.63 \cdot \dot{V}_{comp} \cdot 1.2$ [€]	$\dot{V}_{comp}$ in m^3/h	Botticella et al. [108]	**Solar thermal collector**	$C_{ref} \cdot A_{ref} \cdot \left(\frac{A_{col}}{2.5}\right)^{0.5} \eta_0^{1.2} a_1^{-0.04}$ [€]	C_{ref} in €/m^2 A_{ref}, A_{pan} in m^2	Ferreira et al. [184]
Expansion valve	$114.5 \cdot \dot{m}$ [$]	$\dot{m}$ in kg/s	Sanaye et al. [198]	**GHE**	1500 €	-	Zhou et al. [197]
Solar photovoltaic panel	$A_{pv} \cdot C_{pv}$ [€]	A_{pv} in m^2 C_{pv} in €/m^2	Manufacturer data (see section 4.3.5.3)	**Storage tank (water)**	$3647.5 \cdot \left(\frac{V_{tank}}{0.32}\right)^{0.3} \cdot 0{,}985$ [€]	V_{tank} in m^3	Ferreira et al. [184]
Storage battery	$392.86 \cdot C_{batt}$ [$]	C_{batt} in kWh	Tesla (Tervo et al. [199])	**Storage tank (PCM)**	$-1.4702 \cdot V_{tank}^2 + 2519.9 \cdot V_{tank} + 5007.3$ [€]	V_{tank} in m^3	Fitting from manufacturer data (see section 4.3.5.4)
Fin and tube heat exchanger	$A_{ev,a} \cdot 45$ [€]	$A_{ev,a}$ in m^2	Botticella et al. [108]	**Plate heat exchangers**	$516.62 \cdot A_{ev,co.w} + 268.45$ [$]	$A_{ev,co.w}$ in m^2	Sanaye et al. [198]
Circulating pumps	$705.48 \cdot \dot{W}_{pump}^{0.71} \cdot \left(1 + \frac{0.2}{1 - \eta_{pump}}\right)$ [€]	$\dot{W}_{pump}$ in kW	Sanaye et al. [198]	**Energy specific cost**	0.197 (Greece), 0.202 (France), 0.184 (Finland) [€/kWh]	-	Eurostat [185]

4.3.5 Models calibration and validation

A validation of the whole system is not possible, because no experimental activities like this are available in literature. However, as also clarified in section 3.2.4, the entire model simply puts together several sub-models which calibrations are reported in this section. This should be enough to guarantee, at least, affordable results to analyze trends and patterns for the system investigated, without dwelling too on numerical values.

4.3.5.1 Calibration of the compressor model

The compressor efficiency is calibrated on manufacturer data, with an expression depending on the compression ratio. In detail, the following function has been selected to fit at best all the experimental data:

$$\eta_g = \frac{q_1 \cdot \beta + q_2}{\beta^2 + q_3 \cdot \beta + q_4} \qquad (4.19)$$

Values of calibration coefficients obtained are respectively: $q_1 = 7.74, q_2 = -7.72, q_3 = 4.77$ and $q_4 = 0.077$.

The results for the calibration process are shown in Figure 4.21. Blue dots refer to experimental data, whereas the red continuous line is the model prevision, with an error of $\pm 5\%$ represented by dashed lines. As a matter of fact, the previous expression is able to predict experimental data with a mean absolute percentage error (MAPE) of 2.5%, a mean relative percentage error (MRPE) of -0.1%, a maximum error of approximately 8% and with the 87% of experimental points predicted with an absolute error less than 5%.

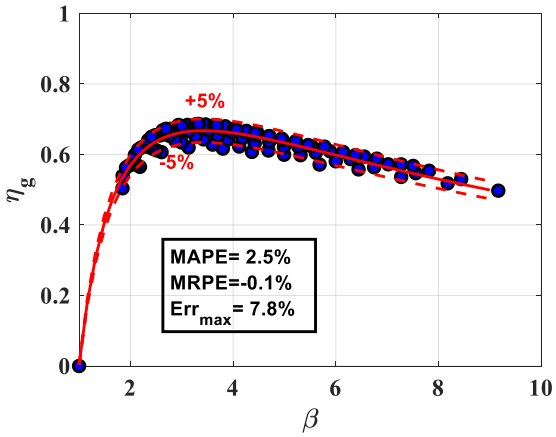
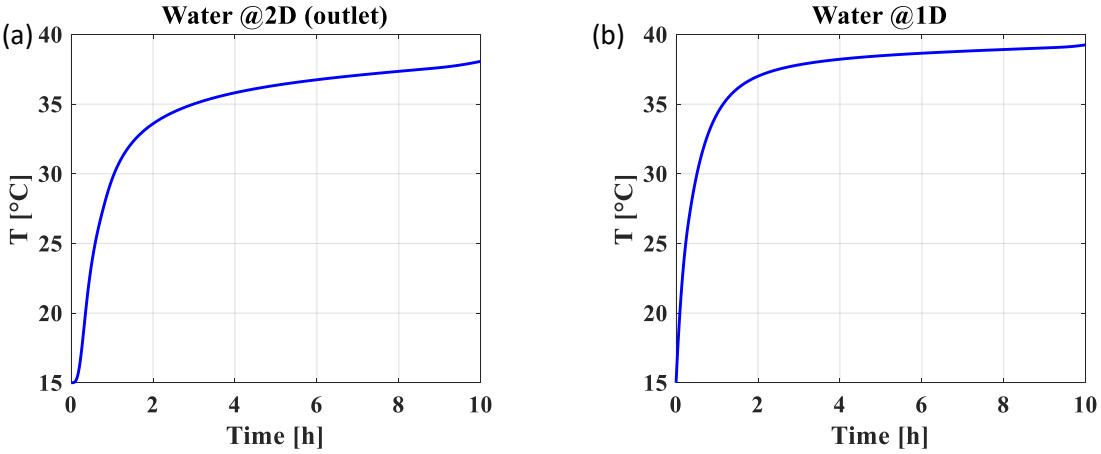


Figure 4.21. Calibration results for the compressor model, comparison with manufacturer data and indication of the prevision accuracy

4.3.5.2 Validation of the storage tank 1D model

In this paper a 1D version of the storage tank model is employed. However, this kind of model has to be validated through a comparison of its results with the ones obtained by the 2D validated model of Zsembinszki et al. [192] [193]. Therefore, values for water and PCM temperatures are reported in figure, both for the 2D (Figure 4.22(a, c)) and the 1D (Figure 4.22(b, d)) versions of the model, in case of charging of the thermal storage, with an initial temperature of 15 °C and an inlet water temperature of 40 °C. Particularly Figure 4.22(a) for the 2D model represents the outlet temperature of the heat transfer water fluid, therefore the one of the last node along the x direction (see Figure 4.15(a)). For the PCM, coloured lines closer to blue are related to external PCM layers, closer to the HTF, whereas colors closer to red are related to the internal slices of PCM. 10 hours are simulated until almost all the thermal storage has reached its maximum state of charge. It can be noticed that, while no significant differences can be noticed between the PCM temperatures of the 1D and 2D models, in case of water the 1D model tends to overestimate outlet water temperature of the storage tank, especially in a first phase of the dynamics.



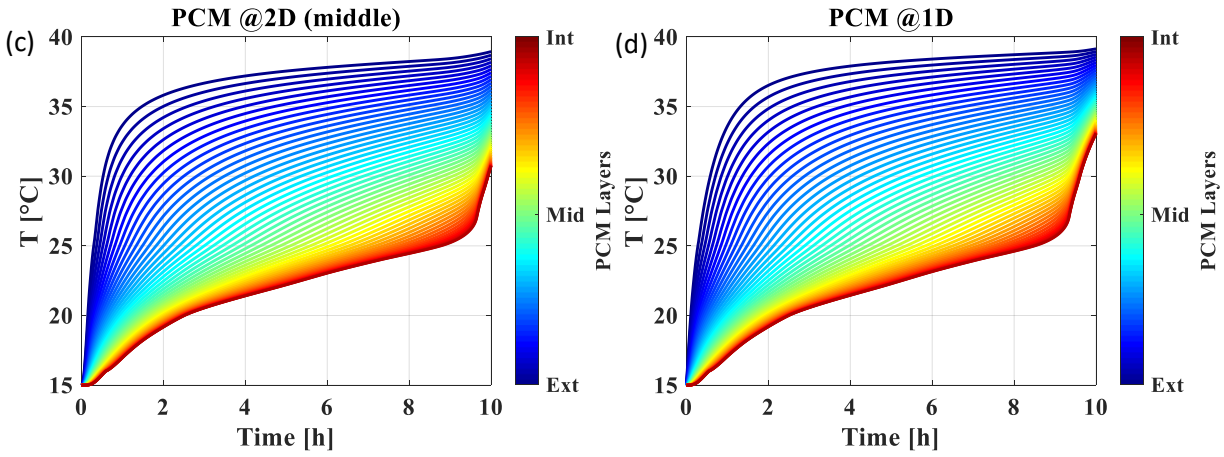


Figure 4.22. Temperature distribution in the storage tank evaluated with the 2D model of Zsembinszki et al. [192] [193] (a, c) and 1D version of the model employed in the work of Pelella et al. [186] (b, d). Water temperature evolution (a, b) and PCM temperature layers (c, d) evolution in 10 hours

Therefore, to quantify the temperature deviations between the 2D and 1D models, all the obtained values are compared each other in Figure 4.23. In Figure 4.23(a), due to the overestimated outlet temperature of the 1D model, a mean absolute error (MAE) of 2.6 °C and a maximum error of approximately 8 °C are obtained. Regarding instead PCM temperatures, compared in Figure 4.23(b), due to less differences of results obtained with the two models, a mean absolute error of 0.4 °C and a maximum error of 3.4 °C are obtained. The maximum temperature differences seem to be at the beginning of the charging process for the external PCM slices (for lower temperatures, see blue dots), and at the end of the process for internal PCM slices (for higher temperatures, see red dots).

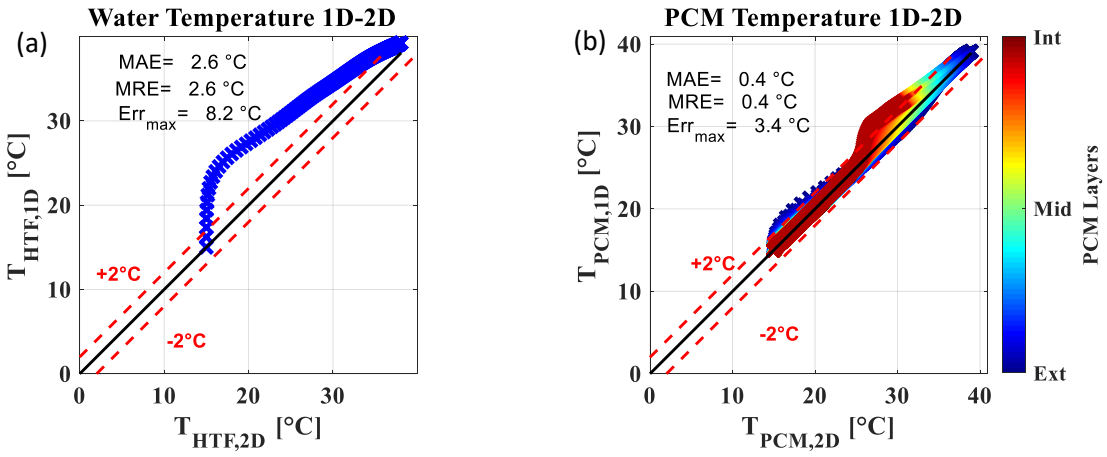


Figure 4.23. Validation of the 1D version of the model employed in the work of Pelella et al. [186] with the 2D model of Zsembinszki et al. [192] [193], for water (a) and PCM (b) temperatures and corresponding prevision errors

At this point it has to be clarified how much these temperature differences between the 1D and the 2D models affect energetic results of all the entire system analyzed, especially in terms of outlet water temperature. Therefore, results in terms of SCOP, electricity consumption and

simulation time are compared between the 1D and 2D versions of the model, as shown in Table 4.8, for 5 different tests whose decisional variable values are reported in Table 4.9. Results show that, in terms of energetic results, differences between the 1D and 2D model never overcome the 2.5%, with a considerable time saving of 20-30 s on average in using the 1D model. For these reasons, the 1D approach has been used in this work.

Table 4.8. Comparison of results in terms of SCOP, electric energy and simulation time between the 1D version of the model employed in the work of Pelella et al. [186] and the 2D model of Zsembinszki et al. [192] [193]

		1D			**2D**			**Differences 1D-2D**		
N° Test	**Climate**	$SCOP$	E_{el} **[kWh/y]**	**Sim. time [s]**	$SCOP$	E_{el} **[kWh/y]**	**Sim. time [s]**	$\Delta SCOP$ **1D-2D [%]**	ΔE_{el} **1D-2D [%]**	$\Delta Sim.time$ **1D-2D [s]**
1	Athens	5.62	2288	243	5.66	2272	273	-0.71	0.70	30
2	Strasbourg	3.56	9305	355	3.62	9166	381	-1.69	1.49	26
3	Helsinki	2.77	17362	366	2.76	17348	398	0.36	0.08	32
4	Athens	4.84	2655	246	4.85	2650	273	-0.21	0.19	27
5	Strasbourg	3.40	9743	369	3.45	9626	400	-1.47	1.20	31
6	Helsinki	2.81	17108	371	2.82	17057	446	-0.36	0.30	75
7	Athens	5.24	2453	247	5.37	2395	273	-2.48	2.36	26

Table 4.9. Values assumed by decisional variables of the seven comparison tests presented in Table 4.8

Test number	A_{col} $[m^2]$	V_{tank} $[l]$	A_{pv} $[m^2]$	**GHE**
1	10	300	10	Yes
2	15	100	0	Yes
3	20	500	0	No
4	5	50	5	No
5	5	500	0	Yes
6	20	50	5	Yes
7	20	200	0	No

4.3.5.3 Efficiencies and specific costs of solar thermal and photovoltaic collectors

Here, values for solar thermal and photovoltaic efficiencies, and costs for solar collects, calibrated on manufacturer data, are reported.

Regarding solar thermal collectors, values of η_0, a_1 and a_2 are reported in Table 4.10 for all the technologies investigated [200] [201]. Furthermore, values for the referenced investment costs, used in the cost function of Ferreira et al. [184], are reported in the last column. It is worth noting that the different measurement unit for the coefficient a_2 depends on if the second term of equation 4.2.1.3 is multiplied or not by the solar radiation.

Table 4.10. Values of efficiency coefficients and of reference costs depending on the thermal solar collector technology employed in the work of Pelella et al. [186]

	Efficiency			**Investment costs**
Collector technology	η_0 [−]	a_1 (W/m^2K)	a_2	$C_{ref}[€/m^2]$
Without glass	0.793	9.503	82.35 (W^2/m^4K^2)	165.8
Plastic	0.896	15.05	3311 (W^2/m^4K^2)	99.5
Flat-plate	0.773	3.675	0.007 (W/m^2K^2)	298.5
Vacuum tube	0.718	0.974	0.005(W/m^2K^2)	298.5

Regarding photovoltaic collectors instead, the following expression is employed for the collector efficiency:

$$\eta_{pv} = u_1 \cdot G^{u_2} + u_3 \tag{4.20}$$

Coefficient a, b and c are calibrated on manufactured data, and values depending on the collector technologies are reported in Table 4.11. Note that the solar collector efficiency depends also on the temperature of the panel surface, therefore calibration coefficients are differently obtained for three superficial temperatures of 10 °C, 40 °C and 70 °C. Finally, the specific cost per square meter of solar collector surface is reported in the last column, depending on the panel technology.

Table 4.11. Values of efficiency coefficient and specific costs depending on the photovoltaic solar collector technology employed in the work of Pelella et al. [186] and on the surface temperature

Panel technology	u_1 @ $T_s =$ 10 °C	u_2 @ $T_s =$ 10 °C	u_3 @ $T_s =$ 10 °C	u_1 @ $T_s =$ 40 °C	u_2 @ $T_s =$ 40 °C	u_3 @ $T_s =$ 40 °C	u_1 @ $T_s =$ 70 °C	u_2 @ $T_s =$ 70 °C	u_3 @ $T_s =$ 70 °C	C_{spec} $\left[\frac{€}{m^2}\right]$
Amorphous	-0.28	-0.74	0.08	-0.18	-0.60	0.07	-0.12	-0.45	0.07	29
CIGS	-0.84	-0.89	0.13	-0.24	-0.49	0.13	-0.23	-0.44	0.13	91
CdTe	-0.17	-0.59	0.15	-0.12	-0.37	0.15	-0.14	-0.32	0.14	91
Polycrystalline	-0.41	-0.70	0.16	-0.31	-0.65	0.14	-0.27	-0.61	0.12	108
Monocrystalline	-0.22	-0.56	0.17	-0.25	-0.60	0.15	-0.19	-0.52	0.13	160
HIT	-0.45	-0.61	0.20	-0.36	-0.53	0.19	-0.27	-0.47	0.17	216

4.3.5.4 PCM storage tank cost

A PCM storage tank cost function has been derived from a calibration based on manufacturer data [202]. The following quadratic expression for the evaluation of capital cost depending on the storage tank volume has been employed:

$$C_{tank,PCM} = -1.4702 \cdot V_{tank}^2 + 2519.9 \cdot V_{tank} + 5007.3 \quad (4.21)$$

The fitting process has been reported in Figure 4.24, and it has been characterized by an almost unitary coefficient of determination R^2.

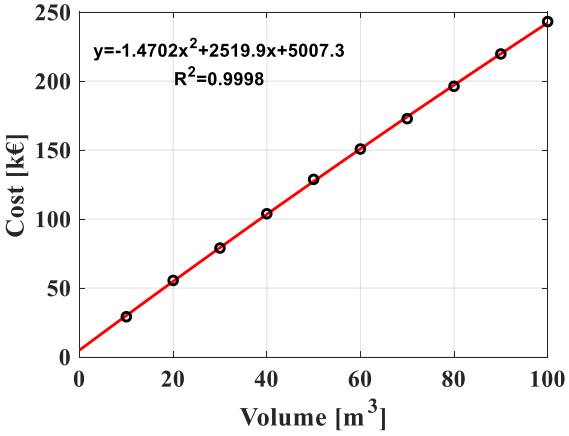


Figure 4.24. Fitting of the PCM storage tank cost function based on manufacturer data [202].

4.3.6 Results

4.3.6.1 Steady state and dynamic results

As regards the static behaviour of the heat pump, two temperature-specific entropy diagrams are reported in Figure 4.25. Particularly, Figure 4.25(a) shows the thermodynamic cycle of the heat pump in case of an air-cooled evaporation which occurs in the fin-and-tube heat exchanger, whereas in Figure 4.25(b) is represented the cycle in case of a water-cooled evaporation in the plate heat exchanger. Both cycles are obtained for fixed conditions of inlet and outlet condenser water temperatures of respectively 40-45 °C, and for the same inlet temperature for the evaporator secondary fluid, both for air and water of 10 °C. Heat exchangers heat transfer surfaces are also fixed. For these fixed conditions, the results show that the water evaporation mode is characterized by a COP which is approximately 15% higher than the air evaporation mode, especially due to a higher evaporation temperature which goes from -8 °C for the air-cooled mode to about -2 °C for the water-cooled mode. The machine then should operate in water evaporation mode in these conditions to maximize the system performance. Generally, depending on heat transfer surfaces and on external conditions, it could be convenient for the machine to operate in one or the other operating mode, therefore a suitable control strategy should be developed in order to operate always in the optimal modality.

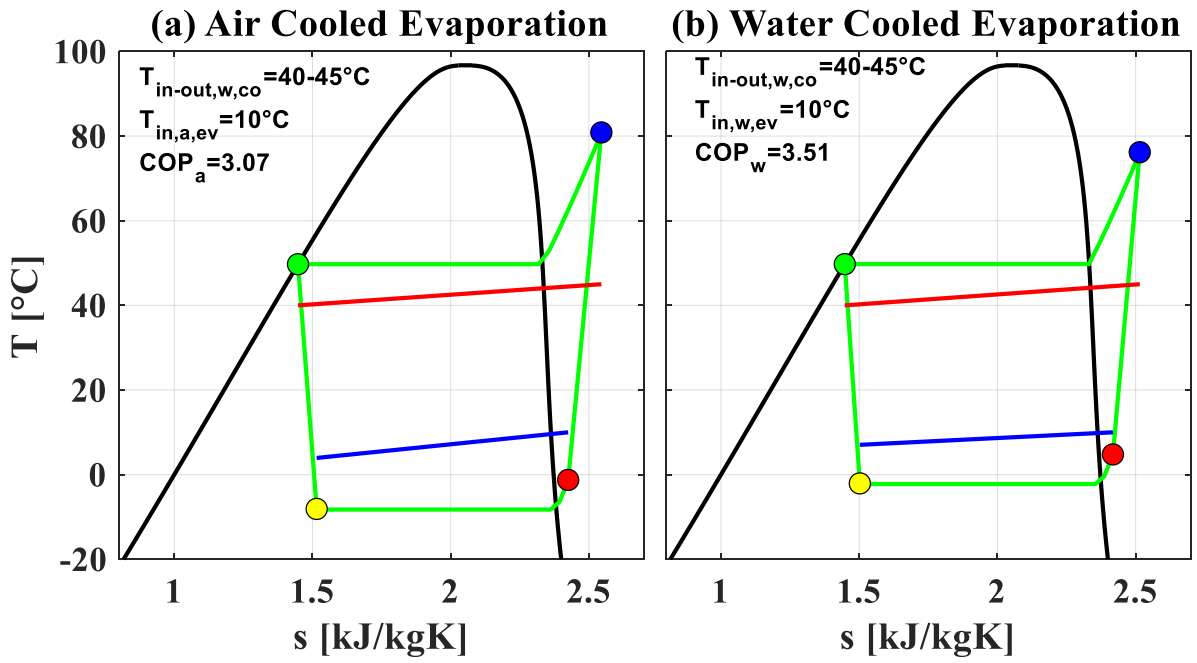


Figure 4.25. Temperature – Specific entropy diagrams in case of air cooled (a) and water-cooled evaporation (b), for fixed conditions of inlet and outlet condenser water temperature of 40-45 °C, for same temperature of air/water inlet at the evaporator of 10 °C, and fixed conditions of heat exchangers heat transfer surfaces

Therefore, applying the control strategy is possible to increase values of COP along the entire year. The evolution of COP values along one year is reported in Figure 4.26, for Athens climate conditions, both for a traditional air-to-water heat pump on the left (Figure 4.26(a)) and for a multi-source heat pump on the right (Figure 4.26(b)), exploiting all the three sources of sun, air and ground investigated in this work. It can be noticed that lowest value of COP between 3.0 and 3.5 characteristics of colder months are replaced by higher values of about 4.0, especially due to the exploitation of the ground source in hours when the ground temperature is higher than the ambient temperature. On the other hand, maximum COP values of 5.5/6 for an only air mode are also replaced by higher maximum COP values, with peaks over 8.5 especially in warmer months due to the water of the solar tank evaporation mode.

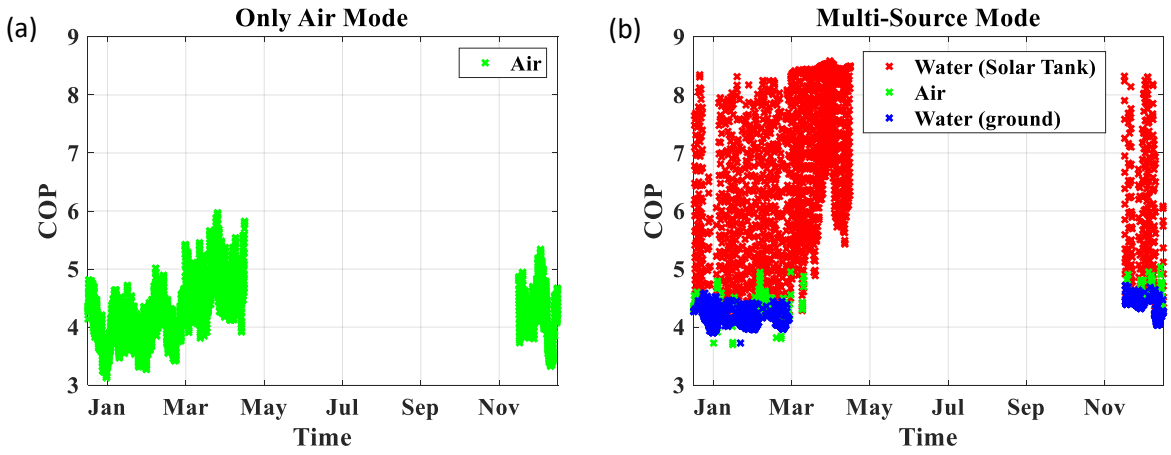


Figure 4.26. COP evolution along one year in heating mode for the system analyzed, in case of only air (a) and multi-source (b) operating modes

In case of sun evaporation mode, the storage tank temperature evolution along an entire year is reported in Figure 4.27, in case of a PCM thermal storage, and for fixed conditions of thermal solar collector surface of 20 m^2, and of storage tank volume of 300 l. The red dashed line is related to the water HTF able to charge/discharge the tank, whereas solid and coloured lines are related to the PCM temperature layers, with red and blue lines related respectively to the internal and external (closer to the HTF) slices. It can be noticed that for this fixed configuration the storage tank charges and discharges almost every day. In this case the external layers of the PCM are able to reach almost 45 °C also during colder climate conditions, with a high stratification which occurs in these months, and more uniform temperatures obtained in warmer months. It has to be clarified that, regarding the different thermal behaviour of using water or PCM thermal storage is that in case of latent heat tanks the inner slices temperature is closer to the selected melting point of the PCM (in figure of 25 °C), and this led to mitigate oscillations

in charging/discharging processes. Otherwise, in case of sensible thermal storage, all the slices assume maximum and minimum temperatures of the oscillation.

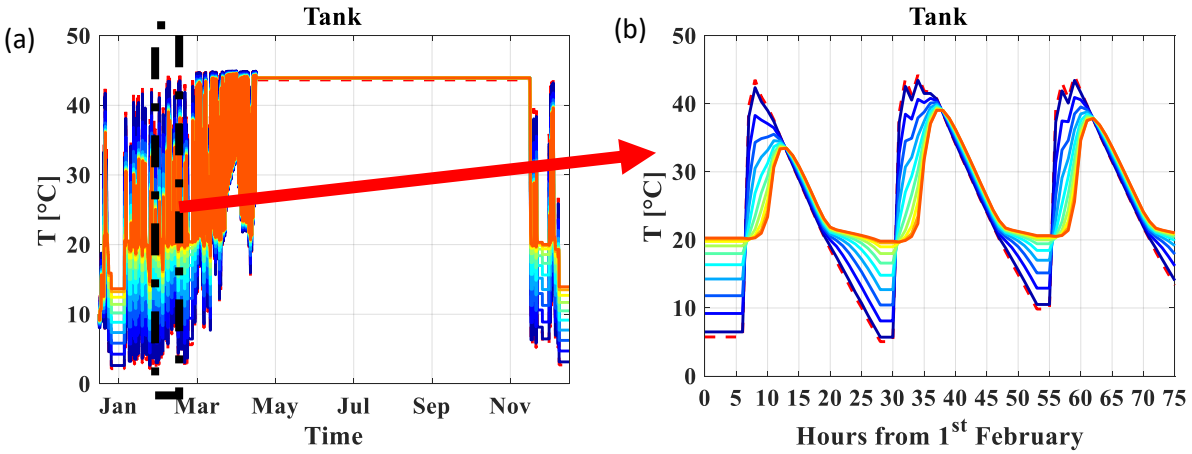


Figure 4.27. Tank temperature evolution in case of a storage tank volume of 300l, thermal solar collector surface of 20m^2 and employment of a PCM material (a), with a zoom on three days in the month of February (b)

4.3.6.2 Sensitivity analysis and Pareto fronts

Considering the variable intervals reported in Table 4.6, a sensitivity analysis is carried out in order to analyze the effect of each variable on the objective functions investigated in this work. Pearson coefficients for each variable and climate conditions are reported in Figure 4.28. It has to be clarified that the Pearson coefficient is related to the increase for each of the decisional variables investigated, whereas in case of "Tank" and "GHE" the increase is related to passing respectively from PCM(0) to Water(1) storage tank, and from absence(0) to presence(1) of the GHE. As expected, the results show that most of the variables investigated give a contrasting effect on objective functions. Regarding for instance the battery capacity, the thermal and photovoltaic collector surface and technology and heat exchangers heat transfer surfaces, an increase of them causes both a SCOP and an investment cost increase, according also to the several experimental evidence analysed in section 4.1. Regarding the exploitation of the solar source, variables such as battery capacity and solar thermal and photovoltaic technology and surface, as expected, they seem to be more effective on performances in warmer cities than in colder climates, whereas they affect costs in a similar way for all climate conditions investigated. For instance, the thermal solar collector surface has even a slight negative effect on SCOP for Helsinki climate condition, whereas the effect of the collector technology is almost negligible. Similar considerations could be done for the storage tank volume which, according to Yumrutas and Ünsal [147], affects positively SCOP for the warmer climate of Athens, and negatively for Strasbourg and Helsinki. Regarding the storage tank typology instead, it seems that it only slightly affects the system seasonal performances, as also observed in Belmonte et

al. [171], with a water tank more suitable in warmer climates (e.g. Athens), and a PCM tank in colder cities (e.g. Helsinki), whereas using a PCM thermal storage causes a huge increase in the component cost. Moreover, in case of a PCM thermal storage usage, the melting temperature of the PCM seems not to particularly affect neither SCOP not investment costs. On the other hand, the exploitation of the ground source through a GHE seems to be more effective on performances for colder climates, for which the soil can be used as an alternative source due to its higher temperature compared to the external ones.

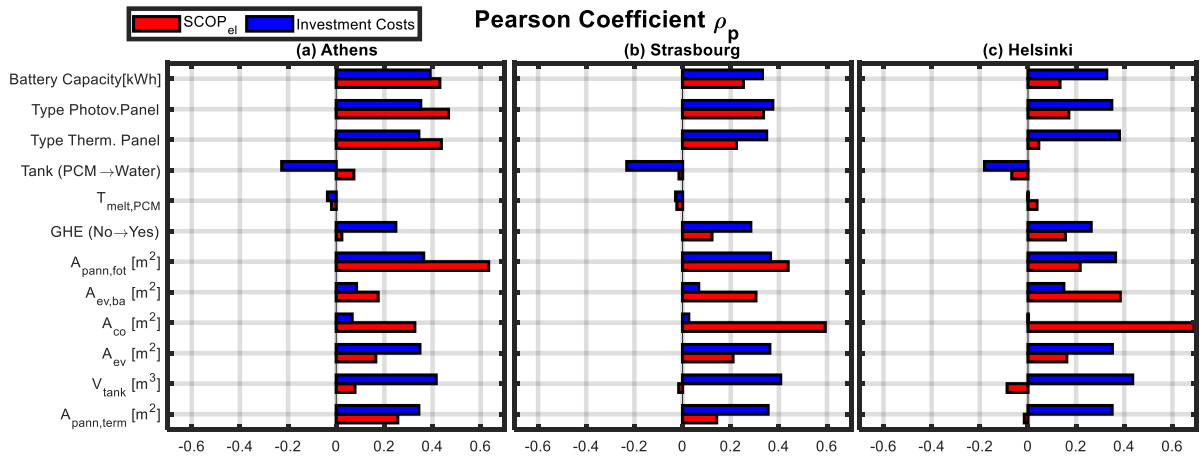


Figure 4.28. Pearson coefficients for the effect of all the decisional variables on the objective function investigated (SCOP in red and investment costs in blue), for Athens (a), Strasbourg (b) and Helsinki (c) climate conditions

Therefore, through the GA, whose settings are reported in section 4.3.4.3, the optimization has been carried out. Results for all the system configurations investigated in terms of investment costs and SCOP for each of the climate conditions investigated are reported in Figure 4.29. The groups of non-dominated solutions of the Pareto fronts are instead indicated with black dashed lines. Point A and C represented on the Pareto fronts are related to non-dominated solutions characterized respectively by the highest SCOP and the lowest total cost, whereas solution B is the closest to the so-called "Utopia-Point", which is an ideal solution having same SCOP of solution A and same investment cost of solution C.

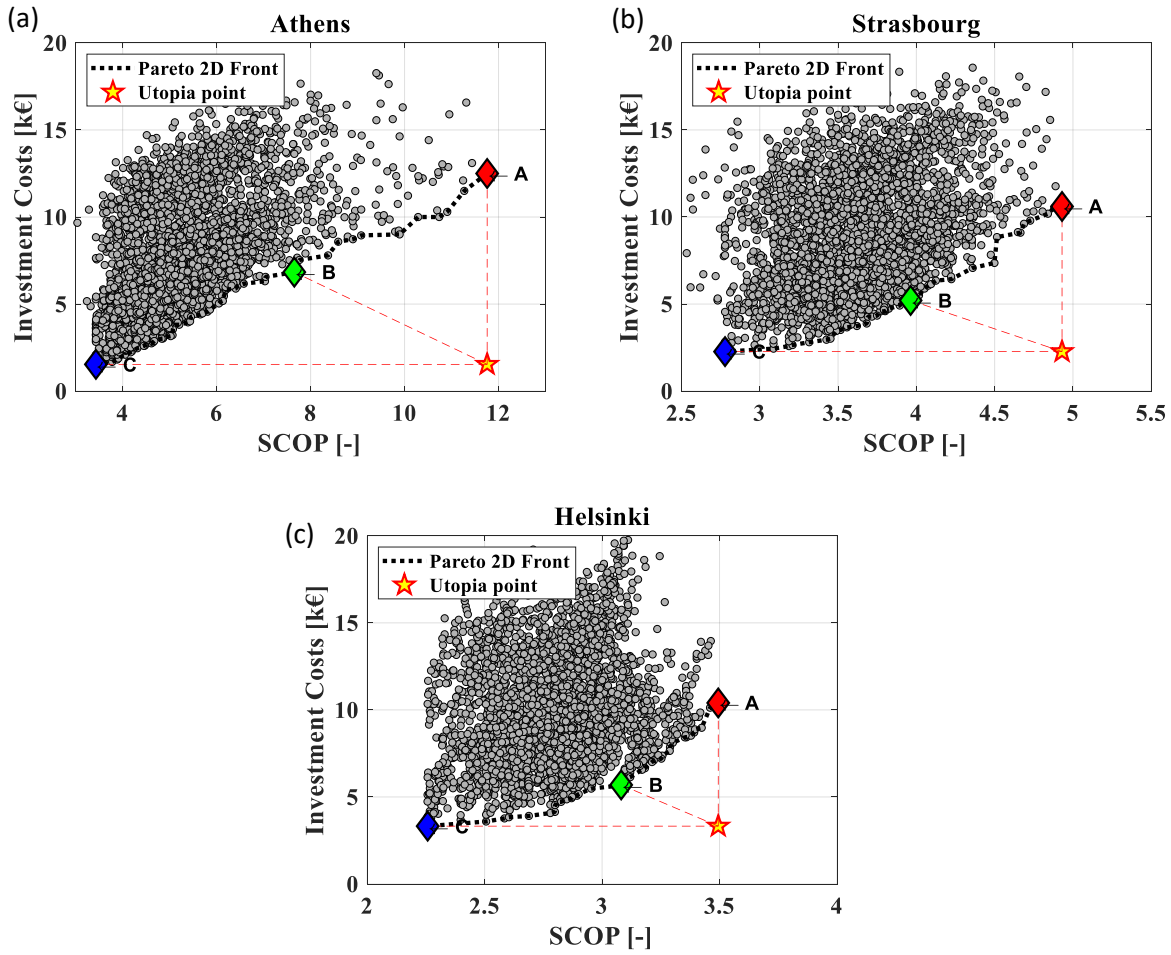


Figure 4.29. Investment costs vs. SCOP and corresponding Pareto 2D front, for climate conditions of Athens (a), Strasbourg (b) and Helsinki (c). Points A and C are respectively the non-dominated solutions with higher SCOP and lower investment costs, whereas solution B is the closest to the "Utopia Point" represented by a star

In Table 4.12 values assumed by decisional variables and objective functions for solutions A, B and C are reported for all the climate conditions investigated. Solution C for all cities can be considered as representative of a traditional air-to-water heat pump, because in that solution no solar or ground loop is employed.

For Athens climate conditions, solution A and B are both characterized by thermal solar collectors, assuming the maximum value of the heat transfer surface, and thermal storage tank assuming the minimum value of the volume. These solutions are also characterized by photovoltaic collectors and a storage battery, with surface area and battery capacity assuming their maximum value for solution A and intermediate values for solution B. Both thermal and photovoltaic collectors are of the best technology for solution A, whereas an intermediate technology is used for photovoltaic collectors in solution B. None of the investigated solutions employs a GHE. Finally, regarding heat exchangers heat transfer surfaces, different values are assumed depending on the investment cost for the chosen solution. Definitely, SCOP increases

from 3.43 to 11.76 passing from solution C to A, whereas the investment cost rises from 1.54 k€ to 12.50 k€.

For Strasbourg climate conditions, only solution A employs both thermal solar collector and a storage tank, whereas solution B is characterized by only thermal panels without a thermal storage. Both solutions A and B employs photovoltaic collectors, with battery capacity assuming the maximum value for solution A and the minimum for solution B, whereas only solution A is characterized by a GHE. Also in this case, heat exchanger heat transfer surfaces depend on investment cost of the solution, except for solution A, which does not empoy a fin-and-tube evaporator. Thermal solar collector technology is the best for both solutions A and B, whereas photovoltaic technology assumes intermediate values. Definitely, passing from solution C to A for this climate conditions, the SCOP increases from 2.79 to 4.93, whereas the investment cost increases from 2.27 k€ to 10.60 k€.

Finally, for Helsinki climate conditions, only solution A is characterized by solar thermal and photovoltaic collectors, with surfaces respectively of 20 and 15 m^2. In none of the solutions investigated a storage tank is present, whereas for both solutions A and B a GHE is employed. Definitely, passing from solution C to A, the SCOP increases from 2.26 to 3.49, whereas the investment cost increases from 3.32 k€ to 10.40 k€.

These results are in accordance with the sensitivity analysis previously carried out. For all the climatic conditions investigated, the heat transfer surface of the water evaporator assumes its maximum value when a storage tank is employed. Finally, due to higher total costs and slight effect on the system performance, none of the non-dominated solutions of the Pareto front employ a latent thermal storage with PCM, for the application and storage tank sizes investigated.

Table 4.12. Values assumed by decisional variables and objective functions for solutions A, B and C of the Pareto fronts, for each climate condition investigated

Point	A_{col} $[m^2]$	V_{tank} $[m^3]$	$A_{ev,w}$ $[m^2]$	$A_{co,w}$ $[m^2]$	$A_{ev,a}$ $[m^2]$	A_{pv} $[m^2]$	GHE	Storage tank type	T_{melt} $[°C]$	Thermal collector type	Photovoltaic panel type	Battery capacity $[kWh]$	$SCOP$	C_{inv} $[k€]$
Athens														
A	20	0.05	0.76	1.17	39.54	20	No	Water	N.D.	4	6	6	11.76	12.50
B	20	0.05	0.76	0.88	9.89	10	No	Water	N.D.	4	4	3	7.65	6.83
C	0	0	0	0.29	9.89	0	No	N.D.	N.D.	N.D.	N.D.	N.D.	3.43	1.54
Strasbourg														
A	20	0.1	0.76	1.17	0	20	Yes	Water	N.D.	4	2	6	4.93	10.60
B	15	0	0	0.88	19.77	20	No	N.D.	N.D.	4	1	1	3.96	5.21
C	0	0	0	0.29	9.89	0	No	N.D.	N.D.	N.D.	N.D.	N.D.	2.78	2.27
Helsinki														
A	20	0	0.76	1.17	19.77	15	Yes	N.D.	N.D.	4	4	3	3.49	10.40
B	0	0	0	1.17	9.89	0	Yes	N.D.	N.D.	N.D.	N.D.	N.D.	3.08	5.69
C	0	0	0	0.29	9.89	0	No	N.D.	N.D.	N.D.	N.D.	N.D.	2.26	3.32

N.D.: Not Defined

4.3.6.3 Total costs analysis in different price scenarios

For solutions A, B and C of the Pareto front, the total cost is evaluated considering the two contributes of investment and operating costs along the entire lifetime of the machine, as also done in Kamazani and Aghanajafi [178]. The latters are evaluated considering a 12 year lifetime and a discount rate of 5%. Moreover, total costs are evaluated for different scenarios in terms of investment costs and energy prices, as follow:

- Baseline Scenario: investment and energy prices from Table 4.7 were considered.
- ECrise (Energy Costs rise) Scenario: doubled energy prices compared to the ones indicated in Table 4.7 are considered, both of purchasing and selling for all the climate conditions investigated, whereas same investment costs of Table 4.7 are considered.
- Inc (Incentives) Scenario: a 20% reduction of the total investment cost is considered compared to the one evaluated with cost functions of Table 4.7, whereas same energy prices are considered.
- Inc + ECrise Scenario: both a 20% reduction of investment costs and doubled energy prices are considered, compared to Table 4.7.

Figure 4.30 shows the results of total costs for points A, B and C for the aforementioned scenarios and for all the climate conditions.

In case of Athens (Figure 4.30(a)), in the baseline scenario solution B is characterized by the lowest total cost, with a value of 7.7 k€, followed by solution C and A with a total cost of respectively 8.1 k€ and 8.6 k€. In an Inc scenario solution A and B assumes similar total costs of respectively 6.1 k€ and 6.3 k€, whereas solution C becomes the most expensive. A more pronounced difference between the solutions occurs instead in case of a doubled energy price scenario, for which solution A is the cheapest by far. For instance, in ECrise scenario, total cost of solution A is approximately 4 times lower than the one of solution C, especially due to the increase of not only the energy purchase, but also the energy retail cost produced by the photovoltaic.

In case of Strasbourg (Figure 4.30(b)), instead, solution C is already the most expensive in a baseline scenario, with a total cost of 23.6 k€ due to a higher number of working hours, with solution B which that becomes the cheapest with a total cost of 19.0 k€. In the Inc scenario, solutions A and B assume similar total costs of about 18.0 k€, whereas in the ECrise and combined scenarios solution A becomes the cheapest with a total cost of approximately 30.0 k€, but with lower percentage differences with other solutions compared with Athens.

Finally, in case of Helsinki (Figure 4.30(c)), in the baseline scenario solutions A and B assume similar value of the total cost of approximately 31.1 k€, whereas in an incentivated scenario the total cost of solution B is slight higher than the one of solution A. All the other effects of cost scenarios on total costs are similar to what observed for Strasbourg climate conditions.

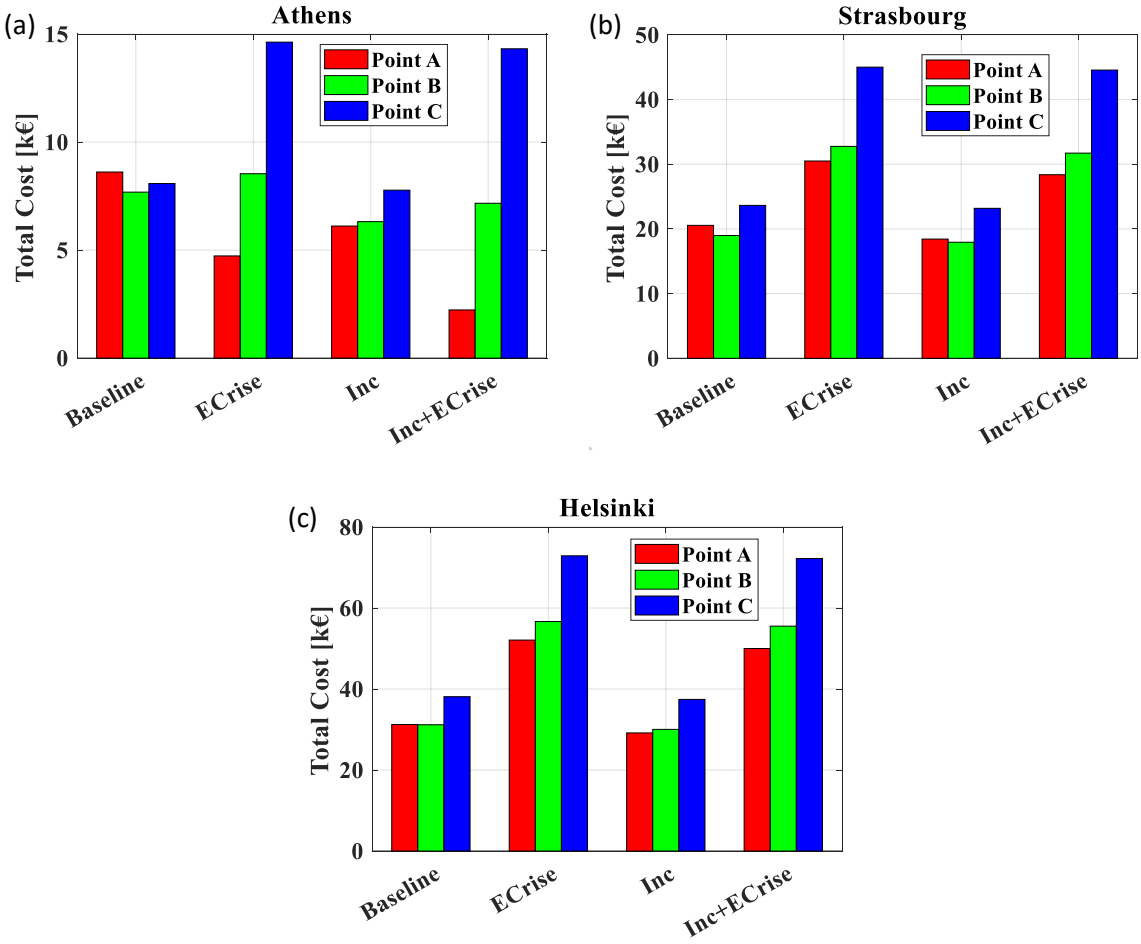


Figure 4.30. Values of total costs assumed by solutions A, B and C in different investment cost and energy price scenarios, for climate conditions of Athens (a), Strasbourg (b) and Helsinki (c)

As already mentioned before, since solution C is for each climate condition investigated representative of a traditional air-to-water heat pump without the exploitation of other energy sources such as sun or ground, it is important to estimate discounted payback (DPB) periods of an innovative solution compared with a traditional one, to understand its effective convenience. Therefore, values of DPB for solutions A and B, referred to the traditional solution C, are reported in Table 4.13. Discounted payback periods are evaluated depending on simple payback periods (SBP), using the following expression [203].

$$DPB = -\frac{log(1 - SPB \cdot a)}{log\ (1 + a)} \tag{4.22}$$

The discount rate a has been fixed equal to 5%. For Athens climate conditions, DPB is of approximately 13 years for solution A, which is higher of the machine lifetime, whereas becomes about 11 years for solution B. For ECrise and Inc scenarios, DPB values become of about 5 years for both solutions, and assuming approximately 2-3 years for a combined scenario. For Strasbourg, in a baseline scenario solution B is characterized by the lowest value of DPB of about 4 against 8 of solution A. Both solutions assume a DPB near 1 year in case of a combined scenario. Finally, for Helsinki, similar results are obtained compared to Strasbourg, with DPB lower than 1 year in an incentive and combined scenario.

Table 4.13. Values of discounted payback period (DPB) of solution A and B referred to solution C (representative of a traditional air-to-water heat pump) for each of the cost scenario and climate condition investigated

DPB compared with solution C (years)	**Baseline**	**ECrise**	**Inc**	**Inc + ECrise**
Athens				
Solution A	12.85	5.43	5.08	2.38
Solution B	10.89	4.73	5.75	2.67
Strasbourg				
Solution A	8.01	3.61	3.10	1.48
Solution B	3.86	1.84	1.90	0.93
Helsinki				
Solution A	5.22	2.45	1.85	0.89
Solution B	2.45	1.19	0.98	0.49

4.4 Conclusions of Part 2

The principal conclusions and quantitative remarks from result of part 2, related to the multi-source exploitation for heat pumps, are here presented. Particularly:

- For the direct expansion dual source (air/sun) heat pumps for commercial application a control strategy has been developed, based on a threshold limit for the solar radiation depending on ambient temperature and number of solar panels, above which it is more convenient to operate in sun mode and below which in air mode. This threshold increases with the ambient temperature and decreases with the number of solar collectors.

- Dynamic simulations have been carried out for Naples, Berlin and Bergen, and a SCOP increase of approximately 14.2% for Naples, 8.9% for Berlin and 7.8% of Bergen is obtained with the employment of 20 solar collectors, with no substantial seasonal performance increase below 10 solar collectors. However, from the economic analysis, it has obtained that, in the actual scenario in terms of investment costs and energy prices, and without the employment of a thermal storage, the total costs of solar assisted heat pump solutions are still higher than the traditional air-source heat pumps.
- Regarding the multi-source indirect expansion heat pump employed with a thermal storage, also in this case a control strategy has been established, to switch among the available sources to maximise the system performance.
- A sensitivity analysis pointed out that most of the decisional variables investigated have a conflicting effect on the two objective functions of SCOP and investment costs, except for the typology of storage tank which seems to influence only the costs and not the SCOP index, whereas the PCM melting temperature does not seem to affect both. Moreover, a storage tank volume, solar thermal collectors and photovoltaic panel surfaces and technologies affect system performances negatively for the colder climates of Strasbourg and Helsinki, and positively for the warmer climate of Athens, whereas the exploitation of the ground source seems to be more convenient for colder climates.
- The optimization shows that, among the non-dominated solutions of the Pareto front, the ones with lowest investment costs always refer to a traditional air source heat pump for all the climate conditions investigated. For Athens, the closest solution to the "Utopia Point" of the Pareto front (solution B) is characterized by the maximum thermal and photovoltaic solar collector surface area, and by the minimum value for the storage tank volume, whereas passing from the non-dominated solution with minimum investment cost (solution C) to the one with the maximum SCOP (solution A) an increment of SCOP from 3.43 to 11.76 occurs, followed by an increase of investment costs from 1.5 k€ to 12.5 k€. For Strasbourg instead, solution B employs only thermal solar collectors without a storage tank, and in this case passing from solution C to A SCOP increases from 2.78 to 4.93, whereas investment costs increase from 2.3 k€ to 10.6 k€. Finally, in Helsinki, passing from solution C to A SCOP increases from 2.26 to 3.49, causing an increase of investment costs from 3.3 k€ to 10.4 k€, whereas solution B employs a GHE, without any solar collector or storage tank. Due to higher capital costs, none of the non-dominated solutions employ a PCM storage tank, for all the climate conditions investigated.

- Finally, different scenarios in terms of incentives on capital costs and rises of energy prices have been considered. In case of an unvaried costs scenario, usually solution C is more convenient for all the climate conditions investigated. The most expensive non-dominated solution on the Pareto front becomes the most convenient in case of a doubled energy cost scenario and in case of incentives on investment costs, therefore better justifying higher capital costs.

5. Conclusions of the thesis

This thesis deals with a deep numerical analysis of residential heat pumps, analysing future perspectives and opportunities of the sector towards a reduction of energy consumptions and total costs. Among the future opportunities for heat pumps, there are the ones related to the development of AI techniques for FDDE purposes, and by the exploitation of multiple alternative sources. In this thesis both these two macro-topic have been analysed respectively in Part 1 and Part 2.

Therefore, conclusions and summaries for both parts investigated in this thesis are here reported.

5.1 Principal outcomes of Part 1

The research activities and the results of Part 1 have been published in two scientific papers (Pelella et al. [104], [121]). These two works analyse the three soft faults of refrigerant leakage, condenser fouling and evaporator fouling, firstly in terms of effect on seasonal performance and on the thermodynamic cycle and then of possibility of detection, diagnosis and evaluation of a fault occurrence. The main outcomes related to Part 1 are here summarized:

- Dynamic simulations regarding different combinations of fault intensity evolution have been carried out, for both heating and cooling modes and, from them, a single maintenance strategy able to simultaneously limit penalized scenario and unnecessary maintenance costs depending on the climate condition investigated cannot be identified. Therefore, this will give the attention to several self-fault detection strategies available with the spread of smart metering devices, AI and ML tools, able to guarantee maintenance operations only when a considerable performance degradation is reached, without running into useless maintenance costs. These results have been published in Pelella et al. [104].
- From the comparison of faulty thermodynamic cycles, it can be concluded that simultaneous occurring of the three soft faults investigated can be detected with commercially available easy measurements of pressures and temperature, whereas a complete FDDE can be performed for different fault severities, depending on the measuring equipment uncertainties and on the fault severity step. These results have been published in Pelella et al. [121], and quantitative values are reported in the conclusions of Part 1 section.

- Finally, ML tools for the FDDE has been developed as proof of the concepts analysed, obtaining good results in terms of prediction accuracy. It is worth noting that the instrumental uncertainties have been neglected in a first phase.

5.2 Principal outcomes of Part 2

The outcomes of Part 2 have been published in two scientific papers (Mastrullo et al. [181] and Pelella et al. [186]). The two works studied two different multi-source heat pump case studies for domestic heating: the first is a 5 kW direct expansion dual source (air/sun) heat pump without a thermal storage and the second is a 10 kW multi-source (air/sun/ground) indirect expansion heat pump with a storage tank. In both cases, control strategies to maximise system performances are developed. In the first case, the effect of solar collector surface is analysed, whereas in the second case a complex optimization with 12 decisional variables has been carried out, with a final study on the effect of several scenarios in terms of incentives on investment costs and increase of energy prices. Principal highlights are here summarized.

- It has been obtained that direct expansion solar assisted heat pumps for heating of commercial users without the employment of a storage tank result to be thermodynamically but not economically convenient, considering the current scenario in terms of capital and energy costs. These results have been published in Mastrullo et al. [181].
- A greater convenience for a multi-source exploitation can be obtained in case of employment of a storage tank, with the solar source to be employed for warmer climates and the ground source for colder climates. High investment cost solutions are better justified in case of increased energy prices and incentivized capital cost scenarios. In this way, the economic advantages of integrating multi-sources to traditional residential heat pumps may introduce both the industrial and private sectors to focus more on renewable sources, in order to achieve further energy consumption savings. These results have been published in Pelella et al. [186].

References

[1] IEA (International Energy Agency), Energy Statistics Data Browser, Paris (2022), https://www.iea.org/data-and-statistics/data-tools/energy-statistics-data-browser.

[2] Deparment of Energy, United Stated of America, Quadriennal Technology Review, An Assessment of Energy Technologies and Research Opportunities Chapter 5: Increasing Efficiency of Building System and Technologies, Semptember 2015.

[3] M. Maasoumy, A. Sangiovanni-Vincentelli, Smart connected buildings design automation: Foundations and trends in Electronic Design Automation, 10(1-2)(2016), 1-143.

[4] IEA (International Energy Agency), Heating, IEA, Paris (2021) https://www.iea.org/reports/heating.

[5] F. Birol, The future of cooling: opportunities for energy-efficient air conditioning. International Energy Agency (2018).

[6] H. Ritchie, M. Roser, P. Rosado, "Energy". Published online at OurWorldInData.org (2020). Retrieved from: 'https://ourworldindata.org/energy' [Online Resource].

[7] IEA (International Energy Agency), Buildings, Paris (2022) https://www.iea.org/reports/buildings.

[8] COP26 Presidency Outcomes. The Glasgow Climate Pact. November 2021 Glasgow (https://ukcop26.org/wp-content/uploads/2021/11/COP26-Presidency-Outcomes-The-Climate-Pact.pdf).

[9] V. Masson-Delmotte, P. Zhai, H.O. Pörtner, D. Roberts, J. Skea, P.R. Shukla, T. Waterfield. Global warming of 1.5 C. An IPCC Special Report on the impacts of global warming of, 1.5. 2018.

[10] European Commission, Communication from the commission to the European parliament, the Euopean council, the council, the European economic and social committee, the committee of the regions and the European investment bank, A Clean Planet for all, A European strategic long-term vision for a prosperous, modern, competitive and climate neutral economy.

[11] European Commission, Communication from the commission to the European parliament, the council, the european economic and social committee and the committee of the regions., Stepping up Europe's 2030 climate ambition investing in a climate-neutral future for benefit of our people (2020).

[12] IEA (International Energy Agency), World Energy Model, Paris(2021) https://www.iea.org/reports/world-energy-model.

[13] L. Cozzi, T. Gould et al., World Energy Outlook 2021. IEA, vol. 2050, 1-461.

[14] T. Nowak, White paper: Heat Pumps - Integrating technologies to decarbonise heating and cooling, European Copper Institute, October 2018.

[15] B.O. Bolaji, Performance of A R22 split-air-conditioner when retrofitted with ozone friendly refrigerants (R410A and R417A), Journal of Energy in Southern Africa 23(3)(2012), 16-22.

[16] Clivet S.p.A., Via Camp Lonc, 25, 32032 Z.I. Villapaiera, Feltre (BL) - Italy, https://www.clivet.com/mono-e-multi-split.

[17] Olimpia Splendid S.p.A., Via Industriale 1/3 25060 Cellatica (BS), Italy, https://www.olimpiasplendid.it/climatizzazione/senza-unita-esterna.

[18] US Department of Energy, Heat Pump Water Heaters, https://www.energy.gov/energysaver/heat-pump-water-heaters.

[19] Ariston Holding N.V. Amsterdam, The Nederlands, https://www.ariston.com/it-it/prodotti/scaldacqua/pompa-di-calore/nuos-primo-80-100.

[20] Daikin Europe N.V., Altherma 3 M, Product catalogue 2022.

[21] J.F. Zhang, Y. Qin, Y, C.C. Wang, Review on CO2 heat pump water heater for residential use in Japan. Renewable and Sustainable Energy Reviews 50(2015), 1383-1391.

[22] Carrier Corporation, VRF Catalog 2020 Edition, CarrierVRF.com.

[23] Mitsubishi Electric, Living Environmental Systems, City Multy Full Product Lineup Catalogue 2018.

[24] P. Li, Y. Li, J.E. Seem, Dynamic modeling and consistent initialization of system of differential-algebraic equations for centrifugal chillers, Proceedings of SimBuild, 4(1)(2010), 386-393.

[25] Johnson Controls, Albert Quay, Cork, Ireland, York, Air-Cooled Chillers and Condensing Units.

[26] Johnson Controls, Albert Quay, Cork, Ireland, York, Water-Cooled Chillers.

[27] United Nations, Amendment to the Montreal Protocol on Substances that Deplete the Ozone Layer, Kigali, 15 October 2016.

[28] European Commission, Preparatory study for a review of Regulation (EC) No 842/2006 on certain fluorinated greenhouse gases, Final Report, September 2011.

[29] IIR (International Institute of Refrigeration), 24th Informative Note on Refrigeration Technologies, January 2014.

[30] The European Parliament and the Council of the European Union, 2014. Regulation (EU) No 517/2014 of the European Parliament and the Council of 16 April 2014 on

fluorinated greenhouse gases and repealing Regulation (EC) No 842/2006, Off. J. Eur. Union 150, 195-230.

[31] S.O. Anderson, E. Bandarra, C. Bhushan et al., Cooling Emissions and Policy Synthesis Report: Benefits of cooling efficiency and the Kigali Amendment, IEA, UN Environment programme (2020).

[32] Commission Delegated Regulation (EU) 2021/340 of 17 December 2020 awith regard to energy labelling requirements for electronic displays, household washing machines and household washer-dryers, light sources, refrigerating appliances, household dishwashers, and refrigerating appliances with a direct sales function (Text with EEA relevance).

[33] Commission Regulation (EU) 2016/2281 of 30 November 2016 implementing Directive 2009/125/EC of the European Parliament and of the Council establishing a framework for the setting of ecodesign requirements for energy-related products, with regard to ecodesign requirements for air heating products, cooling products, high temperature process chillers and fan coil units (Text with EEA relevance).

[34] IEA (International Energy Agency), Heat pumps, Paris (2020), https://www.iea.org/reports/heat-pumps.

[35] EHPA (European Heat Pump Association), Market Report 2022, https://www.ehpa.org/market-data/market-report-2022/.

[36] IEA (International Energy Agency), Heating technology sales in the Sustainable Development Scenario, 2010-2030, Paris (2020) https://www.iea.org/data-and-statistics/charts/heating-technology-sales-in-the-sustainable-development-scenario-2010-2030.

[37] M.S. Breuker, J.E. Braun, Common Fault and Their Impacts for Rooftop Air Conditioners, HVAC&R Research, 4(1998), 303-318.

[38] M. Mehrabi, D. Yuill, Generalized effects of refrigerant charge on normalized performance variables of air conditioners and heat pumps, International Journal of Refrigeration 76(2017), 367-384.

[39] O. Sarfraz, C. Bach, A Literature Review On Heat Exchanger Air Side Fouling In Heating, Ventilation And Air conditioning (HVAC) Applications, 2016.

[40] J.A. Siegel, W.W. Nazaroff, Predicting particle deposition on HVAC heat exchangers, Atmospheric Environment 37 (2003), 5587-5596.

[41] H. Inamdar, E. A. Groll, J. A. Weibel, S V. Garimella, Prediction of Air-Side Particulate Fouling of HVAC&R Heat Exchangers, CTRC Research Publications (2016).

[42] A.H.H. Ali, I.M. Ismail, Evaporator Air-Side Fouling: Effect on Performance of Room Air Conditioners and Impact on Indoor Air Quality, HVAC&R Research 14 (2008), 209-219.

[43] B.C. Pak, E.A. Groll, J.E. Braun, Impact of Fouling and Cleaning on Plate Fin and Spine Fin Heat Exchanger Performance, Ashrae Transaction 111 (2005).

[44] L. Yang, J.E. Braun, E.A. Groll, The role of filtration in maintaining clean heat exchanger coils. Air-Conditioning and Refrigeration Technology Institute (2004).

[45] I. Bellanco, F. Belío, M. Vallés, R. Gerber, J. Salom, Common fault effects on a natural refrigerant, variable-speed heat pump, International Journal of Refrigeration 133(2022), 259-266.

[46] H. Pu, G.L. Ding, X.K. Ma, H-T Hu, Y.F. Gao, Effects of biofouling on air-side heat transfer and pressure drop for finned tube heat exchangers, International Journal of Refrigeration 32 (2009), 1032-1040.

[47] M. Awais, A.A. Bhuiyan, Recent advancements in impedance of fouling resistance and particulate depositions in heat exchangers, International Journal of Heat and Mass Transfer 141 (2019), 580-603.

[48] T. Downey, J. Proctor, What can 13,000 air conditioners tell us? The Proceedings of the 2002 ACEEE Summer Study on Energy Efficiency in Buildings 1(2002), 53-67.

[49] J. Kim, S. Frank, J. E. Braun, D. Goldwasser, Representing Small Commercial Building Faults in EnergyPlus, Part I: Model Development, Buildings 9(2019), 233.

[50] C. Francis, G. Maidment, G. Davies, An investigation of refrigerant leakage in commercial refrigeration, International Journal of Refrigeration 74 (2017), 12-21.

[51] N. Ishii, T. Tsuji, E. Nonoguchi, K. Anami, Y. Terada, T. Morimoto, C.W. Knisely, Empirical Calculation Method of Bypass Leakage in Scroll Compressors, Proceedings of the International Compressor Engineering Conference at Purdue, Paper 2491, West Lafayette, IN, July 11–14, 2016.

[52] Z. Zhou, H. Chen, L. Xing, G. Li, W. Gou, An experimental study of the behavior of a model variable refrigerant flow system with common faults, Applied Thermal Engineering 202(2022), 117852.

[53] L. Lyons, Digitalisation: Opportunities for heating and cooling. Publications Office of the European Union: Luxembourg (2019).

[54] L. Atzori, A. Iera, G. Morabito. The internet of things: A survey. Computer networks, 54 (2010), 2787-2805.

[55] A. Fuller, Z. Fan, C. Day, C. Barlow. Digital twin: Enabling technologies, challenges and open research. IEEE access 8 (2020), 108952-108971.

[56] M.S. Mirnaghi, F. Haghighat, Fault detection and diagnosis of large-scale HVAC systems in buildings using data-driven methods: A comprehensive review, Energy & Buildings 229 (2020).

[57] J. Cirera, J.A. Carino, D. Zurita, J.A. Ortega, Data analytics for performance evaluation under uncertainties applied to an industrial refrigeration plant. IEEE access 7 (2019), 64127-64135.

[58] A. Afram, F. Janabi-Sharifi, Review of modeling methods for HVAC systems, Applied Thermal Engineering 67 (2014), 507-519.

[59] A. Afram, F. Janabi-Sharifi, A. S. Fung, K. Raahemifar,Artificial neural network (ANN) based model predictive control (MPC) and optimization of HVAC systems: A state of the art review and casestudy of a residential HVAC system, Energy and Buildings 141 (2017), 96-113.

[60] R. Isermann, Process Fault Detection Based on Modeling and Estimation—A Survey. Automatica 20(4) (1984), 387-404.

[61] T.M. Rossi, J.E. Braun, A Statistical, Rule-Based Fault Detection and Diagnostic Method for Vapor Compression Air Conditioners, HVAC&R Research 3 (1997), 19-37.

[62] H. Yang, T. Zhang, H. Li, D. Woradechjumroen, X. Liu, HVAC equipment, unitary: fault detection and diagnosis. In Encyclopedia of Energy Engineering and Technology, Second Edition (2014) pp. 854-864, CRC Press.

[63] Y. Zhao, T. Li, X. Zhang, C. Zhang, Artificial intelligence-based fault detection and diagnosis methods for building energy systems: Advantages, challenges and the future, Renewable and Sustainable Energy Reviews 109 (2019), 85-101.

[64] Y. Zhao, S. Wang, F. Xiao, A statistical fault detection and diagnosis method for centrifugal chillers based on exponentially-weighted moving average control charts and support vector regression, Applied Thermal Engineering, 51(2013), 560-572.

[65] Z. Liu, Y. Liu, D. Zhang, B. Cai, C. Zheng, Fault diagnosis for a solar assisted heat pump system under incomplete data and expert knowledge, Energy 87(2015), 41-48.

[66] B.P. Rasmussen, Dynamic modeling for vapor compression systems—Part I: Literature review, HVAC&R Research 18 (2012), 934-955.

[67] K. Arendt, M. Jradi, H.R. Shaker, C. Veje, Comparative analysis of white-, gray-and black-box models for thermal simulation of indoor environment: Teaching building case study, n Proceedings of the 2018 Building Performance Modeling Conference and SimBuild co-organized by ASHRAE and IBPSA-USA, Chicago, IL, USA (pp. 26-28).

[68] B. Citarella, A.W. Mauro, F. Pelella, Use of Artificial Intelligence in the Refrigeration Field, 6th IIR TPTPR Conference, September 1-3, 2021 - Vicenza, Italy, DOI: http://dx.doi.org/10.18462/iir.TPTPR.2021.2061.

[69] L. Yan, P. Hu, C. Li, Y. Yao, L. Xing, F. Lei, N. Zhu, The performance prediction of ground source heat pump system based on monitoring data and data mining technology, Energy and Buildings 127 (2016), 1085-1095.

[70] Z. Wang, X. Liu, H. Shen, Y. Wang, H. Li, Energy performance prediction of vapor-injection air source heat pumps in residential buildings using a neural network model, Energy & Buildings 228 (2020), 110499.

[71] H. Esen, M. Inalli, A.Sengur, M. Esen, Performance prediction of a ground-coupled heat pump system using artificial neural networks, Expert Systems with Applications 35 (2008), 1940–1948.

[72] E. Mathioulakis, G. Panaras, V. Belessiotis, Artificial neural networks for the performance prediction of heat pump hot water heaters, International Journal of Sustainable Energy, 37:2(2018), 173-192.

[73] O. Ekren, S. Sahin, Y. Isler, Comparison of different controllers for variable speed compressor and electronic expansion valve, International Journal of Refrigeration 33 (2010) 1161-1168.

[74] H.D. Vu, K.S. Chai, B. Keating, N. Tursynbek, B. Xu, K. Yang, Data Driven Chiller Plant Energy Optimization with Domain Knowledge, CIKM'17, November 6-10, 2017, Singapore.

[75] T.S. Chan, Y.C. Chang, J.H. Huang, Application of artificial neural network and genetic algorithm to the optimization of load distribution for a multiple-type-chiller plant, Build Simul 10(2017), 711–722.

[76] I. Staffell, D. Brett, N. Brandon, A. Hawkes, A review of domestic heat pumps. Energy & Environmental Science, 5(11)(2012), 9291-9306.

[77] M. Aydin, A. Şişman, A. Gültekin, B. Dehghan, An experimental performance comparison between different shallow ground heat exchangers. In Proceedings World Geothermal Congress (2015), 19-25.

[78] F. Robert, L. Gosselin, New methodology to design ground coupled heat pump systems based on total cost minimization, Applied Thermal Engineering 62.2 (2014), 481-491.

[79] W. Wu, H.M. Skye, Progress in ground-source heat pumps using natural refrigerants, International Journal of Refrigeration, 92(2018), 70-85.

[80] L. Xu, L. Pu, S. Zhang, Y. Li, Hybrid ground source heat pump system for overcoming soil thermal imbalance: A review, Sustainable Energy Technologies and Assessments 44(2021), 101098.

[81] R.S. Kamel, A.S. Fung, P.R.H. Dash, Solar systems and their integration with heat pumps: A review, Energy and Buildings 87 (2015), 395–412.

[82] J. Chu, C.A. Cruickshank, Solar-Assisted Heat Pump Systems: A Review of Existing Studies and Their Applicability to the Canadian Residential Sector, Journal of Solar Energy Engineering 136 (2014).

[83] T.T. Chow, G. Pei, K.F. Fong, Z. Lin, A.L.S. Chan, M. He, Modeling and application of direct-expansion solar-assisted heat pump for water heating in subtropical Hong Kong. Applied Energy, 87(2010), Vol. 2, 643-649.

[84] R. Lazzarin, Heat pumps and solar energy: A review with some insights in the future, International Journal of Refrigeration 116 (2020), 146–160.

[85] Y. Jung, J. Oh, U. Han, H. Lee, A comprehensive review of thermal potential and heat utilization for water source heat pump systems, Energy and Buildings 266 (2022), 112124.

[86] Gazzetta Ufficiale della Repubblica Italiana, Dectreto Legislativo 3 aprile 2206 n.152, VALORI LIMITI DI EMISSIONE IN ACQUE SUPERFICIALI E IN FOGNATURA, Parte terza, Allegato 5, Tabella 3.

[87] D.M. Van de Bor, C.A. Infante Ferreira, A,A, Kiss, Low grade waste heat recovery using heat pumps and power cycles, Energy 89 (2015), 864-873.

[88] O. Bamigbetan, T.M. Eikevik, P. Nekså, M. Bantle, M., C. Schlemminger, The development of a hydrocarbon high temperature heat pump for waste heat recovery, Energy 173(2019), 1141-1153.

[89] Z. Liu, L. Ma, J. Zhang, Application of a heat pump system using untreated urban sewage as a heat source. Applied Thermal Engineering, 62(2014), Vol. 2, 747-757.

[90] M.C. Comstock, J.E. Braun, E.A. Groll, The sensitivity of Chiller Performance to Common Faults, HVAC&R Research 7 (2001), 263-279.

[91] M.C. Comstock, J.E. Braun. Development of analysis tools for the evaluation of fault detection and diagnostics in chillers ASHRAE Research Project 1043-RP; also Ray W. Herrick Laboratories. Purdue University; 1999.

[92] I.N. Grace, D. Datta, S.A. Tassou, Sensitivity of refrigeration system performance to charge levels and parameters for on-line leak detection, Appied Thermal Engineering 25 (2005), 557-566.

[93] B.A. Qureshi, S.M. Zubair, The impact of fouling on performance of a vapor compression refrigeration system with integrated mechanical sub-cooling system, Applied Energy 92 (2012), 750-762.

[94] B.A. Qureshi, S.M. Zubair, Predicting the impact of heat exchanger fouling in refrigeration systems, International Journal of Refrigeration 44 (2014), 116-124.

[95] B.A. Qureshi, S.M. Zubair, The impact of fouling on the condenser of a vapor compression refrigeration system: An experimental observation, Intermational Journal of Refrigeration 38(2014), 260-266.

[96] Z. Du, P.A. Domanski, W. V. Payne, Effect of common faults on the performance of different types of vapor compression systems, Applied Thermal Engineering 98 (2016), 61-72.

[97] M. Mehrabi, D. Yuill, Generalized effects of faults on normalized performance variables of air conditioners and heat pumps, International Journal of Refrigeration 85 (2018), 409–430.

[98] J. Kim, S. Frank, P. Im, J.E. Braun, D. Goldwasser, M. Leach, Representing Small Commercial Building Faults in EnergyPlus, Part II: Model Validation, Buildings 9 (2019), 239.

[99] M. Mehrabi, D. Yuill, Fouling and Its Effects on Air-cooled Condensers in Split System Air Conditioners (RP-1705), Science and Technology for the Built Environment 25(2019), 784-793.

[100] D. Noel, P. Riviere, C. Teuillieres, O. Cauret, D. Marchio, Experimental Characterization of Fault Impacts on the Functioning Variables of an Inverter Driven Heat Pump, 10th International Conference on System Simulation in Buildings, Dec 2018, Liège,Belgium.

[101] Y. Hu, D. P. Yuill , A. Ebrahimifakhar , A. Rooholghodos, An experimental study of the behavior of a high efficiency residential heat pump in cooling mode with common installation faults imposed, Applied Thermal Engineering 184 (2021), 116116.

[102] Y. Hu. D.P.Yuill, S.A. Rooholghodos, A. Ebrahimfakhar, Y. Chen, Impacts of simultaneous operating faults on cooling performance of a high efficiency residential heat pump, Energy and Buildings 242 (2021), 110975.

[103] Y. Hu, D. P. Yuill, Effects of multiple simultaneous faults on characteristic fault detection features of a heat pump in cooling mode, Energy & Buildings 251 (2021), 111355.

[104] F. Pelella, L. Viscito, A.W. Mauro, Combined effects of refrigerant leakages and fouling on air-source heat pump performances in cooling mode, Applied Thermal Engineering 204 (2022), 117965.

[105] A.W. Mauro, G. Napoli, F. Pelella, Effect of refrigerant leakages on energy consumption of an electric heat pump for domestic air-conditioning, 6th IIR TPTPR Conference, September 1-3, 2021 - Vicenza, Italy, DOI: http://dx.doi.org/10.18462/iir.TPTPR.2021.2062.

[106] MATLAB release. Natick, Massachussets, United States, The MathWorks, Inc.

[107] E.W. Lemmon, M.L. Huber., M.O. McLinden, REFPROP, NIST standard reference database 23, version 9.0. National Institute of Standards and Technology (2007), Gaithersburg, MD.

[108] F. Botticella, F. De Rossi, A.W. Mauro, G.P. Vanoli, L. Viscito, Multi-criteria (thermodynamic, economic and environmental) analysis of possible design options for residential heating split systems working with low GWP refrigerants, International Journal of Refrigeration 87 (2018), 131-153.

[109] E. Navarro-Peris, J.M. Corberán, L. Falco, I.O. Martínez-Galván, New non-dimensional performance parameters for the characterization of refrigeration compressors, Int. J. Refrigeration 36 (2013), 1951-1964.

[110] R.K. Shah, D.P. Sekulic, Fundamental of Heat Exchanger Design, John Wiley & Sons, 2003.

[111] K. Gungor, R. Winterton, A general correlation for flow boiling in tubes and annuli, Int. J. Heat Mass Transf. 29 (1986), 351–358.

[112] G. Lillo, R. Mastrullo, A. W. Mauro, L. Viscito, Flow boiling of R32 in a horizontal stainless steel tube with 6.00 mm ID. Experiments, assessment of correlations and comparison with refrigerant R410A, Int. J. of Refrigeration 97 (2019), 143-156.

[113] M.M. Shah, A general correlation for heat transfer during film condensation inside pipes, International Journal of Heat and Mass Transfer 22 (1979), 547-556.

[114] F.W. Dittus, L.M.K. Boelter, Heat transfer in automobile radiators of the tubular type, Univ. Calif. Publ. Eng. 2 (1930), 443–461.

[115] C.C. Wang, Y.Y. Chi, Heat transfer and friction characteristics of plain fin-and-tube heat exchangers: Part II. Correlation, International Journal of Heat and Mass Transfer 43 (2000), 2693-2700.

[116] T.E. Schmidt, Heat transfer calculations for extended surfaces. Refrigerating Engineering, 57 (1949), 351-357.

[117] Z. Rouhani, E. Axelsson, Calculation of volume void fraction in a subcooled and quality region, Int. J. of Heat and Mass Transfer 17(1970), 383-393.

[118] W.A. Beckman, L. Broman, A. Fiksel, S.A. Klein, E. Lindberg, M. Schuler, J. Thornton, TRNSYS The most complete solar energy system modeling and simulation software. Renewable energy, 5(1994), 486-488.

[119] B. Chen, J.E. Braun, Simple Fault Detection and Diagnosis Methods for Packaged Air Conditioners, International Refrigeration and Air Conditioning Conference, International Refrigeration and Air Conditioning Conference (2000).

[120] Y. Hwang, C.I. Ferreira, C.C. Piao, Guideline for life cycle climate performance. December 2015, International Institute of Refrigeration (2015) Paris.

[121] F. Pelella , L. Viscito , A.W. Mauro, Soft faults in residential heat pumps: Possibility of evaluation via on-field measurements and related degradation of performance, Energy Conversion and Management 260 (2022), 115646.

[122] K. Choi, S.M. Namburu, M.S. Azam, J. Luo, K.R. Pattipati, A. Patterson-Hine. Fault diagnosis in HVAC chillers. IEEE Instrumentation & Measurement Magazine, 8(3) (2005), 24-32.

[123] S.A. Tassou, I.N. Grace, Fault diagnosis and refrigerant leak detection in vapour compression refrigeration systems, International Journal of Refrigeration 28 (2005), 680-688.

[124] J. Navarro-Esbrı´, E. Torrella, R. Cabello, A vapour compression chiller fault detection technique based on adaptative algorithms. Application to on-line refrigerant leakage detection, International Journal of Refrigeration 29 (2006) 716–723.

[125] D. Zogg, E. Shafai, H.P. Geering, Fault diagnosis for heat pumps with parameter identification and clustering, Control Engineering Practice 14 (2006), 1435–1444.

[126] S.M. Namburu, M.S. Azam, J. Luo, K.Choi, K.R. Pattipati, Data-Driven Modeling, Fault Diagnosis and Optimal Sensor Selection for HVAC Chillers, IEEE Transactions on Automation Science and Engineering 4 (2007), 469-473.

[127] H. Han, B. Gu, J. Kang, Z.R. Li, Study on a hybrid SVM model for chiller FDD applications, Applied Thermal Engineering 31 (2011), 582-592.

[128] H. Han, B. Gu, Y. Hong, J. Kang, Automated FDD of multiple-simultaneous faults (MSF) and the application to building chillers, Energy and Buildings 43 (2011), 2524-2532.

[129] Z. Sun, H. Jin, J. Gu, Y. Huang, X. Wang, H. Yang, X. Shen, Studies on the online intelligent diagnosis method of undercharging subhealth air source heat pump water heater, Applied Thermal Engineering 169(2020), 114957.

[130] B. Cai, Y. Liu, Q. Fan, Y. Zhang, Z. Liu, S. Yu, R. Ji, Multi-source information fusion based fault diagnosis of ground-source heat pump using Bayesian network, Applied Energy 114 (2014).

[131] P. Wang, R. Gao, On-Line Fault Detection and Diagnosis for Chiller System, 2016 IEEE International Conference on Automation Science and Engineering, Fort Worth, TX, USA, August 21-24, 2016.

[132] K. Yan, Z. Ji, W. Shen, Online fault detection methods for chillers combining extended kalman filter and recursive one-class SVM, Neurocomputing 228 (2017), 205-212.

[133] Y.H. Eom, J.W. Yoo, S.B. Hong, M.S. Kim, Refrigerant charge fault detection method of air source heat pump system using convolutional neural network for energy saving, Energy 187(2019).

[134] Z. Zhou, J. Wang, H. Chen, W. Wei, C. Xu, An online compressor liquid floodback fault diagnosis method for variable refrigerant flow air conditioning system, International Journal of Refrigeration 111 (2020), 9-19.

[135] J. Wang, G. Li, H. Chen, J. Liu, Y. Guo, Y. Hub, J. Li, Liquid floodback detection for scroll compressor in a VRF system under heating mode, Applied Thermal Engineering 114 (2017), 921-930.

[136] J.K. Hwang, P.N. Duhirwe, G.Y. Yun, S.Lee. H. Seo, I. Kim, M. Santamouris, A Novel Hybrid Deep Neural Network Model to Predict the Refrigerant Charge Amount of Heat Pumps, Sustainability 12(2020), 2914.

[137] W. Kim, J.E. Braun, Development, implementation, and evaluation of a fault detection and diagnostics system based on integrated virtual sensors and fault impact models, Energy & Buildings 226(2020), 110368.

[138] K. Yan, A. Chong, Y. Mo, Generative adversarial network for fault detection diagnosis of chillers, Building and Environment 172 (2020), 106698.

[139] Z. Zhang, H. Han, X. Cui, Y. Fan, Novel application of multi-model ensemble learning for fault diagnosis in refrigeration systems, Applied Thermal Engineering 164 (2020), 114516.

[140] W. Kim, J-H. Lee, Fault detection and diagnostics analysis of air conditioners using virtual sensors, Applied Thermal Engineering 191(2021), 116848.

[141] H. Li, J.E. Braun, Decoupling features and virtual sensors for diagnosis of faults in vapor compression air conditioners, Int. J. Refrig. 30:3 (2007), 546–564.

[142] O. Comakli, K. Kaygusuz, T. Ayhan, Solar-assisted heat pump and energy storage for residential heating, Solar energy, 51(5)(1993), 357-366.

[143] V. Trillat-Berdal, B. Souyri, G. Fraisse, Experimental study of a ground-coupled heat pump combined with thermal solar collectors. Energy and Buildings, 38(2006), Vol.12, 1477-1484.

[144] Z. Han, M. Zheng, F. Kong, F. Wang, Z. Li, T. Bai, Numerical simulation of solar assisted ground-source heat pump heating system with latent heat energy storage in severely cold area, Applied Thermal Engineering 28(11-12) (2008), 1427-1436.

[145] X. Wang, M. Zheng, W. Zhang, S. Zhang, T. Yang, Experimental study of a solar-assisted ground-coupled heat pump system with solar seasonal thermal storage in severe cold areas. Energy and Buildings, 42 (2010), Vol.11, 2104-2110.

[146] S.J. Sterling, M.R. Collins, Feasibility analysis of an indirect heat pump assisted solar domestic hot water system, Applied Energy 93(2012), 11-17.

[147] R. Yumrutaş, M. Ünsal, Energy analysis and modeling of a solar assisted house heating system with a heat pump and an underground energy storage tank. Solar Energy, 86(2012), Vol. 3, 983-993.

[148] A. Arteconi, C. Brandoni, G. Rossi, F. Polonara, Experimental evaluation and dynamic simulation of a ground coupled heat pump for a commercial building. International journal of energy research, 37(2013), Vol. 15, 1971-1980.

[149] V. Verma, K. Murugesan, Optimization of solar assisted ground source heat pump system for space heating application by Taguchi method and utility concept. Energy and Buildings 82(2014), 296-309.

[150] C.J. Banister, M.R. Collins. Development and performance of a dual tank solar-assisted heat pump system, Applied Energy 149 (2015), 125-132.

[151] A.A. Safa, A.S. Fung, R. Kumar, Heating and cooling performance characterisation of ground source heat pump system by testing and TRNSYS simulation, Renewable Energy 83(2015), 565-575.

[152] N. Zhu, P. Hu, Y. Lei, Z. Jiang, F. Lei, Numerical study on ground source heat pump integrated with phase change material cooling storage system in office building, Applied Thermal Engineering 87(2015), 615-623.

[153] J. Ji, J. Cai, W. Huang, Y. Feng, Experimental study on the performance of solar-assisted multi-functional heat pump based on enthalpy difference lab with solar simulator, Renewable Energy 75 (2015), 381-388.

[154] J. Cai, J. Ji, Y. Wang, W. Huang, Numerical simulation and experimental validation of indirect expansion solar-assisted multi-functional heat pump, Renewable Energy 93 (2016), 280-290.

[155] L. Ni, D. Qv, Y. Yao, F. Niu, W. Hu, An experimental study on performance enhancement of a PCM based solar-assisted air source heat pump system under cooling modes. Applied Thermal Engineering 100(2016), 434-452.

[156] L. Croci, L. Molinaroli, P. Quaglia, Dual Source Solar Assisted Heat Pump Model Development, Validation and Comparison to Conventional Systems, AiCARR 50th International Congress; Beyond NZEB Buildings, 10-11 May 2017, Matera, Italy.

[157] A.R. Starke, J.M. Cardemil, R. Escobar, S. Colle, Thermal analysis of solar-assisted heat pumps for swimming pool heating, Journal of the Brazilian Society of Mechanical Sciences and Engineering, 39(6)(2017), 2289-2306.

[158] A.R. Starke, J.M. Cardemil, S. Colle, Multi-objective optimization of a solar-assisted heat pump for swimming pool heating using genetic algorithm. Applied Thermal Engineering 142(2018), 118-126.

[159] J.M. Corberán, A. Cazorla-Marín, J. Marchante-Avellaneda, C. Montagud, Dual source heat pump, a high efficiency and cost-effective alternative for heating, cooling and DHW production International Journal of Low-Carbon Technologies 13 (2018), 161–176.

[160] M.J. Kim, B.M. Seo, J.M. Lee, J.M. Choi, K.H. Lee, Operational behavior characteristics and energy saving potential of vertical closed loop ground source heat pump system combined with storage tank in an office building, Energy and Buildings, 179(2018), 239-252.

[161] M. Dannemand, B. Perers, S. Furbo, Performance of a demonstration solar PVT assisted heat pump system with cold buffer storage and domestic hot water storage tanks. Energy and Buildings 188 (2019), 46-57.

[162] E. Hervás-Blasco, E. Navarro-Peris, J.M. Corberán, Optimal design and operation of a central domestic hot water heat pump system for a group of dwellings employing low temperature waste heat as a source. Energy 188(2019), 115979.

[163] M.T. Plytaria, E. Bellos, C. Tzivanidis, K.A. Antonopoulos, Financial and energetic evaluation of solar-assisted heat pump underfloor heating systems with phase change materials. Applied Thermal Engineering 149 (2019), 548-564.

[164] D.U. Shin, S.R. Ryu, K.W. Kim, Simultaneous heating and cooling system with thermal storage tanks considering energy efficiency and operation method of the system, Energy and Buildings 205 (2019), 109518.

[165] J. Huang, J. Fan, S. Furbo, Demonstration and optimization of a solar district heating system with ground source heat pumps. Solar Energy 202(2020), 171-189.

[166] C. Kutlu, Y. Zhang, T. Elmer, Y. Su, S. Riffat, A simulation study on performance improvement of solar assisted heat pump hot water system by novel controllable crystallization of supercooled PCMs. Renewable Energy 152(2020), 601-612.

[167] J. Ma, A.S. Fung, M. Brands, N. Juan, O.M.A Moyeed, Performance analysis of indirect-expansion solar assisted heat pump using CO2 as refrigerant for space heating in cold climate. Solar Energy 208 (2020), 195-205.

[168] T. Sun, L. Yang, L. Jin, Z. Luo, Y. Zhang, Y. Liu, Z. Wang, A novel solar-assisted ground-source heat pump (SAGSHP) with seasonal heat-storage and heat cascade utilization: Field test and performance analysis. Solar Energy 201(2020), 362-372.

[169] Y. Wang, Z. Rao, J. Liu, S. Liao, An optimized control strategy for integrated solar and air-source heat pump water heating system with cascade storage tanks, Energy and Buildings 210 (2020), 109766.

[170] J. Zhou, Z. Zhu, X. Zhao, Y. Yuan, Y. Fan, S. Myers, Theoretical and experimental study of a novel solar indirect-expansion heat pump system employing mini channel PV/T and thermal panels, Renewable Energy 151(2020), 674-686.

[171] J.F. Belmonte, M. Díaz-Heras, J.A. Almendros-Ibáñez, L.F. Cabeza, Simulated performance of a solar-assisted heat pump system including a phase-change storage tank for residential heating applications: A case study in Madrid, Spain, Journal of Energy Storage 47 (2022), 103615.

[172] M. Koşan, M. Aktaş, Experimental investigation of a novel thermal energy storage unit in the heat pump system, Journal of Cleaner Production 311(2021), 127607.

[173] B. Lei, Z.J. Duan, Y.T. Wu, Thermodynamic investigations on an integrated heat pump with thermal storage for wind-solar hybrid heating, Energy Conversion and Management 254(2022), 115276.

[174] Y. Li, A. Mojiri, G. Rosengarten, C. Stanley, Residential demand-side management using integrated solar-powered heat pump and thermal storage, Energy and Buildings 250(2021), 111234.

[175] M. Nasouri, G.N. Bidhendi, M.J. Amiri, N. Delgarm, S. Delgarm, K. Azarbad, Performance-based Pareto optimization and multi-attribute decision making of an actual indirect-expansion solar-assisted heat pump system, Journal of Building Engineering 42 (2021), 103053.

[176] T. Ural, G.K. Dolgun, O.V. Güler, A. Keçebaş, Performance analysis of a textile based solar assisted air source heat pump with the energy and exergy methodology, Sustainable Energy Technologies and Assessments 47(2021), 101534.

[177] A.M. Bulmez, V. Ciofoaia, G. Năstase, G. Dragomir, A.I. Brezeanu, A. Şerban, An experimental work on the performance of a solar-assisted ground-coupled heat pump using a horizontal ground heat exchanger. Renewable Energy 183 (2022), 849-865.

[178] M.A. Kamazani, C. Aghanajafi, Multi-objective optimization and exergoeconomic evaluation of a hybrid geothermal-PVT system integrated with PCM. Energy 240(2022), 122806.

[179] M. Lee, D. Lee, M.H. Park, Y.T. Kang, Y. Kim. Performance improvement of solar-assisted ground-source heat pumps with parallelly connected heat sources in heating-dominated areas. Energy 240 (2022), 122807.

[180] L.W. Yang, N. Hua, J.H. Pu, Y. Xia, W.B. Zhou, R.J. Xu, T. Yang, Y. Belyayev, H.S. Wang, Analysis of operation performance of three indirect expansion solar assisted air source heat pumps for domestic heating, Energy Conversion and Management 252 (2022), 115061.

[181] R. Mastrullo, A.W. Mauro, F. Pelella, L. Viscito, Dual source (air-solar) heat pump: thermo-economic analysis of sizing factors depending on climate conditions, 15th IIR-Gustav Lorentzen conference on Natural Refrigerants, June 13-15, Trondheim, Norway.

[182] C.C. Smith, T.A. Weiss, Design application of the Hottel-Whillier-Bliss equation. Solar energy 19(1977), Vol. 2, 109-113.

[183] Berliner Energieagentur GmbH, Meeting cooling demands in SUMMER, Summerheat Publischable Report, April 2009.

[184] A.C. Ferreira, A. Silva, J.C. Teixeira, S. Teixeira, Multi-Objective Optimization of Solar Thermal Systems Applied to Portuguese Dwellings, Energies 2020, 13, 6739.

[185] Eurostat, Electricity prices (including taxes) for household consumers, second half 2021, https://ec.europa.eu/eurostat/statistics-explained/index.php?title=Electricity_price_statistics#:~:text=The%20EU%20average%20price%20in,was%20%E2%82%AC0.2369%20per%20kWh.

[186] F. Pelella, G. Zsembinszki, L. Viscito, A.W. Mauro, L.F. Cabeza, Thermo-economic optimization of a multi-source (air/sun/ground) residential heat pump with a water/PCM thermal storage, Applied Energy (in review).

[187] A.W. Mauro, G. Napoli, F. Pelella, L.Viscito, Numerical analysis of a Solar-Assisted Dual-Source heat pump coupled with a thermal storage for residential heating, 16th International Conference of Heat Transfer, Fluid Mechanics and Thermodynamics (HEFAT), 8-10 August 2022, Virtual.

[188] G.A. Longo, S. Mancin, G. Righetti, C. Zilio, A new model for refrigerant boiling inside Brazed Plate Heat Exchangers (BPHEs). International Journal of Heat and Mass Transfer 91(2015), 144-149.

[189] H. Martin, A theoretical approach to predict the performance of chevron-type plate heat exchangers. Chemical Engineering and Processing: Process Intensification 35 (1996), Vol. 4, 301-310.

[190] M. Krarti, C. Lopez-Alonzo, D. E. Claridge, J. F. Kreider, Analytical Model to Predict Annual Soil Surface Temperature Variation, Journal of Solar Energy Engineering 117 (1995).

[191] E. Skoplaki, J.A. Palyvos, On the temperature dependence of photovoltaic module electrical performance: A review of efficiency/power correlations, Solar energy, 83 (2009), Vol. 5, 614-624.

[192] A. Crespo, G. Zsembinszki, D. Vérez, E. Borri, C. Fernández, L.F. Cabeza, A. de Gracia, Optimization of design variables of a phase change material storage tank and comparison of a 2D implicit vs. 2D explicit model, Energies 14(2021), Vol.9, 2605.

[193] G. Zsembinszki, P. Moreno, C. Solé, A. Castell, L.F. Cabeza, Numerical model evaluation of a PCM cold storage tank and uncertainty analysis of the parameters, Applied thermal engineering 67(2014), Vol 1-2, 16-23.

[194] Rubitherm Technologies GmbH - Imhoffweg 6 - 12307 Berlin, PCM RT-Line: https://www.rubitherm.eu/en/index.php/productcategory/organische-pcm-rt.

[195] J.C. Helton, F.J. Davis, Latin hypercube sampling and the propagation of uncertainty in analyses of complex systems. Reliability Engineering & System Safety, 81(2003), Vol. 1, 23-69.

[196] S. Forrest, Genetic algorithms. ACM Computing Surveys (CSUR) 28 (1996), Vol.1, 77-80.

[197] K. Zhou, J. Mao, H. Zhang, Y. Li, X. Yu, F. Chen, M. Li, Design strategy and techno-economic optimization for hybrid ground heat exchangers of ground source heat pump system, Sustainable Energy Technologies and Assessments 52 (2022), 102140.

[198] S. Sanaye, A. Shirazi, Thermo-economic optimization of an ice thermal energy storage system for air-conditioning applications, Energy and Buildings 60 (2013), 100–109.

[199] E. Tervo, K. Agbim, F. DeAngelis, J. Hernandez, H. K. Kim, A. Odukomaiya, An economic analysis of residential photovoltaic systems with lithium ion battery storage

in the United States. Renewable and Sustainable Energy Reviews, 94(2018), 1057-1066.

[200] Solarbayer - Solar systems - High performance collectors - https://www.solarbayer.com/solar-systems.html.

[201] SvizzeraEnergia, Ufficio federale dell'energia UFE Mühlestrasse 4, CH-3063 Ittigen. Indirizzo postale : CH-3003 Berna - https://www.svizzeraenergia.ch/.

[202] PCM Products Ltd - Unit 32 Mere View Industrial Estate, Yaxley, Unit 32 Mere View Industrial Estate, Yaxley, Peterborough, Cambridgeshire, PE7 3HS - https://www.pcmproducts.net/.

[203] S.B. Bhandari, Discounted payback period-some extensions, Journal of Business and Behavioral Sciences, 21 (2009), 28-38.

Summary of Figures

Figure 2.1. Total global final energy consumption by sector for the period from 1990 to 2019 (a) and percentages for year 2019 (b), according to the International Energy Agency (IEA) database [1].....10
Figure 2.2. Percentages of final use energy consumption, for commercial (a) and residential (b) buildings 11
Figure 2.3. Growing of space cooling energy demand between 1990 and 2016, divided by source, according to IEA [5].....11
Figure 2.4. (a) Global primary energy consumption by fossil fuels and renewable sources, between 1990 and 2020, according to [6]. (b) Percentage of energy sources in buildings in 2021, according to IEA [7] 12
Figure 2.5. CO_2 total emission trends by 2050 (a) and temperature rise prediction in 2100, in the three future scenarios STEPS, APS and NZE defined by IEA [12].....13
Figure 2.6. (a) CO2 emission trends in buildings up to 2030 for space heating, water heating, cooking and other in the APS and NZE scenarios. (b) Final energy consumption divided by fuel in buildings with future prevision in APS and NZE scenarios.....14
Figure 2.7. Energy consumption trend for space cooling up to 2050, in a baseline and efficient cooling scenarios, and divided per country, according to [5].....14
Figure 2.8. General scheme of a vapor compression technology system (a), and thermodynamic cycle on the temperature – specific entropy diagram (b).....16
Figure 2.9. Example of a split system (a) and schematic according to Bolaji (2012) [15] (b).....17
Figure 2.10. Example of a water heat pump (a) and schematic according to [18] 18
Figure 2.11. Example of a VRF system (a) and schematic (b).....18
Figure 2.12. Example of a water chiller (a) and schematic according to Li et al. [24](b).....19
Figure 2.13. Energy efficiency values of available commercial air conditioning systems, according to [5], with minimum, maximum and average available on the market.....24
Figure 2.14. Heat pump stock (blue, left axis) and sales (red, right axis) in Europe, between 2004 and 2020 according to the EHPA Market Report 2022 [35].....26
Figure 2.15. Heat Pump sales per typology between ground source, air to water and air to air, in Europe between 2008 and 2020 according to the EHPA Market Report 2022 [35].....27
Figure 2.16. System percentage of heating technology sales in the world between 2010 and 2030 in an NZE scenario, according to [36].....27
Figure 2.17. List of common faults on heat pumps and air conditioning systems, categorized in hard and soft faults.....29
Figure 2.18. Classification of FDDE methods according to Zhao et al. [63].....34
Figure 2.19. Ground temperature distribution depending on the depth and on the month of the year. Source: Aydin et al. [77].....37
Figure 2.20. Ground source heat pump classification based on the circuitry, on the kind of system and on the GHE orientation (left). Representation of open-loop, horizontal trenches and vertical boreholes systems (right).....38
Figure 2.21. Solar assisted heat pump classification based on the kind of solar source, on the kind of system and on the connection between the solar source and the heat pump (left). Representation of DX and IDX systems and of a dual source configuration. Source: Chu and Cruickshanks [82].....40
Figure 3.1. Schematic and piping of the residential air source heat pump studied in Pelella et al. [95] for domestic heating and cooling.....48
Figure 3.2. Elementary geometry of a fin-and-tube heat exchanger considered in the paper of Pelella et al. [95].(a) Clean surfaces. (b) Condenser fouling: presence of dust along fins for the first row. (c) Evaporator fouling : presence of dust only on the face-front filter.....52
Figure 3.3. Steps for the resolution algorithm of the model presented in Pelella et al. [95], both in normal and in faulty operating conditions 54

Figure 3.4. Fans characteristic curves on the static pressure drop - volumetric flow rate diagram, and coupling with characteristic curves of heat exchanger coils, in case of absence of fouling. (a) Axial fan of the external unit. (b) Tangential blower of the internal unit.....57
Figure 3.5. Calibration curves for volumetric (a) and global (b) compressor efficiencies depending on the compression ratio and on inlet compressor densities, and comparison with manufacturer data.....58
Figure 3.6. Validation of the valve mass flow rate model, and comparison with manufacturer data 58
Figure 3.7. Performance maps in cooling mode in terms of COP value, depending on ambient temperature and fault intensities, for a fixed condition of the indoor temperature of 26 °C. (a) Evaporator fouling. (b) Condenser fouling. (c) Refrigerant leakage 60
Figure 3.8. 3-D contour plot for COP depending on the three fault intensities, for ambient and indoor temperatures of respectively 35 °C and 26 °C (a). Projection of the 3-D plot considering the absence, respectively, of evaporator fouling ($FIev = 0$, b), of condenser fouling ($FIco = 0$, c) and of refrigerant leakage ($FIleak = 0$,d).....61
Figure 3.9. Temperature – specific entropy diagrams for fixed conditions of ambient and indoor temperature of 35 °C and 26 °C, obtained in case of a 40% refrigerant leakage (a), a 40% condenser fouling (b) and a 40% evaporator fouling (c). Solid and dashed lines are related respectively to fault-free and faulty thermodynamic cycles 63
Figure 3.10. Temperature – specific entropy diagrams in case of multiple simultaneous faults, for fixed conditions of ambient and indoor temperature of 35 °C and 26 °C. 40% condenser fouling (a), 40% evaporator fouling (b) and 30% refrigerant leakage (b) reported respectively standalone (green solid lines) or combined with another fault (coloured dashed lines), and simultaneous combination of all the three faults analysed (d). In all cases the fault-free thermodynamic cycles are represented with red solid lines.....65
Figure 3.11 Cooling load provided by the machine (red) and requested by the user (blue) depending on the external ambient temperature.....68
Figure 3.12. Number of operating hours vs. external temperature (a) and external temperature evolution in months between May and September (b), for the climate conditions of Naples, Miami and Shanghai 69
Figure 3.13. Example of fault intensity evolution along one year, in case of a 20%/year refrigerant leakage (a), a maximum condenser fouling of 40%, with the 90% reached in 2000h(b) and a maximum evaporator fouling of 20%, with the 90% reached in 3000h. The 90% limit is represented by the black dashed lines 71
Figure 3.14. COP evolution (a, b) and corresponding fault intensities evolution (c, d) along the entire machine lifetime in cooling mode for Naples climate conditions, for a 10%/year refrigerant leakage, a maximum condenser fouling of 40% and a maximum evaporator fouling of 20%, in case of a not-planned (a, c) and every two years (b, d) maintenance scenarios. 73
Figure 3.15. Percentages of scenario for which SCOP results to be penalized more than 15% (a), 10% (b) and 5% (c), for the cooling mode, depending on the climate condition and on the maintenance scenario investigated.....82
Figure 3.16. Performance maps in heating mode in terms of COP value, depending on ambient temperature and fault intensities, for a fixed condition of the indoor temperature of 20 °C. (a) Evaporator fouling. (b) Condenser fouling. (c) Refrigerant leakage 84
Figure 3.17. Temperature – specific entropy diagrams for fixed conditions of ambient and indoor temperature of 7 °C and 22 °C, obtained in case of a 40% refrigerant leakage (a), a 40% condenser fouling (b), a 40% evaporator fouling (c), and combined a 40% for all the fault intensities(d). Solid and dashed lines are related respectively to fault-free and faulty thermodynamic cycles 86
Figure 3.18. Number of operating hours vs. external temperature (a) and external temperature evolution in months between October and April (b), for the climate conditions of New York, Beijing and Vienna 87
Figure 3.19. COP evolution and corresponding fault intensities evolution along the entire machine lifetime in heating mode for New York climate conditions, for a 10%/year refrigerant leakage, a

maximum condenser fouling of 10% and a maximum evaporator fouling of 20%, in case of a not-planned (a) and every two years (b) maintenance scenarios 89
Figure 3.20. Percentages of scenario for which SCOP results to be penalized more than 15% (a), 10% (b) and 5% (c), for the heating mode, depending on the climate condition and on the maintenance scenario investigated 96
Figure 3.21. Graphical scheme for the two steps carried out in this work. The first is to generate data of thermodynamic cycles through the physics-based model and compared each other, the second is to understand if from this data it is possible to trace back to the cycle and detect, diagnoses and/or evaluate a fault 97
Figure 3.22. Indication of the number and the position of pressure and temperature sensors employed in the FDDE processes 103
Figure 3.23. Fault detection domain depending on fault intensities analysed. Instrumental uncertainties of ±3 bar & ±3 °C (a) and of ±1 bar & ±1 °C (b) 104
Figure 3.24. Fault diagnosis and evaluation domain depending on fault intensities, for an identification step of 10% and for uncertainties of ±1 bar and ±0.7 °C. (a) Entire domain. (b) First identification surface rotated by 90° and COP penalization for each point. Point A, B, C and D are further investigated in Figure 3.25 and Table 3.18 105
Figure 3.25. Temperature – specific entropy diagrams for condition A, B, C and D of Figure 3.24. (a) Point A: 20% refrigerant leakage and 20% evaporator fouling. (b) Point B: 40% refrigerant leakage. (c) Point C: 20% condenser fouling and 20% evaporator fouling. (d) Point D: 10% condenser fouling and 30% evaporator fouling. In all cases solid grey lines refer to similar thermodynamic cycles of other faulty conditions similar to the investigated points 107
Figure 3.26. Fault diagnosis and evaluation domain depending on fault intensities, for an identification step of 10% and for uncertainties of ±0.3 bar and ±0.7 °C. (a) Entire domain. (b) First identification surface rotated by 90° and COP penalization for each point 108
Figure 3.27. Fault diagnosis and evaluation domain depending on fault intensities, for an identification step of 20% and for uncertainties of ±1 bar and ±2.3 °C. (a) Entire domain. (b) First identification surface rotated by 90° and COP penalization for each point 109
Figure 3.28. Fault diagnosis and evaluation domain depending on fault intensities, for an identification step of 5% and for uncertainties of ±0.2 bar and ±0.5 °C. (a) Entire domain. (b) First identification surface rotated by 90° and COP penalization for each point 109
Figure 3.29. Fault diagnosis and evaluation domain depending on fault intensities, for an identification step of 5% and for uncertainties of ±0.2 bar and ±0.2 °C. (a) Entire domain. (b) First identification surface rotated by 90° and COP penalization for each point 110
Figure 3.30 – Confusion matrixes for the ML based models in the prediction of refrigerant leakage (a), condenser fouling(b) and evaporator fouling (c) 111
Figure 3.31. COP evolution and comparison between fault intensities predicted with the physics-based approach (solid lines) and the machine-learning based approach (coloured dots), with indications for the mean absolute errors. (a) 3%/year refrigerant leakage, 40% maximum condenser fouling and absence of evaporator fouling. (b) 40% maximum condenser fouling, 40% maximum evaporator fouling an absence of refrigerant leakage 112
Figure 4.1. Schematic of the direct expansion solar assisted heat pump studied in Mastrullo et al. [157] 128
Figure 4.2. Example of thermal solar collector efficiency, according to Hottel-Whiller-Bliss equation [158], depending on the solar radiation and on the difference between the external ambient and the evaporation temperatures 130
Figure 4.3. Steps of the resolution algorithm for the model of Mastrullo et al. [157] 131
Figure 4.4. Performance maps in terms of COP values against ambient temperature in heating mode, for air (dashed black lines) and sun (coloured solid lines) evaporation modes, for a fixed indoor temperature of 20 °C. Effect of different solar radiations for 10 solar collectors (a) and effect of the number of solar collectors for a fixed solar radiation of 263 W/m^2(b) 132

Figure 4.5. Solar radiation threshold, depending on the ambient temperature and the number of solar collectors, above which is more convenient to operate in sun mode, and below in air mode 132
Figure 4.6. Number of operating hours (a) and solar radiation (b) vs. ambient temperature, for the climate conditions investigated of Naples, Berlin and Bergen, according to the TRNSYS meteorologic database [109].....133
Figure 4.7. COP evolution along a year and valued of SCOP for a number of thermal solar collectors of 5 (a, c, e) and 15 (b, d, f), for the climate conditions of Naples (a, b), Berlin (c, d) and Bergen (e, f). Red points refer to the working hours of the heat pump operating in sun mode, whereas blue points are related to air evaporation working hours.....135
Figure 4.8. Investment, operating and total costs results depending on the number of thermal solar panels, for Naples (a), Berlin (b) and Bergen (c) climate conditions.....138
Figure 4.9. Total costs vs. SCOP (a) and vs. TEWI (b) for all the configurations and climate conditions investigated. The diamonds refer to the baseline configuration of a traditional air-to-air heat pump .138
Figure 4.10. Schematic of the system analysed in Pelella et al. [162], conceived to simulate all the possible configurations of multi-source (sun, ground, air) heat pump considered 141
Figure 4.11. User requested load evolution along a year. Instantaneous evaluated through expression 4.1 (black line), and attenuated by building inertia (red line) 142
Figure 4.12. Temperature profiles at the evaporator (a) and at the condenser (b), depending on the heat transfer surfaces for evaporating, condensing, superheating and de-superheating.....144
Figure 4.13. Evolution of ambient temperature (green line), solar radiation (red lined) and ground temperature (black line) evaluated with the model of Krarti et al. [138], for external climate conditions of Naples 145
Figure 4.14. Example of photovoltaic solar collector efficiency, according to Skoplaki and Palyvos [167], depending on the solar radiation and on the surface temperature of the collector.....146
Figure 4.15. Elementary geometry of the PCM storage tank model of Zsembinszki et al. [168], [169] (a) and for the 1D version of the model employed in this work (b).....147
Figure 4.16. Specific heat capacity for the considered PCM material depending on the temperature level, in case of a melting temperature of 25 °C, according to PCM manufacturer data [141]. Melting and solidification curves are respectively reported in red and blue.....147
Figure 4.17. System control strategy for the solar loop, the user loop and the heat pump.....149
Figure 4.18. System control strategy for the storage battery 149
Figure 4.19. Steps for the resolution algorithm used to simulate the entire system, coupling single component models of Pelella et al. [162].....151
Figure 4.20. Number of operating hours (a) and solar radiation (b) vs. ambient temperature, for the climate conditions investigated of Athens, Strasbourg and Helsinki, according to TRNSYS meteorologic database [109].....153
Figure 4.21. Calibration results for the compressor model, comparison with manufacturer data and indication of the prevision accuracy 158
Figure 4.22. Temperature distribution in the storage tank evaluated with the 2D model of Zsembinszki et al. [168] [169] (a, c) and 1D version of the model employed in the work of Pelella et al. [162] (b, d). Water temperature evolution (a, b) and PCM temperature layers (c, d) evolution in 10 hours.....160
Figure 4.23. Validation of the 1D version of the model employed in the work of Pelella et al. [162] with the 2D model of Zsembinszki et al. [168] [169], for water (a) and PCM (b) temperatures and corresponding prevision errors 160
Figure 4.24. Fitting of the PCM storage tank cost function based on manufacturer data [178]. 163
Figure 4.25. Temperature – Specific entropy diagrams in case of air cooled (a) and water-cooled evaporation (b), for fixed conditions of inlet and outlet condenser water temperature of 40-45 °C, for same temperature of air/water inlet at the evaporator of 10 °C, and fixed conditions of heat exchangers heat transfer surfaces.....164
Figure 4.26. COP evolution along one year in heating mode for the system analyzed, in case of only air (a) and multi-source (b) operating modes 165

Figure 4.27. Tank temperature evolution in case of a storage tank volume of 300l, thermal solar collector surface of 20m^2 and employment of a PCM material (a), with a zoom on three days in the month of February (b).....166
Figure 4.28. Pearson coefficients for the effect of all the decisional variables on the objective function investigated (SCOP in red and investment costs in blue), for Athens (a), Strasbourg (b) and Helsinki (c) climate conditions.....167
Figure 4.29. Investment costs vs. SCOP and corresponding Pareto 2D front, for climate conditions of Athens (a), Strasbourg (b) and Helsinki (c). Points A and C are respectively the non-dominated solutions with higher SCOP and lower investment costs, whereas solution B is the closest to the "Utopia Point" represented by a star 168
Figure 4.30. Values of total costs assumed by solutions A, B and C in different investment cost and energy price scenarios, for climate conditions of Athens (a), Strasbourg (b) and Helsinki (c).....172

Summary of Tables

Table 2.1. Mass of refrigerant banked, leaked and leakage rate data from 11000 air conditioning systems in Hungary [28], distinguished for type of refrigerant 21
Table 2.2. Values for refrigerant charge amount, installation emission factor, operating emissions, refrigerant remaining at the disposal and recovered for several typology of refrigeration and air-conditioning equipment, according to [29] 22
Table 2.3. High GWP refrigerants in common use and lower GWP alternatives depending on the refrigeration and air-conditioning sector, according to [31] 23
Table 2.4. Minimum seasonal efficiency to guarantee within the 1st January 2021 for different heating and cooling systems, according to the Eco-design regulation [33] 25
Table 3.1. State of the art regarding the effect of soft faults on performances and measured parameters of the machines, divided per Application/system studied, method, fault investigated and analysis of simultaneous faults 44
Table 3.2. Case study rated characteristics of a 2.6 kW residential heat pump, and geometrical features of the heat exchangers 56
Table 3.3. Values of measured parameters on the machine in cooling mode, in case of fault-free and faulty conditions, for fixed conditions of ambient and indoor temperature of 35 °C and 26 °C. In brackets are reported the differences between the faulty and fault-free specific cases 64
Table 3.4. Effect of standalone and simultaneous faults on measured variables of the machine. The differences are reported in brackets for each specific case 67
Table 3.5. Number of operating hours for which the external temperature rises above 26 °C, for climate conditions of Naples, Miami and Shanghai 69
Table 3.6. Results in terms of SCOP, TEWI and number of maintenance interventions in cooling mode, for all the 64 possible combinations of fault intensities evolutions, for climate conditions of Naples, Miami and Shanghai, and for a not-planned maintenance scenario 74
Table 3.7. Results in terms of SCOP, TEWI and number of maintenance interventions in cooling mode, for all the 64 possible combinations of fault intensities evolutions, for climate conditions of Naples, Miami and Shanghai, and for an ordinary every 4 year maintenance scenario 75
Table 3.8. Results in terms of SCOP, TEWI and number of maintenance interventions in cooling mode, for all the 64 possible combinations of fault intensities evolutions, for climate conditions of Naples, Miami and Shanghai, and for an ordinary every 2 year maintenance scenario 76
Table 3.9. Results in terms of SCOP, TEWI and number of maintenance interventions in cooling mode, for all the 64 possible combinations of fault intensities evolutions, for climate conditions of Naples, Miami and Shanghai, and for an ordinary every year maintenance scenario 78
Table 3.10. Extract of the previous tables for Naples climate conditions, and considering the fault free case and the standalone maximum value for each of the fault intensities considered 80
Table 3.11. Values of measured parameters on the machine in heating mode, in case of fault-free and faulty conditions, for fixed conditions of ambient and indoor temperature of 7 °C and 20 °C. In brackets are reported the differences between the faulty and fault-free specific cases 86
Table 3.12. Number of operating hours for which the external temperature drops below 20 °C, for climate conditions of New York, Beijing and Vienna 88
Table 3.13. Results in terms of SCOP, TEWI and number of maintenance interventions in heating mode, for all the 64 possible combinations of fault intensities evolutions, for climate conditions of New York, Beijing and Vienna, and for a not-planned maintenance scenario 90
Table 3.14. Results in terms of SCOP, TEWI and number of maintenance interventions in heating mode, for all the 64 possible combinations of fault intensities evolutions, for climate conditions of New York, Beijing and Vienna, and for an ordinary every 4 year maintenance scenario 91
Table 3.15. Results in terms of SCOP, TEWI and number of maintenance interventions in heating mode, for all the 64 possible combinations of fault intensities evolutions, for climate conditions of New York, Beijing and Vienna, and for an ordinary every 2 year maintenance scenario 92

Table 3.16. Results in terms of SCOP, TEWI and number of maintenance interventions in heating mode, for all the 64 possible combinations of fault intensities evolutions, for climate conditions of New York, Beijing and Vienna, and for an ordinary every year maintenance scenario 94
Table 3.17. State of the art of FDDE works, divided per Application/System studied, method, fault investigate and presence of simultaneous faults 99
Table 3.18. Fault conditions for points A, B, C, D and for similar thermodynamic cycle to each of the investigated points 107
Table 4.1. State of the art of multi-source heat pumps, divided per typology of energy source, application, type of thermal storage and other categories 118
Table 4.2. Rated characteristics of the solar assisted heat pump studied in Mastrullo et al. [157], and geometrical characteristics of heat exchangers 128
Table 4.3. Numeric results of annual hours in air and sun modes, thermal and electric energy, SCOP, primary energy and TEWI depending on the number of solar collectors, for the three climate conditions investigated 136
Table 4.4. Expressions for the evaluation of coefficient F of the equation 4.6, depending on the flow arrangement of the heat exchanger, according to Shah and Sekulic [101]..... 143
Table 4.5. Main rated characteristics of the case study, and simulation data 152
Table 4.6. List of decisional variables with relative variation ranges, and objective functions employed in the work of Pelella et al. [162] 154
Table 4.7. List of cost functions employed in Pelella et al. [162] for each of the system components 157
Table 4.8. Comparison of results in terms of SCOP, electric energy and simulation time between the 1D version of the model employed in the work of Pelella et al. [162] and the 2D model of Zsembinszki et al. [168] [169]..... 161
Table 4.9. Values assumed by decisional variables of the seven comparison tests presented in Table 4.8 161
Table 4.10. Values of efficiency coefficients and of reference costs depending on the thermal solar collector technology employed in the work of Pelella et al. [162] 162
Table 4.11. Values of efficiency coefficient and specific costs depending on the photovoltaic solar collector technology employed in the work of Pelella et al. [162] and on the surface temperature 162
Table 4.12. Values assumed by decisional variables and objective functions for solutions A, B and C of the Pareto fronts, for each climate condition investigated 170
Table 4.13. Values of discounted payback period (DPB) of solution A and B referred to solution C (representative of a traditional air-to-water heat pump) for each of the cost scenario and climate condition investigated 173

Acknowledgements

Here we are, at the end of this three-year of PhD. It seems yesterday that I began this experience, that I think has strongly contributed to develop my skills and knowledge about the world of research in all its facets. I do not hide all the difficulties that I have to face with, especially during the first year and half, due the pandemic situation which relegated us in our home distorting the real nature of a PhD. Therefore, in the following few lines I would like to thank all those have contributed to the achievement of this goal, until the end of it.

Firstly, I want to acknowledge my PhD tutors, prof. Alfonso William Mauro, and prof. Rita Mastrullo, that, thanks to their great expertise, strongly helped me in the development of the PhD topics presented in this thesis. I would also thank to Luca Viscito, which assisted me as a sort of co-tutor, in overcoming several practical difficulties I met during the three years.

I would like to acknowledge my family member, my mother, my father, my grandmother and my two brothers, which in their everyday life supported me during all this period. I would thank also to all the other people of my family, aunts, uncles and cousins which, also remotely have always made me feel their presence and support.

I want to dedicate a special acknowledgement to my life partner Simona, which for more than ten years is by my side, supporting my choices and bear me especially in this last period, in which I have been a bit distracted due to deadlines and commitments. I am aware that you believe in me every day, and I love you for that. Thank you.

I would thank all my university colleagues and friends, Giovanni and Alice, which are sharing with me this PhD experience for three years now in the same research group. Thanks also to all the other colleagues of the lab, PhD and researchers of the office and of the research group, actual and future, for all the coffees, lunches, celebrations and moments spent together.

I would acknowledge all my friends, Riccardo, Lucio, Elvira, Marco, Sara, Flavia, Luca, (yes, both of you are here this time), Giampiero, Fab®io, with which I have spent numerous moments together that contributed somehow to the achievement of this goal.

Finally, I would thank you, who are reading this thesis and searching your name the acknowledgment section, deliberately written at the end. Apologise me if, due to my thoughtlessness, I forgot to insert your name in here. If you are reading these words, it means that you are present and somehow important for me. I would really appreciate if you can sign yourself in the following blanks, in a way to be in the acknowledgement section and to give me a memory of your presence.

_____

_____

_____

_____

_____

Thank you again and best regards

Francesco